APPLIED COMPUTATIONAL ELECTROMAGNETICS SOCIETY JOURNAL

August 2018
Vol. 33 No. 8
ISSN 1054-4887

The ACES Journal is abstracted in INSPEC, in Engineering Index, DTIC, Science Citation Index Expanded, the Research Alert, and to Current Contents/Engineering, Computing & Technology.

The illustrations on the front cover have been obtained from the research groups at the Department of Electrical Engineering, The University of Mississippi.

EMERITUS ASSOCIATE EDITORS-IN-CHIEF

EMERITUS EDITORIAL ASSISTANTS

AUGUST 2018 REVIEWERS: REGULAR PAPERS

Erkan Afacan
Giulio Antonini
Marco Arjona
Emrah Cetin
William Coburn
Qian Ding
Alistair Duffy
Ibrahim Elshafiey
Ian Flintoft
Alessandro Formisano
Jose Maria Gonzalez-Arbesu
He Huang
Bassem Jmai
Kenichi Kagoshima
Omid Manoochehri
Sofiane Mendaci
Abbas Omar
Antonio Orlandi
Andrew Peterson
Vince Rodriguez
Wei Song
Sellakkutti Suganthi
Xuezhe Tian
Yunus Uzun
Ioannis Vardiambasis
Jiangong Wei
Steven Weiss
Fan Yang
Ali Yapar
Xingqiu Yuan
Huapeng Zhao

AUGUST 2018 REVIEWERS: EXPRESS PAPERS

Vinh Dang
Ozgur Ergul
Ozlem Ozgun

THE APPLIED COMPUTATIONAL ELECTROMAGNETICS SOCIETY JOURNAL

Vol. 33 No. 8 August 2018

TABLE OF CONTENTS – REGULAR PAPERS

TABLE OF CONTENTS – EXPRESS PAPERS

Single-Snapshot Time-Domain Direction of Arrival Estimation under Bayesian Group-Sparse Hypothesis and Vector Sensor Antennas

Marco Muzi[1,2], Nicola Tedeschi[1], Luca Scorrano[3], Vincenzo Ferrara[1], and Fabrizio Frezza[1]

[1]Department of Information Engineering, Electronics, and Telecommunications,
"La Sapienza", University of Rome, Via Eudossiana 18, 00184, Rome, Italy.
marco.muzi@uniroma1.it, nicola.tedeschi@uniroma1.it, fabrizio.frezza@uniroma1.it

[2]Engineering departmental faculty, Campus Bio-Medico University of Rome,
Via Alvaro del Portillo 21, 00128, Rome, Italy.

[3]Elettronica Group, Via Tiburtina Valeria Km 13.700, 00131, Rome, Italy.
Luca.Scorrano@elt.it

Abstract ─ In this work, an optimal single-snapshot, time domain, group-sparse optimal Bayesian DOA estimation method is proposed and tested on a vector sensors antenna system. Exploiting the group-sparse property of the DOA and the Bayesian formulation of the estimation problem, we provide a fast and accurate DOA estimation algorithm. The proposed estimation method can be used for different steering matrix formulations since the optimal standardization matrix is computed directly from the knowledge of the steering matrix and noise covariance matrix. Thanks to this, the algorithm does not requires any kind of calibration or human supervision to operate correctly. In the following, we propose the theoretical basis and details about the estimation algorithm and a possible implementation based on FISTA followed by the results of our computer simulations test.

Index Terms ─ Bayesian optimization, DOA estimation, group-sparsity norm, single snapshot signal, vector sensor antennas.

I. INTRODUCTION

Classic Direction of Arrival (DOA) estimation methods, like ESPRIT [1] and MUSIC [2], based on the signal and noise subspaces subdivision, ensure good performances in the cases of long-snapshots data scenarios. However, the performance of such algorithms degenerates into the presence of short-snapshot signals; as well as when the sources are correlated, or in the presence of low SNR.

An interesting alternative to the subspace methods is the Minimum Norm or the Bayesian approaches, especially after the recent development of the compressive sensing theory [3-6]. Indeed, it is possible to explain the unknown parameter probability distributions as the parameter set that maximizes their a-posteriori probability.

The application of the compressive sensing to electromagnetic problems is reported for example in [7-9], where the problem of the DOA identification of a certain number of incoming waves is studied, and a possible resolution method based on single and long snapshot noisy electromagnetic field measurement is proposed.

Most literature on DOA estimation algorithms, takes into account antenna array configurations for the ease of the steering matrix computation. Usually, the array antennas are sensitive only to one polarization, further simplifying the mathematical model.

Despite the analytical model simplification, the antenna array needs a certain space for the installation.

Thanks to the vector sensor antennas, it is possible to obtain an unambiguous DOA estimation through the simultaneous measurement of the electric and magnetic fields, univocally defining the Poynting vector direction.

As it is known, the field measured by a vector sensor antenna depends on the polarization of the impinging wave. Generally, we must take into account the polarization angle or, at least, the horizontal and vertical components of the wave polarization vector. A way to overcome this problem is to consider the horizontal and the vertical polarizations as different cases, allowing the system to be sensitive only to one of them at a time.

The use of a vector sensor antenna allows measuring simultaneously all the electromagnetic field components permitting a DOA estimation regardless the actual field polarization.

In this work, the adoption of a time domain, single snapshot, optimal group-sparse Bayesian algorithm for the DOA estimation problem is proposed, and its performances are reported.

Submitted On: November 30, 2017
Accepted On: July 27, 2018

The choice of the group-sparse solution hypothesis, allows us to simplify the construction of the steering matrix, thanks to the superposition effect of the components of the polarization vector. Indeed, the group sparsity on the problem solution (i.e., the elevation and azimuth angles of the DOA impinging waves) means that the sparsity is imposed on the number of the impinging waves and not on their singular components, as in the case of a simply sparse solution. The main advantage of the group sparsity hypothesis, with respect to the simple sparsity hypothesis, consists in the mitigation of spurious elements in the estimated solution.

II. METHODS

The first step in the DOA estimation is the steering matrix definition. We suppose that the impinging wave is homogeneous and plane, without restraint about the polarization.

We define the steering matrix associated with an ideal vector sensor antenna, with all the elements co-located, able to measure all the six components of the electric and magnetic field according to [10]:

$$A(\theta,\varphi,\gamma,\eta)=\left[\ldots,a_k\left(\theta_k,\varphi_k,\gamma_{k,l},\eta_{k,l}\right),\ldots\right]= \begin{bmatrix} \cos(\theta_k)\cos(\varphi_k) & -\sin(\varphi_k) \\ \cos(\theta_k)\sin(\varphi_k) & \cos(\varphi_k) \\ -\sin(\theta_k) & 0 \\ \ldots, \quad -\sin(\varphi_k) & -\cos(\theta_k)\cos(\varphi_k),\ldots \\ \cos(\varphi_k) & -\cos(\theta_k)\sin(\varphi_k) \\ 0 & \sin(\theta_k) \end{bmatrix} \begin{bmatrix} \sin(\gamma_{k,l})e^{j\eta_{k,l}} \\ \cos(\gamma_{k,l}) \end{bmatrix}, \tag{1}$$

where: $a_k\left(\theta_k,\varphi_k,\gamma_{k,l},\eta_{k,l}\right)$ is the k–th steering vector representing the Green function associated to the k–th incoming wave with: elevation angle $\theta_k\in[0,2\pi]$; azimuth angle $\varphi_k\in[0,\pi]$; auxiliary polarization angle $\gamma_{k,l}$ and polarization phase difference $\eta_{k,l}$. In our case, we assume that $\eta_{k,l}$ is equal to zero and $\gamma_{k,l}$ is alternately equal to zero or $\pi/2$ for each k-value: in this way we obtain a group of two steering vectors defining the φ - and θ – wave polarization components for each DOA, obtaining a steering matrix with a number of columns twice the number of DOA taken into account for its construction:

$$A\left(\theta,\varphi,0,\left[0,\frac{\pi}{2}\right]\right)=\left[\ldots,a_k\left(\theta_k,\varphi_k,0,\left[0,\frac{\pi}{2}\right]\right),\ldots\right]= =\begin{bmatrix} \cos(\theta_k)\cos(\varphi_k) & -\sin(\varphi_k) \\ \cos(\theta_k)\sin(\varphi_k) & \cos(\varphi_k) \\ -\sin(\theta_k) & 0 \\ \ldots, \quad -\sin(\varphi_k) & -\cos(\theta_k)\cos(\varphi_k),\ldots \\ \cos(\varphi_k) & -\cos(\theta_k)\sin(\varphi_k) \\ 0 & \sin(\theta_k) \end{bmatrix}. \tag{2}$$

The steering matrix obtained from Eq. (2) is purely real, and each column element defines the gain of the system as a function of the wave polarization components and DOA.

Once defined the steering matrix, we can write the measurement model as follows:

$$S(t)=A\left(\theta_k,\varphi_k,0,\left[0,\frac{\pi}{2}\right]\right)X(t)+n(t), \tag{3}$$

where: $S(t)$ is the signal recorded by the electromagnetic sensors; $X(t)$ is the time-varying signal of the incoming electromagnetic wave; $n(t)$ is a zero-mean Gaussian additive noise with covariance matrix Ψ_n: $N(0,\Psi_n)$. For real signals, we can make use directly of Eq. 3 with the steering matrix defined in Eq. 2.

A. Optimal Bayesian group-sparse DOA estimation method

Vector sensor antennas allow unambiguous DOA estimation. In this work, we propose an approach for the DOA estimation different from the classic ones based on MUSIC or on the direct computation of the Poynting vector from the measured fields. In fact, unlike MUSIC, we use only a single-snapshot for the estimation and, in place of the direct Poynting vector, we take into account all the field components, mitigating the contribution of noise spikes on the single field components.

As proposed in [11] it is possible to solve efficiently a severely ill-posed linear system (i.e., with a number of unknowns many order of magnitude greater than the number of equations) under the hypothesis of the existence of a sparse solution.

As usual in the resolution of ill-posed ill-conditioned minimization problems, we must resolve a so-called, fat and short matrix. In this kind of problems, the choice of a proper pre-conditioner is of fundamental importance, since it can ensure the correct estimation of the sparse solution.

In this work, we propose an optimal Bayesian group-sparse method, able to provide an unbiased DOA estimator derived from the Bayesian formulation of the DOA estimation problem for the group-sparse regularized problem.

The unknown parameters vector X is supposed to be sparse, thanks to the limited number of expected DOA to estimate. The simple sparsity condition, however, can lead to a wrong solution especially if the wave does not presents a dominant polarization component. It is possible to overcome this issue through the group sparse hypothesis. Since the chosen model associates a group of parameters at each DOA, we consider all the elements of the group as a unique entity (e.g., through the L_2^2 norm evaluated over the group or a similar metric) and then we impose that only a small amount of these entities present non-zero metric obtaining a group sparse condition. This change allows a better identification of the polarization components of the impinging wave and, finally of the DOA.

Recalling Eq. (3), we can state that after the elision of the dependencies:

$$S\text{-}AX=n \rightarrow S\text{-}AX\sim N(0,\Psi_n). \tag{4}$$

Then we can formulate the following likelihood function for the signal revealed by the sensors from the

generic impinging EM field as a function of its DOA components:

$$p(S|X) \propto \exp(-0.5[AX-S]^T[\Psi^N]^{-1}[AX-S]), \quad (5)$$

we assume that the impinging field can be decomposed into a finite and restrained number of elementary plane waves (i.e., the actual DOA number is of the order of few unities, eventually just equal to one), each one characterized by their polarization components. Then we can define the following likelihood function for the polarization component magnitudes:

$$p(X|\lambda) \propto \exp\left(-\sum_{k=1:N} \lambda_{X_k}\left[X_k^T \Psi^{X_k} X_k\right]^{0.5}\right) = \exp\left(-\lambda_X [X^T \Psi^X X]^{0.5}\right), \quad (6)$$

where we denote with X_k the k-th steering vector associated to the k-th DOA; the matrix Ψ^X is, for construction, a block diagonal matrix with the task to select, and eventually weight, only the steering vectors associated to the k-th DOA; and λ is a diagonal matrix with entries described by the exponential probability distribution:

$$p(\lambda_X) = \exp\left(-\beta \sum_{k=1:N} \lambda_{X_k}\right), \quad (7)$$

where the parameter β is such that the mean value is near zero and then the realization of $p(X|\lambda)$ can be considered sparse.

Finally, we define the probability that an impinging plane wave from a certain DOA can produce the measured signal combining Eqs. 5-7 thanks to the Bayesian chain rule:

$$p(X|S) \propto p(S|X)p(X|\lambda)p(\lambda) = \exp\left(-0.5[AX-S]^T[\Psi^N]^{-1}[AX-S] - \lambda_X (X^T \Psi^X X)^{0.5} - \beta\lambda_X\right). \quad (8)$$

We impose the change of variable: $Z = [\Psi^X]^{0.5} X$, and then Eq. 8 becomes:

$$p(Z|S) \propto \exp(-0.5\left[A[\Psi^X]^{-0.5}Z-S\right]^T[\Psi^N]^{-1}\left[A[\Psi^X]^{-0.5}Z-S\right] - \lambda_X (Z^T Z)^{0.5} - \beta\lambda_X). \quad (9)$$

Since the exponent argument is composed by the sum of positive defined matrices, we can assert that the optimal DOA weights array $\hat{Z}$ is such to maximize the a posteriori probability density expressed in Eq. 8; in other words:

$$\hat{Z} = \min_Z F(Z) = \min_Z (0.5[A[\Psi^X]^{-0.5}Z - S]^T * [\Psi^N]^{-1}[A[\Psi^X]^{-0.5}Z - S] + \lambda_X (Z^T Z)^{0.5} + \beta\lambda_X) \quad (10)$$

The minimum point $\hat{Z}$, thanks to the convexity of $F(Z)$, must satisfy the nullification of the first-derivative of the argument of Eq. 10:

$$\left.\frac{\partial F(Z)}{\partial Z}\right|_{Z=\hat{Z}} = 0.5\left[A\left[\Psi^X\right]^{-0.5}\hat{Z}-S\right]^T\left[\Psi^N\right]^{-1}A\left[\Psi^X\right]^{-0.5} + 0.5\lambda_X\left(\hat{Z}^T\hat{Z}\right)^{-0.5}\hat{Z}^T = 0. \quad (11)$$

Rearranging the Eq. 11 terms we obtain the following expression for $\hat{Z}$ value:

$$\hat{Z} = \left[[\Psi^X]^{-0.5}A^T[\Psi^N]^{-1}A[\Psi^X]^{-0.5} + \lambda_X\left(\hat{Z}^T\hat{Z}\right)^{-0.5}I\right]^{-1} * A^T[\Psi^N]^{-1}[\Psi^X]^{-0.5}S. \quad (12)$$

Now we can derive the expression of the matrix Ψ^X. Note that, although Eq. 12 is implicit, the quantity $\lambda_X\left(\hat{Z}^T\hat{Z}\right)^{-0.5}$ is the inverse of the L_2 norm of the unknown solution multiplied by the unknown parameter λ_X; since both multiplicands are unknowns, we can take into account them as a single unknown parameter.

The optimal definition of the standardization matrix Ψ^X is an active branch of the inverse-problems research, and the formulation is related to the form of the minimum problem to be solved. The role of the standardization matrix consists in the minimization of the correlation between the steering matrix columns in order to mitigate the DOA estimation error. The structure of the optimal standardization matrix is strictly related to the steering matrix singular values spectrum and to the restrains terms imposed to the minimum problem solution. Since the steering matrix is related to the actual antenna system, it is important to provide an optimal standardization matrix for any given steering matrix, ensuring the optimality of the computed solution independently of the particular form of the steering matrix.

In this work, we provide the optimal formulation of Ψ^X, ensuring the maximal independence between the DOAs (i.e., the covariance matrix must be proportional to the identity matrix). In particular, we impose that the estimated solution covariance matrix must be diagonal:

$$E\{\hat{Z}\hat{Z}^T\} = \left(\left[\hat{\Psi}^X\right]^{-0.5}A^T[\Psi^N]^{-1}A\left[\hat{\Psi}^X\right]^{-0.5} + \lambda_X\left(\hat{Z}^T\hat{Z}\right)^{-0.5}I\right)^{-1} * * \left[\hat{\Psi}^X\right]^{-0.5}A^T[\Psi^N]^{-1}E\{SS^T\}[\Psi^N]^{-1}A\left[\hat{\Psi}^X\right]^{-0.5} * * \left(\left[\hat{\Psi}^X\right]^{-0.5}A^T[\Psi^N]^{-1}A\left[\hat{\Psi}^X\right]^{-0.5} + \lambda_X\left(\hat{Z}^T\hat{Z}\right)^{-0.5}I\right)^{-1} \propto I. \quad (13)$$

Since: $E\{SS^T\} = \Psi^N$, from Eq. 13, with some algebra, we obtain:

$$\left(1-2\lambda_X\left(\hat{Z}^T\hat{Z}\right)^{-0.5}\right)I \propto A^T[\Psi^N]^{-1}A\left[\hat{\Psi}^X\right]^{-1} + +\lambda_x^2\left(\hat{Z}^T\hat{Z}\right)^{-1}(A^T[\Psi^N]^{-1}A)^{-1}\left[\hat{\Psi}^X\right]. \quad (14)$$

Since, for invertible matrices, the relation: $AB^{-1} = BA^{-1}$ holds, from Eq. 14 we obtain:

$$\frac{1-2\lambda_X\left(\hat{Z}^T\hat{Z}\right)^{-0.5}}{1+\lambda_x^2\left(\hat{Z}^T\hat{Z}\right)^{-1}}I \propto A^T[\Psi^N]^{-1}A\left[\hat{\Psi}^X\right]^{-1}. \quad (15)$$

The left-hand side term of Eq. 15 is a diagonal matrix, then, since $\hat{\Psi}^X$ is a diagonal block matrix, we can assert that:

$$\left[\hat{\Psi}_k^X\right] = \mathrm{diag}(a_k^T[\Psi^N]^{-1} * a_k). \quad (16)$$

The estimated solution covariance matrix $\hat{\Psi}^X$, in the form presented in Eq. 16, ensures the maximal independence between the estimated elements.

B. Numerical results

The simplest way to obtain a group-sparse solution is a proper numerical code able to solve the problem in Eq. 9. Indeed, the minimization problem in Eq. (9) is solved by FISTA [11], with a modified shrinkage

operator implementation for the group-sparse property imposition.

We use a hard threshold shrinkage instead of the soft one proposed in the original work in order to obtain a gain in terms of computation time. In our experience, this choice does not affect the algorithm performances in terms of estimation precision.

The group-sparse shrinkage operator is obtained by the suppression of all the solution elements that present a group L_2 norm lower than the user-defined threshold value.

The estimation performances, in term of RMS estimation error, are evaluated for different SNR levels: 30 dB, 20 dB, 10 dB, 5 dB and 0 dB. For each SNR value, the algorithm is tested for different steering matrices, with the spatial resolution equal to 1, 2 and 4 degrees, in order to evaluate the influence of the resolution on the final estimation result. The same simulations are been executed with and without the optimal standardization.

The effects of the optimal standardization are evaluated by the introduction of a uniformly distributed scalar gain (defined in the interval 0.5-1) in the steering vectors, in order to simulate a generic anisotropic antenna system gain pattern, and then evaluate the capability of the algorithm to recover the antenna system isotropy.

The algorithm is implemented in MATLAB on a PC with a CPU Intel i7 @ 3.07GHz, RAM 24 GB, and Windows 10 OS.

The synthetic data are generated making use of Eq. 3; varying the DOA angles (θ,φ) in the interval $[0,\pi] \times [0,2\pi]$ in order to cover the field of view of the sensor antenna. The different polarization angles are obtained by the weighted sum of the group steering vectors correspondent to the k-th DOA couple angle: i.e., for each DOA, the algorithm is tested for eight different polarization angles.

The average execution time, estimated over two and half million algorithm runs (i.e., five SNR values, for eight different polarization angles, and 180 for 360 different DOA directions), is reported in Table 1 as a function of the steering matrix spatial resolution.

The run-time do not takes into account the computation of the standardization matrix and of the steering matrix, since they depend only on a priori known parameters like the noise covariance matrix and the sensor antenna configuration and gain pattern, and then they can be pre-computed and stored once the antenna system is defined.

Table 1: Algorithm run-time as a function of the steering matrix resolution

Steering Matrix Resolution	Average Run-Time
1 degree	0.050 s
2 degrees	0.028 s
4 degrees	0.015 s

III. DISCUSSION

As shown in Table 2, the RMS estimation errors degrade, as expected, with the SNR, and the estimation can be considered poor for SNR values lower than 5 dB SNR. It is important to note that the SNR, here, is defined on the single time snapshot, and then without any information about the time course of the signal; then the SNR is to be intended as the residual SNR from the filtering step.

It is interesting to note that the steering matrix spatial resolution does not affect the estimation error when greater than 10 dB; this result can be used to choose the steering matrix resolution in function of the expected SNR level, with a significant computation time saving.

As expected, the adoption of the optimal standardization matrix (Table 2, normal entries) ensures an improvement of the estimation accuracy. In fact, when the standardized steering matrix is adopted, the RMS estimation error is significantly lower; this is evident in the higher SNR level cases, where the estimation error is equal, in the worst cases, to half of the steering vectors spatial resolution. In general, the estimation accuracy is considered "good" until the threshold of 10 dB SNR, where the RMS estimation error is less than five degrees in elevation and azimuth angles, regardless the spatial resolution.

IV. CONCLUSIONS

In this work, an optimal single snapshot, time domain, group-sparse Bayesian DOA estimation method is proposed and tested on a vector sensor antenna system. As reported in the discussion section, it is possible to obtain an accurate DOA estimation also in the presences of imperfections in the steering matrix definition and with a single, noisy, time signal snapshot. The algorithm can be extended to sensors array configuration, or more complex sensor antennas elements [12-14], just with a proper definition of the steering matrix.

Table 2: RMS error percentile distributions (in degree) for optimally (bold) and non-optimally (plain) standardized steering matrix for 1, 2 and 4 degrees steering matrix resolution

SNR (Res.)	Low Limit	25-Perc.	Median	75-Perc.	Up Limit	Low Limit	25-Perc.	Median	75-Perc.	Up Limit
	Elevation RMSE					Azimuth RMSE				
30 dB (1°)	**0**/0	**0.1**/2.2	**0.2**/3.5	**0.2**/4.7	**0.5**/8.5	**0**/0	**0.1**/3.5	**0.2**/5.7	**0.2**/10	**0.5**/21
30 dB (2°)	**0**/0	**0**/3	**0.5**/4.5	**1**/6.5	**1**/11	**0**/0	**0**/5	**0**/8	**1**/16	**1**/32
30 dB (4°)	**0**/0	**0**/4	**1**/6	**1**/8	**2**/14	**0**/0	**1**/7	**1**/11	**2**/24	**3**/49
20 dB (1°)	**0**/0	**0.1**/2.2	**0.2**/3.5	**0.2**/4.7	**0.5**/8.5	**0**/0	**0.1**/4	**0.2**/6	**0.2**/9	**0.5**/20
20 dB (2°)	**0**/0	**0**/3	**0.2**/4	**0.5**/7	**1**/10	**0**/0	**0**/5	**0**/7	**1**/17	**2.2**/32
20 dB (4°)	**0**/0	**0**/4	**1**/6	**1.2**/8	**2**/14	**0**/0	**1**/7	**1**/11	**2**/25	**3.5**/49
10 dB (1°)	**0**/0	**1.1**/2.7	**1.8**/4	**2.5**/5.3	**4.5**/9	**0**/0	**1.8**/4	**2.3**/5.5	**3.5**/10	**4.8**/22
10 dB (2°)	**0**/0	**1.2**/3	**1.7**/5	**2.5**/8	**4**/11	**0**/0	**2**/6	**2.7**/8	**3.5**/20	**5**/35
10 dB (4°)	**0**/0	**1.5**/6	**2**/8	**2.7**/12	**4.5**/18	**0**/0	**2**/7	**2.8**/11	**4.5**/25	**5**/49
5 dB (1°)	**0**/0	**3.8**/5	**6.2**/7	**8.5**/9	**15**/16	**0**/0	**6.3**/6	**9**/8	**11**/11	**20**/23
5 dB (2°)	**0**/0	**4**/5.5	**6.2**/8	**8.5**/10	**15**/18	**0**/0	**6**/9	**9**/14	**12**/24	**20**/47
5 dB (4°)	**0**/0	**4**/6	**6**/9	**8**/12	**15**/19	**0**/0	**6**/11	**9**/17	**12**/37	**21**/77
0 dB (1°)	**0**/0	**19**/19	**27**/28	**38**/37	**68**/69	**0**/0	**43**/41	**61**/63	**87**/30	**154**/157
0 dB (2°)	**0**/0	**18**/19	**27**/28	**38**/39	**68**/70	**0**/0	**43**/44	**62**/60	**88**/90	**155**/158
0 dB (4°)	**0**/0	**17**/18	**27**/28	**38**/38	**68**/70	**0**/0	**42**/43	**63**/64	**88**/90	**154**/155

REFERENCES

[1] R. Roy and T. Kailath, "ESPRIT-estimation of signal parameters via rotational invariance techniques," *IEEE Transactions on Acoustics, Speech, and Signal Processing*, vol. 37, no. 7, pp. 984-995, 1989.

[2] R. Schmidt, "Multiple emitter location and signal parameter estimation," *IEEE Transactions on Antennas and Propagation*, vol. 34, no. 3, pp. 276-280, 1986.

[3] D. L. Donoho, "Compressed sensing," *IEEE Transactions on Information Theory*, vol. 52, no. 4, 1289-1306, 2006.

[4] D. L. Donoho and Y. Tsaig, "Extensions of compressed sensing," *Signal Processing*, vol. 86, no. 3, pp. 533-548, 2006.

[5] S. S.Chen, D. L. Donoho, and M. A. Saunders, "Atomic decomposition by basis pursuit," *SIAM Review*, vol. 43, no. 1, pp. 129-159, 2001.

[6] E. J. Candes and T. Tao, "Near-optimal signal recovery from random projections: Universal encoding strategies," *IEEE Transactions on Information Theory*, vol. 52, no. 12, pp. 5406-5425, 2006.

[7] W. Zhu and B. X. Chen, "Novel methods of DOA estimation based on compressed sensing," *Multidimensional Systems and Signal Processing*, vol. 26, no. 1, pp. 113-123, 2015.

[8] M. Carlin, P. Rocca, G. Oliveri, F. Viani, and A. Massa, "Directions-of-arrival estimation through Bayesian compressive sensing strategies," *IEEE Transactions on Antennas and Propagation*, vol. 61, no. 7, pp. 3828-3838, 2013.

[9] A. Massa, P. Rocca, and G. Oliveri, "Compressive sensing in electromagnetics - A review," *IEEE Antennas and Propagation Magazine*, vol. 57, no. 1, pp. 224-238, 2015.

[10] A. Nehorai and E. Paldi, "Vector-sensor array processing for electromagnetic source localization," *IEEE Transactions on Signal Processing*, vol. 42, no. 2, pp. 376-398, 1994.

[11] A. Beck and M. Teboulle, "A fast iterative shrinkage-thresholding algorithm for linear inverse problems," *SIAM Journal on Imaging Sciences*, vol. 2, no. 1, pp. 183-202, 2009.

[12] M. Parise, "Exact EM field excited by a short horizontal wire antenna lying on a conducting soil," *AEU - International Journal of Electronics and Communications*, vol. 70, pp. 676-680, 2016.

[13] M. Parise, "Transverse magnetic field of infinite line source placed on ground surface," *Electronics Letters*, vol. 51, pp. 1478-1480, 2015.

[14] M. Parise, "An exact series representation for the EM field from a circular loop antenna on a lossy half-space," *IEEE Antennas and Wireless Propagation Letters*, vol. 13, pp. 23-26, 2014.

Marco Muzi received his B.S. in Biomedical Engineering in 2009. He received his Ph.D. in Applied Physics in 2014 with a dissertation on MEG Inverse Problems. He currently works on low frequency dielectric behavior and characterization of biological cell culture,

optimization problems and metamaterials design at "La Sapienza" university of Rome.

Nicola Tedeschi received the Master degree in Electronic Engineering, from "La Sapienza" University of Rome in 2009. He received the Ph.D. in Electromagnetics from the same University in 2013. His research interests concern microwave amplifiers, electromagnetic scattering by objects near to interfaces, propagation of inhomogeneous waves in dissipative media, and the characterization of dispersive properties of natural and artificial materials.

Luca Scorrano (M'12) received the B.S. degree (summa cum laude) in Electrical Engineer from University Roma Tre, Rome, Italy in 2005 and the M.S. (summa cum laude) in Electrical Engineer from University Roma Tre, Rome, Italy in 2007. He earned the Ph.D. in Applied Electromagnetics in 2011. From 2015 he is a System Engineer in the Research & Innovation Department at Elettronica S.p.A., Rome, Italy.

His research interests are in the field of broadband antennas and arrays, Frequency Selective Surfaces (FSS), Artificial Magnetic Conductors (AMC), composite material, meta-materials, electromagnetic theory, photonics and plasmonics. He currently serves as peer reviewer for many IET journals in the field of electromagnetics and optics and for IEEE APS Letters. He is co-author of a book, author of more than 40 international publications, and 6 patent applications.

Vincenzo Ferrara joined the Department DIET, Sapienza University of Rome, as Associate Professor of Electronics since 2001, and he is scientific responsible of Electronics for the Environment Lab of the DIET. The scientific research concerns different topics, focusing electronic systems for the environment, such as technologies for planning and sustainable development, satellite navigation, WSN, energy harvesting and so on.

Fabrizio Frezza was born in Rome, Italy, on October 31, 1960. He received the "Laurea" (degree) "cum laude" in Electronic Engineering in 1986 and the Doctorate degree in Applied Electromagnetics and Electrophysical Sciences in 1991, both from "La Sapienza" University of Rome. In 1986, he joined the Department of Electronics of the same University, where he has been Full Professor of Electromagnetic Fields since 2005. His research activity has concerned guiding structures, antennas and resonators for microwaves and millimeter waves, numerical methods, scattering, optical propagation, plasma heating, anisotropic media, artificial materials and metamaterials, cultural-heritage applications. Frezza is a Member of Sigma Xi and Senior Member of IEEE and OSA.

Efficient Sub-Gridded FDTD for Three-Dimensional Time-Reversed Electromagnetic Field Shaping

Xiao-Kun Wei, Wei Shao, Xiao Ding, and Bing-Zhong Wang

School of Physics
University of Electronic Science and Technology of China, Chengdu, Sichuan 610054, China
weixiaokun1990@163.com, weishao@uestc.edu.cn, xding@uestc.edu.cn, bzwang@uestc.edu.cn

Abstract ─ Based on the space-time focusing property of the time reversal technique, the electromagnetic field shaping of arbitrary patterns is easily realized by using an efficient sub-gridded finite-difference time-domain (FDTD) method in this paper. It is an electrically large and multiscale problem if the desired shaping field requires high resolution. With the advantage of the sub-gridded scheme, the electromagnetic field shaping region can be locally discretized with dense grids, which is embedded in global coarse grids. Then, the Courant-Friedrich-Levy (CFL) limit can be extended by employing the spatial filtering scheme to filter out the unstable harmonics inside the dense grid region. Thus, the number of total unknowns is largely reduced and a common time step size chosen from the CFL limit of the coarse grid is used throughout the computational domain. Simulation results with two kinds of boundary conditions are provided to demonstrate the availability of the spatially-filtered sub-gridded FDTD method for electromagnetic field shaping.

Index Terms ─ Electromagnetic field shaping, finite-difference time-domain (FDTD) method, sub-gridded scheme, time reversal (TR) technique.

I. INTRODUCTION

The time reversal (TR) technique, which is very promising in controlling electromagnetic waves in complex media due to its space-time focusing property [1]-[4] and super-resolution characteristic [5]-[7], has been widely employed in wireless communications, microwave imaging and detection, medical treatment, and wireless power transformation [8], [9]. Based on the TR technique, the "L"-shaped electromagnetic field was generated through experiment in an aluminum cavity [10], which provides an effective way to physically generate arbitrarily shaped microwave fields inside an interested region. Source reconstruction, realized by using several methods [11]-[14], is very similar to the electromagnetic field shaping. Different from the field shaping, the source reconstruction is to find unknown sources by using the received signals at preselected output locations.

To numerically solve such a time-domain electromagnetic problem, the finite-difference time-domain (FDTD) method is often employed because of its simplicity and versatility [15]. Usually, there are ten to twenty wavelengths along each direction in the computational region of electromagnetic field shaping. If a predefined field pattern requires high spatial resolution, this area is discretized with fine grids. In the FDTD simulation, a maximal size of the time step should be determined by a minimal size of the spatial grid in order to keep numerical stability, according to the Courant-Friedrich-Levy (CFL) condition [15]. Thus, the computational efficiency of FDTD with uniform dense grids is strictly constrained due to the large number of unknowns and a very small time step size.

On the one hand, to reduce the number of total unknowns of an electrically large structure, a sub-gridded scheme in which local dense grids are located inside global coarse grids is a good fit [16]. On the other hand, to extend the CFL limit imposed by the minimal grid size of a computational domain involving multiscale grid division, the spatial filtering scheme can be used to filter out the unstable harmonics inside the sub-gridded region [17], [18]. In this paper, combined with two procedures of the TR technique, an efficient spatially-filtered sub-gridded FDTD method is employed to implement the electromagnetic field shaping in three-dimensional (3D) space with two different boundary conditions. According to the CFL limit of the coarse grid, a common time step size can be chosen for the whole computational domain in a stable fashion. In the numerical experiments, "L"-shaped and "E"-shaped microwave fields are generated within a perfectly electric conductor (PEC) cavity, as presented in [10], to demonstrate the availability of the proposed method. Furthermore, these two desired patterns are generated in free space truncated by the perfectly matched layer (PML) [19]. For the free space case, more TR antenna elements are needed to have a high-quality shaped microwave field.

The rest of this paper is organized as follows. In Section II, the numerical implementation for generating

Submitted On: June 11, 2018
Accepted On: August 11, 2018

an arbitrarily shaped electromagnetic field is given. Section III verifies the accuracy and efficiency of the spatially-filtered sub-gridded FDTD method and shows the numerical results of generating various field patterns. The conclusion is presented in Section IV.

II. THEORIES AND FORMULATIONS

Based on the TR technique, the microwave field is generated by locating a shaping antenna array inside the electromagnetic shaping region and by placing a TR antenna array outside, as shown in Fig. 1.

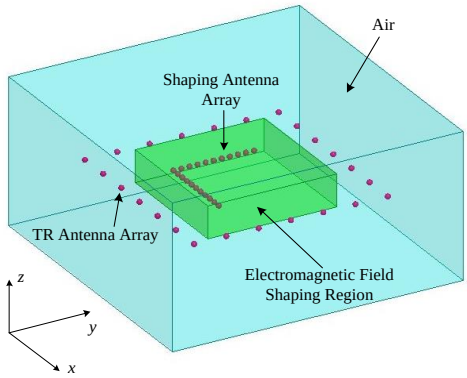

Fig. 1. Computational domain of generating a predefined electromagnetic field based on the TR technique.

With reference to [20], the time-reversed electric field vector can be rewritten in frequency domain as:

$$\boldsymbol{E}^{\mathrm{TR}}(\boldsymbol{r},\boldsymbol{r}_s;\omega)=-\frac{\omega\mu}{\lambda}\left\{\left(\overline{\overline{I}}+\frac{\nabla\nabla}{k^2}\right)\left(\frac{\sin k|\boldsymbol{r}-\boldsymbol{r}_s|}{k|\boldsymbol{r}-\boldsymbol{r}_s|}\right)\right\}\boldsymbol{i}^*(\omega), \tag{1}$$

which indicates that $\boldsymbol{E}^{\mathrm{TR}}(\boldsymbol{r}, \boldsymbol{r}_s; \omega)$ will be maximized at the original source point $\boldsymbol{r}_s$. The time-domain time-reversed electric field vector can also be given by inverse Fourier transform as:

$$\boldsymbol{E}^{\mathrm{TR}}(\boldsymbol{r},\boldsymbol{r}_s;t)=\mu\frac{\partial}{\partial t}\int_{-\infty}^{+\infty}\left\{\overline{\overline{G}}^{*}(\boldsymbol{r},\boldsymbol{r}_s)-\overline{\overline{G}}(\boldsymbol{r},\boldsymbol{r}_s)\right\}\boldsymbol{i}^*(\omega)\,\mathrm{e}^{\mathrm{j}\omega t}\mathrm{d}\omega, \tag{2}$$

which means that the time-reversed electric field vectors $\boldsymbol{E}^*(\boldsymbol{r}, \boldsymbol{r}_s)$ will simultaneously arrive at $\boldsymbol{r}_s$ and accumulated with each other, wherever the $\boldsymbol{E}^*(\boldsymbol{r}, \boldsymbol{r}_s)$ is located. The combination of (1) and (2) demonstrates the space-time focusing property of the time-reversed electromagnetic waves. Based on this property, we can closely place several shaping antenna elements to generate a smooth field of the desired shape.

To numerically realize the electromagnetic field shaping with an arbitrary microwave pattern, an efficient sub-gridded FDTD with extended CFL limit is a good choice. Since the spatial filtering scheme is employed to filter out the unstable harmonics of the dense grid, the 3D CFL limit inside the sub-gridded region can be extended and rewritten as:

$$\Delta t \le \Delta t_{\mathrm{CFL}} \times CE, \tag{3}$$

where Δt_{CFL} is the conventional CFL limit of the dense grid, and *CE* is a CFL extension factor that is defined as:

$$CE=\frac{1}{\sin\dfrac{k_{\max}\Delta}{2\sqrt{3}}}, \tag{4}$$

where Δ is the spatial grid size, $k_{\max}$ is the maximal value of the numerical wavenumbers determined by a desired *CE* factor. To implement the spatial filtering scheme, three additional stages are incorporated into the FDTD time-stepping algorithm. Firstly, the magnetic field components inside the sub-gridded region are transformed into frequency domain by Fourier transform. Secondly, a spherical low-pass spatial filter is defined as:

$$\overline{\boldsymbol{F}}(\boldsymbol{k})=\begin{cases}1, & \text{for } \sqrt{k_x^2+k_y^2+k_z^2}\le k_{\max}\\ 0, & \text{otherwise}\end{cases}, \tag{5}$$

which is applied to the frequency-domain magnetic field components inside the sub-gridded region. Thirdly, the filtered magnetic field components are transformed back to the space domain by inverse Fourier transform. Thus, a common time step size calculated from the CFL limit of the coarse grid can be used throughout the computational region, and no interpolation and extrapolation is needed to synchronize coarse and dense grids in temporal domain.

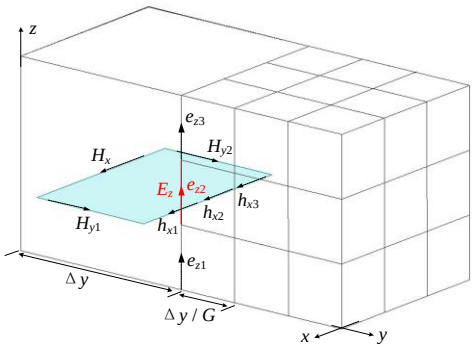

Fig. 2. Electromagnetic field component arrangement at the coarse-dense grid interface for a mesh refinement ratio of three.

In spatial domain, the tangential electric field components are located on the interfaces of the coarse and dense grids. Here, the grid refinement ratio *G* is chosen as 3. Then, the data are exchanged via contour integrals of weighted coarse and dense fields, as shown in Fig. 2. Field components in the coarse grid are denoted by capital letters and those in the dense grid are shown with the lower case letters. To illustrate the data-exchanging scheme on the interfaces, the electric field component of E_z is taken as an example.

On the interfaces, the update equation of E_z, constructed from the integral form of the Maxwell's equations, is given as:

$$E_z^{n+1}\Big|_{i,j,k+\frac{1}{2}} = E_z^{n}\Big|_{i,j,k+\frac{1}{2}} + \frac{\Delta t}{\varepsilon_0 \Delta x}\left(H_y^{n+\frac{1}{2}}\Big|_{i+\frac{1}{2},j,k+\frac{1}{2}} - H_y^{n+\frac{1}{2}}\Big|_{i-\frac{1}{2},j,k+\frac{1}{2}} \right) - \frac{\Delta t}{\varepsilon_0 \Delta y}\left(H_x^{n+\frac{1}{2}}\Big|_{i,j+\frac{1}{2},k+\frac{1}{2}} - H_x^{n+\frac{1}{2}}\Big|_{i,j-\frac{1}{2},k+\frac{1}{2}} \right). \quad (6)$$

As revealed in Fig. 2, the effective area of the contour on the interface is changed. Therefore, the formulation to update E_z is a modified form of (6), which is:

$$E_z^{n+1} = E_z^{n} + \frac{\Delta t}{\varepsilon_0 \Delta x}\left(H_{y1}^{n+\frac{1}{2}} - H_{y2}^{n+\frac{1}{2}} \right) - \frac{\Delta t}{\varepsilon_0 \Delta y \dfrac{G+1}{2G}}\left(\sum_{i=1}^{G} \frac{1}{G} h_{xi}^{n+\frac{1}{2}} - H_x^{n+\frac{1}{2}} \right), \quad (7)$$

and e_z is directly calculated from E_z by:

$$e_{zi}(i = 1, 2, \cdots, G) = E_z. \quad (8)$$

Once the electric field components e_z on the interfaces are obtained from (8), both electric and magnetic field components can be updated with a large time step size inside the sub-gridded region.

The flowchart in which the spatially-filtered sub-gridded FDTD method and the TR technique are combined to generate a desired electromagnetic field is shown in Fig. 3. The TR process defines the original excitation and boundary condition of a predefined electromagnetic field shaping scenario and sends those initial parameters to the spatially-filtered sub-gridded FDTD simulation. Then, the spatially-filtered sub-gridded FDTD calculates wave propagation and returns the time-domain waveforms back to the TR technique. Finally, the desired microwave field can be achieved.

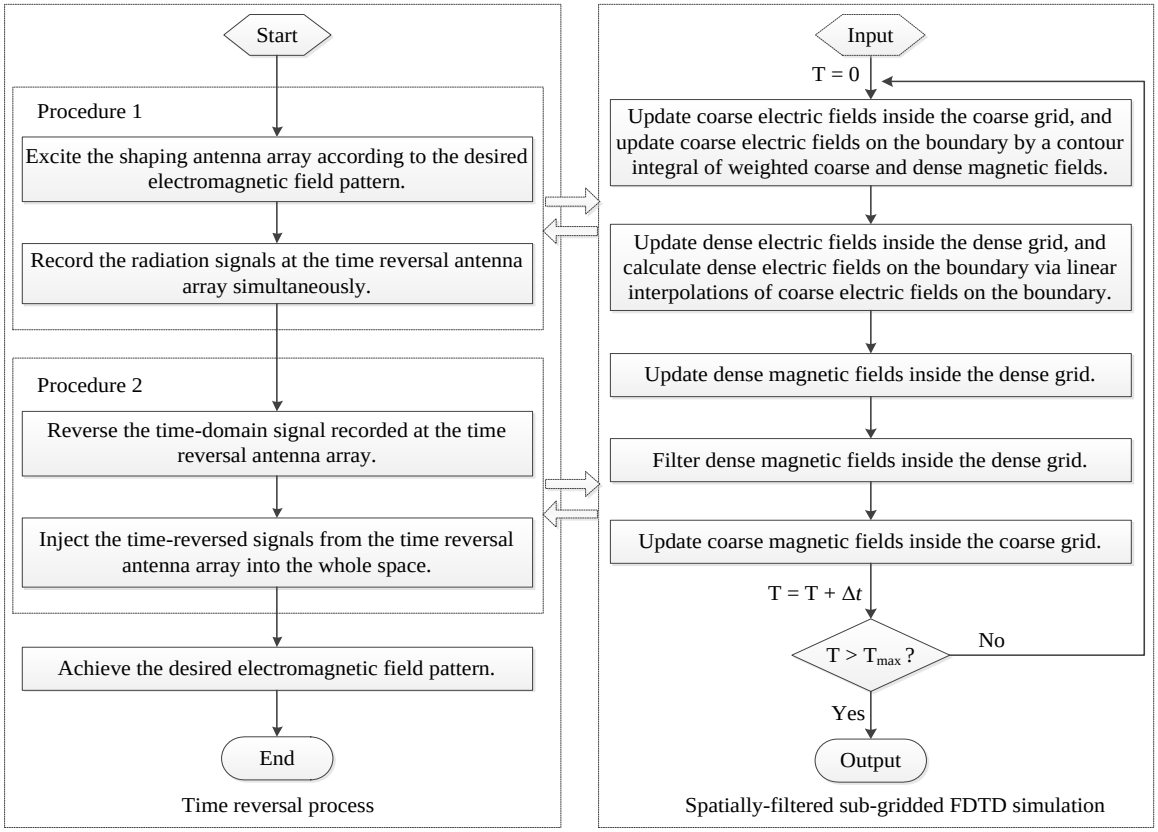

Fig. 3. Flowchart of the numerical implementation to generate an arbitrarily shaped electromagnetic field.

III. NUMERICAL RESULTS

Numerical examples of the time-reversed electromagnetic field shaping with different boundary conditions are provided in this section, demonstrating the accuracy and efficiency of the spatially-filtered sub-gridded FDTD method for solving multiscale and electrically large TR problems. Here, all calculations are performed on an Intel(R) Core(TM) i7-4790×8 CPU @ 3.60 GHz machine with 16 GB RAM.

A. Numerical validation

To begin with, a PEC cavity, whose size is 6 cm ×

9 cm × 6 cm along the *x*-, *y*- and *z*-directions, respectively, is calculated by the FDTD, sub-gridded FDTD and spatially-filtered sub-gridded FDTD methods. The cubic dense grids with Δ_{dense} = 1 mm are used in the FDTD simulation. For the two sub-gridded FDTD methods, a sub-gridded region locally discretized by cubic dense grids is embedded in the global region divided into cubic coarse grids with Δ_{coarse} = 3 mm. The time step size for both FDTD and sub-gridded FDTD is determined by the CFL limit of the dense grid, and 3000 time-marching steps are needed to obtain the time-domain waveforms. For the spatially-filtered sub-gridded FDTD, a time step size defined by the CFL limit of the coarse grid can be employed throughout the computational domain, enabled by the spatial filtering, and only 1000 time-marching steps are required to cover the same time interval.

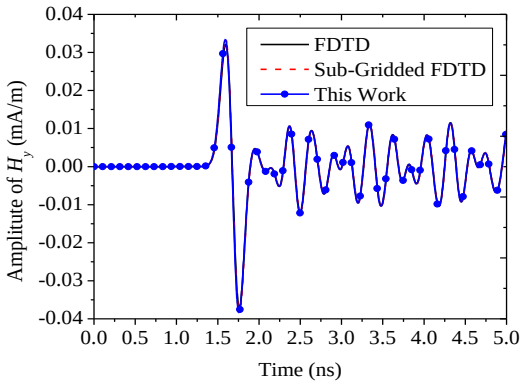

Fig. 4. Time-domain waveforms of the PEC cavity calculated from the three methods.

Table 1: Comparison of execution time and memory requirement for the three methods

Methods	CPU Time (s)	Memory (MB)
FDTD	756.94	189.37
Sub-gridded FDTD	71.09	25.34
This work	46.56	26.68

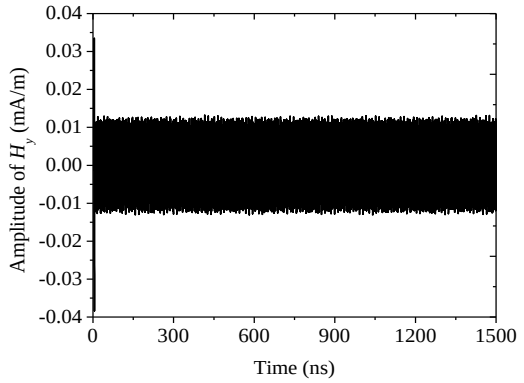

Fig. 5. Stability verification of the spatially-filtered sub-gridded FDTD method by running 300000 time-marching steps.

The excitation is a Gaussian pulse where the maximal frequency is 900 MHz. The time-domain waveforms in Fig. 4 show the excellent agreement among the three methods and demonstrate the numerical accuracy of the spatially-filtered sub-gridded FDTD. The execution time and memory requirement of the three methods are presented in Table 1, indicating that the CPU time of the proposed method is largely reduced compared with the other two methods. Furthermore, the late time stability of the spatially-filtered sub-gridded FDTD is also verified by running 300000 time-marching steps, as shown in Fig. 5.

B. PEC boundary condition

The electromagnetic field shaping within a metal cavity implemented by PEC boundary condition is considered here, as shown in Fig. 1. The maximal frequency of a Gaussian pulse which is employed as the excitation is 2.45 GHz, and the corresponding wavelength λ is 122.45 mm in free space. The whole computational domain is 2.16 m × 2.16 m × 1.08 m and it is divided into cubic coarse grids with Δ_{coarse} = 9 mm. A sub-gridded region with spatial size of 0.48 m × 0.48 m × 0.12 m, which is located in the center of the cavity, is divided into cubic dense grids with Δ_{dense} = 3 mm. As before, the time step size of the sub-gridded FDTD is defined by the CFL limit of the dense grid and 90000 time-marching steps are required. However, a time step size assigned by the CFL limit of the coarse grid can be used in the spatially-filtered sub-gridded FDTD, and only 30000 time-marching steps are needed. The FDTD simulation with a uniform dense grid requires too large memory and execution time, and it is omitted.

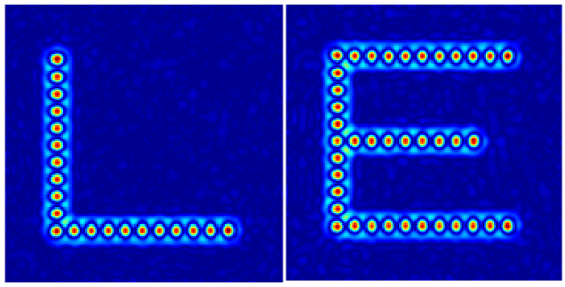

Fig. 6. Shaped electromagnetic field patterns calculated by the spatially-filtered sub-gridded FDTD within a metal cavity: (a) "L"-shaped field, and (b) "E"-shaped field.

Table 2: Computational effort for the PEC case

Methods	CPU Time (h)	Memory (GB)
Sub-gridded FDTD	54.56	2.78
This work	25.42	3.03

In the TR antenna array, there are 48 elements and the distance between two elements is 0.12 m. The shaping

antenna array is ranged according to the desired pattern of the electromagnetic field. Here, both "L"-shaped and "E"-shaped fields are considered, and the distance between two shaping antennas is 0.03 m. Figure 6 shows the results of two desired field patterns calculated by the spatially-filtered sub-gridded FDTD method with extended CFL limit of the dense grid. The execution time and memory requirement of the two methods are presented in Table 2, revealing the reduced CPU time enabled by the spatial filtering scheme in cost of slightly larger memory requirement.

C. PML boundary condition

In this part, the electromagnetic field shaping in the free space implemented by 10-cell-thick PML is also considered. The time-marching steps for the sub-gridded FDTD and spatially-filtered sub-gridded FDTD are 9000 and 3000, respectively. The set-up of this problem is same as that of the PEC case. The results of "L"-shaped and "E"-shaped field patterns are presented in Fig. 7.

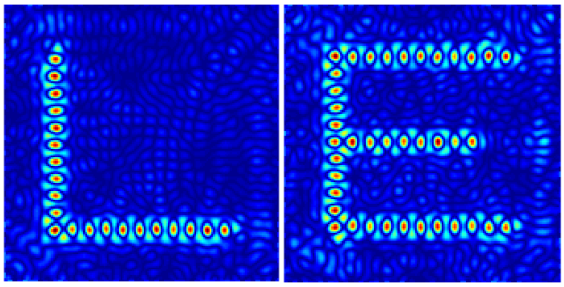

(a) (b)

Fig. 7. Shaped electromagnetic field patterns in free space calculated by the spatially-filtered sub-gridded FDTD with 48 elements in the TR antenna array: (a) "L"-shaped field, and (b) "E"-shaped field.

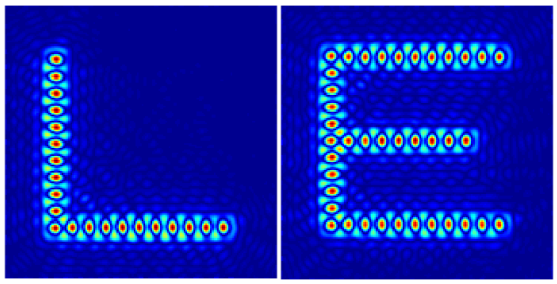

(a) (b)

Fig. 8. Shaped electromagnetic field patterns in free space calculated by the spatially-filtered sub-gridded FDTD with 192 elements in the TR antenna array: (a) "L"-shaped field, and (b) "E"-shaped field.

When the TR array consists of 192 elements, the shaped fields are revealed in Fig. 8. Table 3 also gives the computational efforts of the two methods in free space and demonstrates the efficiency of the spatially-filtered sub-gridded FDTD.

Table 3: Computational effort for the PML case

Methods	CPU Time (h)	Memory (GB)
Sub-gridded FDTD	24.61	11.61
This work	8.82	12.46

D. Discussion

To begin with, due to the multipath propagating property of the metal cavity, the time-reversed electromagnetic field can be focused on a predefined pattern with a relatively large number of time-marching steps. Furthermore, the electromagnetic waves are multi-reflected inside the closed region without attenuation, and thus 48 elements in the TR antenna array are enough to capture required signals. However, for the free space case, since the electromagnetic field is absorbed and attenuated in the PML region, more elements in the TR antenna array are required to obtain a high quality shaped electric field. Fewer time-marching steps are needed in this case because of the PML truncation. It can be pointed out that the generated microwave fields in Figs. 6 and 8 have almost the same quality. The other shaped patterns of the electromagnetic field can also be easily achieved in the same way.

IV. CONCLUSION

In this paper, an efficient sub-gridded FDTD method is employed for simulating the electrically large and multiscale TR electromagnetic field shaping of arbitrary microwave patterns, whose electric size is approximately $18\,\lambda \times 18\,\lambda \times 9\,\lambda$. Enabled by the spatial filtering scheme, both the coarse and dense grids are run with a large time step size defined by the CFL limit of the coarse grid, and two patterns of electromagnetic field with both PEC and PML boundary conditions are realized. The simulation results demonstrate that the spatially-filtered sub-gridded FDTD is powerful in solving electrically large TR scenarios with locally fine grid division. In the future work, the codes will be implemented in a parallel manner to further improve the computational efficiency.

ACKNOWLEDGMENT

This work was supported by the National Natural Science Foundation of China under Grant 61471105 and Grant 61331007.

REFERENCES

[1] G. Lerosey, J. de Rosny, A. Tourin, et al., "Time reversal of electromagnetic waves," *Phys. Rev. Lett.*, vol. 92, no. 19, Art. no. 193904, May 2004.

[2] X. Xu, H. Liu, and L. V. Wang, "Time-reversed ultrasonically encoded optical focusing into scattering media," *Nature Photon.*, vol. 5, pp. 154-

157, Mar. 2011.

[3] X. K. Wei, W. Shao, S. B. Shi, Y. F. Cheng, and B. Z. Wang, "An optimized higher order PML in domain decomposition WLP-FDTD method for time reversal analysis," *IEEE Trans. Antennas Propag*., vol. 64, no. 10, pp. 4374-4383, Oct. 2016.

[4] X. K. Wei, W. Shao, H. Ou, and B. Z. Wang, "An efficient higher-order PML in WLP-FDTD method for time reversed wave simulation," *J. Comput. Phys*., vol. 321, no. 9, pp. 1206-1216, Aug. 2016.

[5] J. de Rosny and M. Fink, "Focusing properties of near-field time reversal," *Phys. Rev. A*, vol. 76, no. 6, Art. no. 065801, 2007.

[6] G. Lerosey, J. de Rosny, A. Tourin, and M. Fink, "Focusing beyond the diffraction limit with far-field time reversal," *Science*, vol. 315, no. 5815, pp. 1120-1122, Feb. 2007.

[7] X. K. Wei, W. Shao, H. Ou, and B. Z. Wang, "Efficient WLP-FDTD with complex frequency-shifted PML for super-resolution analysis," *IEEE Antennas Wireless Propagat. Lett*., vol. 16, pp. 1007-1010, 2017.

[8] D. Zhao, Y. Jin, B. Z. Wang, and R. Zang, "Time reversal based broadband synthesis method for arbitrary structured beam-steering arrays," *IEEE Trans. Antennas Propag*., vol. 60, no. 1, pp. 164-173, Jan. 2012.

[9] M. D. Hossain, A. S. Mohan, and M. J. Abedin, "Beamspace time-reversal microwave imaging for breast cancer detection," *IEEE Antennas Wireless Propag. Lett*., vol. 12, pp. 241-244, 2013.

[10] D. Zhao, and M. Zhu, "Generating microwave spatial fields with arbitrary patterns," *IEEE Antennas Wireless Propag. Lett*., vol. 15, pp. 1739-1742, 2016.

[11] W. Fan, Z. Chen, and W. J. R. Hoefer, "Source reconstruction from wideband and band-limited responses by FDTD time reversal and regularized least squares," *IEEE Trans. Microw. Theory Techn*., vol. 65, no. 12, pp. 4785-4793, Dec. 2017.

[12] H. Zhao, Y. Zhang, J. Hu, and Z. Chen, "Hybrid sparse reconstruction-method of moments for diagnosis of wire antenna arrays," *Appl. Comput. Electrom. Society J*., vol. 32, no. 10, pp. 882-887, Oct. 2017.

[13] Y. F. Shu, X. C. Wei, R. Yang, and E. X. Liu, "An iterative approach for EMI source reconstruction based on phaseless and single-plane near-field scanning," *IEEE Trans. Electromagn. Compat.*, vol. 60, no. 4, pp. 937-944, Aug. 2018.

[14] H. Zhao, Y. Zhang, J. Hu, and E. P. Li, "Iteration-free phase retrieval for directive radiators using field amplitudes on two closely-separated observation planes," *IEEE Trans. Electromagn. Compat.*, vol. 58, no. 2, pp. 607-610, Apr. 2016.

[15] A. Taflove and S. C. Hagness, *Computational Electromagnetics: The Finite-Difference Time-Domain Method*. Norwood, MA, USA: Artech House, 2005.

[16] K. Xiao, D. J. Pommerenke, and J. L. Drewniak, "A three-dimensional FDTD subgridding algorithm with separated temporal and spatial interfaces and related stability analysis," *IEEE Trans. Antennas Propag*., vol. 55, no. 7, pp. 1981-1990, July 2007.

[17] C. Chang and C. D. Sarris, "A spatially filtered finite-difference time-domain scheme with controllable stability beyond the CFL limit: Theory and applications," *IEEE Trans. Microw. Theory Techn.*, vol. 61, no. 1, pp. 351-359, Jan. 2013.

[18] X. K. Wei, X. Zhang, N. Diamanti, W. Shao, and C. D. Sarris, "Sub-gridded FDTD modeling of ground penetrating radar scenarios beyond the Courant stability limit," *IEEE Trans. Geosci. Remote Sensing*, vol. 55, no. 12, pp. 7189-7198, Dec. 2017.

[19] S. D. Gedney, "An anisotropic perfectly matched layer-absorbing medium for the truncation of FDTD lattices," *IEEE Trans. Antennas Propag*., vol. 44, no. 12, pp. 1630-1639, Dec. 1996.

[20] D. Cassereau and M. Fink, "Time reversal of ultrasonic fields—Part III: Theory of the closed time-reversal cavity," *IEEE Trans. Ultrasonic, Ferroelectron., Frequency Control*, vol. 39, no. 5, pp. 579-592, Sep. 1992.

Xiao-Kun Wei was born in Tianshui, Gansu Province, China, in 1990. He received the B.S. degree in Electronic Information Science and Technology and the M.Sc. degree in Electronics and Communication Engineering from the University of Electronic Science and Technology of China (UESTC), Chengdu, Sichuan, China, in 2013 and 2015, respectively. Now, he is currently pursuing the Ph.D. degree in Radio Physics at UESTC.

From Sep. 2016 to Aug. 2017, he was an International Visiting Graduate Student with the Department of Electrical and Computer Engineering, University of Toronto, Toronto, ON, Canada. His research interests include unconditionally stable and fast time-domain numerical methods and optimization techniques in electromagnetics.

Wei Shao was born in Chengdu, China, in 1975. He received the B.E. degree in Electrical Engineering from UESTC in 1998, and received M.Sc. and Ph.D. degrees in Radio Physics from UESTC in 2004 and 2006, respectively.

He joined the UESTC in 2007 and is now a Professor there. From 2010 to 2011, he was a Visiting Scholar in the Electromagnetic Communication Laboratory, Pennsylvania State University, State College, PA. From 2012 to 2013, he was a Visiting Scholar in the Department of Electrical and Electronic Engineering, Hong Kong University. His research interests include computational electromagnetics and antenna design.

Xiao Ding received the Ph.D. degree in Radio Physics from UESTC in 2014.

In 2013, he was a Visiting Scholar with the Department of Electrical and Computer Engineering, South Dakota School of Mines and Technology, SD, USA. From June 2016 to June 2017, he was a Visiting Scholar with the Applied Electromagnetics Laboratory, University of Houston, TX, USA. He joined the UESTC in 2014 and he is currently an Associate Professor. His research interests include antenna theory and computational electromagnetics.

Bing-Zhong Wang received the Ph.D. degree in Electrical Engineering from UESTC in 1988.

He joined the UESTC in 1984 where he is currently a Professor. He has been a Visiting Scholar at the University of Wisconsin-Milwaukee, a Research Fellow at the City University of Hong Kong, and a Visiting Professor in the Electromagnetic Communication Laboratory, Pennsylvania State University, State College, PA. His current research interests are in the areas of computational electromagnetics, antenna theory and technique, and electromagnetic compatibility analysis.

Effect of Symmetry on Insertion Loss in SRR and CSRR Transmitarray Unit Cells Implementing the Element Rotation Method

Emre Erdil [1], Kagan Topalli [2], and Ozlem Aydin Civi [1]

[1] Department of Electrical and Electronics Engineering
Middle East Technical University, Ankara, Turkey
eerdil@gmail.com, ozlem@metu.edu.tr

[2] TUBITAK Space Technologies Research Institute
Microwave and Antenna Systems Group, Ankara, Turkey
kagan.topalli@tubitak.gov.tr

Abstract ─ Insertion loss variation with respect to rotation angle is examined for geometrically symmetrical and unsymmetrical split ring resonators (SRR) and complementary split ring resonators (CSRR) transmitarray unit cells implementing the element rotation method. Generalized design conditions for the implementation of the method on transmitarrays are derived. Based on the S-parameters obtained by full-wave electromagnetic simulations and field analysis, it is shown that the symmetry of CSRR unit cells has an important effect on decreasing insertion loss variation with respect to rotation angle. Up to 3 dB improvement in insertion loss is achieved for the symmetrical single ring double split CSRR type unit cell. It is also shown for two nested non symmetric SRR unit cells that, insertion loss is almost independent of the element rotation when the transmission is mainly provided by the symmetrical part of the unit cell.

Index Terms ─ CSRR, element rotation method, SRR, transmitarray.

I. INTRODUCTION

The element rotation method is used to control the phase of the waves scattered from the structures excited by circularly polarized electromagnetic waves in reflectarrays and transmitarrays. The conditions for element rotation required to achieve phase shifting are derived for reflectarrays [1], [2] and transmitarrays [3]. The element rotation method is employed in several antennas [1]-[13]. The conditions for transmitarrays [3] cover symmetrical structures with respect to all orthogonal planes. In this letter, the generalized conditions are derived without being restricted by symmetry.

Since the design of a transmitarray is implemented through the analysis of a unit cell, it is crucial to analyze the parameters that may affect the overall characteristics of the transmitarray at the unit cell level. Insertion loss is a parameter that has an influence on the gain and efficiency of a transmitarray. Therefore, besides analyzing the insertion loss of a unit cell and its variation with respect to rotation angle, it is also important to determine the factors affecting insertion loss and to propose a solution to alleviate the variations of insertion loss.

To the author's knowledge, although variations of reflection and transmission magnitude with respect to rotation angle are presented in the literature, the reasons of these variations are not clarified [3]. Therefore, to understand the physics behind these amplitude variations with rotating angle, this work focuses on the sources of insertion loss variations with respect to rotation angle in a group of SRR and CSRR type transmitarray unit cells employing the element rotation method. The investigation by full wave EM simulations is found to be sufficient, as the simulations provide a controlled environment and eliminate some other effects that might arise in manufacturing and measurement. It is shown by simulations that, for the presented structures, insertion loss variation depends on the axial symmetry of the element and symmetry has an effect on decreasing the value of the variation.

II. GENERALIZED DESIGN CONDITIONS AND MAGNITUDE VARIATION IN THE ELEMENT ROTATION METHOD

In this section, the conditions that should be satisfied by the unit cells to implement the element rotation method are derived in the most general sense. The transmission magnitude on the derived circularly-polarized *S*-parameters is investigated.

The most practical method of obtaining the phase design curve of a unit cell is the infinite array approach. In this approach, the array is formed by replicating identical unit cells. The approach provides an opportunity for designing array structures by analyzing only a single

Submitted On: January 16, 2017
Accepted On: April 21, 2018

element, i.e., unit cell with periodic boundary conditions, including the effect of mutual coupling between the elements. Infinite array approach is implemented using Finite Element Method (FEM) solver of Ansys HFSS®. In HFSS®, in order to satisfy this periodicity, periodic boundary conditions are implemented by master and slave boundaries on the unit cell walls. The E-field in any point of the slave boundary matches the correspondent point of the master boundary with a phase difference [14]. The periodic arrangement of the array allows the approximation of the infinite array fields with Floquet modal expansion. Floquet ports are defined on the apertures of the unit cell as an interface to unbounded medium and the fields on the ports are represented by a set of Floquet modes. A Floquet mode is a plane wave function and these modes define the discrete directions where an infinite array radiates plane waves. The number of the propagating modes is related to the dimensions of the unit cell and the incidence angle. The dominant mode corresponds to the main beam of the antenna whereas higher order modes correspond to the grating lobes and when the unit size is less than half a wavelength, only the dominant mode propagates [3]. The propagating modes can be decomposed into orthogonal modal functions, TE and TM, for simplicity. This normalization is useful in layered structures as these orthogonal modal functions propagate without producing the other transverse mode for homogeneous and isotropic media. That is, TE (TM) mode will not produce a TM (TE) mode [15]. Therefore, for a unit cell smaller than half a wavelength the propagating dominant mode is decomposed into one TE and one TM propagating modes and individual analysis of these modes are performed by using HFSS®. In the infinite array approach since the analysis is carried out by using a single unit cell, the computation time and the utilization of the computational resources are reduced. However, in this approach, infinite extension of the unit cell causes ignoring of the edge effects and the mutual coupling only includes the coupling between identical elements. These conditions may affect the phase response of the structure. Different approaches taking into account the coupling of non-identical cells are implemented to make a comparison with the infinite array approach in [16]. The infinite array approach is widely used in large array structures and it provides results in very good agreement with measurements by offering a very fast computation.

In the simulations of this study, only the dominant Floquet mode incidence is considered and it is decomposed as *x*- and *y*-polarized wave modes for a plane wave propagating along the *z*-axis [3].

The relation between the incident, *a*, and scattered, *b*, wave modes can be written in terms of S-parameters as,

$$\begin{bmatrix} b_1^x \\ b_1^y \\ b_2^x \\ b_2^y \end{bmatrix} = \begin{bmatrix} s_{11}^{xx} & s_{11}^{xy} & s_{12}^{xx} & s_{12}^{xy} \\ s_{11}^{yx} & s_{11}^{yy} & s_{12}^{yx} & s_{12}^{yy} \\ s_{21}^{xx} & s_{21}^{xy} & s_{22}^{xx} & s_{22}^{xy} \\ s_{21}^{yx} & s_{21}^{yy} & s_{22}^{yx} & s_{22}^{yy} \end{bmatrix} \begin{bmatrix} a_1^x \\ a_1^y \\ a_2^x \\ a_2^y \end{bmatrix}, \quad (1)$$

where the subscripts and superscripts of *a* and *b* represent the number of the Floquet port and the direction of polarization, respectively. Following the same procedure in [3], circularly polarized S-parameters are obtained in terms of linearly polarized ones and are given as,

$$s_{11}^{lr} = \frac{1}{2}\left[\left(s_{11}^{xx} + s_{11}^{yy}\right) - j\left(s_{11}^{xy} - s_{11}^{yx}\right)\right], \quad (2\text{-}3)$$

$$s_{11}^{ll} = \frac{1}{2}\left[\left(s_{11}^{xx} - s_{11}^{yy}\right)e^{+j2\psi} \mp j\left(s_{11}^{xy} + s_{11}^{yx}\right)e^{+j2\psi}\right], \quad (4\text{-}5)$$

$$s_{12}^{ll} = \frac{1}{2}\left[\left(s_{12}^{xx} + s_{12}^{yy}\right) - j\left(s_{12}^{yx} - s_{12}^{xy}\right)\right], \quad (6\text{-}7)$$

$$s_{12}^{lr} = \frac{1}{2}\left[\left(s_{12}^{xx} - s_{12}^{yy}\right)e^{+j2\psi} \mp j\left(s_{12}^{yx} + s_{12}^{xy}\right)e^{+j2\psi}\right], \quad (8\text{-}9)$$

$$s_{21}^{ll} = \frac{1}{2}\left[\left(s_{21}^{xx} + s_{21}^{yy}\right) - j\left(s_{21}^{xy} - s_{21}^{yx}\right)\right], \quad (10\text{-}11)$$

$$s_{21}^{rl} = \frac{1}{2}\left[\left(s_{21}^{xx} - s_{21}^{yy}\right)e^{+j2\psi} \mp j\left(s_{21}^{xy} + s_{21}^{yx}\right)e^{+j2\psi}\right], \quad (12\text{-}13)$$

$$s_{22}^{rl} = \frac{1}{2}\left[\left(s_{22}^{xx} + s_{22}^{yy}\right) - j\left(s_{22}^{xy} - s_{22}^{yx}\right)\right], \quad (14\text{-}15)$$

$$s_{22}^{rr} = \frac{1}{2}\left[\left(s_{22}^{xx} - s_{22}^{yy}\right)e^{+j2\psi} \mp j\left(s_{22}^{yx} + s_{22}^{xy}\right)e^{+j2\psi}\right], \quad (16\text{-}17)$$

where the superscripts *l* and *r* denote the sense of the polarization, i.e., left hand and right hand, respectively whereas ψ denotes the rotation angle. For the equations above, each line includes two separate equations where the first one is given by the upper superscripts.

In a transmitarray design, minimization of reflection is an important design consideration to increase the antenna efficiency. For an efficient transmitarray unit cell design, all the reflections should be minimized as,

$$s_{11}^{xx} = s_{11}^{yy} = s_{22}^{xx} = s_{22}^{yy} = s_{11}^{xy} = s_{11}^{yx} = s_{22}^{xy} = s_{22}^{yx} = 0. \quad (18)$$

It is seen from the equations that for each sense of polarization, two transmission parameters exist i.e., when we illuminate the structure by a left-hand circularly polarized wave from port 1, left and right-hand circularly polarized transmissions, s_{21}^{ll} and s_{21}^{rl}, take place. The transmission with the same sense of polarization is not affected from rotation and forms cross-pol radiation. To eliminate the scattered transmission fields independent of rotation, following conditions should be satisfied in the design,

$$s_{mn}^{xx} = -s_{mn}^{yy}, \quad (19)$$

$$s_{mn}^{xy} = s_{mn}^{yx} \text{ for } m, n = 1,2 \text{ and } m \neq n. \quad (20)$$

Satisfying these, four parameters are left; (8), (9), (12), and (13). Two of these parameters, (9) and (13) are advancing the transmitted phase twice the rotation angle, whereas (8) and (12) are delaying it. Also, the sense of

polarization changes for the transmitted wave.

(18)–(20) together with the maximization of transmission are the general conditions for applying the element rotation method in the transmitarrays. Although the implementation of (20) requires no phase difference between s_{mn}^{xy} and s_{mn}^{yx}, minimizing these components also reduces the cross-pol radiation even if there is a phase difference between them.

Further simplification is also possible for symmetrical structures with respect to the *xy*-plane. If we define, s_{21}^{xx} and s_{12}^{xx} as T_x; s_{21}^{yy} and s_{12}^{yy} as T_y; s_{21}^{xy} and s_{12}^{xy} as T_{xy}; s_{21}^{yx} and s_{12}^{yx} as T_{yx} for a symmetrical structure with respect to *xy*-plane; minimizing reflection, maximizing T_x and T_y and having 180° of phase difference between them when they have equal magnitude as implied by (19) and having 0° of phase difference between T_{xy} and T_{yx} when they have equal magnitude as implied by (20) or minimizing them are the sufficient conditions to design a transmitarray employing element rotation method.

The circularly polarized transmission parameters after satisfying conditions, (8), (9), (12), and (13) demonstrate that the phase of the transmitted wave changes twice the rotation angle without changing the magnitude. However, full-wave EM simulations indicate that the magnitude changes with the change in the rotation angle. This is mainly because the amount of the existing electromagnetic coupling between the elements changes with the rotation angle [2]. Since this coupling affects overall array characteristics [4], it is important to determine the parameters reducing the adverse effects of it on insertion loss. It should also be noted here that the element rotation method assumes the rotation of the entire structure with its environment including the lattice, around its surface normal [3]. However, in an array, the edges of the unit cell generate a boundary that does not rotate with the rotation of the array element. Therefore, even if all the components of the radiators inside the unit cell rotate, the array and the unit cell boundaries are stationary which has an effect on the magnitude of transmitted and reflected fields.

A. CSRR designs

Figures 1 (a)-(d) show the schematics and the transmission magnitudes of the examined CSRR unit cells which are, nested CSRR (N-CSRR), single ring double split CSRR (DS-CSRR), and single ring single split CSRR (SS-CSRR). All the structures satisfy the conditions for shifting the phase linearly with respect to rotation angle at the operating frequency. The size of the unit cells is 10.16 mm × 10.16 mm, the substrate is glass, (ε_r=4.6, tan δ=0.005), having a thickness of 6 mm and the operating frequency is 9.9 GHz in all structures. The dimensions of the structures are given in Table 1. From transmission magnitudes of the unit cells, it is realized that transmission behaviors of the structures are similar and the magnitude varies with the change in rotation angle. Insertion loss is less for the symmetrical structure, DS-CSRR.

To extract the relationship between symmetrical geometry and insertion loss level, insertion loss levels of DS-CSRR and SS-CSRR structures are examined. Ideal cases are constructed by evaluating linearly polarized S-parameters at $\psi = 0°$ from simulations and then taking the rotation angle (ψ) into account using equation (12). In Fig. 1 (e), insertion loss values as a function of rotation angle directly obtained from full wave simulations are compared with the values of ideal cases. It is observed that insertion loss calculated through full wave simulations of DS-CSRR is more similar to insertion loss obtained by applying (12) on DS-CSRR. The reason why the variation of insertion loss of the symmetrical structure (DS-CSRR) is smaller compared to that of the unsymmetrical structure (SS-CSRR) is not evident from analytical expressions, since the values of the linearly polarized S-parameters do not change when the structure is rotated. This is investigated in the following sections by analyzing fields and currents.

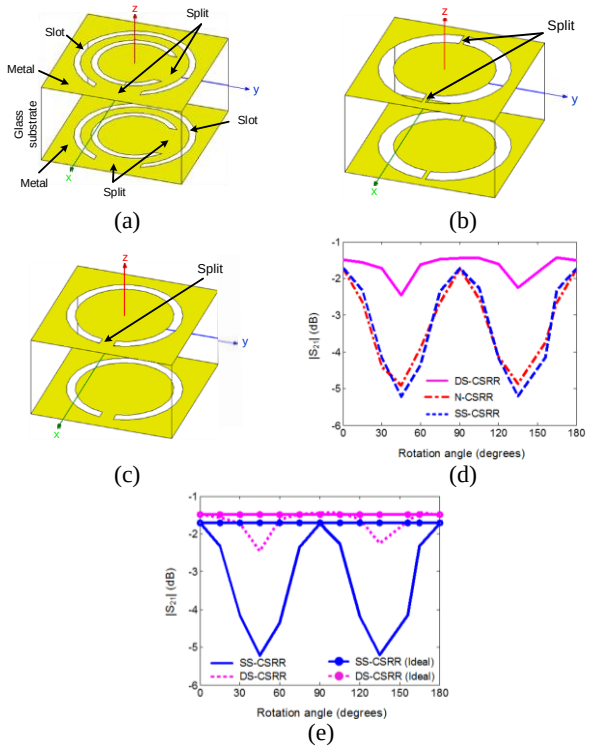

Fig. 1. CSRR unit cells: (a) N-CSRR, (b) DS-CSRR, (c) SS-CSRR, (d) circularly polarized transmission coefficients of the CSRR unit cells with respect to the rotation angle, and (e) circularly polarized transmission coefficients of DS-CSRR and SS-CSRR unit cells with respect to rotation angle and compared to their ideal cases.

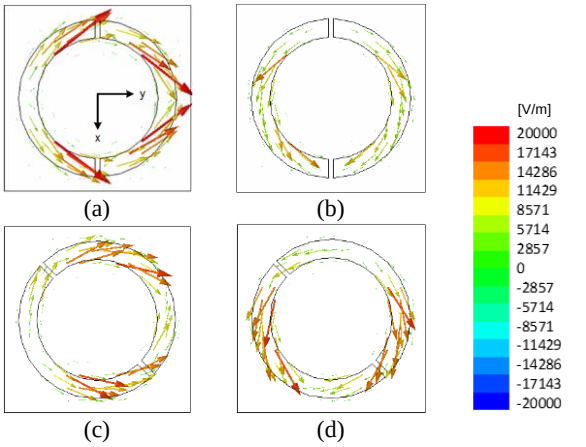

Fig. 2. Magnetic surface current density distributions for the DS-CSRR: (a) for *x*-polarized wave modes at 0°, (b) for *y*-polarized wave modes at 0°, (c) for *x*-polarized wave modes at 45°, and (d) for *y*-polarized wave modes at 45°.

Table 1: Dimensions of the CSRR unit cells

	SS-CSRR	DS-CSRR	N-CSRR
Split length (mm)	1	0.26	3.3 (both splits)
Ring slot width (mm)	4 – 3.38	4.3 – 3.3	4.2 – 3.75 (outer ring) 3 – 2.55 (inner ring)

B. Field analysis of CSRR designs

A field analysis is carried out on the designs to show the relation between the symmetry and the variation of insertion loss. Magnetic surface current density distributions (tangential electric field on the slot), M_s, on the ring slots of the DS-CSRR obtained for *x*- and *y*-polarized incident waves at 9.9 GHz are plotted in Fig. 2. It is observed that the symmetrical distribution of M_s is not affected by rotation for both polarizations. Figure 3 depicts M_s for the SS-CSRR. At $\psi = 45°$, the distribution is significantly denser at one arm of the ring which increases the cross-polarized radiation. Comparing Fig. 2 and Fig. 3, it is seen that the symmetry of M_s is more distorted by rotation for the SS-CSRR compared to the DS-CSRR. This increases the cross-polarized terms in the *S*-parameters and cross-polarized radiation, which in turn affect the transmission characteristics of the element.

C. SRR designs

Figures 4 (a) and (b) show the SRR schematics. There is a single split on each design which disturbs the symmetrical geometry. The split takes place on the inner ring for one design whereas it takes place on the outer ring for the other design. These are called inner split SRR (IS-SRR) and outer split SRR (OS-SRR), respectively. As in the CSRR designs, the conditions for linear phase shifting are satisfied at 9.9 GHz for the substrate thickness of 6 mm. Other parameters of the structures are given in Table 2. It is observed from Fig. 4 (c) that, although both structures are unsymmetrical for the same plane, IS-SRR has much less insertion loss variation with the rotation angle.

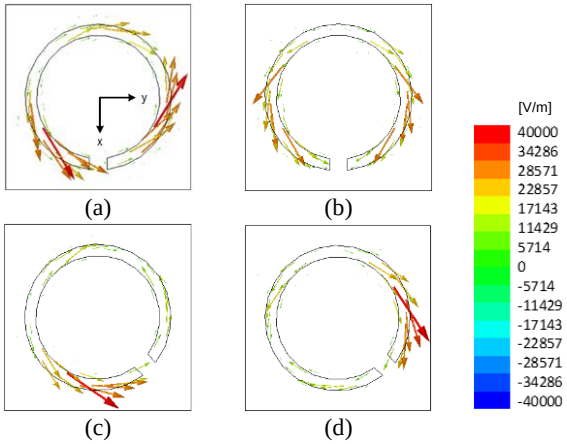

Fig. 3. Magnetic surface current density distributions for the SS-CSRR: (a) for *x*-polarized wave modes at 0°, (b) for *y*-polarized wave modes at 0°, (c) for *x*-polarized wave modes at 45°, and (d) for *y*-polarized wave modes at 45°.

Table 2: Dimensions of the SRR unit cells

	IS-SRR	OS-SRR
Split length (mm)	1.2	1.2
Ring width (mm)	4.29 – 3.49 (outer ring) 3.17 – 2.37 (inner ring)	3.95 – 3.45 (outer ring) 1.7 – 1.2 (inner ring)

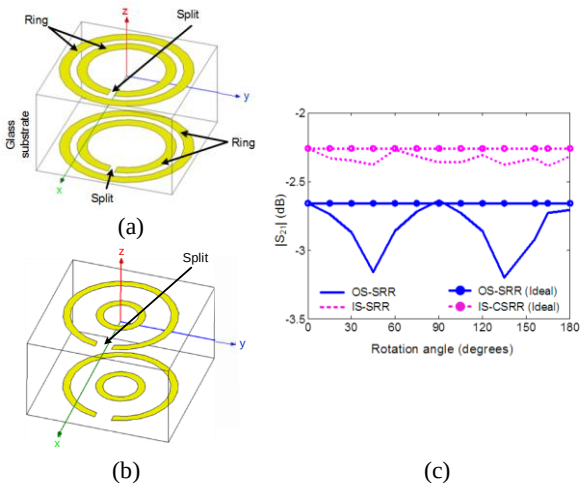

Fig. 4. (a) The inner split SRR (IS-SRR), (b) the outer split SRR (OS-SRR), and (c) circularly polarized transmission coefficient of the SRR unit cells.

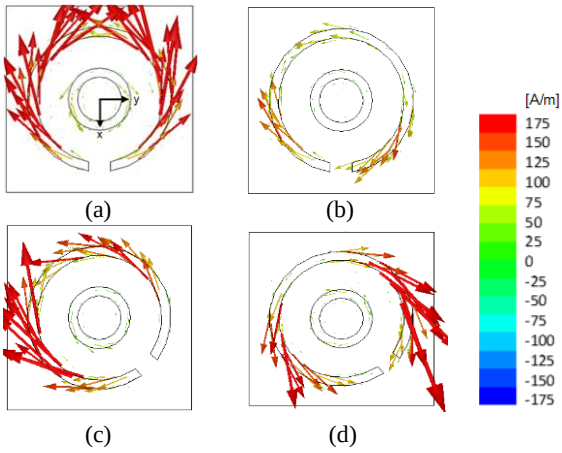

Fig. 5. Electric surface current density distributions for the OS-SRR: (a) for *x*-polarized wave modes at 0°, (b) for *y*-polarized wave modes at 0°, (c) for *x*-polarized wave modes at 45°, and (d) for *y*-polarized wave modes at 45°.

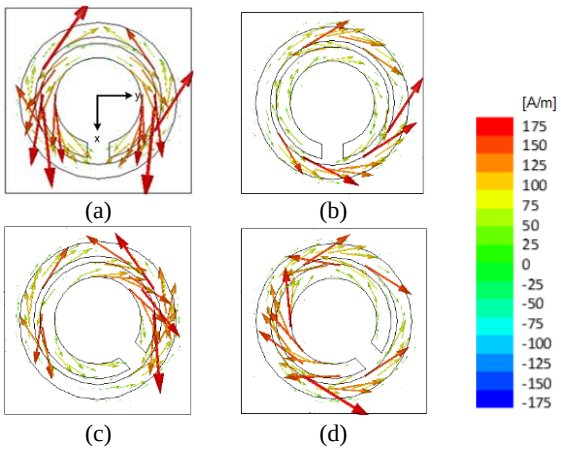

Fig. 6. Electric surface current density distributions for the IS-SRR: (a) for *x*-polarized wave modes at 0°, (b) for *y*-polarized wave modes at 0°, (c) for *x*-polarized wave modes at 45°, and (d) for *y*-polarized wave modes at 45°.

The J_s diagrams for OS-SRR, in Fig. 5, show that for both polarizations the resonance is mainly determined from the outer ring due to a strong current flow on that ring. Therefore, the disturbance on the current distribution on the outer ring affects the radiation and the transmission magnitude. When the OS-SRR is rotated to $\psi = 45°$, it is seen in Figs. 5 (c) and (d) that the cross-polarized radiation increases which in turn increases the insertion loss. When the J_s diagrams for IS-SRR in Figs. 6 (a) and (b) are examined, it is observed that for x-polarized excitation, the outer ring and the inner ring generate the resonance together whereas for y-polarized excitation, the resonance is mainly determined from the outer ring due to a stronger current flow on that ring. As the rings get closer to each other, the coupling between them is stronger. When the rings are rotated, the symmetrical distribution on the inner ring is distorted which in turn affects the distribution on the outer ring due to coupling. This situation is less pronounced for y- polarized excitation as the outer ring is dominant on the determination of the resonance for that polarization. Therefore, the current distributions over the rings are more uniform for y-polarization which result in less insertion loss variation. Smaller variation of insertion loss for IS-SRR is mainly due to two reasons: (i) the outer ring where the current distribution is denser for one of the polarizations does not have a split, i.e., the outer ring is symmetrical to the orthogonal planes, and (ii) the split is closer to the center of the unit cell which results in lower coupling levels among adjacent cells when the unit cell is rotated.

III. CONCLUSION

The effect of symmetrical geometry on insertion loss of CSRR and SRR-based transmitarray unit cells is demonstrated. The symmetrical geometry decreases cross-polarized scattering, which in turn decreases insertion loss variation with respect to rotation. It is also shown for unsymmetrical SRR structures that if the resonance is mainly provided by the symmetrical part of a unit cell, element rotation does not adversely affect the insertion loss. This work proposes a methodology to increase the transmission magnitude for SRR and CSRR-based transmitarray unit cells and is useful in understanding of the sources of the degradation of the radiation characteristics of transmitarrays.

ACKNOWLEDGMENT

This work was supported in part by TUBITAK, Project No. 113R033.

REFERENCES

[1] J. Huang and R. J. Pogorzelski, "A Ka-band micro-strip reflectarray with elements having variable rotation angles," *IEEE Trans. Antennas Propag.*, vol. 46, no. 5, pp. 650-656, May 1998.

[2] C. Guclu, J. Perruisseau-Carrier, and O. Aydin Civi, "Proof of concept of a dual-band circularly-polarized RF MEMS beam-switching reflect-array," *IEEE Trans. Antennas Propag.*, vol. 60, no. 11, pp. 5451-5455, Nov. 2012.

[3] R. H. Phillion and M. Okoniewski, "Lenses for

circular polarization using planar arrays of rotated passive elements," *IEEE Trans. Antennas Propag*., vol. 59, no. 4, pp. 1217-1227, Apr. 2011.

[4] A. E. Martynyuk, J. I. Martinez Lopez, and N. A. Martynyuk, "Spiraphase-type reflectarrays based on loaded ring slot resonators," *IEEE Trans. Antennas Propag*., vol. 52, no. 1, pp. 142-153, 2004.

[5] B. Strassner, C. Han, and K. Chang, "Circularly polarized reflectarray with microstrip ring elements having variable rotation angles," *IEEE Trans. Antennas Propag*., vol. 52, pp. 1122-1125, Apr. 2004.

[6] M. Euler and V. F. Fusco, "Frequency selective surface using nested split ring slot elements as a lens with mechanically reconfigurable beam steering capability," *IEEE Trans. Antennas Propag*., vol. 58, no. 10, pp. 3417-3421, Oct. 2010.

[7] T. Smith, U. Gothelf, O.S. Kim, and O. Breinbjerg, "Design, manufacturing, and testing of a 20/30-GHz dual-band circularly polarized reflectarray antenna," *IEEE Antennas and Wireless Propagation Letters*, vol. 12, pp. 1480-1483, 2013.

[8] M.-Y. Zhao, G.-Q. Zhang, X. Lei, J.-M. Wu, and J.-Y. Shang, "Design of new single-layer multiple-resonance broadband circularly polarized reflect-arrays," *IEEE Antennas and Wireless Propagation Letters*, vol. 12, pp. 356-359, 2013.

[9] S. Zainud-Deen, S. Gaber, H. Malhat, and K. Awadalla, "Single feed dual-polarization dual-band transmitarray for satellite applications," *ACES Journal*, vol. 29, no. 2, Feb. 2014.

[10] E. Erdil, K. Topalli, N. S. Esmaeilzad, O. Zorlu, H. Kulah, and O. A. Civi, "Reconfigurable nested ring-split ring transmitarray unit cell employing the element rotation method by microfluidics," *IEEE Trans. Antennas Propag.*, vol. 63, no. 3, pp. 1163-1167, Mar. 2015.

[11] S. Zainud-Deen, S. Gaber, H. Malhat, and K. Awadalla, "Single feed dual-polarization dual-band transmitarray for satellite applications," *ACES Journal*, vol. 29, no. 2, 2014.

[12] S. H. Zainud-Deen, W. M. Hassan, and H. A. Malhat, "Near-field focused folded transmitarray antenna for medical applications," *ACES Journal*, vol. 31, no. 3, 2016.

[13] A. Hassan, F. Yang, A. Z. Elsherbeni, and P. Nayeri, *Analysis and Design of Transmitarray Antennas*. Morgan and Claypool, 2017.

[14] ANSYS® HFSS, Version 13, Online Help, Master and Slave Boundaries.

[15] A. K. Bhattacharyya, *Phased Array Antennas: Floquet Analysis, Synthesis, BFNs, and Active Array Systems*. Hoboken, NJ: Wiley, 2006.

[16] M-A. Milon, R. Gillard, D. Cadoret, and H. Legay, "Comparison between the "infinite array approach" and the "surrounded-element approach" for the simulation of reflectarray antennas," *2006 IEEE Antennas and Propagation Society International Symposium*, Albuquerque, NM, pp. 4339-4342, 2006.

Emre Erdil was born in 1979. He received B.Sc., M.Sc. and Ph.D. degrees in Electrical and Electronics Engineering from Middle East Technical University (METU), Ankara, Turkey, in 2001, 2005, and 2007, respectively. Since 2002, he has been working at Capital Markets Board of Turkey. Erdil's recent research interests include reconfigurable transmitarrays and reflectarrays. He has also conducted research on MEMS-based reconfigurable antennas. Erdil is the the recipient of "METU Thesis of the Year Award" in 2015.

Kagan Topalli was born in 1979. He received B.Sc. and Ph.D. degrees in Electrical and Electronics Engineering from Middle East Technical University (METU), Ankara, Turkey, in 2001 and 2007, respectively. Between 2001 and 2007, he has worked as a Research Assistant at METU in the Department of Electrical and Electronics Engineering. Between 2007 and 2010, he has worked as a Research Engineer at the METU-MEMS (MicroElectroMechanical Systems) Center. Topalli worked as a Post-doctoral Researcher at ElectroScience Laboratory of the Ohio State University between February 2010 and February 2012. He worked as a Faculty at TED University, Department of Electrical and Electronics Engineering in Ankara, Turkey. Topalli worked as a faculty at Bilkent University, National Nanotechnology Research Center (UNAM), Institute of Materials Science and Nanotechnology. He is currently working as a Chief Research Scientist at TUBITAK-Space Technologies Research Institute. Topalli's recent research interests include THz sensors and THz imaging systems. He has also conducted research on the development, characterization, and integration of novel RF MEMS structures for RF front ends at microwave and millimeter-wave, reconfigurable antennas, phased arrays, microwave packaging, and microfabrication technologies. He has published more than 60 journal and international conference papers. Topalli received the "METU Thesis of the Year Award" in 2007 for his Ph.D. dissertation, which was awarded by the Prof. Mustafa N. Parlar Education and Research Foundation. He received the "URSI (Union of Radio Science-International)

Young Scientist Award" in 2011. He received "Research Incentive Award" in 2013 given by the Prof. Mustafa N. Parlar Education and Research Foundation. He is the co-advisor to the recipient of "METU Thesis of the Year Award" in 2015. He is a Senior Member of IEEE.

Özlem Aydin Civi received B.Sc., M.Sc. and Ph.D. degrees in 1990, 1992 and 1996 respectively in Electrical and Electronics Eng. Department of the Middle East Technical University (METU) in Ankara, Turkey. She was a Research Assistant in METU between 1990-1996. In 1997-1998 she was a Visiting Scientist at the ElectroScience Laboratory, Ohio State University. Since 1998, she has been with the Department of Electrical and Electronics Engineering, METU, where she is currently a Professor. Her research interests include analytical, numerical and hybrid techniques in EMT problems, especially fast asymptotic/hybrid techniques for the analysis of large finite periodic structures, multi-function antenna design, reconfigurable antennas, phased arrays, reflectarrays and RF-MEMS applications. She has published more than hundred and fifty journal and international conference papers. She was a recipient of 1994 Prof. Mustafa Parlar Foundation Research and Encouragement Award with METU Radar Group and 1996 URSI Young Scientist Award. She was the Chair of IEEE Turkey Section in 2006 and 2007, the Chair of IEEE AP/MTT/ED/EMC Chapter between 2004 and 2006. She is Vice Chair of the Turkish National Committee of URSI. She was an Associate Editor of the IEEE Transaction on Antennas and Propagation between 2010-2016.

Semi-inverse Method to the Klein-Gordon Equation with Quadratic Nonlinearity

Wei Yan [1,2*], Quan Liu [1], ChongMing Zhu [3], Yang Zhao [1], and Yuxiang Shi [3]

[1] School of Electric and Automation Engineering
Nanjing Normal University, Nanjing, Jiangsu 210042, China

[2] UAV Research Institute
Nanjing Aeronautics and Astronautics University, Nanjing, Jiangsu 210016, China

[3] State Grid Electric Power Research Institute
NARI Group Corporation, Nanjing, Jiangsu 211000, China
*61197@njnu.edu.cn

Abstract ─ Nonlinear electrical and mechanical systems have been widely used in the industry electronics and consumer devices. Many numerical algorithms can be employed to obtain the numerical solutions of the nonlinear dynamics or electromagnetic equations. However, it takes a lot of time and decreases the solution accuracy. In this paper, a novel method, called Semi-Inverse Method, is proposed to seek solitary solutions of nonlinear differential equations. The Klein-Gordon equation with quadratic nonlinearity is selected to illustrate the effectiveness and simplicity of the suggested method.

Index Terms ─ Dynamics equation, electromagnetic transmission, nonlinear equation, semi-inverse method, solitary solution.

I. INTRODUCTION

With the development of electrical, mechanical and control engineering, lots of nonlinear and chaotic problems and equations need to be solved [1-5]. The present numerical algorithm can obtain the numerical solutions with much time and low accuracy [6-9]. The growing recognition that the way to solving exact soliton solutions of nonlinear equations is a crucial factor in progress of nonlinear dynamics and a key access to understanding the nonlinear equations to a large extent has fueled much research on the determination of soliton solutions. In recent years, new exact solutions may help to find new phenomena. A variety of powerful methods, such as the Exp-function method [10-11], Tanh-function method [12], algebraic method [13], F-expansion method [14], auxiliary equation method [15], decomposition method [16], extended Jacobi elliptic function expansion method and others were used to develop nonlinear dispersive and dissipative problems.

The present paper is motivated by the desire to the Semi-inverse method to the Klein-Gordon equation with quadratic nonlinearity, which reads:

$$u_{tt} - \alpha^2 u_{xx} + \beta u - \gamma u^2 = 0, \tag{1}$$

where α, β and γ are known constants. Jacobi elliptic function solutions.

II. SEMI-INVERSE METHOD

As shown in Eq. (1), there are two variables, partial differential equation and strong nonlinearity. However, it should be mentioned that the solution of Eq. (1) satisfies the electromagnetic field wave equation. In order to seek its travelling wave solution, we use the following transformation:

$$u\ \eta\ = u\ \ x,t\ \ , \tag{2}$$

$$\eta\ = x + \lambda t\,, \tag{3}$$

where λ is a constant to be determined later. It describes the relationship between variable x and t.

Substituting Eq. (2) and Eq. (3) into Eq. (1), we have:

$$\lambda^2 - \alpha^2\ \ u'' + \beta u - \gamma u^2 = 0\,, \tag{4}$$

where the prime expresses the derivative with respect to η. As shown in Eq. (4), the partial differential equation becomes ordinary differential equation.

According to the method and Eq. (4), we can obtain the following variation formulation:

$$J\ \ u\ \ = \int_0^{\infty} \left(\frac{\lambda^2 - \alpha^2}{2} u'^2 - \frac{\beta}{2} u^2 + \frac{\gamma}{3} u^3 \right) du\ . \tag{5}$$

III. THE KLEIN-GORDON EQUATION WITH QUADRATIC NONLINEARITY

Any function can be represented by a Fourier series or exponential expansion. According to the semi-inverse method, we assume the solution can be expressed in the

Submitted On: June 30, 2016
Accepted On: June 17, 2018

following form:

$$u\ \eta\ = p\,sech^2\ q\eta\ , \tag{6}$$

where p and q are unknown constants to be further determined.

Substituting Eq. (6) into Eq. (5), and by simple calculation, we can obtain:

$$J\ u\ = \frac{p^2\left[-15\beta+8p\gamma-12q^2\ \ \alpha^2-\lambda^2\ \right]}{45q}. \tag{7}$$

Making $J(u)$ stationary with respect to p and q results in:

$$\frac{\partial J}{\partial p}=\frac{8p^2\gamma}{45q}+\frac{2p\left[-15\beta+8p\gamma-12q^2\ \ \alpha^2-\lambda^2\ \right]}{45q}, \tag{8}$$

$$\frac{\partial J}{\partial q}=\frac{8p^2\ \ \lambda^2-\alpha^2}{15}+\frac{p^2\left[15\beta-8p\gamma+12q^2\ \ \alpha^2-\lambda^2\ \right]}{45q^2}. \tag{9}$$

From Eq. (8) and Eq. (9), the differential equations can be established to solve p and q:

$$\begin{aligned}&\frac{8p^2\gamma}{45q}+\frac{2p\left[-15\beta+8p\gamma-12q^2\ \ \alpha^2-\lambda^2\ \right]}{45q}=0\\&\frac{8p^2\ \ \lambda^2-\alpha^2}{15}+\frac{p^2\left[15\beta-8p\gamma+12q^2\ \ \alpha^2-\lambda^2\ \right]}{45q^2}=0\end{aligned} \tag{10}$$

From Eq. (10), we obtain:

$$p=\frac{3\beta}{2\gamma},\quad q=\pm\frac{\sqrt{\beta}}{2\sqrt{\alpha^2-\lambda^2}}. \tag{11}$$

Substituting Eq. (11) into Eq. (2), Eq. (3) and Eq. (6), we have:

$$u\ \ x,t\ \ =\frac{3\beta}{2\gamma}\mathrm{sech}^2\left(\frac{\sqrt{\beta}(x+t\lambda)}{2\sqrt{\alpha^2-\lambda^2}}\right). \tag{12}$$

It is the solitary solution of the Klein-Gordon equation with quadratic nonlinearity. By substituting Eq. (12) into Eq. (1), it can verify the method is effectiveness.

IV. THEORETICAL ANALYSYS

Concerned different parameters of the Klein-Gordon equation with quadratic nonlinearity, three cases have been analyzed.

CASE 1. The Solution of Equation (α=1, β=2, λ=3)

Based on the formula (11), when α=1, β=2, λ=3, the solution of equation was shown in Fig. 1, which can validate the solitary solution the Klein-Gordon equation with quadratic nonlinearity.

CASE 2. The Solution of Equation (α=1, β=5, λ=3)

Based on the formula (11), when α=1, β=5, λ=3, the solution of equation was shown in Fig. 2, which can validate the solitary solution the Klein-Gordon equation with quadratic nonlinearity.

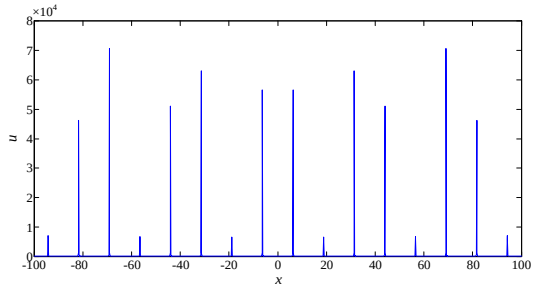

(a) The solution of equation with different position (t=0)

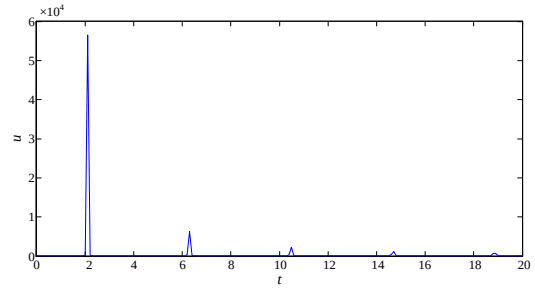

(b) The solution of equation (x=0)

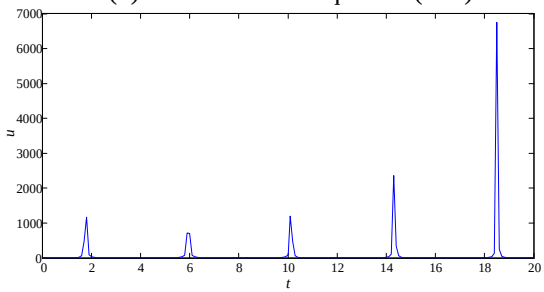

(c) The solution of equation (x=1)

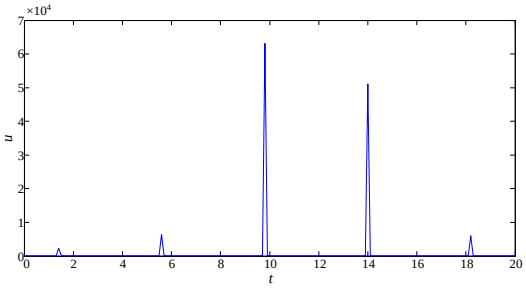

(d) The solution of equation (x=2)

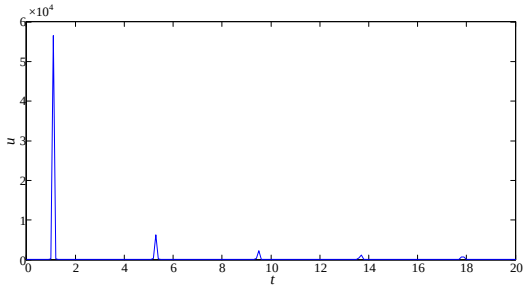

(e) The solution of equation (x=3)

Fig. 1. The solution of equation (α=1, β=2, λ=3).

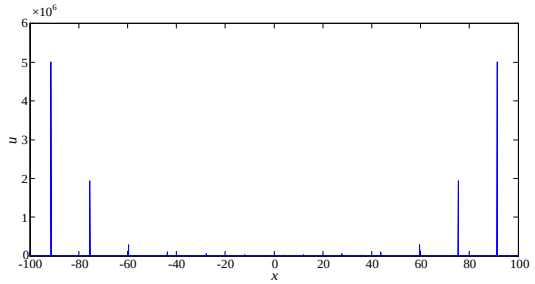

(a) The solution of equation with different position (t=0)

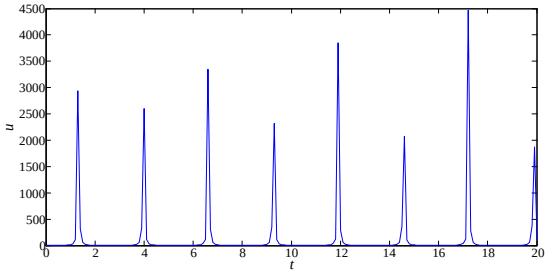

(b) The solution of equation (x=0)

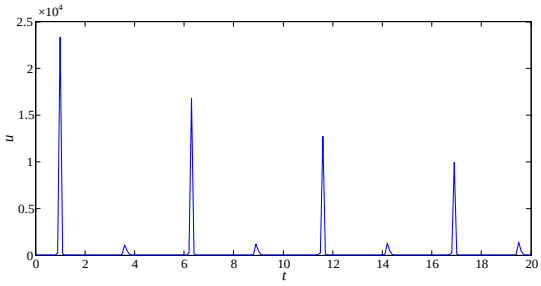

(c) The solution of equation (x=1)

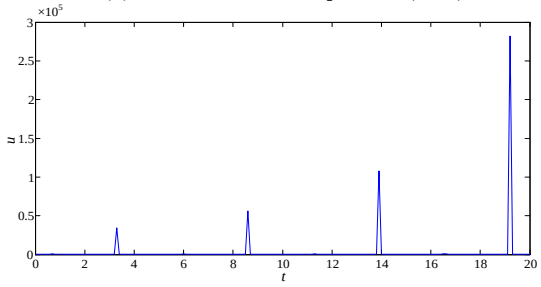

(d) The solution of equation (x=2)

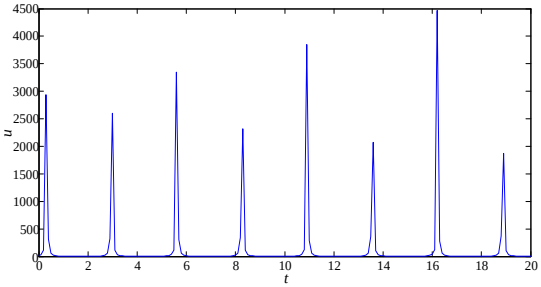

(e) The solution of equation (x=3)

Fig. 2. The solution of equation (α=1, β=5, λ=3).

CASE 3. The Solution of Equation (α=2, β=2, λ=3)

Based on the formula (11), when α=2, β=2, λ=3, the solution of equation was shown in Fig. 3, which can validate the solitary solution the Klein-Gordon equation with quadratic nonlinearity.

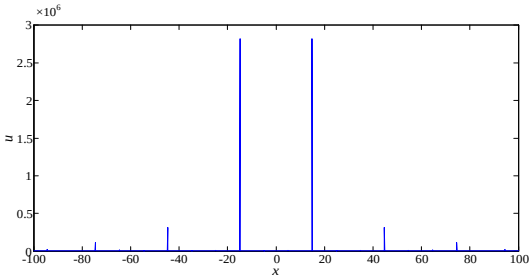

(a) The solution of equation with different position (t=0)

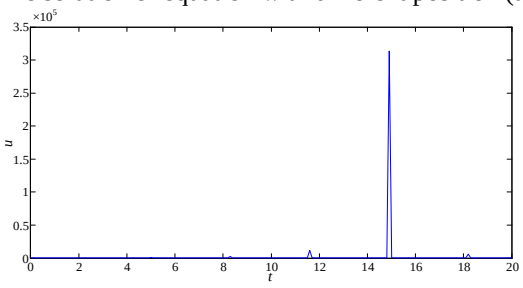

(b) The solution of equation (x=0)

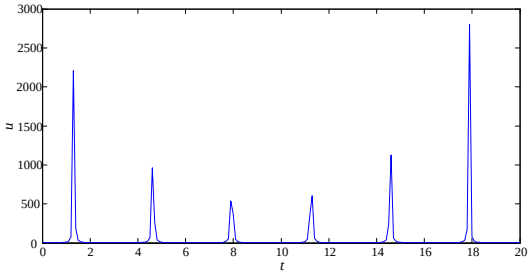

(c) The solution of equation (x=1)

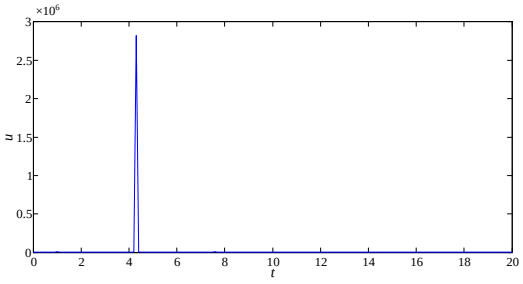

(d) The solution of equation (x=2)

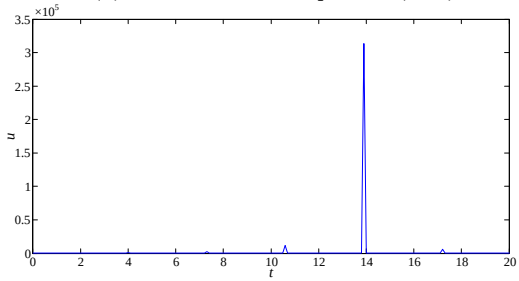

(e) The solution of equation (x=3)

Fig. 3. The solution of equation (α=2, β=2, λ=3).

V. CONCLUSION

In summary, the Semi-inverse method with a computerized symbolic computation has been proposed to obtain the generalized solitary solutions to nonlinear evolution equations arising in mathematical physics. As a result, some new solutions for the physically important NLEEs have easily been found too. It is worthwhile to mention that the proposed Semi-inverse method is of utter straightforward and concise.

ACKNOWLEDGMENT

This paper is supported by Project Supported by National Natural Science Foundation of China (51475246); National Natural Science Foundation of Jiangsu Province (BK20161019); Aviation Science Foundation (20172552017).

REFERENCES

[1] D. M. Diego and R. Adroaldo, "Electromagnetic modeling of electronic device by electrical circuit parameters," *Applied Computational Electromagnetics Society Journal*, vol. 31, pp. 58-65, 2016.

[2] M. Naser-Moghadasi, "Harmonic suppression of parallel coupled-line bandpass filters using defected microstrip structure," *Applied Computational Electromagnetics Society Journal*, vol. 31, pp. 568-573, 2016.

[3] W. Yan, Q. Tang, and E. Wang, "Radiated emission mechanism for semi-active control strategy of magneto-rheological damper,"*International Journal of Applied Electromagnetics and Mechanics*, vol. 51, pp. 185-198, 2016.

[4] W. Yan, J. Yu, and Q. Tang, "Analysis and mitigation on conducted electromagnetic interference of semi-active control strategy for magneto-rheological damper," *International Journal of Applied Electromagnetics and Mechanics*, vol. 50, pp. 247-254, 2016.

[5] I. Mahmoud, M. Fathallah, and H. Rehaoulia, "Nonlinear modelling approach for linear switched reluctance motor and its validation by two dimensional FEA," *Applied Computational Electromagnetics Society Journal*, vol. 31, pp. 195-203, 2016.

[6] R. G. Ilinger and D. B. Davidson, "The computational performance and power consumption of the parallel FDTD on a smartphone platform," *Applied Computational Electromagnetics Society Journal*, vol. 30, pp. 1262-1268, 2015.

[7] R. K. Murphy, H. A. Sabbagh, and E. H. Sabbagh, "A multiscale algorithm for eddy-current nondestructive evaluation based on volume-integral equations: Initial concepts," *Applied Computational Electromagnetics Society Journal*, vol. 31, pp. 333-339, 2016.

[8] H. Xu, D. Z. Ding, and R. S. Chen, "A hybrid explicit-implicit scheme for spectral-element time-domain analysis of multiscale simulation," *Applied Computational Electromagnetics Society Journal*, vol. 31, pp. 444-449, 2016.

[9] L. E. Sun and W. C. Chew, "Modeling of anisotropic magnetic objects by volume integral equation methods," *Applied Computational Electromagnetics Society Journal*, vol. 30, pp. 1256-1261, 2015.

[10] J.-H. He and L.-N. Zhang, "Generalized solitary solution and compacton-like solution of the Jaulent-Miodek equations using the Exp-function method," *Physics Letters A*, vol. 372, pp. 1044-1047, 2008.

[11] F. Xu and W. Yan, "Evaluation of two-dimensional ZK-MEW equation using the Exp-function method," *Computers & Mathematics with Applications*, vol. 58, pp. 2307-2312, 2009.

[12] A. M. Wazwaz, "The extended tanh method for the Zakharov-Kuznetsov (ZK) equation, the modified ZK equation, and its generalized forms," *Communications in Nonlinear Science and Numerical Simulation*, vol. 13, pp. 1039-1047, 2008.

[13] H. Zhao, "Applications of the generalized algebraic method to special-type nonlinear equations," *Chaos, Solitons & Fractals*, vol. 36, pp. 359-369, 2008.

[14] C. H. Schmidt and T. F. Eibert, "Integral equation methods for near-field far-field transformation," *Applied Computational Electromagnetics Society Journal*, vol. 25, pp. 15-22, 2010.

[15] Y. Xu, H. Yang, and W. Yu, "Scattering analysis of periodic composite metallic and dielectric structures with synthetic basis functions," *Applied Computational Electromagnetics Society Journal*, vol. 30, pp. 1059-1067, 2015.

[16] M. F. Xue and J. M. Jin, "Finite-element domain decomposition methods for analysis of large-scale electromagnetic problems," *Applied Computational Electromagnetics Society Journal*, vol. 29, pp. 990-1002, 2014.

Wei Yan Doctor & Assoc. Professor from Nanjing Normal University. He obtained the Physics and Electronics Ph.D and Electrical Engineering M.S. from Nanjing Normal University in 2014 and 2011. He is the Senior Member of China Electrical Technology Association and the evaluation expert of the Electromagnetic Compatibility Calibration Specification of China.

Quan Liu Master Student from Nanjing Normal University. He obtained the Physics bachelor from North China Electric Power University in 2014.

Stochastic Analysis of Multi-conductor Cables with Uncertain Boundary Conditions

Gang Zhang, Jinjun Bai, Lixin Wang, and Xiyuan Peng

School of Electrical Engineering and Automation
Harbin Institute of Technology, Harbin, 150001, China
zhang_hit@hit.edu.cn, 13B906024@hit.edu.cn, wlx@hit.edu.cn, pxy@hit.edu.cn

Abstract ─ This paper provides two novel Stochastic Galerkin Method strategies to undertake stochastic analysis of the crosstalk in the multi-conductor cables with uncertain boundary conditions. Two different uncertain boundary conditions, stochastic lumped source and stochastic lumped load, are considered into stochastic Transmission Line Model. With the help of the Feature Selective Validation, it is verified that the proposed strategies is accurate by comparing with the reference results provided by Monte Carlo Method. At last, advantage of the proposed strategies in computational efficiency is presented.

Index Terms ─ EMC simulation, stochastic Galerkin method, uncertain boundary conditions, uncertainty analysis.

I. INTRODUCTION

Recent years, in order to reasonably accomplish simulation recurrence of actual situation, Electromagnetic Compatibility (EMC) community is facing a growing demand for developing uncertainty analysis into simulations. Among these new-type simulations, input parameters can be modeled by random variables, due to the lack of knowledge or the existence of tolerance factor [1, 2].

Solving stochastic Transmission Line Model is a typical uncertainty analysis problem in EMC simulation. For example, in calculating crosstalk of the wires in a cable bundle, the height of the wires might be uncertain in the complicated actual situation. In this case, the crosstalk voltages at terminations will be no longer deterministic. Obtaining these uncertain outputs is what uncertainty analysis does.

Many uncertainty analysis methods are presented to deal with this typical problem. Monte Carlo Method (MCM) is a widely used uncertainty analysis method, which owns high accuracy [1-3]. It is easy to realize as there is no need to change solver during uncertainty analysis. However, low computational efficiency makes MCM uncompetitive in EMC simulation, especially in some complicated problems.

Stochastic Galerkin Method (SGM) is another accurate uncertainty analysis method that provides high computational efficiency [4, 5]. Discussion of the crosstalk problem can be seen in literatures [6-8]. It shows that SGM is as accurate as MCM, and much more effective than MCM. Nevertheless, the original solver must be changed during uncertainty analysis in SGM. This character limits the application of SGM. If the solver of the problem is complex, realizing of SGM will become difficult. In existing literatures of SGM, only the uncertainty in telegraph equations is considered. Thus, further studies about applying SGM are still necessary to solve more complex problems.

In this paper, in order to improve the applicable scope of SGM in solving complex EMC problems, uncertain boundary conditions will be considered in stochastic Transmission Line Model. Novel SGM strategies will be introduced in detail towards two different uncertain boundary conditions, stochastic lumped source and stochastic lumped load. By using Feature Selective Validation [9-12], the strength of the SGM strategies will be testified.

The structure of the paper is as follows. Section II employs a brief description of Stochastic Galerkin Method; solving of stochastic Transmission Line Model with uncertain boundary conditions is presented in Section III; algorithm validation is presented in Section IV; Section V provides a summary of this paper.

II. SGM OVERVIEW

In traditional EMC simulation models, all input parameters are supposed certain. However, in actual situation, some parameters might be unknown as the lack of knowledge, or may change arbitrarily like the cables in a moving car, or may be random as the existence of manufacturing tolerance. In this case, some input parameters of the simulation must be uncertain in order to improve the reliability of simulation results. In such simulation, the output parameters which we are interested in will be influenced by the uncertainty inputs. Uncertainty analysis methods can provide these uncertain outputs.

Submitted On: June 16, 2016
Accepted On: June 13, 2018

SGM is an effective uncertainty analysis method which is rooted in the generalized Polynomial Chaos (gPC) theory, and it has been successfully applied in many fields [4, 5].

Modeling the uncertain inputs is the primary task of SGM. And random events θ , which are caused by the uncertain input parameters, can be modeled by random variable space $\xi(\theta)$. The random variable space $\xi(\theta)$ is made up by several random variables, shown in (1). Moreover, each random variable has its own distribution:

$$\xi(\theta) = \{\xi_1(\theta),\ \xi_2(\theta),\ \cdots,\ \xi_n(\theta)\}. \tag{1}$$

Independence of the random variables in the random variable space is an essential requirement in the application of SGM. Karhunen-Loeve expansion can provide technical support for such independence [5].

Based on the gPC theory, the outputs of uncertainty analysis can be unfolded by polynomial form shown in (2):

$$V(\xi) = v_0\varphi_0(\xi) + v_1\varphi_1(\xi) + \cdots + v_P\varphi_P(\xi), \tag{2}$$

where $V(\xi)$ is the output result which is influenced by the random variable space ξ, and $\varphi_i(\xi)$ stands for the Chaos polynomial of the random variables which is given by the Askey rule. Where P+1 is total number of the polynomial, and v_i is the polynomial coefficient, which needs to be solved.

Table 1 presents the Askey rule. The form of polynomial is determined by distribution of the random variables. The Askey rule can guarantee best convergence of the polynomial expansion according to the gPC theory [5].

Table 1: Askey rule

Random Variables	Wiener-Askey Chaos	Support
Gaussian	Hermite-chaos	$(-\infty,+\infty)$
Gamma	Laguerre-chaos	$[0,+\infty)$
Beta	Jacobi-chaos	[0, 1]
Uniform	Legendre-chaos	[–1, 1]

Suppose that there are two random variables ξ_1 and ξ_2 in a random variable space $\xi = \{\xi_1,\ \xi_2\}$. ξ_1 is in Gaussian distribution, and ξ_2 is in Uniform distribution. First three polynomials of the Hermite-chaos are $\varphi_0(\xi_1) = 1$, $\varphi_1(\xi_1) = \xi_1$ and $\varphi_2(\xi_1) = \xi_1^2 - 1$. First three polynomials of the Legendre-chaos are $\varphi_0(\xi_2) = 1$, $\varphi_1(\xi_2) = \xi_2$ and $\varphi_2(\xi_2) = 3\times\xi_2^2 - 1$. The polynomial expansion of ξ is in form of tensor product, as Table 2 shown.

Table 2: Polynomial for the case with two random variables

The Number of Polynomial *P*	The Order *d*	Polynomial
0	0	1
1	1	ξ_1
2	1	$1.732\times\xi_2$
3	2	$0.707\times(\xi_1^2 - 1)$
4	2	$1.732\times\xi_1\times\xi_2$
5	2	$1.118\times(3\times\xi_2^2 - 1)$

If the order of the polynomial is *d* and the number of the random variables is *n*, the number of polynomials P+1 will be calculated by following relationship:

$$(P+1) = \frac{(n+d)!}{n!d!}. \tag{3}$$

The polynomials given by the Askey rule are orthogonal to each other, which implies that,

$$\langle \phi_i,\ \phi_j \rangle = \langle \phi_i^2 \rangle \delta_{ij}. \tag{4}$$

Where δ_{ij} is Kronecker function which leads to the relation:

$$\delta_{ij} = \begin{cases} 1 & (i = j) \\ 0 & (i \neq j) \end{cases}. \tag{5}$$

Inner product computation $\langle .\ ,\ . \rangle$ is defined as:

$$\langle \phi_i,\ \phi_j \rangle = \int \phi_i(\xi)\phi_j(\xi)w(\xi)d\xi, \tag{6}$$

where $w(\xi)$ is weight function, and it can be obtained by the joint probability density of the random variables because the random variables are independent. In the same way, the supports of the integration are the joint supports of every random variable.

III. SOLUTION OF STOCHASTIC TRANSMISSION LINE MODEL

Transmission line equations include two types of equations, and they are telegraph equations and boundary conditions equations. Previous research only focuses on uncertain analysis of telegraph equations, shown in [6-8]. In contract, little attention is gained about boundary conditions equations. Therefore, this study aims to undertake uncertainty analysis in boundary conditions equations.

Boundary conditions equations are given as (7) and (8):

$$V(0) = \mathrm{V}_s - Z_s I(0), \tag{7}$$

$$V(L) = \mathrm{V}_l + Z_l I(L), \tag{8}$$

where L is the length of the transmission line. $I(0)$ and $V(0)$ stand for the current value and the voltage value in source end. $I(L)$ and $V(L)$ are the current value and the

voltage value in load end. V_s is the voltage source in the source end, and V_l presents the voltage source in load end. Z_s and Z_l present the loads in source end and load end respectively.

Two different uncertain boundary conditions are considered. One is stochastic lumped source, and the other is stochastic lumped load.

A. Stochastic lumped source

In the first model, uncertainty in lumped source V_s is considered, and equation (7) is translated into:

$$V(0,\xi) = V_s(\xi) - Z_s I(0,\xi), \tag{9}$$

where $V_s(\xi)$ is the uncertain input which is inference by the random event ξ. $V(0,\xi)$ and $I(0,\xi)$ are outputs of the calculation.

According to the gPC theory, the output parameters can be expanded by the polynomial of the random variables like (2), so they become:

$$\begin{cases} V(0,\xi) = v_0\varphi_0(\xi) + v_1\varphi_1(\xi) + v_2\varphi_2(\xi) \\ I(0,\xi) = i_0\varphi_0(\xi) + i_1\varphi_1(\xi) + i_2\varphi_2(\xi) \end{cases}. \tag{10}$$

Substituting (10) into (9), (9) can be expanded as:

$$\begin{aligned} &v_0\varphi_0(\xi) + v_1\varphi_1(\xi) + v_2\varphi_2(\xi) = \\ &V_s(\xi) - Z_s(i_0\varphi_0(\xi) + i_1\varphi_1(\xi) + i_2\varphi_2(\xi)). \end{aligned} \tag{11}$$

Using Galerkin progress, inner product computation with $\varphi_0(\xi)$ is taken on both sides of (11). And (11) is rewritten as:

$$\begin{aligned} &v_0\langle\varphi_0(\xi),\varphi_0(\xi)\rangle + v_1\langle\varphi_1(\xi),\varphi_0(\xi)\rangle + \\ &v_2\langle\varphi_2(\xi),\varphi_0(\xi)\rangle = \langle V_s(\xi),\varphi_0(\xi)\rangle - \\ &Z_s(i_0\langle\varphi_0(\xi),\varphi_0(\xi)\rangle + i_1\langle\varphi_1(\xi),\varphi_0(\xi)\rangle + \\ &i_2\langle\varphi_2(\xi),\varphi_0(\xi)\rangle). \end{aligned} \tag{12}$$

Considering the properties given in (4), (12) can be rearranged to obtain:

$$v_0 = \langle V_s(\xi),\varphi_0(\xi)\rangle - Z_s i_0, \tag{13}$$

where $\langle V_s(\xi),\varphi_0(\xi)\rangle$ is integral calculation, so its result is a constant.

Inner product computation with $\varphi_1(\xi)$ and $\varphi_2(\xi)$ is done in the similar way like (12), Equation (14) is got:

$$\begin{bmatrix} v_0 \\ v_1 \\ v_2 \end{bmatrix} = \begin{bmatrix} \langle V_s(\xi),\varphi_0(\xi)\rangle \\ \langle V_s(\xi),\varphi_1(\xi)\rangle \\ \langle V_s(\xi),\varphi_2(\xi)\rangle \end{bmatrix} - Z_s \begin{bmatrix} i_0 \\ i_1 \\ i_2 \end{bmatrix}. \tag{14}$$

Compared with the original equation in (7), the random variable ξ is disappeared, and (14) only includes three certain equations. Randomness is transferred into the Polynomial chaos in (10).

Traditional EMC simulation method can be used to solve the equations in (14), and coefficients like v_0 and i_0 can be calculated. After substituting these coefficients into the Polynomial chaos in (10), uncertainty analysis results of the SGM are presented. If the random variables in (10) are sampled, the statistical property which we need will be obtained, such as the expectation, the standard deviation, the worst case values, the probability density curves, and so on.

B. Stochastic lumped load

In the second model, stochastic lumped load is considered into boundary conditions equation (7). The equation will become:

$$V(0,\xi) = V_s - Z_s(\xi) I(0,\xi). \tag{15}$$

Compared with the equation (9), the lumped source V_s is a certain input, but the lumped load is turned into an uncertain value, $Z_s(\xi)$.

The output parameters $V(0,\xi)$ and $I(0,\xi)$ can also be expanded by substituting (10), equation (15) is unfolded as:

$$\begin{aligned} &v_0\varphi_0(\xi) + v_1\varphi_1(\xi) + v_2\varphi_2(\xi) = \\ &V_s - Z_s(\xi)(i_0\varphi_0(\xi) + i_1\varphi_1(\xi) + i_2\varphi_2(\xi)). \end{aligned} \tag{16}$$

Taking inner product computation on both sides with $\varphi_0(\xi)$, (16) is rewritten as:

$$\begin{aligned} &v_0\langle\varphi_0(\xi),\varphi_0(\xi)\rangle + v_1\langle\varphi_1(\xi),\varphi_0(\xi)\rangle + \\ &v_2\langle\varphi_2(\xi),\varphi_0(\xi)\rangle = \langle V_s,\varphi_0(\xi)\rangle - \\ &(i_0\langle Z_s(\xi)\varphi_0(\xi),\varphi_0(\xi)\rangle + i_1\langle Z_s(\xi)\varphi_1(\xi),\varphi_0(\xi)\rangle + \\ &i_2\langle Z_s(\xi)\varphi_2(\xi),\varphi_0(\xi)\rangle). \end{aligned} \tag{17}$$

Using the inner product properties given in (4), (17) should be:

$$\begin{aligned} &v_0 = V_s - (i_0\langle Z_s(\xi)\varphi_0(\xi),\varphi_0(\xi)\rangle + \\ &i_1\langle Z_s(\xi)\varphi_1(\xi),\varphi_0(\xi)\rangle + i_2\langle Z_s(\xi)\varphi_2(\xi),\varphi_0(\xi)\rangle). \end{aligned} \tag{18}$$

It is worth noting that the first Chaos polynomial $\varphi_0(\xi)$ is equal to 1. Thus, the calculating progress like (19) can be obtained:

$$\langle V_s,\varphi_0(\xi)\rangle = \langle V_s\,\varphi_0(\xi),\varphi_0(\xi)\rangle = V_s. \tag{19}$$

In the similar way, (20) and (21) can be shown as the relations:

$$\langle V_s,\varphi_1(\xi)\rangle = \langle V_s\,\varphi_0(\xi),\varphi_1(\xi)\rangle = 0, \tag{20}$$

$$\langle V_s,\varphi_2(\xi)\rangle = \langle V_s\,\varphi_0(\xi),\varphi_2(\xi)\rangle = 0. \tag{21}$$

Taking inner product computation with $\varphi_1(\xi)$ and $\varphi_2(\xi)$, the Galerkin Process results can be rearranged to get:

$$\begin{bmatrix} v_0 \\ v_1 \\ v_2 \end{bmatrix} = \begin{bmatrix} V_s \\ 0 \\ 0 \end{bmatrix} - T \begin{bmatrix} i_0 \\ i_1 \\ i_2 \end{bmatrix}, \tag{22}$$

$$T = \begin{bmatrix} \langle Z_s(\xi)\varphi_0,\varphi_0\rangle & \langle Z_s(\xi)\varphi_1,\varphi_0\rangle & \langle Z_s(\xi)\varphi_2,\varphi_0\rangle \\ \langle Z_s(\xi)\varphi_0,\varphi_1\rangle & \langle Z_s(\xi)\varphi_1,\varphi_1\rangle & \langle Z_s(\xi)\varphi_2,\varphi_1\rangle \\ \langle Z_s(\xi)\varphi_0,\varphi_2\rangle & \langle Z_s(\xi)\varphi_1,\varphi_2\rangle & \langle Z_s(\xi)\varphi_2,\varphi_2\rangle \end{bmatrix}, \tag{23}$$

where T is only an intermediate variable. The random variable ξ in the Chaos polynomial $\varphi_1(\xi)$ is ignored to simplify the expression.

Unlike (14), equations (22) and (23) provide an augmented certain equation. Traditional EMC simulation method can also be used to calculate the coefficients in (10), like v_0 and i_0. Final uncertainty analysis results can also be got by sampling equation (10).

IV. ALGORITHM VALIDATION

In this section, algorithm validation of the proposed strategies is presented. The validation model is got by improving a published model mentioned in literature [6]. Only geometrical uncertainty has been considered in [6]. In our model, uncertain boundary conditions will also be considered at the same time.

The validation model is to calculate crosstalk between two coupled lines, and it is shown in Fig. 1.

The radius of the radiating conductor and the disturbed conductor are both 0.1mm. The horizontal distance between two conductors is 0.05m. The height of the disturbed conductor is 0.035m, and the height of the radiating conductor H_g obeys Gaussian distribution $N(0.04,0.005)$m. All the loads are supposed 50Ω, except for Z_{load} under identified. The amplitude of the excitation source U_{source} is another undefined value. The radiating conductor and the disturbed conductor are surrounded by vacuum. The relative dielectric constant and the relative magnetic permeability of the vacuum are both 1.

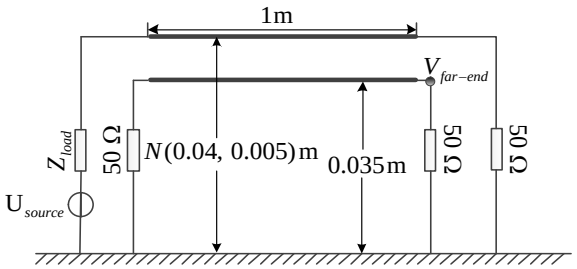

Fig. 1. Basic Stochastic Transmission Line Model.

A random variable can be used to express the uncertainty in the height of the radiating conductor, and it shows in:

$$H_g = 0.04+0.005\times\xi_1, \tag{24}$$

where, ξ_1 is standard normal distribution.

A. Validation of the first strategy

The strategy about the stochastic lumped source is validated at first. Uncertainty in lumped source is considered as:

$$U_{source} = 1.1+0.1\times\xi_2, \tag{25}$$

where ξ_2 is the Uniform distribution in $[-1, 1]$.

On the contrary, the lumped load is a certain value shown as:

$$Z_{load} = 50. \tag{26}$$

In this case, the random variable space is $\{\xi_1, \xi_2\}$, thus Chaos polynomials should be chosen as Table 2. Using the process given in Section III, the probability density curve of crosstalk voltage value $V_{far-end}$ at the far end of the disturbed conductor can be calculated. Figure 2 shows the results of the crosstalk voltage value at single frequency point 20 MHz and 5 MHz.

Results calculated by MCM can be regarded as reference data, and 20000 times of sampling are used. The sampling times judgment is based on the method given in [13], in order to make sure that MCM is convergence.

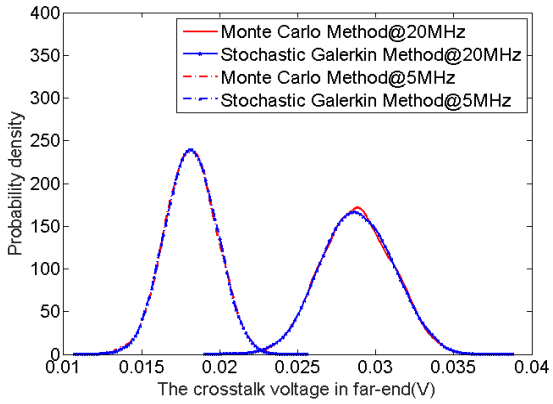

Fig. 2. Results at single frequency point.

Figure 2 indicates that the results given by the first SGM strategy and MCM are nearly the same at these two frequency points.

Figure 3 shows the expectation results of $V_{far-end}$ with frequency from 1MHz to 100 MHz. Meanwhile, Fig. 4 presents the 'worst case' information.

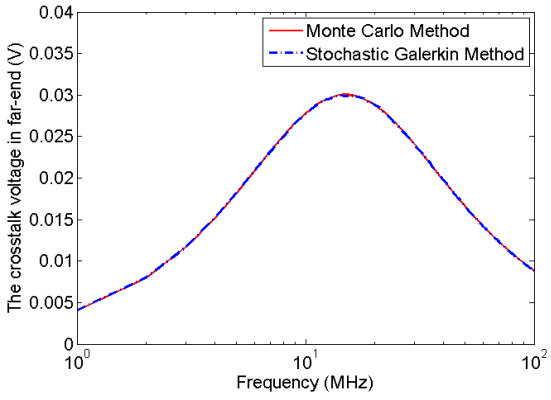

Fig. 3. Expectation results of crosstalk voltage value from 1MHz to 100 MHz.

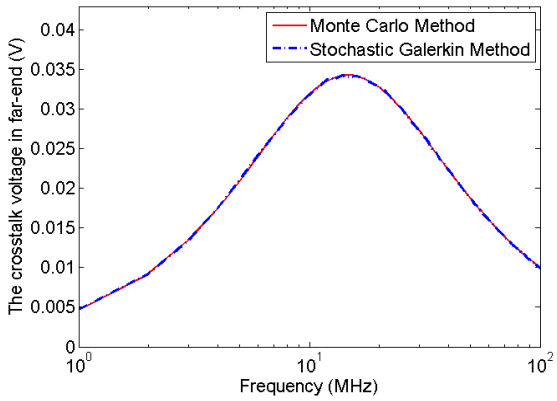

Fig. 4. Worst case values of crosstalk voltage value from 1MHz to 100 MHz.

By using FSV, the Total-GDM of the results between two methods in Fig. 3 is 0.036. It indicates that the results in the first strategy are an 'Excellent' match with the results in MCM. The Total-GDM of the results according to Fig. 4 is 0.043, and it is also an 'Excellent' match. The details about FSV can be found in [9, 10]. In Fig. 5, all the relative errors between SGM and MCM in every frequency point are less than 1%, and it means that SGM and MCM are in the same accuracy level.

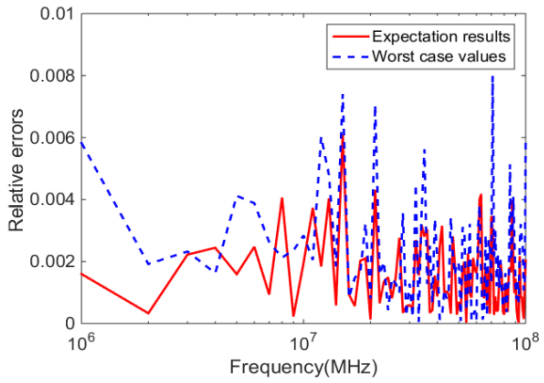

Fig. 5. Relative errors between SGM and MCM in the first strategy.

According to all Total-GDM results above, it is testified that the first SGM strategy in considering the stochastic lumped source is as accurate as MCM.

B. Validation of the second strategy

Uncertainty in the lumped load is considered in this part, it shows in:

$$Z_{load} = 55+5\times\xi_3, \tag{27}$$

where ξ_3 is also the Uniform distribution in $[-1, 1]$.

The lumped source is a certain value this time, and it should be:

$$U_{source} = 1. \tag{28}$$

The random variable space turns to be $\{\xi_1, \xi_3\}$, the Chaos polynomials also can be provided by Table 2. In this case, the random variable ξ_2 in the table is changed to be ξ_3.

By using the process provided in Section III, the uncertain crosstalk results can be obtained. Fig. 6 also gives the PDF results at single frequency point 20 MHz and 5 MHz. It shows that the MCM results are quite similar to the results given by the second SGM strategy.

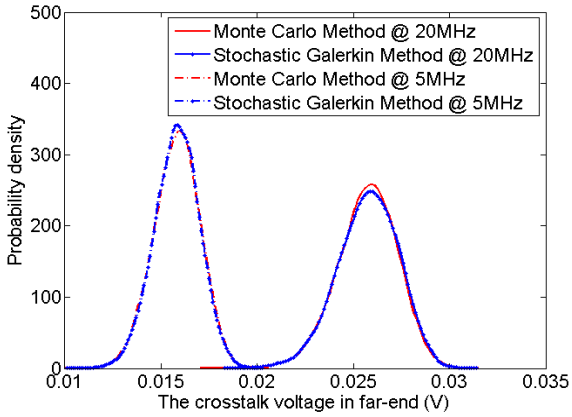

Fig. 6. Results at single frequency point.

The expectation results and Worst case values at the whole frequency from 1MHz to 100 MHz are presented in Fig. 7 and Fig. 8 respectively.

In the same way, by using FSV, the Total-GDM of the results between two methods in Fig. 7 is 0.014, and it is 0.020 in Fig. 8. Both of them indicate the 'Excellent' match. Furthermore, the relative errors given in Fig. 9 can provide the same conclusion.

In a word, it is demonstrated that the accuracy of the second SGM strategy is also in the same level with MCM in considering the stochastic lumped load.

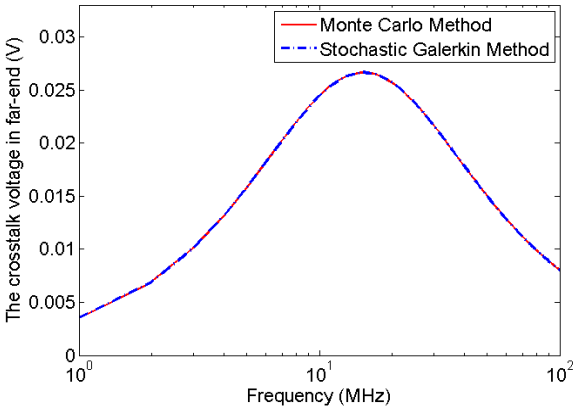

Fig. 7. Expectation results of crosstalk voltage value from 1MHz to 100 MHz.

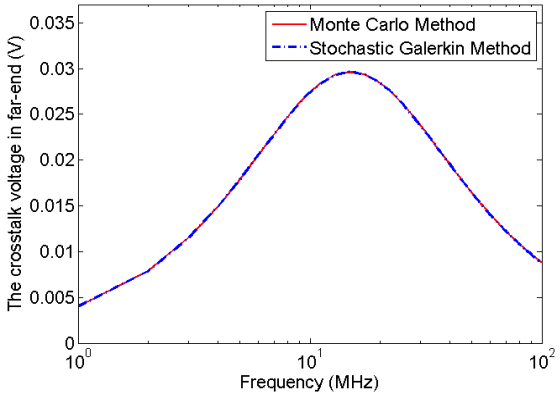

Fig. 8. Worst case values of crosstalk voltage value from 1MHz to 100 MHz.

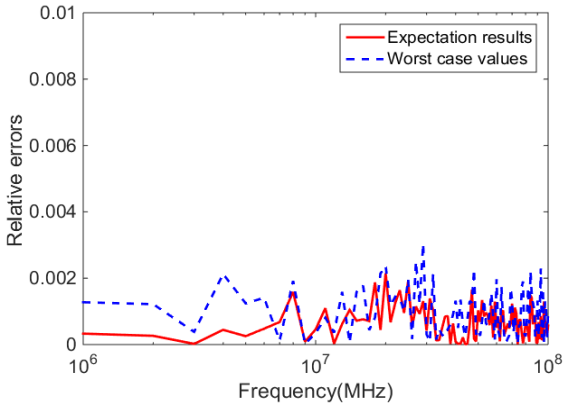

Fig. 9. Relative errors between SGM and MCM in the second strategy.

C. Discussion of computational efficiency

The simulation time comparison between SGM and MCM in two strategies is shown in Table 3. The total time includes pre-processing time, calculating time and post processing time.

For pre-processing time, some inner product computations must be calculated firstly in using SGM. On the contrary, nothing needs to be done in MCM. In calculating time, several certain equations like (14) or an augmented equation like (23) should be solved in SGM, thus the calculated quantity of the SGM is equal to several times of the original equation like (7). However, 20000 times of the original equation like (7) need to be calculated in MCM. As to the post processing time, statistical properties of the results can be obtained. The SGM samples the random variables before statistical properties calculation, so it needs a little more time than MCM.

Therefore, the difference in computational efficiency between SGM and MCM is decided by the calculating time. If the single simulation time in solving equation (7) is long, the difference will be more obvious.

Table 3: The simulation time comparison between the SGM and the MCM

	Pre-Processing	Calculating	Post Processing	Total
MCM(1)	0s	373.83s	0.15s	372.98s
SGM(1)	10.25s	0.26s	0.81s	11.32s
MCM(2)	0s	355.29s	0.21s	355.5s
SGM(2)	10.84s	0.25s	0.97s	12.06s

In short, the computational efficiency of SGM is much higher than MCM.

V. CONCLUSION

In this paper, considering uncertain boundary conditions, two novel strategies based on Stochastic Galerkin Method are presented to solve the stochastic transmission line equations. By using Feature Selective Validation, the proposed strategies are demonstrated as accurate as Monte Carlo Method. Furthermore, the computation efficiency of the strategies is proved much higher than that of Monte Carlo Method. In a word, the proposed strategies improve the competitiveness of the Stochastic Galerkin Method in solving complex multi-conductor cables problems.

At last, the usage of uncertainty analysis results is discussed. Expectation results are the most likely values, so it is useful in EMC prediction field. Standard deviation information plays an important role in sensitivity analysis and robustness analysis of EMC simulation. Worst case values are a special focus in EMC field, and it is an important value in EMC optimization design.

ACKNOWLEDGMENT

This work was supported by the National Natural Science Foundational of China under Grant 51507041.

REFERENCES

[1] S. Sun, G. Liu, J. L. Drewniak, et al., "Hand-assembled cable bundle modeling for crosstalk and common-mode radiation prediction," *IEEE Transactions on Electromagnetic Compatibility*, vol. 49, no. 3, pp. 708-718, 2007.

[2] D. Bellan and S. A. Pignari, "Efficient estimation of crosstalk statistics in random wire bundles with lacing cords," *IEEE Transactions on Electromagnetic Compatibility*, vol. 53, no. 1, pp. 209-218, 2011.

[3] G. Spadacini and S. A. Pignari, "Numerical assessment of radiated susceptibility of twisted-wire pairs with random nonuniform twisting," *IEEE Transactions on Electromagnetic Compatibility*, vol. 55, no. 5, pp. 956-964, 2013.

[4] D. Xiu and G. E. Karniadakis, "The Wiener Askey polynomial chaos for stochastic differential equations," *SIAM Journal on Scientific Computing*, vol. 24, no. 2, pp. 619-644, 2002.

[5] D. Xiu, *Numerical Methods for Stochastic Computations*. Princeton University Press, pp. 1-23, 2010.

[6] I. S. Stievano, P. Manfredi, and F. G. Canavero, "Stochastic analysis of multiconductor cables and interconnects," *IEEE Transactions on Electromagnetic Compatibility*, vol. 53, no. 2, pp. 501-507, 2011.

[7] P. Manfredi and F. G. Canavero, "Numerical calculation of polynomial chaos coefficients for stochastic per-unit-length parameters of circular conductors," *IEEE Transactions on Magnetics*, vol. 50, no. 3, pp. 74-82, 2014.

[8] P. Manfredi and F. Canavero, "Statistical analysis of multiconductor cables and interconnects with internal variability and field coupling," *42nd European Microwave Conference*, pp. 348-351, 2012.

[9] IEEE Standard for Validation of Computational Electromagnetics Computer Modeling and Simulations. IEEE STD 15971-2008, pp. 1-41, 2008.

[10] IEEE Recommended Practice for Validation of Computational Electromagnetics Computer Modeling and Simulations. IEEE STD 15972-2010, pp. 1-124, 2011.

[11] A. Duffy, A. Orlandi, and G. Zhang, "Review of the feature selective validation method (FSV). Part I: Theory," *IEEE Transactions on Electromagnetic Compatibility*, vol. 6, no. 4, pp. 814-821, 2018.

[12] A. Orlandi, A. P. Duffy, and G. Zhang, "Review of the feature selective validation method. Part II: Performance analysis and research fronts," *IEEE Transactions on Electromagnetic Compatibility*, vol. 6, no. 4, pp. 1029-1035, 2018.

[13] J. Bai, L. Wang, and D. Wang, "Validity evaluation of the uncertain EMC simulation results," *IEEE Transactions on Electromagnetic Compatibility*, vol. 59, no. 3, pp. 797-804, 2017.

Design of a Microstrip-Fed Printed-Slot Antenna Using Defected Ground Structures for Multiband Applications

Nasr H. Gad [1, 2] and Matjaz Vidmar [1]

[1] Radiation and Optics Laboratory, Faculty of Electrical Engineering
University of Ljubljana, Ljubljana 1000, Slovenia
nasr.gad@fe.uni-lj.uni.si, matjaz.vidmar@fe.uni-lj.uni.si

[2] Physics Department, Faculty of Science
Ain Shams University, Cairo11566, Egypt
ngad@sci.asu.edu.eg

Abstract ─ This paper presents the design of a microstrip-fed, planar-printed, slot antenna using defected ground structures (DGSs) for multiband applications. The antenna structure consists of two groups of five straight slot elements. The slot elements in each group are of the same width but different lengths on the ground plane and separated by a small strip and a slot cut on both sides of the strip to interconnect the group of slots with each other. The microstrip line is designed on the front side of the PCB with a right angle for all the slots to make it easy to mount the slots and the microstrip with a monolithic microwave integrated circuit (MMIC). The proposed antenna is designed and simulated using an electromagnetic simulator based on the method of moment (MoM). For the validation the antenna was fabricated on a double-sided substrate material that was 0.79 mm thick with an area of 45 × 40 mm^2. The simulation and measurement results show that the antenna has good input-impedance bandwidths of $S_{11} \leq -10$ dB at the five operating frequencies of 3.5, 4.1, 5, 6.4, and 6.8 GHz and that extends in the range 2 to 7.5 GHz. The measurements were found to be in good agreement with the simulation results for S_{11} and provide a stable radiation pattern.

Index Terms ─ Defected ground structure (DGS), microstrip line, multiband applications, printed slot antenna.

I. INTRODUCTION

The rapid growth in wireless communications means everything around us is being upgraded to wireless and the need for planar printed antennas has increased in recent years. The printed-slot antenna is one type of printed antenna that has been investigated extensively for several decades because of its attractive features, light weight, low profile, compactness and because it easy to integrate with other circuits. Its multiband characteristics make it the most suitable choice for modern wireless-communication systems.

The interests of researchers in studying planar, printed-slot antennas with a microstrip line can be seen in the literature for dual-band applications [1-4]. The design of a dual-frequency band using different stub configurations has increased the whole area of the antenna and controlled the frequency bands [5]. Many researchers have been concerned about the design of printed antennas in the area of tri-band [6-8] and quad-band [9-11] applications. A defected ground structure (DGS) is realized by etching the slots or defects on the ground plane under the microstrip line. DGSs with broad cell shapes have been studied with respect to designing microwave circuits such as filters and antennas [12, 13]. In [9], a microstrip-fed right-angle slot antenna with different lengths for quad-band applications with an end offset feed is presented. In [10], a four-band microstrip fed slot antenna is proposed based on the rectangular slot in the ground plane and by adding T- and E-shaped stubs to produce four frequency bands. In the work reported in [11], a microstrip line with a right-angle-fed, rectangular, wide-slot antenna is developed for quad-band applications.

In this paper the study of a planar-printed slot antenna with a microstrip line feeder for multiband applications is presented. The proposed antenna is designed and fabricated based on a Taconic (TLT-9) substrate of 45 mm × 40 mm. Five slots with a narrow rectangular shape are etched on the ground plane as the DGS cells. The centers of all the slots are filled with a 0.5-mm strip divided into two groups of slots: right and left. The left group of slots is longer than the right group by 0.5 mm, having a cut of two slots with a 1-mm width around the strip to connect each group of slots together. The proposed printed-slot antenna is simulated and designed using an electromagnetic simulator program based on MoM to visualize the simulation results, which show the five bandwidths around the operating

Submitted On: June 5, 2018
Accepted On: August 21, 2018

frequencies of 3.5, 4.1, 5, 6.4, and 6.8 GHz. By adjusting the length of the left group of the DGS slots to be smaller than the right group by 0.5 mm, another group of operating frequencies with the bandwidths is created with 3.6, 4.2, 5.2, 6.8, and 7.3 GHz. On the other hand, by moving the strips between the two groups of slots far from the central strip and the microstrip line the wide bandwidth is obtained around the operating frequency of 5.5 GHz with a 1.666-GHz bandwidth. The proposed antenna design is based on DGS rectangular cells (narrow slots) and a microstrip line, without the need for other stubs [9, 10] or modifying the microstrip line structure with an L shape [8, 11], and not based on large aperture slots [10, 11]. The proposed antenna and the antenna with the left group of slots smaller than the right group by 0.5 mm are suitable for the long-term evolution (LTE) band 42 (3.4-3.6 GHz), band 43 (3.6-3.8 GHz), band 48 (3.55-3.7 GHz), while intelligent transportation systems (ITSs) is the technology that can provide the variety of service in the future and the C-band applications.

II. ANTENNA DESIGN

The geometry of the proposed planar printed-slot antenna is shown in Fig. 1. The slot antenna is printed on a double-sided Taconic (TLT-9) substrate with a dielectric constant $\varepsilon_r = 2.55$, a loss tangent tan (δ) = 0.0018 and substrate height h = 0.79 mm with a copper cladding of thickness t = 0.035 mm on both sides of the PCB. All the antenna dimensions are designed on a total surface area of 45 × 40 mm^2. On the front side of the substrate, a microstrip line feeder with 50 Ω and fixed width (Wf = 2.2 mm) and feeding length (Lf = 31 mm) are designed.

The ground plane of the proposed antenna consists of two groups of five straight slots extended horizontally with different lengths. The two groups of slots are separated by a 0.5 × 8.25 mm^2 strip with a right angle for all the slots and fills the slot area parallel to the microstrip line in a symmetrical position around the origin of the x-axis. The left group of the slots are shifted by 0.5 mm to the left due to the microstrip line view of the antenna. On both sides around this strip, there is a cut spaced with a slot width (S = 1 mm) and all the slots are connected together for each group of slots.

The two groups of five slots are positioned around the strip. The right and left designed groups of slots on the ground plane are created with the following lengths for the right group, Ls1r, Ls2r, Ls3r, Ls4r, and Ls5r, and for the left group with lengths Ls1l, Ls2l, Ls3l, Ls4l, and Ls5l, and a fixed width (S = 1 mm) for all the slots. The separation between the slots controls the impedance bandwidth of the antenna, the separation between slots is fixed with (S1 = S2 = S4 = 0.75 mm) and the only different separation is (S3 = 1 mm) between Ls3 and Ls2 for both groups, left and right (as shown in Fig. 1 (b)), and with the length (Lm = 0.75 mm) between the open end of the microstrip line and the smallest slots (Ls1r and Ls1l) for adjusting the impedance (as shown in Fig. 1 (a)).

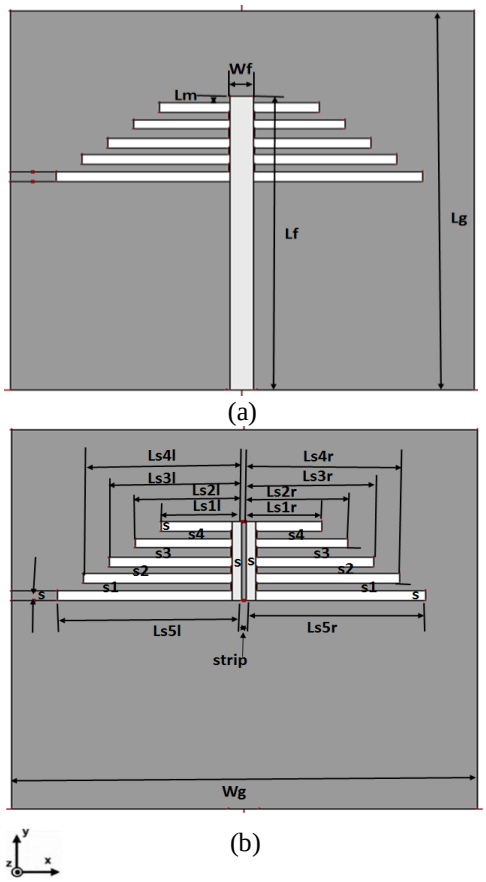

Fig. 1. Geometrical layout of the proposed planar printed slot antenna: (a) top layer and (b) bottom layer.

All the parameters for the proposed antenna are shown in Table 1.

Table 1: Dimensions of all the elements of the proposed antenna

Para-meter	Size (mm)	Para-meter	Size (mm)	Para-meter	Size (mm)
Wg	45	Ls1r	7.25	Ls1l	7.75
Lg	40	Ls2r	9.75	Ls2l	10.25
Wf	2.2	Ls3r	12.25	Ls3l	12.75
Lf	31	Ls4l	15.25	Ls4r	14.75
Lm	0.75	Ls5l	17.75	Ls5r	17.25
S	1	S1	0.75	S2	0.75
S3	1	S4	0.75	strip	0.5

In order to achieve multiband operation for the printed-slot antenna, the slot length of each radiating element must be around $\lambda_g/2$ [14]. The slot antenna length is referred to the guide wavelength λ_g, which is given by:

$$\lambda_g = \frac{c}{f\sqrt{\varepsilon_e}}, \quad (1)$$

where ε_e is the effective dielectric constant:

$$\varepsilon_e \approx \frac{(\varepsilon_r + 1)}{2}, \quad (2)$$

The slots (Ls5r + Ls4r + S1) and (Ls5l + Ls4l + S1) produce the bandwidth around the operating frequency for 3.5 GHz, (Ls4r + Ls3r + S2) and (Ls4l + Ls3l + S2) produce the bandwidth around the operating frequency for 4.1 GHz, (Ls3r + Ls2r + S3) and (Ls3l + Ls2l + S3) produce the bandwidth around the operating frequency for 5 GHz, (Ls2l + Ls1l + S4) produce the operating frequency for 6.4 GHz and finally (Ls2r + Ls1r + S4) produce the operating frequency for 6.8 GHz. All the radiating elements are shaped like an unequal U-slot as the DGS cell. The shortest slots are the active radiators and the longest slots are to improve the impedance matching for the first three operating frequencies (3.5, 4.1, and 5 GHz). Table 2 shows all the operating frequencies with the radiating slot length.

Table 2: Radiating slot length for all the operating frequencies

Freq./ λg(mm)	Length of the Radiating Slot Right Group	Length of the Radiating Slot Left Group
3.5GHz/ 59.04	Ls5r + Ls4r + S1 = 32.75 mm = 0.55λg	Ls5l + Ls4l + S1 = 33.75mm = 0.57λg
4.1GHz/ 50.4	Ls4r + Ls3r + S2 = 27.75 mm = 0.55λg	Ls4l + Ls3l + S2= 28.75 mm = 0.57λg
5GHz/41.33	Ls3r + Ls2r + S3 = 23 mm = 0.556λg	Ls3l + Ls2l + S3 = 24 mm = 0.58λg
6.4GHz/ 32.29		Ls2l + Ls1l + S4 = 18.75 mm = 0.58λg
6.8GHz/ 30.39	Ls2r + Ls1r + S4 = 17.75 mm = 0.58λg	

By changing the slot lengths of the left group of the proposed antenna without changing the slot lengths of the right group, shown in Table 3, a comparison is made between the proposed antenna and other three different antennas (antenna 1, antenna 2, and antenna 3) for the simulated return loss shown in Fig. 4.

All the left group of slots in antenna 1 equal the right one, and for antenna 2 all the left slots are shorter than the same group in the proposed antenna by 1 mm and the other five operating frequencies with their bandwidths are obtained. For antenna 3 all the left slots are longer than the same group in the proposed antenna by 0.5 mm, and the other eight operating frequencies with their bandwidths are created. By shifting the strips between the slots in the proposed antenna on both sides of the central strip, the wideband slot antenna is obtained with an operating frequency at 5.5 GHz with a radiating length Ls5l = 17.75 mm, with λ_g = 37.57 mm leading to Ls5l = 0.47 λ_g. It is also calculated for Ls5r = 17.25 mm, leading to Ls5r = 0.46 λ_g. Figure 4 shows S_{11} for all the antenna configurations.

Table 3: Three antennas based on different lengths of left slots for the proposed antenna (PA)

Antenna Name	Left Slots (mm)				
	Ls1l	Ls2l	Ls3l	Ls4l	Ls5l
PA	7.75	10.25	12.75	15.25	17.75
Antenna 1	7.25	9.75	12.25	14.75	17.25
Antenna 2	6.75	9.25	11.75	14.25	16.75
Antenna 3	8.25	10.75	13.25	15.75	18.25

III. RESULTS AND DISCUSSION

The proposed planar-printed slot antennas were designed and simulated using the IE3D electromagnetic simulator software based on the method of moments (MoM). The simulated results, including the current distribution, return losses, gains, efficiency, and radiation patterns are numerically derived using the IE3D commercial software. In the IE3D software the larger the number of cells per wavelength, the better the accuracy of the simulation. However, increasing the number of cells increases the total simulation time and the memory required for simulating the structure. In many simulations, using 20 to 30 cells per wavelength should provide enough accuracy. All the parameters that affect the antenna's performance were simulated based on the method of moments. The simulated proposed antenna was printed and fabricated on double-sided metallic layers on a TLT-9 substrate.

To verify the obtained results from the electromagnetic simulator program, the structure is fabricated using the laser-based PCB prototyping LPKF protoLaser S4 and the fabricated antenna's important parameters are measured. To validate the predicted performance of this proposed slot antenna, a prototype antenna was then fabricated and measured. Figure 2 shows the photographs of the top and bottom sides of the fabricated antenna.

(a) (b)

Fig. 2. Fabricated prototype of the proposed planar printed slot antenna: (a) top side and (b) bottom side.

Measurements on the fabricated antenna were carried out using a Rohde & Schwarz ZVA67 Vector Network Analyzer for measuring the return loss (S_{11}) and an anechoic chamber for the radiation-pattern measurements.

The detailed results are provided in the following for a comparative study.

The current distributions of the proposed antenna for the five resonant frequencies and the wideband antenna for the resonant frequency of 5.5 GHz are shown in Fig. 3.

Figure 3 shows how the current distribution affects the different parts of the proposed printed-slot antenna, depending on the frequency level (max. E-current = 26.59 (A/m)). When it reaches 3.5 GHz, the current distribution is concentrated in between the largest slots (Ls5l, Ls4l) and (Ls5r, Ls4r) with a straight shape. At a frequency of 6.4 GHz the current distribution concentrated in between the slots (Ls2l, Ls1l), and when the frequency reaches 6.8 GHz, the current distribution concentrated in the smallest slots (Ls2r, Ls1r). By moving the horizontal strips between the slots a wideband antenna is obtained with a bandwidth around 5.5 GHz (max. E-current = 22.972 (A/m)).

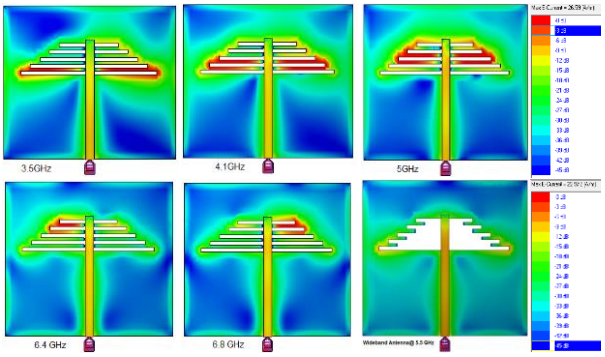

Fig. 3. Current distribution of the proposed antenna and the wideband antenna at the operating frequencies.

The return loss for all the antenna configurations is shown in Fig. 4. The simulated and measured return loss (S_{11}) of the proposed designed antenna is depicted in Fig. 4 (a). The results show good agreement with each other for all the operating bands in the range 2–7.5 GHz. The measured impedance bandwidths achieved are 3.295–3.542 GHz with a bandwidth of 0.247 GHz (7.23%), 3.893–4.156 GHz with bandwidth of 0.263 GHz (6.53%), 4.708–5.052 GHz with a bandwidth of 0.344 GHz (7.05%), and two integrated bandwidths around 6.656 GHz with (S_{11}= -15.2 dB) in the range of 5.789–6.656 GHz with a bandwidth of 0.867 GHz (13.93%), 6.656–7.035 GHz with a bandwidth of 0.379 GHz (5.54%), and the last two bands are considered as a wideband of 5.789–7.035 GHz with a bandwidth of 1.246 GHz (19.43%) for $|S_{11}| < -10$ dB. A comparison of the S_{11} data for all the operating frequencies is shown in Table 4.

The simulation results for the return loss of the proposed antenna (45 mm × 40 mm) in comparison with the large ground plane antenna (50 mm × 45 mm) and the wideband antenna that is obtained from the proposed antenna by moving the strip between the slots are shown in Fig. 4 (b). The simulated S_{11} for antenna 1, antenna 3, and the proposed antenna are plotted in Fig. 4 (c). Figure 4 (d) shows the simulated S_{11} for antenna 2 and the proposed antenna, and is shown in Fig. 4 (e) for the proposed antenna that consists of two groups of five slots plotted in comparison with two-, three-, and four-groups of slots, right and left.

Table 4: Simulated and measured S-parameters for the proposed slot antenna

Resonant Freq. (GHz)		**S_{11} (dB) at Resonant Freq.**		**Freq. Range (GHz)**	
Sim.	**Meas.**	**Sim.**	**Meas.**	**Sim.**	**Meas.**
3.5	3.456	-21.72	-21.17	3.317-3.571	3.295-3.542
4.1	4.028	-29.15	-37.39	3.933-4.193	3.893-4.156
5	4.952	-24.13	-26.14	4.851-5.098	4.708-5.052
6.4	6.516	-33.74	-36.02	5.889-6.6	5.789-6.656
6.8	6.884	-29.48	-45.17	6.6-6.996	6.656 - 7.035

As presented in Fig. 4 (a) and in Table 2, we can conclude that we have a good agreement between the simulation and measurement results. It is clear that in Fig. 4 (b) the proposed antenna has a good return loss performance in comparison to the other antenna by changing the ground plane to 50 × 45 mm^2, with no impact on the operating frequency by increasing the ground plane. On the other hand, by shifting the horizontal strips between the slots and leaving 2.5 mm for all four slots ((Ls1r, Ls2r, Ls3r, Ls4r, and Ls1l, Ls2l, Ls3l, Ls4l), the right and left are the same and the largest slot (Ls5r, and Ls5l) with 5 mm remains from the original configuration of the proposed antenna and the wide bandwidth is obtained around the operating frequency of 5.5 GHz with its band (4.796-6.462 GHz) having a 1.666 GHz bandwidth (29.6%).

Figure 4 (c) shows the comparison for the three antenna configurations between antenna 1, proposed antenna, and antenna 3. For antenna 1 and the proposed antenna we see the effect of increasing the left group of slots more than the right group by 0.5 mm and good impedance matching is verified for all the operating frequencies. For antenna 3 by increasing the left slots more than the proposed antenna by 0.5 mm eight operating frequencies are created (3.3, 3.5, 3.9, 4.1, 4.7, 5, 6.1, and 6.8 GHz) and its S11 at -14.6, -21, -18.9, -17, -12, -12.1, -24.8, and -26.5 dB, respectively, and the radiating slots are 34.75, 32.75, 29.75, 27.75, 25, 23, 19.75, and 17.75 mm.

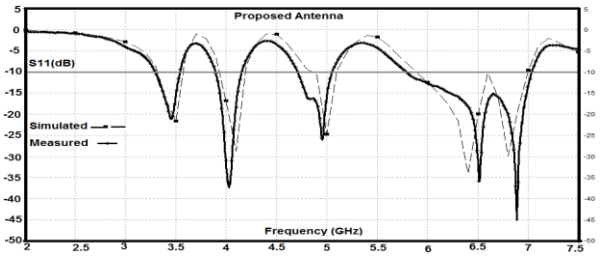

(a) Simulated and measured proposed antenna

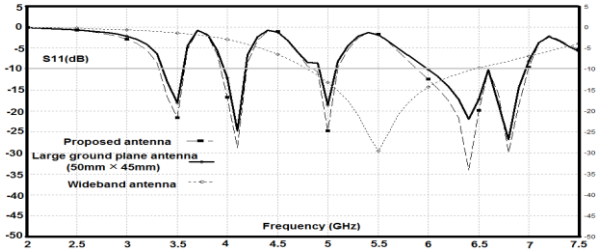

(b) Simulated (proposed, large ground plane, and wideband) antennas

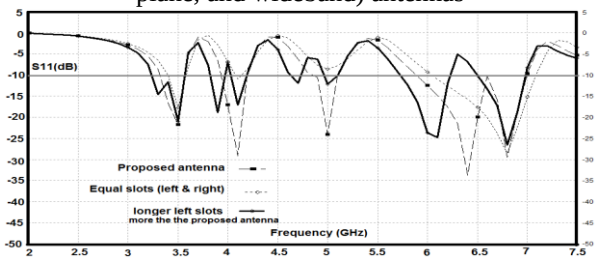

(c) Simulated proposed antenna, antenna 3 (longer left slots), and antenna 1 (equal slots)

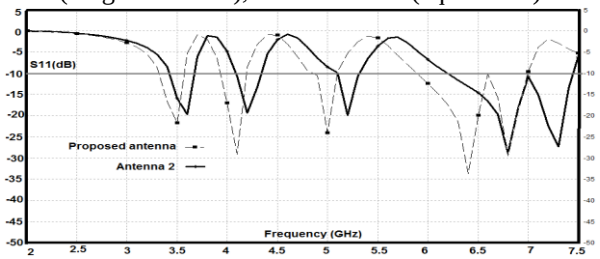

(d) Simulated proposed antenna and antenna 2

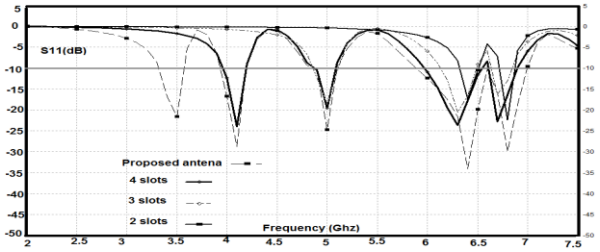

(e) Simulated proposed antenna and 2-, 3-, and 4-group of slots right and left

Fig. 4. Return loss of different antenna configurations.

The most useful comparison is shown in Fig. 4 (d), which shows that the proposed antenna with five operating frequencies at 3.5, 4.1, 5, 6.4, and 6.8 GHz and antenna 2 operates at frequencies 3.6, 4.2, 5.2, 6.8, and 7.3 GHz with its S_{11} at -19.8, -19.38, -19.95, -28.9, and -27.35 dB, respectively.

Figure 4 (e) shows the sequence of the proposed design for two groups of two-, three-, and four-slots for right and left in comparison with the proposed antenna.

The simulated peak gains of the proposed planar printed-slot antenna fed by a microstrip line are plotted in Fig. 5. The simulated results of the gain show the values 4.316, 4.334, 4.42, and 5.529 dBi at 3.5, 4.1, 5, and 6.4 GHz, respectively. For a higher frequency of 6.8 GHz (over the bandwidth) the gain was found to have a value of 5.38 dBi.

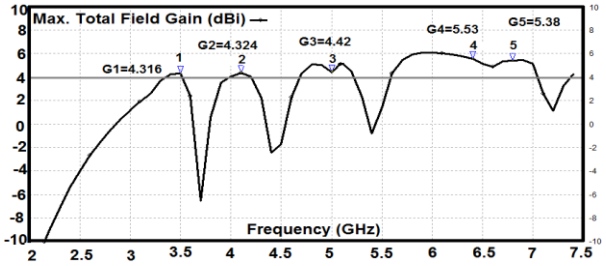

Fig. 5. Simulated gains of the proposed antenna.

The simulated efficiency versus frequency of the proposed planar printed slot antenna is plotted in Fig. 6. The simulated antenna efficiency at the operating frequencies is given by 94.8% at 3.5 GHz, 86.74% at 4.1 GHz, 84.92% at 5 GHz, 91.9% at 6.4 GHz, and finally 90.08% at 6.8 GHz.

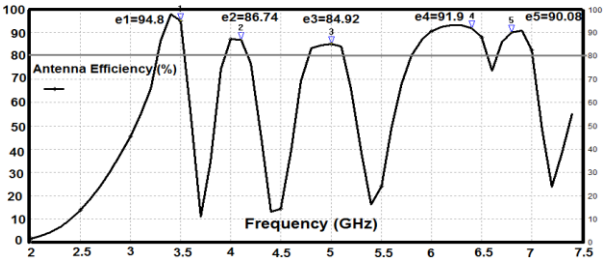

Fig. 6. Simulated efficiency of the proposed antenna.

The maximum directivity measured with the radiation-pattern measurements and the values at the operating frequency in the E-plane (DE) and H-plane (DH) is given in Table 5.

For making a rough estimation about the measured gain, the simulated efficiency is used to calculate the gain based on the measured directivity that is obtained from the radiation-pattern measurements, and it is shown in Table 5.

The radiation-pattern measurements are obtained by using a HP 8650B sweep oscillator (2–26.5 GHz) as a signal generator connected with a standard horn antenna at the corresponding operating frequencies. The

proposed antenna is held on a rotary for covering all the angles of the pattern and the whole system is built inside three covered walls with microwave absorbers. The antenna is connected with a homemade, high-frequency detector and a lock-in amplifier [15], which is interfaced to a personal computer. Therefore, the data can be stored. The simulated and measured far-field radiation patterns (E_{tot}) for the five resonant frequencies (3.5, 4.1, 5, 6.4, and 6.8 GHz) are shown in Fig. 7.

Table 5: The measured directivity (DE, DH) and gain

Freq. (GHz)	3.5	4.1	5	6.4	6.8
DE (dBi)	3.8	4.62	5.31	6.13	5.8
DH (dBi)	3.8	5.68	6.63	6.23	6.13
D (dBi)	3.8	5.182	6.02	6.18	5.97
Gain (dBi)	3.6	4.495	5.11	5.68	5.379

The radiation patterns of the proposed antenna are measured in the anechoic chamber for a verification of the simulated radiation patterns in the E-plane (Y-Z plane) and the H-plane (X-Z plane). It is clear that the radiation patterns in the E-plane for all frequencies under test have a bidirectional pattern; however, the radiation patterns for the H-plane are found to be approximately omnidirectional.

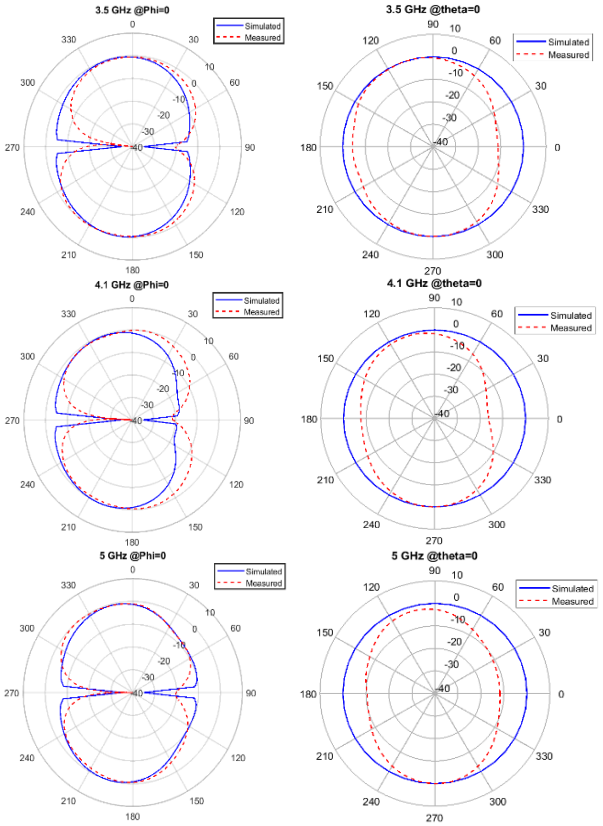

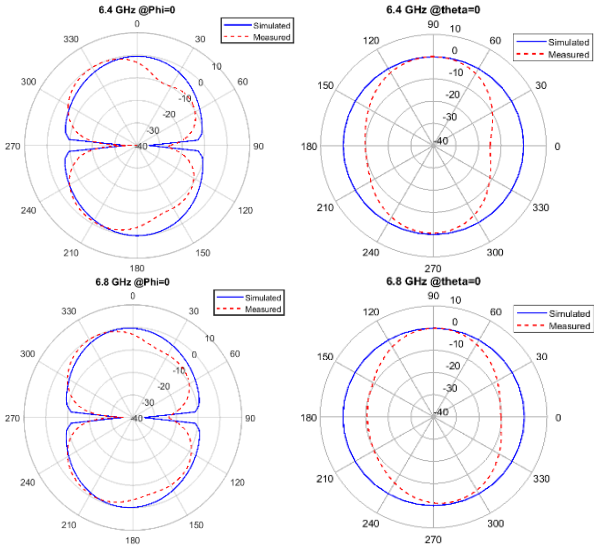

(a) E-plane at 3.5, 4.1, 5, 6.4, and 6.8 GHz (b) H-plane at 3.5, 4.1, 5, 6.4, and 6.8 GHz.

Fig. 7. Simulated and measured radiation patterns of the proposed multiband printed slot antenna.

IV. CONCLUSION

A novel planar-printed slot antenna with slot defects on the ground plane that operates at five bands has been successfully designed and simulated using the IE3D electromagnetic simulator and fabricated using LPKF technology based on a TLT-9 substrate to validate the simulation results. The measured results show good agreement with the simulation results for the return loss and provide a stable radiation pattern for the operating frequencies. The proposed antenna is designed and fabricated on a double-sided PCB, and the obtained results show that the printed-slot antenna can operate effectively at five frequencies with a useful radiation pattern. The impedance bandwidth contains three narrowbands around the operating frequencies (3.5 GHz with (7.23%), 4.1 GHz with (6.53%), and at 5 GHz with (7.05%)) and for the other two integrated in wideband and divided around (6.4 GHz with (13.93%), and 6.8 GHz with (5.54%). The gain varied from 4.316 to 5.529 dBi at the operating frequencies. The design process aimed at the best return losses and fine quality radiation characteristics over all the penta-bands. This makes the antenna design suitable for multiband applications.

ACKNOWLEDGMENT

All the authors thanks to Mr. Bojan Zalar from LPKF Laser & Electronics for fast and precise fabrication of the antenna samples using LPKF ProtoLaser.

REFERENCES

[1] M. N. Mahmoud and R. Baktur, "A dual band microstrip-fed slot antenna," in *IEEE Transactions on Antennas and Propagation*, vol. 59, no. 5, pp. 1720-1724, May 2011.

[2] C. Hsieh, T. Chiu, and C. Lai, "Compact dual-band slot antenna at the corner of the ground plane," in *IEEE Transactions on Antennas and Propagation*, vol. 57, no. 10, pp. 3423-3426, Oct. 2009.

[3] X. L. Bao and M. J. Ammann, "Microstrip-fed dual-frequency annular-slot antenna loaded by split-ring-slot," *IET Microwaves, Antennas & Propagation*, vol. 3, no. 5, pp. 757-764, Aug. 2009.

[4] O. Amjad, S. W. Munir, S. T. Imeci, and A. O. Ercan, "Design and implementation of dual band microstrip patch antenna for WLAN energy harvesting system," *Applied Computational Electromagnetic Society (ACES) Journal*, vol. 33, no. 7, pp. 746-751, July 2018.

[5] C. Y. Pan, T. S. Horng, W. S. Chen, and C. H. Huang, "Dual wideband printed monopole antenna for WLAN/WiMAX applications," *IEEE Antennas and Wireless Propagation Letters*, vol. 6, pp. 149-151, 2007.

[6] M. H. B. Ucar and Y. E. Erdemli, "Triple-band microstripline-fed printed wide-slot antenna for WiMAX/WLAN operations," *Applied Computational Electromagnetic Society (ACES) Journal*, vol. 29, no. 10, pp. 793-800, Oct. 2014.

[7] F. B. Zarrabi, S. Sharma, Z. Mansouri, and F. Geran, "Triple band microstrip slot antenna for WIMAX/WLAN applications with SRR shape ring," *Fourth International Conference on Advanced Computing & Communication Technologies*, Rohtak, India, pp. 368-371, 2014.

[8] W. Ren and C. Jiang, "Planar triple-band balance-shaped slot antenna," *Microwave and Optical Technology Letters*, vol 58. no. 5, pp. 1078-1082, May 2016.

[9] P. Rakluea, N. Anantrasirichai, K. Janchitrapongvej, and T. Wakabayashi, "Multiband microstrip-fed right angle slot antenna design for wireless communication systems," *ETRI Journal*, vol. 31, no. 3, pp. 271-281, 2009.

[10] Y. F. Cao, S. W. Cheung, and T. I. Yuk, "A multiband slot antenna for GPS/WiMAX/WLAN systems," *IEEE Transactions on Antennas and Propagation*, vol. 63, no. 3, pp. 952-958, Mar. 2015.

[11] L. Xiong, P. Gao, and P. Tang, "Quad-band rectangular wide-slot antenna for GPS/WiMAX/ WLAN applications," *Progress In Electromagnetics Research C*, vol. 30, pp. 201-211, 2012.

[12] M. K. Khandelwal, B. K. Kanaujia, and S. Kumar, "Defected ground structure: Fundamentals, analysis, and applications in modern wireless trends," *Hindawi International Journal of Antennas and Propagation*, vol. 2017, 1-23, 2017.

[13] D. Guha and Y. M. M. Antar, *Microstrip and Printed Antennas: New Trends, Techniques and Applications*. Ch. 12, Wiley, UK, 2011.

[14] R. Garg, P. Bhartia, I. Bahl, and A. Ittipiboon, *Microstrip Antenna Design Handbook*. Artech House, Norwood, MA, 2001.

[15] M. Vidmar, "Lock-in receiver with a source up to 12 GHz," http://lea.hamradio.si/~s53mv/lockin/ lockin.html

Nasr Gad received his B.Sc. and M.Sc. degrees in Electronics from Faculty of Science Ain Shams University, Cairo, Egypt in 2005 and 2012 respectively. Currently, he is pursuing his Ph.D. degree in Electrical Engineering from the University of Ljubljana, Slovenia. His current research interests include planar printed antenna designing for multiband applications.

Matjaž Vidmar received his B.S.E.E., M.S.E.E., and Ph.D. degrees from University of Ljubljana, Slovenia, in 1980, 1983 and 1992, respectively. His doctoral research concerned the development of a single-frequency GPS ionospheric correction receiver. He currently teaches undergraduate and postgraduate courses in Electrical Engineering at Ljubljana University, where he is Head of the Radiation and Optics Laboratory (LSO), Department for Electrical Engineering. His current research interests include microwave and high-speed electronics ranging from avionics to optical-fiber communications. Under his leadership, the LSO has developed most of the 10-Gb/s electronics (pulse modulator, clock recovery) used in the Ester (ACTS 063) Project and many 40-Gb/s circuits used in the ATLAS (IST 10626) Project: EAM drivers, transmitter clock distribution, 40- and 80-Gb/s clock-recovery circuits, and 40-Gb/s PMD compensation receiver electronics. He has also developed and built satellite hardware flown in space in 1990 on the Microsat mission and in 2000 on the AMSAT-P3D satellite.

Design of Reconfigurable Antenna Feeding Network Using Coupled-line Switch for 5G Millimeter-wave Communication System

Sangkil Kim [1] and Jusung Kim [2*]

[1] Department of Electronics Engineering
Pusan National University, Busan, 46241, South Korea
ksangkil3@pusan.ac.kr

[2] Department of Electronics and Control Engineering
Hanbat National University, Daejeon, 34158, South Korea
jusungkim@hanbat.ac.kr*

Abstract ─ In this paper, a reconfigurable antenna feeding network using coupled line switches for 5G communication system is presented. Two quarter-wave impedance transformers were integrated to support TDD operation and a single stage coupled line filter was used as a DC block for RF switches instead of using conventional surface mounting components. Design equations and theoretical analysis for the proposed reconfigurable antenna feeding network are also presented. To demonstrate the performance of the proposed reconfigurable antenna feeding system for MIMO, two monopole antennas were integrated orthogonally to the designed feeding network. Vertical or horizontal polarization was successfully formed and the radiation pattern can be selectable by manipulating the switches.

Index Terms ─ 5G communication system, coupled line switch, MIMO antenna, mmWave antenna, reconfigurable antenna feeding network, System-on-Package (SoP) technology.

I. INTRODUCTION

The millimeter wave (mmWave) communication system is promising technology for 5G communication. The 5G mmWave communication technology has received great attention from many researchers and industry, and there has been a lot of reported research efforts on mmWave-based 5G communication system [1-3]. It is possible to achieve high network throughput and data rate as high as gigabits per second (Gbps) by leveraging massive multiple-input multiple-output (MIMO) technology. It can also handle over thousand times more mobile traffic than previous mobile communication networks such as 4G LTE [2]. It is reported that time-division duplex (TDD) is more efficient in a wireless backhaul network that uses massive MIMO in small cells compared to frequency-division duplex (FDD) [3]. Since TDD can handle asymmetric data rates in the uplink and downlink, TDD does not require the same frequency spectrum as FDD. Therefore, TDD provides more flexibility in 5G communication (Tx/Rx). It can also dynamically allocate channel capacity based on the communication traffic load. In the case of massive MIMO, the 5G communication system also requires an array antenna with dual polarization capability.

In this paper, a polarization and radiation pattern reconfigurable antenna feeding network consisting of coupled line switches and quarter-wave impedance transformers is presented. This paper also provides a computational design and modeling idea for 5G mmWave module designs consisting of an RFIC and an antenna array. Two quarter-wave impedance transformers are integrated to support TDD operation and reduces the number of antennas for system miniaturization. The uplink (Tx) and downlink (Rx) paths are successfully isolated by the designed quarter-wave impedance transformer. A coupled line-based PIN diode switch is proposed to decouple the DC bias path from RF signal path because there are not many available SMD passive components such as inductors or capacitors working in the frequency band above 28 GHz. Two monopole antennas were placed orthogonally through the coupled line RF switch to reconstruct the antenna polarization and radiation pattern for MIMO applications. The proposed reconfigurable antenna feeding network can be easily extended to a large array system, but a single Tx/Rx pair is discussed in this paper as a proof-of-concept without loss of generality.

This paper is organized as follows. Section II discusses the design of the proposed reconfigurable antenna feeding network for mmWave applications using coupled line switches. Section III shows the system performance by integrating two monopole antennas with the reconfigurable feeding network shown in Section II.

Submitted On: May 2, 2018
Accepted On: July 22, 2018

It is followed by conclusion.

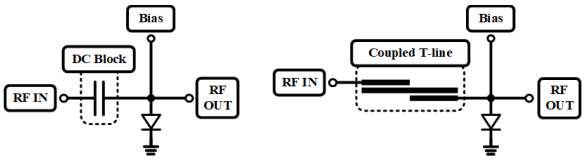

(a) (b)

Fig. 1. (a) A conventional SPST switch, and (b) the proposed coupled line switch for mmWave applications.

II. RECONFIGURABLE ANTENNA FEEDING NETWORK

It is important to select proper fabrication technology for a design because fabrication resolution (metal-to-metal distance, metal width/thickness, *etc.*) and electrical material properties (ε_r, and tan δ) are critical design parameters for design feasibility and system implementation.System-on-Package (SoP) technology using flip chip ball grid array (FCBGA) packaging has been chosen because it offers fine feature sizes up to 20 μm and is widely used in RFIC industry for high system integrity and multi-die handling capability [4]. A 15 μm thick copper layer is deposited on a 40 μm thick substrate material which has dielectric constant (ε_r) of 3.4 and loss tangent (tan δ) of 0.0044 at 28 GHz [5]. The microstrip line structure was chosen in the system design because it is easy to implement the design and it is enough to show the proof-of-concept presented in this paper. It has been proved with many reported research efforts that the microstrip and strip line structures can be fabricated with high reliability along with good correlation between simulation and measurement results [6,7].

A. Ports and lumped elements models

It is important to set the ports appropriately and build lumped elements models for the accuracy of the simulation results. A voltage or a current source is a good excitation model that describes voltage or current flow from the IC. Therefore, bumps of IC chip should be excited by a lumped port model. Other ports for the transmission lines should be excited by a waveguide port to excite the quasi-TEM mode of the microstrip line.

The PIN diode switch can be modeled as a series or a parallel RLC tank when it is turned 'on' or 'off'. It has low resistance when the diode switch is on, and it has high resistance when the switch is off. For the Finite Element Method (FEM), the lumped element can be modeled as a 2D rectangular sheet (width: *w*, length: *l*) having tangential E and H fields (E_t, H_t) for the sheet. The lumped impedance (Z_l) is described by voltage (V) and current (I) as $Z_l = V/I$. The current, I, flows in the length-direction and the voltage difference, V, is measured between the two terminals along the length. The field impedance (Z_f) is also described by the tangential field components as $Z_f = E_t/H_t$. Z_l and Z_f can be related by the definition of $V = \int E_t dl = E_t \cdot l$ and $I = \oint_c H_t dc = H_t \cdot w$ where c is a closed contour surrounding the sheet. Therefore, the Z_l and Z_f can be described as $Z_f = \left(\frac{w}{l}\right) Z_l$.

There are many important issues with building accurate EM model in mmWave. Those are parasitic coupling, passive/active component models, signal dispersion and loss of transmission line [8]. Three-dimensional full wave FEM analysis was chosen to capture all the possible couplings and radiations in the proposed circuit in this paper. The nonlinear diode switch was modeled as a parallel passive RC tank depending on its state as discussed. Surface roughness and metal thickness were also considered for better modeling of the mmWave SoP technology.

B. Coupled line switch for mmWave applications

Figure 1 (a) shows a simplified conventional single-pole single-throw (SPST) RF switch. It consists of a single PIN diode and a DC bias circuit. A DC block capacitor is an important component of the switch operation to decouple the RF signal from the DC bias of the PIN diode. A high capacitance value (nF ~ μF or higher) with sufficient quality factor (Q) in the GHz frequency band is desirable because it provides low RF impedance (almost short circuit) while isolating the RF path from the DC bias circuit. Surface-mount devices (SMDs) are widely used as DC block capacitors since they are small enough to be considered lump components (< $\lambda_0/20$) in the frequency band below 10 GHz. However, it is challenging to use lumped SMDs for mmWave applications operating at 28 GHz or higher. It is due to the low self-resonant frequency (SRF) of the SMDs, high parasitic values, and the large size of the components compared to the wavelength at 28 GHz.

Figure 1 (b) shows the proposed coupled microstrip line switch for mmWave applications. The coupled microstrip line separates the DC bias path from RF signal path, and suppresses even harmonics from RF circuit (RF_{IN}). The proposed design does not require SMDs for the DC block and the coupled line can be designed to achieve better harmonic rejection or the desired phase shift.

C. Quarter-wave transformer section

Two quarter-wave ($\lambda/4$) impedance transformers are designed to transform the output (input) impedance of PA (LNA) as shown in Fig. 2. For instance, the PA output pin is connected to the $\lambda/4$ transformer at pin ① and the transformer at pin ② is connected to ground at Tx mode. Theoretically, the load impedance of the $\lambda/4$ transformer

at pin ① is the output impedance of PA (Z_{L1}) when the impedance at pin ② is 0 Ω (Z_{L2}). The impedance seen looking into the pin ③ ($Z_{in,\lambda/4}$) can be expressed as (1):

$$Z_{in,\lambda/4} = \left[Z_1 \frac{Z_{L1}+jZ_1\tan(\beta\cdot l_{Q1})}{Z_1+jZ_{L1}\tan(\beta\cdot l_{Q1})}\right] || \left[Z_2 \frac{Z_{L2}+jZ_2\tan(\beta\cdot l_{Q2})}{Z_2+jZ_{L2}\tan(\beta\cdot l_{Q2})}\right], \quad (1)$$

where β is a propagation constant. Z_1 and l_{Q1} are the characteristic impedance and length of the $\lambda/4$ transformer at ①-③ while Z_2 and l_{Q2} are those of the transformer at ②-③. Since $\beta \cdot l_{Q1} = \beta \cdot l_{Q2} = \pi/2$ for a quarter-wave transmission line, $Z_{in,\lambda/4}$ can be simplified as (2) when $Z_1 = Z_{L1}$ (matched case):

$$Z_{in,\lambda/4} = Z_{L1} || \infty = Z_{L1}. \quad (2)$$

Therefore, the impedance seen looking into a bump (①: Tx, Z_{L1} or ②: Rx, Z_{L2}) shows up at pin ③ ($Z_{in,\lambda/4}$) without loading each other due to the impedance transformation. An antenna can be shared with the Tx and Rx modes due to the quarter-wave impedance transformer, which reduces the number of required antennas.

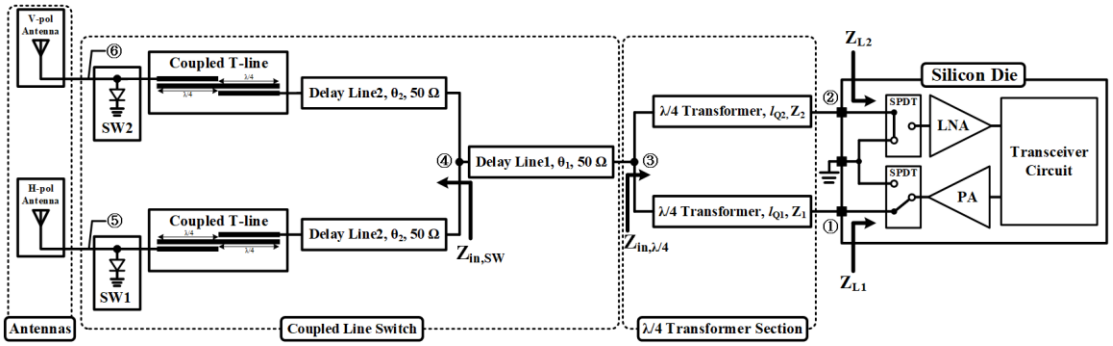

Fig. 2. Block diagram of the proposed reconfigurable antenna feeding network for 5G mmWave communication system.

Figure 3 shows the S-parameters of a quarter-wave transformer using a microstrip line structure. The distance between Tx/Rx bumps is 300 μm. In this design, the quarter-wave length (l_{Q1}, l_{Q2}) at 28 GHz is about 1700 μm, and the width of the 50 Ω microstrip line is about 81 μm according to the design equations reported in [9]. The insertion loss (IL) of the designed quarter-wave transformer section is about 0.25 dB, and it has broad fractional bandwidth of 70.1% (17.08 GHz ~ 36.71 GHz) at 28 GHz. The bandwidth is wide enough to cover 5G communication frequency band of 26.65 GHz ~ 29.19 GHz used in Korea and North America. It also provides a good isolation level of 35 dB between the Tx and Rx paths at the operation frequency

D. Coupled line impedance transformer and switch

The parallel coupled microstrip line is a critical part of the proposed system because it separates the DC bias circuit from RF signal path. It also suppresses even harmonics from a non-linear circuit since it follows coupled T-line bandpass filter theory. The single branch of the coupled line switch shown in Fig. 2 consists of a coupled line impedance transformer and a PIN diode switch. The coupled line impedance transformer can be modeled as a single stage (N=1) coupled line filter having a delay line as shown in Fig. 4. The coupling effect between the two parallel microstrip lines is modeled as admittance inverter, $\boldsymbol{J}$, because of the capacitive coupling [10]. The electrical length of the coupled lines (θ_3) is set to 90° (π/2) at the center frequency of the passband (28 GHz) to obtain band-pass frequency response. The delay line2 compensates the phase required to transform a low impedance to a high impedance ($Z_{in,SW}$), such as a quarter-wave impedance transformer, when the switch is turned on (short circuit) at ⑤/⑥ as shown in Fig. 4 (a). The delay line1 connects the coupled switches to the quarter-wave transformer. There is no impedance transformation through delay line1 because it is matched to the transformer and the switch section. The electrical length of delay line1 (θ_1) can be appropriately selected to achieve the desired phase delay.

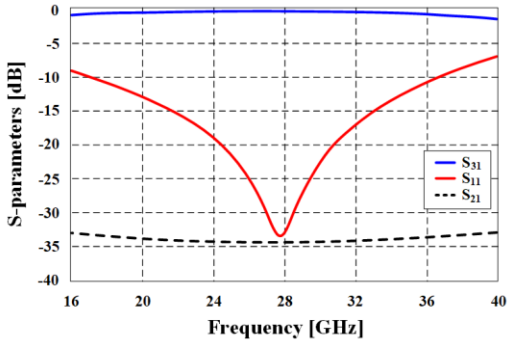

Fig. 3. S-parameters of the designed $\lambda/4$ transformer section.

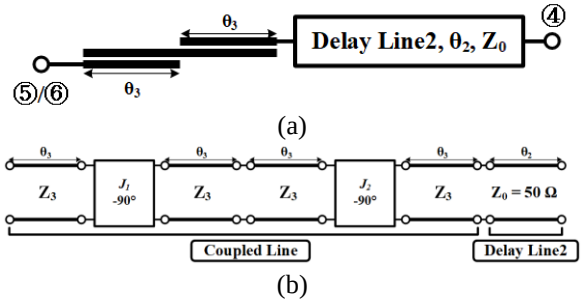

Fig. 4. (a) Proposed coupled line impedance transformer without diode switch, and (b) its equivalent transmission line model.

The design equations of the coupled microstrip line is written as (3) ~ (5) according to the coupled line band-pass filter theory when the length of the coupled line is quarter-wavelength ($\theta_3 = \pi/2$) [11]. The transformed impedance ($Z_3\boldsymbol{J}_1$ and $Z_3\boldsymbol{J}_2$) can be calculated as (3) and (4) where Δ is a fractional bandwidth and g_1/g_2 are element values for maximally flat lowpass filter prototypes:

$$Z_3\boldsymbol{J}_1 = \sqrt{\frac{\pi\Delta}{2g_1}}, \tag{3}$$

$$Z_3\boldsymbol{J}_2 = \sqrt{\frac{\pi\Delta}{2g_1g_2}}. \tag{4}$$

The even (Z_{3e}) and odd mode (Z_{3o}) impedances can be extracted from (5) using characteristic impedance (Z_3) of the transmission line:

$$\begin{cases} Z_{3e} = Z_3 \cdot (1 + \boldsymbol{J}Z_3 + (\boldsymbol{J}Z_3)^2) \\ Z_{3o} = Z_3 \cdot (1 - \boldsymbol{J}Z_3 + (\boldsymbol{J}Z_3)^2) \end{cases}. \tag{5}$$

For simplicity and symmetry of design, $g_1 = g_2 = 2$ and $Z_3 = 50\ \Omega$ were chosen as the initial values. The fractional bandwidth, Δ, was set to 0.7 which has the same bandwidth as the quarter-wave transformer presented in the previous section. The calculated initial Z_{3e} and Z_{3o} were 114.56 Ω and 40.42 Ω, respectively. It requires 22.8 μm width and 14.0 μm gap which are not practical. Generally, fabrication resolution varies by manufacturer, but for most manufacturers, a 25 μm width and a 20 μm gap are most widely accepted minimum width/gap feature sizes [5]. Final even/odd impedance values (Z_{3e}/Z_{3o}) and physical dimensions (line width/gap) are iteratively derived using the design equations starting at the initial values by adjusting the fractional bandwidth (Δ) and characteristic impedance (Z_3). The final design parameter values are: $\Delta = 0.32$, $Z_3 = 60\ \Omega$, $Z_{3e} = 105.2\ \Omega$, $Z_{3o} = 45\ \Omega$. The final line width and the gap of the coupled line were 30 μm and 20 μm, respectively.

Figure 5 shows the impedance of a single coupled line switch segment (Fig. 4) at 27.5~28.5 GHz on Smith chart when diode switch 1 is on (shorted to GND). Delay line2 successfully transforms low impedance to high impedance and requires an electrical length of about $0.19\lambda_g$ (about 1300 μm). Figure 6 shows S-parameters of the proposed single coupled line switch. The insertion loss is 0.89 dB and the 3-dB bandwidth is 8.96 GHz (fractional bandwidth: 31.7%). A DC block using a SMD capacitor for millimeter wave application is also shown in Fig. 6 for comparison purposes. The capacitance value of the SMD was 82 pF (0.07 Ω at 28 GHz), and its size was 1.4 mm × 0.5 mm (0502 SMD standard). It has an operation frequency range of up to 40 GHz [12]. The IL of the DC block utilizing SMD capacitor is 1.21 dB and it has reflection coefficient of -7.54 dB at 28 GHz. It has 0.3 dB higher loss and relatively poor reflection coefficient than the proposed coupled line-based DC block. S_{54} of the proposed RF switch network shows the band-pass response in contrast to the flat S_{54} of a conventional RF switch. Therefore, the proposed RF switch provides more immunity to out-of-band interferences.

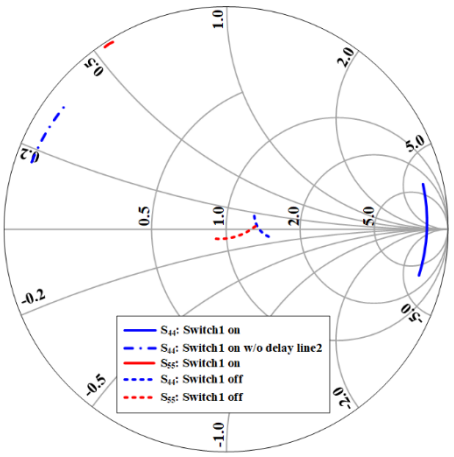

Fig. 5. Impedance of the switch: On/Off states.

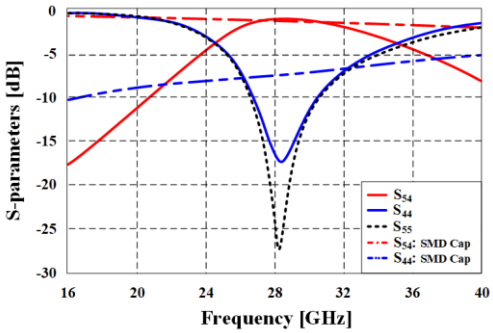

Fig. 6. S-parameters of the designed coupled line impedance transformer and a conventional DC block using SMD capacitor for mmWave applications.

E. Reconfigurable antenna feeding network

In this section, a reconfigurable antenna feeding network was constructed by integrating the designed quarter-wave impedance transformer and two coupled

line switches. The signal input pins were ① (Tx mode)/② (Rx mode) and the output pins were ⑤ (H-pol antenna)/ ⑥ (V-pol antenna) (shown in Fig. 2). The switches (SW1 and SW2) exclusively direct the signal to the desired path. For example, signal is directed to ⑥ from ① when SW1 is 'on' and SW2 is 'off' while input pin of LNA, ②, is pull-down to ground in case of Tx mode.

Figure 7 summarizes the performance of the proposed reconfigurable antenna feeding network. The total IL at 28 GHz is 1.57 dB, and 3-dB bandwidth is 25.17 GHz ~ 30.78 GHz (5.61 GHz) which is wide enough to cover the target bandwidth (26.65 GHz ~ 29.19 GHz). The total insertion loss (between ① and ⑤/ ⑥) includes the loss of $\lambda/4$ transformer (0.25 dB), coupled line switch (0.89 dB), T-junction (connecting two coupled line switches for V-/H- antennas: 0.43 dB). It should be noted that there is almost no difference between switch operation modes (SW1-on/SW2-off or SW1-off/SW2-on cases). The isolation level between antenna ports (⑤ and ⑥) is 42.59 dB. It also provides the 2nd harmonic suppression of 31.92 dB at 56 GHz. It is demonstrated that the RF signal path can be reconfigured with a high isolation level.

III. RECONFIGURABLE ANTENNA SYSTEM

All proposed designs were integrated and two monopole antennas were also placed at the output ports of the designed system to demonstrate re-configurability as shown in Fig. 8. The length of the monopole antenna (L1) is 2250 μm and its width (W3) is 60 μm. The distance between the coupled line switch and the monopole antenna (L2) is 1000 μm. The width (W2) and the length (C2) of the single segment of the coupled microstrip line is 30 μm and 1720 μm, respectively, while the gap (G1) between the coupled lines is 20 μm as shown in Fig. 8 (b). The two coupled line switches were arranged orthogonally to enable dual polarization (V- and H-polarization) capability using two linearly polarized antennas. The delay line 1 and 2 have the same width (W1) of 81 μm because they are 50 Ω transmission lines. The length of delay line1 (D1) is 925 μm, and that of delay line2 (D2) is 1305 μm. The geometry of the quarter-wave transformer is shown in Fig. 8 (c). It consists of two quarter-wave impedance transformers with a length of 1708 μm and a width of 81 μm. Fig. 8 (d) shows a design example of MIMO application using the monopole antennas. The Tx/Rx bumps of the IC chip feed each V/H branch to drive the antennas. The points from P1 to P4 are DC bias points as well as antenna feeding points. More compact module can be designed using multi-layers. Patch-type antennas can be easily integrated with the proposed feeding network on different layers by placing vias at P1 ~ P4. The hairpin type coupled line structure can further reduce the overall size of the proposed system.

The frequency responses of the proposed reconfigurable antenna system are shown in Fig. 9. The -10 dB bandwidth of each antenna mode is 26.13 GHz ~ 29.46 GHz (fractional bandwidth: 11.9%) which is wide enough to cover design goal of 26.65 GHz ~ 29.19 GHz (9.1%) for 5G communication frequency band. It should be noted that the reflection coefficient (S_{11}) values of the four antennas (Tx/Rx & H-/V-pol) are almost the same as shown in Fig. 9. The small discrepancy between the vertical polarization (V-pol) and the horizontal polarization (H-pol) mode is due to the T-junction where the delay line1 and 2 meet because it is not symmetric geometry, but it is negligible.

Figure 10 shows the normalized radiation patterns of the designed reconfigurable antenna system. The radiation patterns were changed according to the operation mode. The maximum realized gain of H-pol case was 2.54 dB and that of V-pol was 2.49 dB. E-plane of the proposed reconfigurable antenna system changed from *YZ*-plane to *XZ*-plane when the switch 1 was 'on' and switch 2 was 'off', or vice versa.

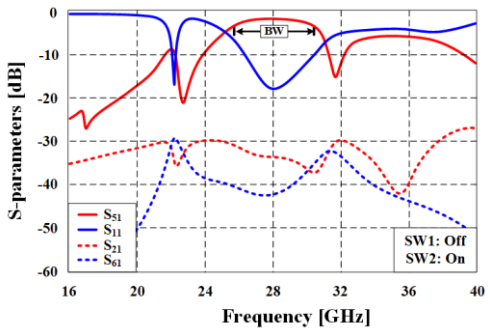

(a)

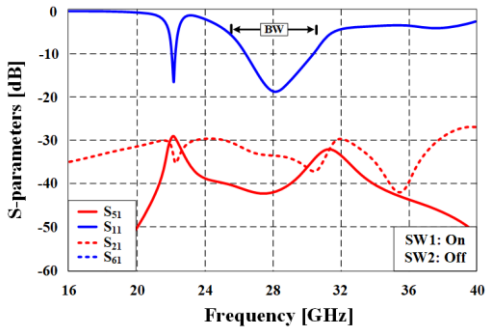

(b)

Fig. 7. S-parameters of the integrated coupled line switch and the quarter-wave transformer: (a) SW1-off/SW2-on case, and (b) SW1-on/SW2-off case.

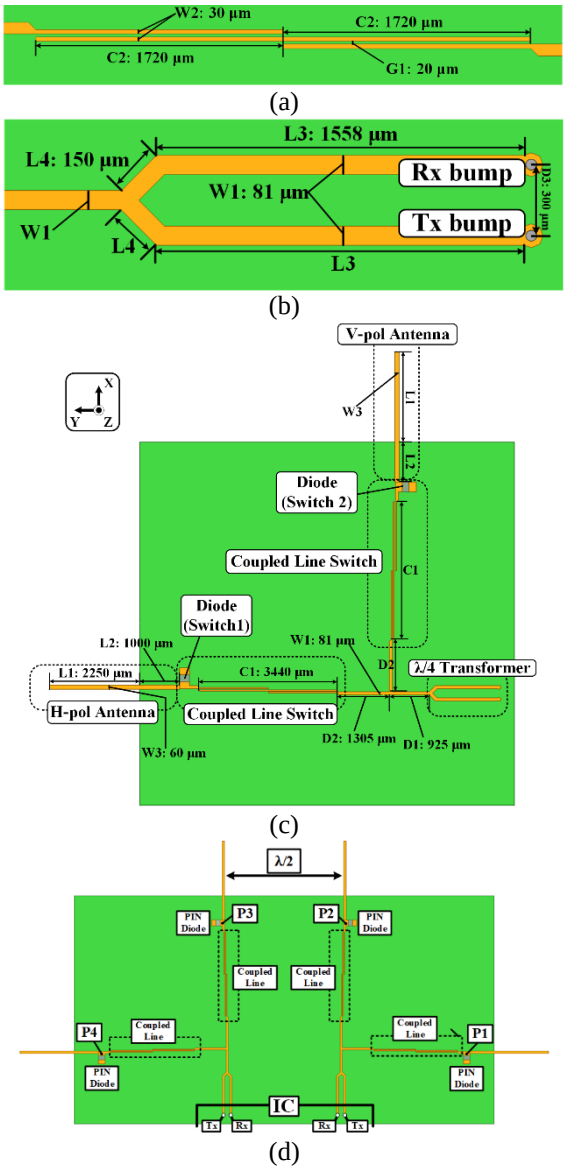

Fig. 8. System Geometry: (a) reconfigurable feeding network with dipole antennas, (b) coupled line section, (c) quarter-wave transformer section, and (d) a design example for MIMO application.

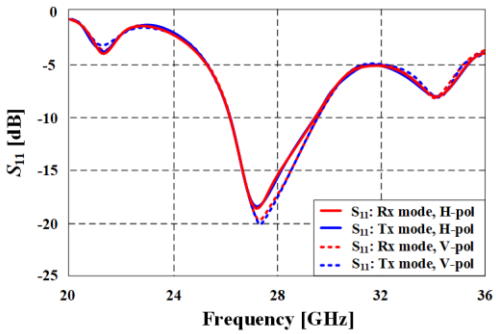

Fig. 9. S_{11} of the antenna system.

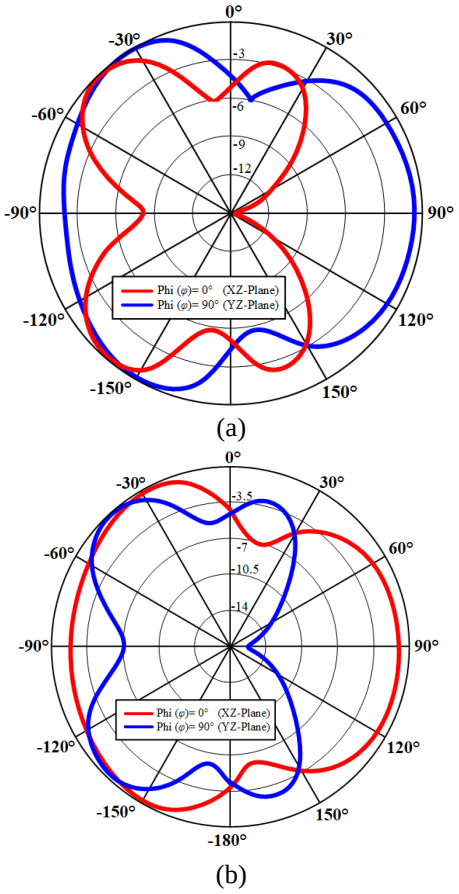

Fig. 10. Radiation patterns of the antenna system: (a) H-pol mode and (b) V-pol mode.

VI. CONCLUSION

A reconfigurable antenna feeding network using SoP technology is successfully presented in this paper. Two segments of the quarter-wave impedance transformer isolate the Tx and Rx modes by converting the low impedance of the in-active port to high

impedance. A single stage coupled microstrip line filter was proposed instead of SMD type device to separate the DC bias and RF signal path of the diode switch. The proposed switch network provides better insertion loss and suppress higher order even harmonics. The system performance was verified by integrating two monopole antennas with the re-configurable feeding network. Radiation patterns and polarization can be easily switched by manipulating the diode switches. The presented reconfigurable system is suitable for 5G communication systems and MIMO applications due to its polarization and radiation pattern re-configurability.

ACKNOWLEDGMENT

This work was supported by a 2-Year Research Grant of Pusan National University. This work was supported by the National Research Foundation of Korea

(NRF) grant funded by the Korea Government (MSIP) (No. 2016R1C1B1012042).

REFERENCES

[1] Q. Li, H. Niu, A. Papathanassiou, and G. Wu, "5G network capacity: Key elements and technologies," *IEEE Veh. Technol. Mag.*, vol. 9, no. 1, pp. 71-78, Mar. 2014.

[2] O. Elijah, C. Y. Leow, T. A. Rahman, S. Nunoo, and S. Z. Iliya, "A comprehensive survey of pilot contamination in massive MIMO–5G system," *Commun. Surveys Tuts.*, vol. 18, no. 2, pp. 905-923, 2016.

[3] Z. Gao, L. Dai, D. Mi, Z. Wang, M. A. Imran, and M. Z. Shakir, "MmWave massive-MIMO-based wireless backhaul for the 5G ultra-dense network," *IEEE Wirel. Commun.*, vol. 22, no. 5, pp. 13-21, Oct. 2015.

[4] K. Lim, S. Pinel, M. Davis, A. Sutono, C. Lee, D. Heo, A. Obatoynbo, J. Laskar, M. Tentzeris, and R. Tummala, "RF-system-on-package (SoP) for wireless communications," *IEEE Microw. Mag.*, vol. 3, no. 1, pp. 88-99, Mar. 2002.

[5] [Online] http://www.statschippac.com/documentlibrary/fcBGA.pdf

[6] Y. Liu, L. Xia, and R. Xu, "A broadband microstrip-to-microstrip vertical via interconnection for low temperature co-fired ceramic applications," *Applied Computational Electromagnetics Society (ACES) Express Journal*, vol. 32, no. 12, Dec. 2017.

[7] T. Sarrazin, R. Crunelle, O. Lafond, M. Himdi, N. Rolland, and L. Roy, "A 60GHz aperture-coupled micromachined microstrip antenna for heterogeneous 3D integration (system-in-package)," *Proc. 27th Int. Review of Progress in Applied Computational Electromagnetics (ACES)*, Williamsburg, Virginia, USA, Mar. 2011.

[8] K. C. Gupta, "Emerging trends in millimeter-wave CAD," *IEEE Trans. Microw. Theory Tech.*, vol. 46, no. 6, pp. 747-755, June 1998.

[9] K. C. Gupta, R. Garg, and I. J. Bahl, *Microstrip Lines and Slotlines*. Artech House, Dedham, Mass., 1979.

[10] D. M. Pozar, *Microwave Engineering*. 3rd ed., Hoboken, NJ, USA: Wiley, 2005.

[11] S. B. Cohn, "Parallel-coupled transmission-line-resonator filters," *IRE Trans. Microw. Theory Tech.*, vol. 6, no. 2, pp. 223-231, Apr. 1958.

[12] [Online] http://www.knowlescapacitors.com/dilabs/en/globalnavigation/products/broadband-blocking-capacitors#Milli_Cap

Multi-Beamformer with Adjustable Gain: Projection Approach

Jie Chen [1] and Yingzeng Yin [2]

[1] School of Electronic Engineering
Xi'an Aeronautical University, Xi'an, 710077, China
chenbinglin88888@163.com

[2] National Key Laboratory of Antenna and Microwave Technology
School of Electronic Engineering, Xidian University, Xi'an, 710071, China
yyzeng@mail.xidian.edu.cn

Abstract ─ In this paper, a new multi-beam forming approach is presented. First, we divide the steering vectors into two parts. The first part is the beam vector space. The second part is the side lobe vector space. Given that the inner product of two orthogonal vectors is zero, to minimize the gains of the side lobes, the excitation vector of the antenna array elements has to be placed in the orthogonal projection matrix of the side lobe vector space. Then, we obtain a vector by linearly combining the beam vectors and orthogonally projecting the combined vector into the orthogonal projection matrix of the side lobe vector space, and this projection vector is just the solution of the excitation vector of the antenna array elements. Since the combined vector is the linear combination of the beam vectors, we can control the beam gain by adjusting the linear combination coefficients. This new method can be easily used to form multi-beams and adjust each beam gain. The results of simulations show, that the new method acts effectively and efficiently.

Index Terms — Antenna array, array manifold, beam forming, linear space, orthogonal projection.

I. INTRODUCTION

Beam forming technologies have been well studied in past decades. Many articles have been published in this domain. The well-known analytical function approaches, such as Taylor and Chebyshev beam forming, were the earliest method developed to form beams. These methods generally investigated radiation beam forming. Microwave beam forming (MBF) is another developing approach. Several techniques of MBF have been developed to accomplish adaptive beam forming (ABF) [1, 2].

In recent years, along with the development of the digital processing and microelectronic technologies, digital beam forming has become a hot topic for researchers. A beam forming approach used in wide band multiple-input multiple-output (MIMO) systems was discussed in reference [3]. Reference [4] adopted the compressed sensing method to form beams. Under the constraint of $l1$-norm minimization, article [5] developed a new beam forming method. In reference [6], to adapt to real time beam forming, real weight adaptive processing based on a direct data domain least squares approach was presented. The optimization of an arbitrary side lobe attenuation level was proposed in reference [7]. Article [8] put forward a multiple beam forming approach. Reference [9] developed a beam forming means for a phase-configurable antenna array. In reference [10], a differential evolution genetic algorithm beam forming approach was presented. In reference [11], many digital processing methods were discussed. In reference [12], beam forming was viewed as a space filtering issue. Phased array beam steering through serial control of the phase shifters was presented in another article [13]. Reference [14] studied the phase and pattern characteristics of a sub-wavelength broadband reflectarray unit element based on triple concentric circular-rings.

In this paper, a new multi-beam forming approach is presented. First, we divide the steering vectors into two parts. The first part is the beam vector space. The second part is the side lobe vector space. Given that the inner product of two orthogonal vectors is zero, to minimize the gains of the side lobes, the excitation vector of the antenna array elements has to be settled on the orthogonal projection matrix of the side lobe vector space. Then, we obtain a vector by linearly combining the beam vectors and orthogonally projecting the combined vector into the orthogonal projection matrix of the side lobe vector space, and this projection vector is just the solution of the excitation vector of the antenna array elements. Since the combined vector is obtained from the linear combination of the beam vectors, we can control the beam gain by adjusting the linear combination coefficients. Compared with

Submitted On: March 1, 2017
Accepted On: August 11, 2018

conventional methods, this new method can be easily used to form multi-beams and adjust each beam gain. The results of the simulations show, that the new method acts effectively and efficiently.

The remainder of this paper is organized as follows: Section II presents the beam forming paradigm; Section III presents the new projection beam forming approach; Section IV shows several simulations of the new approach; and Section V draws a conclusion.

II. BEAM FORMING PARADIGM

We aim to investigate the beam forming of a uniform linear antenna array. This array has N isotropic antenna elements, which are arranged along a line with spacing d. The far field is considered, and the narrow band signal centered at a wave length of λ is transmitted by each antenna element. The element arrangement numbered from 1 to N is shown in figure 1. The angle between the transmitting signal and the axis of the array denoted as θ in figure 1 is the signal transmitting angle.

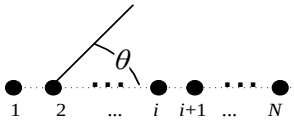

Fig. 1. Arrangement of the elements in the uniform linear array.

The beam pattern formed by the array in Fig. 1 in the far field can be written as:

$$f(\theta)=\sum_{i=1}^{N} I_i e^{j2\pi(i-1)d\cos\theta/\lambda}. \quad (1)$$

In equation (1), I_i is the current excitation of the i^{th} antenna element. We define $\mathbf{a}(\theta)=[1,e^{j2\pi d\cos\theta/\lambda},...,e^{j2\pi d(N-1)\cos\theta/\lambda}]^{\mathrm{T}}$ as the steering vector and denote the antenna element excitation vector as $\mathbf{W}=[I_1,I_2,...,I_i,...,I_N]^{\mathrm{T}}$, where the superscript T denotes the transpose operation. Hence, equation (1) can be rewritten as:

$$f(\theta)=\mathbf{a}^{\mathrm{T}}(\theta)\mathbf{W}. \quad (2)$$

Because the pattern formed is the periodic function of the signal transmitting angle θ, we set θ in a cycle from 0° to 180°. For convenience, we denote θ as discrete values of θ_1, θ_2, ..., θ_k, ..., θ_K in sequence. Let the expected beam vector be:

$$\mathbf{P}=[P(\theta_1),P(\theta_2),...,P(\theta_k),...,P(\theta_K)]^{\mathrm{T}}. \quad (3)$$

Then, the beam forming issue is transformed to design the array element excitation vector **W** to make the following equation valid:

$$\begin{aligned}\mathbf{P}&=abs(f(\theta))\\&=abs([\mathbf{a}(\theta_1),\mathbf{a}(\theta_2),...,\mathbf{a}(\theta_k),...,\mathbf{a}(\theta_K)]^{\mathrm{T}}\mathbf{W}),\end{aligned} \quad (4)$$

where *abs* denotes the absolution value operation.

Let $\mathbf{A}=[\mathbf{a}(\theta_1),\mathbf{a}(\theta_2),...,\mathbf{a}(\theta_k),...,\mathbf{a}(\theta_K)]$, where **A** is called the array manifold matrix. Then, equation (4) can be rewritten as:

$$\mathbf{P}=abs(\mathbf{A}^{\mathrm{T}}\mathbf{W}). \quad (5)$$

The least square solution of equation (5) is:

$$\mathbf{W}_{\mathrm{LS}}=((\mathbf{A}^{\mathrm{T}})^{\mathrm{H}}\mathbf{A}^{\mathrm{T}})^{-1}(\mathbf{A}^{\mathrm{T}})^{\mathrm{H}}\mathbf{P}. \quad (6)$$

III. BEAM FORMING OF THE PROJECTION APPROACH

If the beam points to the direction of θ_n, as well as in other directions, there is no beam. The beam forming process can be mathematically expressed as:

$$\mathbf{a}(\theta_n)^{\mathrm{T}}\mathbf{W}\neq 0, \quad (7)$$

$$\mathbf{a}(\theta_m)^{\mathrm{T}}\mathbf{W}=0 \quad \forall m\neq n, \quad (8)$$

where both m and n are integer variables. Let,

$$\mathbf{B}=\mathbf{a}(\theta_n), \quad (9)$$

and

$$\mathbf{Z}=[\mathbf{a}(\theta_1),\mathbf{a}(\theta_2),...,\mathbf{a}(\theta_{n-1}),\mathbf{a}(\theta_{n+1})...,\mathbf{a}(\theta_K)], \quad (10)$$

where matrix **B** is called the beam matrix, and matrix **Z** is named as the null matrix.

Obviously, both matrix **Z** and **B** are a division of matrix **A** and they can be combined into **A**.

Then, equation (7) and (8) can be rewritten as:

$$\mathbf{B}^{\mathrm{T}}\mathbf{W}\neq 0, \quad (11)$$

$$\mathbf{Z}^{\mathrm{T}}\mathbf{W}=\mathbf{0}. \quad (12)$$

Equation (12) means that vector **W*** is perpendicular to the column vector space of matrix **Z** with the superscript * indicating the conjugate operation. Hence, vector **W*** must locate in the orthogonal projection space of the column vector space of matrix **Z**, which can be mathematically written as:

$$\mathbf{W}^{*}=(\mathbf{I}-\mathbf{Z}(\mathbf{Z}^{\mathrm{H}}\mathbf{Z})^{-1}\mathbf{Z}^{\mathrm{H}})\mathbf{Y}, \quad (13)$$

where **I** denotes the unit matrix, the superscript H indicates the conjugate transpose operation, and **Y** is an arbitrary vector.

Let,

$$\mathbf{Y}=\mathbf{B}\mathbf{X}, \quad (14)$$

where **X** is an arbitrary vector, and its length equals the column vector number of matrix **B**. Equation (14) means that **Y** is a linear combination of the column vectors of matrix **B**. Substituting equation (14) into (13), we can obtain:

$$\mathbf{W}^{*}=(\mathbf{I}-\mathbf{Z}(\mathbf{Z}^{\mathrm{H}}\mathbf{Z})^{-1}\mathbf{Z}^{\mathrm{H}})\mathbf{B}\mathbf{X}. \quad (15)$$

It is easy to verify that **W** in equation (15) satisfies equation (11) and (12).

It is necessary to point out that if the expected pattern has multiple beams that direct to several different directions, matrix **B** has to include the steering vectors of these directions, and on the other hand, matrix **Z** has to exclude the steering vectors of these directions.

To further improve the flexibility, in equation (15), we can add a small perturbation to the diagonal

elements of the unit matrix **I**, which can be mathematically expressed as:

$$\mathbf{W}^{*} = (s\mathbf{I} - \mathbf{Z}(\mathbf{Z}^{\mathrm{H}}\mathbf{Z})^{-1}\mathbf{Z}^{\mathrm{H}})\mathbf{B}\mathbf{X}. \quad (16)$$

In equation (16), $s = ue^{j\varphi}$ where u is a real number and φ is an arbitrary angle.

IV. SIMULATIONS OF THE NEW APPROACH

In this section, several examples are given to demonstrate the new approach and its performance.

We aim to investigate the beam forming of a uniform linear antenna array. It has N isotropic antenna elements, which are arranged along a line with spacing d. Let $d=\lambda/2$.The far field is considered and the narrow band signal centered at the wave length of λ is transmitted by each antenna element. The antenna array element arrangement is shown in Fig. 1.

Let the discrete values of θ, θ_1, θ_2, ..., θ_k, ..., θ_K, be equal to 0°, 1°, …, 179°, 180° respectively, which is in accord with the real practice and is convenient for digital processing. The pattern can be formed through following algorithm steps: i) Determine the beam directions and then use their steering vectors to make up matrix **B**; ii) Determine the non-beam directions and then use their steering vectors to make up matrix **Z**; iii) Obtain vector $\mathbf{W}_{\mathrm{LS}}$ and **W** respectively through equation (6) and (16); iv) Obtain the formed pattern using equation (5).

In the first example, let N=12, the expected beams direct to θ_{40}=40° and θ_{90}=90°, let $\mathbf{X}=[1+\mathrm{j}157/4\pi, 1+\mathrm{j}157/4\pi]^{\mathrm{T}}$, $s=1+\mathrm{j}1000\pi$, and the pattern generated by equation (16) is shown in Fig. 2. It can be seen in Fig. 2 that two beams pointing to the directions of θ_{40}=40° and θ_{90}=90° have the same gain. Then, we let the pattern generated by equation (16) be the vector **P** in equation (6). Thus, the weight vector $\mathbf{W}_{\mathrm{LS}}$ can be obtained from equation (6). The pattern created by $\mathbf{W}_{\mathrm{LS}}$ is also shown in Fig. 2. In the legend of Fig. 2, the new method indicates the pattern generated by equation (16), and LS refers to the pattern created by $\mathbf{W}_{\mathrm{LS}}$. Figure 2 shows that the new method has a better performance than the least square method.

In the second example, still let N=12, the expected beams direct to θ_{40}=40° and θ_{90}=90°, let $\mathbf{X}=[1000+\mathrm{j}157/4\pi, 500+\mathrm{j}157/4\pi]^{\mathrm{T}}$, $s=1+\mathrm{j}1000\pi$, and the pattern generated by equation (16) is shown in Fig. 3. It can be learned easily from Fig. 3 that the beam pointing to the direction of θ_{90}=90° has an approximately 6 dB attenuation compared with the beam directing to θ_{40}=40°. Then, we let the pattern generated by equation (16) be the vector **P** in equation (6). Thus, the weight vector $\mathbf{W}_{\mathrm{LS}}$ can be obtained from equation (6). The pattern created by $\mathbf{W}_{\mathrm{LS}}$ is also shown in Fig. 3. In the legend of Fig. 3, the new method indicates the pattern generated by equation (16), and LS refers to the pattern created by $\mathbf{W}_{\mathrm{LS}}$. Figure 3 shows that the new method has a better performance than the least square method.

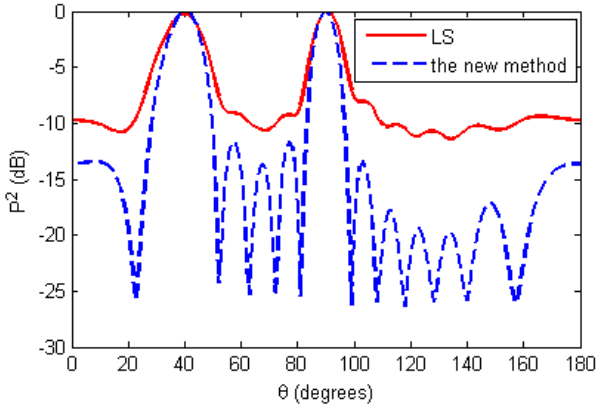

Fig. 2. The outcome of the first example (N=12).

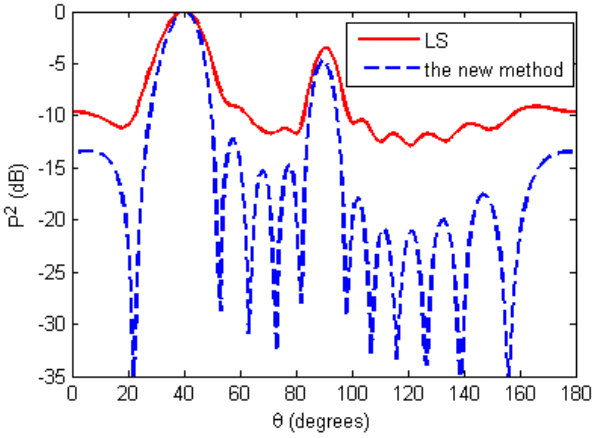

Fig. 3. The outcome of the second example (N=12).

In the third example, let N=24, the expected beams direct to θ_{40}=40°, θ_{90}=90° and θ_{120}=120°, let $\mathbf{X}=[1+\mathrm{j}157/4\pi, 1+\mathrm{j}157/4\pi, 1+\mathrm{j}157/4\pi]^{\mathrm{T}}$, $s=1+\mathrm{j}1000\pi$, and the pattern generated by equation (16) is shown in Fig. 4. It can be learned from Fig. 4 that three beams pointing to the directions of θ_{40}=40°, θ_{90}=90° and θ_{120}=120° have the same gain. Then, we let the pattern generated by equation (16) be the vector **P** in equation (6). Thus, the weight vector $\mathbf{W}_{\mathrm{LS}}$ can be obtained from equation (6). The pattern created by $\mathbf{W}_{\mathrm{LS}}$ is also shown in Fig. 4. In the legend of Fig. 4, the new method indicates the pattern generated by equation (16), and LS refers to the pattern created by $\mathbf{W}_{\mathrm{LS}}$. Figure 4 shows that the new method has a better performance than the least square method.

In the fourth example, still let N=24, the expected beams direct to θ_{40}=40°, θ_{90}=90° and θ_{120}=120°, let $\mathbf{X}=[500+\mathrm{j}157/4\pi, 1000+\mathrm{j}157/4\pi, 500+\mathrm{j}157/4\pi]^{\mathrm{T}}$, $s=1+\mathrm{j}1000\pi$, and the pattern generated by equation (16)

is shown in Fig. 5. It can be seen easily from Fig. 5 that the beams pointing to the directions of θ_{40}=40° and θ_{120}=120° have an approximately 6 dB attenuation compared with the beam directing to θ_{90}=90°. Then, we let the pattern generated by equation (16) be the vector **P** in equation (6). Thus, the weight vector $\mathbf{W}_{LS}$ can be obtained from equation (6). The pattern created by $\mathbf{W}_{LS}$ is also shown in Fig. 5. In the legend of Fig. 5, the new method indicates the pattern generated by equation (16), and LS refers to the pattern created by $\mathbf{W}_{LS}$. Figure 5 shows that the new method has a better performance than the least square method.

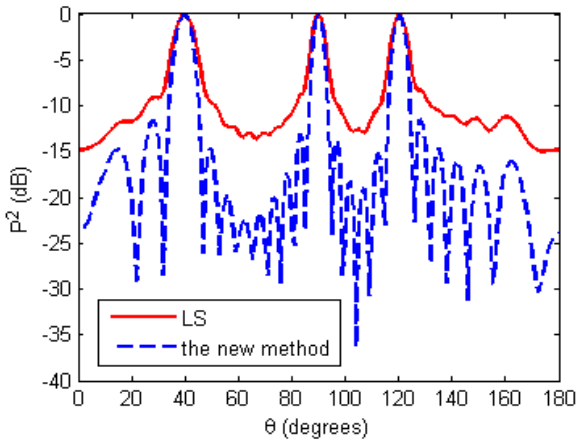

Fig. 4. The outcome of the third example (N=24).

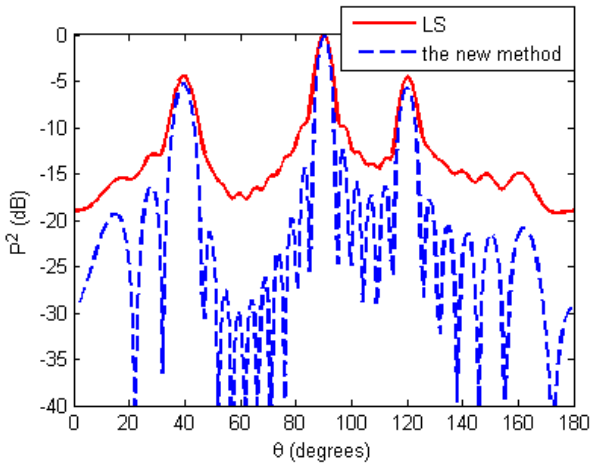

Fig. 5. The outcome of the fourth example (N=24).

According to our simulations, the beam gain is mainly determined by the image part of s and the real part ratio of the elements of **X**. To easily adjust the beam gain, the real parts of the elements of **X** should be a number of several hundreds, and the image parts of the elements of **X** have little effect on the beam gain. Additionally, the image part of s is no less than 3π, while the real part of s is equal to 1. To estimate the computational complexity of the new method, we compare equation (16) with equation (6). Since both **B** and **Z** are a part of matrix **A**, the computational complexity of equation (16) is similar to that using equation (6) to form the pattern. We simulate the new approach using the MATLAB software platform on an HP notebook PC with a core i5-5200U CPU and a 4G memory. All simulations in this paper take approximately less than one second to obtain the final outcomes.

V. CONCLUSION

For an antenna array whose manifold matrix has been determined, we divide the matrix into two parts. The first part is the beam vector space. The second part is the side lobe vector space. We obtain a vector by linearly combining the beam vectors and orthogonally projecting the combined vector into the orthogonal projection matrix of the side lobe vector space, and this projection vector is just the solution of the excitation vector of the antenna array elements. Since the combined vector is obtained from the linear combination of the beam vectors, we can control the beam gain by adjusting the linear combination coefficients. This new method can be easily used to form multi-beams and adjust each beam gain. The results of the simulations show, that the new method acts effectively and efficiently.

ACKNOWLEDGEMENT

This work has been supported in part by the Chinese Government under the National Natural Science Foundation No. 61501340, and Education Department of Shanxi province under the Special Science and Technology Foundation No. 17JK0397.

REFERENCES

[1] T. Ohira, "Adaptive array antenna beamforming architectures as viewed by a microwave circuit designer," *Proc. Asia–Pacific Microw. Conf.*, Sydney, Australia, pp. 828-833, Dec. 2000.

[2] S. Denno and T. Ohiro, "Modified constant modulus algorithm for digital signal processing adaptive antennas with microwave analog beam-forming," *IEEE Trans. Antennas Propag.*, vol. 50, no. 6, pp. 850-857, June 2002.

[3] H. He, P. Stoica, and J. Li, "Wideband MIMO systems: Signal design for transmit beampattern synthesis," *IEEE Transactions on Signal Process-ing*, vol. 59, no. 2, pp. 618-628, Feb. 2011.

[4] G. Oliveri and A. Massa, "Bayesian compressive sampling for pattern synthesis with maximally sparse non-uniform linear arrays," *IEEE Trans-actions on Antennas Propagation*, vol. 59, no. 2, pp. 467-481, Feb. 2011.

[5] H. Chen, Q. Wang, and R. Fan, "Beampattern

synthesis using reweighted *l*1-norm minimization and array orientation diversity," *Radioengineering*, vol. 22, no. 2, pp. 602-609, June 2013.

[6] W. Choi, T. K. Sarkar, H. Wang, and E. L. Mokole, "Adaptive processing using real weights based on a direct data domain least squares approach," *IEEE Trans. Antennas Propagat.*, vol. 54, no. 1, pp. 182-191, Jan. 2006.

[7] A. Morabito and P. Rocca, "Optimal synthesis of sum and difference patterns with arbitrary side-lobes subject to common excitations constraints," *IEEE Antennas Wireless Propag. Lett.*, vol. 9, pp. 623-626, July 2010.

[8] T. K. Sarkar, S. Bhumkar, N. Yilmazer, et al., "Non-statistical multi-beamformer," *Journal of Signal and Information Processing*, vol. 3, no. 1, pp. 26-29, Jan. 2012.

[9] A. F. Morabito, A. Massa, P. Rocca, and T. Isernia, "An effective approach to the synthesis of phase-only reconfigurable linear arrays," *IEEE Trans. Antennas Propag.*, vol. 60, no. 8, pp. 3622-3631, Aug. 2012.

[10] X. Li, W. T. Li, X. W. Shi, et al., "Modified differential evolution strategy for antenna array pattern synthesis," *Progr. Electromagn. Res.*, vol. 137, no. 2, pp. 371-388, Feb. 2013.

[11] X. D. Zhang, *Modern Signal Processing*. Tsinghua University Press, Beijing, 2012.

[12] T. K. Sarkar, J. Koh, R. Adve, et al., "A pragmatic approach to adaptive antennas," *IEEE Acoust., Speech, and Signal Processing Mag.*, vol. 42, no. 2, pp. 39-55, Feb. 2000.

[13] R. L. Haupt, "Phased array beam steering through serial control of the phase shifters," *Appl. Comput. Electrom. Society Journal*, vol. 32, no. 12, pp. 1140-1143, Dec. 2017.

[14] J. Nourinia, C. Ghobadi, B. Mohammadi, and F. Alizadeh, "Study of phase and patterns characteristics of a sub-wavelength broadband reflectarray unit element based on triple concentric circular-rings," *Appl. Comput. Electrom. Society Journal*, vol. 33, no. 6, pp. 714-718, June 2018.

Jie Chen is now an Associate Professor of School of Electronic Engineering, Xi'an Aeronautical University, No.259 Xi'an West Second Ring Road, Xi'an, 710077, China. He received his bachelor and master degree in Electronic Science and Technology major from School of Electronic and Information, Xi'an Jiaotong University in 1997 and 2004 respectively. In 2013, he achieves doctor degree in Electromagnetic Theory and Microwave Technique major from School of Electronic Engineering, Xidian University. His research interests are in the areas of smart antenna, antenna array, microwave circuit design, wireless communication and RFID technique.

Yingzeng Yin is now a Professor of Xidian University. He works in National Key Laboratory of Antenna and Microwave Technology, School of Electronic Engineering, Xidian University, Xi'an, 710071, China. His research activities are in the fields of microwave circuit design, antenna design, smart antenna design and RFID technique.

A Novel Design of Wideband Koch like Sided Sierpinski Square Carpet Multifractal Antenna

Amandeep K. Sidhu and Jagtar S. Sivia

Department of Electronics and Communication Engineering
Yadavindra College of Engineering, Punjabi University GKC, Talwandi Sabo, Bathinda, Punjab (151302), India
sdeepaman93@gmail.com, jagtarsivian@gmail.com

Abstract ─ This paper reveals Koch Like Sided Sierpinski Square Carpet Multifractal Antenna (KLSSSCMA) having wideband features and comprises a new hybrid geometry using Sierpinski carpet and Koch curve geometries. The antenna is designed using square patch having dimensions 29.4 mm × 29.4 mm over Roger RT/Duroid substrate having height equal to 3.18 mm and dimensions 48.48 mm × 48.48 mm. The proposed antenna is analyzed and simulated using FEM (Finite Element Method) based Ansoft HFSS^{TM} v.13 software successfully up to fourth iteration. Simulation results show that KLSSSCMA has wideband characteristics from 2 to 8 GHz that covers S and C bands for WiMAX, WPAN, WLAN and Wi-Fi applications. The projected antenna is capable of achieving a good impedance bandwidth with S_{11} less than -9 dB over the whole range of BW and also exhibits almost stable radiation patterns.

Index Terms ─ Carpet, fractal, gain, Koch curve, patch, VSWR.

I. INTRODUCTION

This paper focuses on the generation of Koch Like Sided Sierpinski Square Carpet Multifractal (KLSSSCM) geometry. As in earlier studies, the fractal antenna geometries are inspired by nature. They possess features of fractals that exist in nature [1]. The proposed geometry also represents the hybrid structure of two geometries [2]. A lot of research has been done on individual fractal geometries using different techniques with exciting features such as wide band, miniaturize size, multiband resonance behavior etc. The recent trend towards the combination of two geometries with different methods is being popular as studied in the literature [3-5]. Multifractal geometries reserved the merits and overcome the limitations of mono fractals. Since these multi fractals have not been used broadly in antenna design structures, therefore this is an encouraging topic in fractal structures and needs to be examined and technologically advanced in more depth. Fractal antenna engineering is a new kind of antenna design technology [1] that gives a lot of scope for research to enhance the performance of designed antenna. This concept gives better response in terms of bandwidth, enhancement in radiation pattern, lesser reflection coefficient, multi-resonance, miniaturization of antenna size and also wideband / UWB [4-6]. Due to self-similar and space filling properties, fractal and multifractal antennas reveal multiband, wideband and miniaturization of antenna size [7-11]. Different techniques have been applied to fractal antenna yet to attain more bandwidth. A planer multiband Koch snowflake fractal antenna for cognitive radio [12], wideband square gap coupled fractal antenna [13], CPW feed KLSSHCMF monopole antenna [3], UWB monopole based on Sierpinski carpet fractal shape slot antenna [14], microstrip patch antenna designed with Sierpinski and Koch fractal geometries [15], star-shaped microstrip wideband antenna [16] and ultra-wideband hexagonal fractal antenna using Koch shape with an enhancement in bandwidth [17] have been designed to optimize the performance of antenna. In this paper, the Koch curve and Sierpinski carpet geometries are united together to design KLSSSCMA. The proposed antenna is fed by coax probe feed at the right upper corner. Feed position is optimized to match the impedance of feed to the antenna. The effect of substrate height on bandwidth is also analyzed. The final iteration S_2K_2 of KLSSSCMA is fabricated and tested.

II. ANTENNA DESIGN

The KLSSSCMA is designed up to 4th iteration. Roger RT/Duroid 5880 (TM) material having thickness 3.18 mm is used as the substrate. This material provides a higher gain and more bandwidth depending on the substrate thickness. The specifications of RT/Duroid substrate material are mentioned in Table 1. Resonant frequency of 3.2497 GHz is chosen for the proposed antenna that lies in S-band with multiple applications that enables it to operate the antenna in S as well as in C-bands of the communication field. Transmission line model is used to calculate the dimensions of the patch as this model is an easy and correct model for rectangular microstrip patch antenna.

Submitted On: December 6, 2016
Accepted On: July 16, 2018

Table 1: Substrate specifications

Relative dielectric constant (ε_r)	2.2
Loss tangent	0.0009
Substrate thickness (h)	3.18 mm
Acceptable frequency range	<10 GHz

Equations (1) to (4) are used to calculate the width and length of the patch as described in transmission model. These equations give the values of width and length of patch as 29.4 mm each respectively. The information of 'ε_r', the resonant frequency 'f_r' and height of substrate 'h' is required to calculate other parameters. Practical width of a radiating patch as in [18] is given by:

$$W = \frac{1}{2 f_r \sqrt{\mu_0 \varepsilon_0}} \sqrt{\frac{2}{\varepsilon_r + 1}} = \frac{v_0}{2 f_r} \sqrt{\frac{2}{\varepsilon_r + 1}}, \quad (1)$$

where v_0 denotes the velocity of light in free-space. The effective dielectric constant of microstrip antenna [18] is given by:

$$\varepsilon_{reff} = \frac{\varepsilon_r + 1}{2} + \frac{\varepsilon_r - 1}{2} \left[1 + 12 \frac{h}{W} \right]^{-\frac{1}{2}}. \quad (2)$$

Table 2: Design parameters of antenna

S. No	Parameters	Dimension (mm)
1	Width of patch (W_P)	29.4
2	Length of patch (L_P)	29.4
3	Effective dielectric constant ε_{reff}	1.995
4	Width of substrate	48.48
5	Length of substrate	48.48
6	Width of centermost block in S_1 K_1 (W_1)	9.8
7	Length of centermost block in S_1 K_1 (L_1)	9.8
8	Width of other 8 blocks in S_2 K_1	3.267
9	Length of other 8 blocks in S_2 K_1	3.267

Once W is calculated using Equation (1), consider the extension in actual length of patch due to fringing effect as in [18] and is given by:

$$\Delta L = h \frac{\left(\varepsilon_{reff} + 0.3 \right) \left(\frac{W}{h} + 0.264 \right)}{\left(\varepsilon_{reff} - 0.25 \right) \left(\frac{W}{h} + 0.8 \right)}. \quad (3)$$

After calculating the extended length of patch, the actual length of patch is determined as in [18] as:

$$L = \frac{1}{2 f_r \sqrt{\varepsilon_{reff}} \sqrt{\varepsilon_0 \mu_0}} - 2\Delta L. \quad (4)$$

Dimensions of ground plane are calculated using Equations (5) and (6):

$$\text{Length of ground } L_g = 6h + L, \quad (5)$$

$$\text{Width of ground } W_g = 6h + W. \quad (6)$$

The calculated dimensions are shown in Table 2.

A. IFS (Iterative Function System) for first iteration of proposed geometry

IFS used to generate the Koch curve geometry on Sierpinski carpet sides. The initiator is required to generate the IFS of geometry using a set of affine transformation matrices. IFS for standard Koch curve is given in [9] and IFS for standard Sierpinski carpet geometry is given in [21]. The proposed IFS for the first iteration geometry of the proposed antenna is given by a set of W_1 to W_{16} matrices given as follows:

$$W_1 \begin{pmatrix} x' \\ y' \end{pmatrix} = \begin{bmatrix} \frac{1}{12} & 0 \\ 0 & \frac{1}{12} \end{bmatrix} \begin{bmatrix} x \\ y \end{bmatrix} + \begin{bmatrix} 0 \\ 0 \end{bmatrix},$$

$$W_2 \begin{pmatrix} x' \\ y' \end{pmatrix} = \begin{bmatrix} \frac{1}{24} & -\frac{\sqrt{3}}{24} \\ -\frac{\sqrt{3}}{24} & \frac{1}{24} \end{bmatrix} \begin{bmatrix} x \\ y \end{bmatrix} + \begin{bmatrix} \frac{1}{12} \\ 0 \end{bmatrix},$$

$$W_3 \begin{pmatrix} x' \\ y' \end{pmatrix} = \begin{bmatrix} \frac{1}{24} & \frac{\sqrt{3}}{24} \\ -\frac{\sqrt{3}}{24} & \frac{1}{24} \end{bmatrix} \begin{bmatrix} x \\ y \end{bmatrix} + \begin{bmatrix} \frac{1}{18} \\ \frac{\sqrt{3}}{24} \end{bmatrix},$$

$$W_4 \begin{pmatrix} x' \\ y' \end{pmatrix} = \begin{bmatrix} \frac{1}{12} & 0 \\ 0 & \frac{1}{12} \end{bmatrix} \begin{bmatrix} x \\ y \end{bmatrix} + \begin{bmatrix} \frac{1}{6} \\ 0 \end{bmatrix},$$

$$W_5 \begin{pmatrix} x' \\ y' \end{pmatrix} = \begin{bmatrix} 0 & -\frac{1}{12} \\ \frac{1}{12} & 0 \end{bmatrix} \begin{bmatrix} x \\ y \end{bmatrix} + \begin{bmatrix} \frac{1}{4} \\ 0 \end{bmatrix},$$

$$W_6 \begin{pmatrix} x' \\ y' \end{pmatrix} = \begin{bmatrix} -\frac{\sqrt{3}}{24} & -\frac{1}{24} \\ \frac{1}{24} & -\frac{\sqrt{3}}{24} \end{bmatrix} \begin{bmatrix} x \\ y \end{bmatrix} + \begin{bmatrix} \frac{1}{4} \\ \frac{1}{12} \end{bmatrix},$$

$$W_7 \begin{pmatrix} x' \\ y' \end{pmatrix} = \begin{bmatrix} \frac{\sqrt{3}}{24} & -\frac{1}{24} \\ \frac{1}{24} & -\frac{\sqrt{3}}{24} \end{bmatrix} \begin{bmatrix} x \\ y \end{bmatrix} + \begin{bmatrix} \frac{1}{4} - \frac{\sqrt{3}}{24} \\ \frac{1}{8} \end{bmatrix},$$

$$W_8 \begin{pmatrix} x' \\ y' \end{pmatrix} = \begin{bmatrix} 0 & -\frac{1}{12} \\ \frac{1}{12} & 0 \end{bmatrix} \begin{bmatrix} x \\ y \end{bmatrix} + \begin{bmatrix} \frac{1}{4} \\ \frac{1}{6} \end{bmatrix},$$

$$W_9 \begin{pmatrix} x' \\ y' \end{pmatrix} = \begin{bmatrix} -\frac{1}{12} & 0 \\ 0 & -\frac{1}{12} \end{bmatrix} \begin{bmatrix} x \\ y \end{bmatrix} + \begin{bmatrix} \frac{1}{4} \\ \frac{1}{4} \end{bmatrix},$$

$$W_{10} \begin{pmatrix} x' \\ y' \end{pmatrix} = \begin{bmatrix} -\frac{1}{24} & -\frac{\sqrt{3}}{24} \\ -\frac{\sqrt{3}}{24} & -\frac{1}{24} \end{bmatrix} \begin{bmatrix} x \\ y \end{bmatrix} + \begin{bmatrix} \frac{1}{6} \\ \frac{1}{4} \end{bmatrix},$$

$$W_{11} \begin{pmatrix} x' \\ y' \end{pmatrix} = \begin{bmatrix} -\frac{1}{24} & \frac{\sqrt{3}}{24} \\ \frac{\sqrt{3}}{24} & -\frac{1}{24} \end{bmatrix} \begin{bmatrix} x \\ y \end{bmatrix} + \begin{bmatrix} \frac{1}{8} \\ \frac{1}{4} - \frac{\sqrt{3}}{24} \end{bmatrix},$$

$$W_{12} \begin{pmatrix} x' \\ y' \end{pmatrix} = \begin{bmatrix} -\frac{1}{12} & 0 \\ 0 & -\frac{1}{12} \end{bmatrix} \begin{bmatrix} x \\ y \end{bmatrix} + \begin{bmatrix} \frac{1}{12} \\ \frac{1}{4} \end{bmatrix},$$

$$W_{13} \begin{pmatrix} x' \\ y' \end{pmatrix} = \begin{bmatrix} 0 & \frac{1}{12} \\ -\frac{1}{12} & 0 \end{bmatrix} \begin{bmatrix} x \\ y \end{bmatrix} + \begin{bmatrix} 0 \\ \frac{1}{4} \end{bmatrix},$$

$$W_{14} \begin{pmatrix} x' \\ y' \end{pmatrix} = \begin{bmatrix} \frac{\sqrt{3}}{24} & \frac{1}{12} \\ -\frac{1}{24} & -\frac{\sqrt{3}}{24} \end{bmatrix} \begin{bmatrix} x \\ y \end{bmatrix} + \begin{bmatrix} 0 \\ \frac{1}{6} \end{bmatrix},$$

$$W_{15}\begin{pmatrix}x'\\y'\end{pmatrix}=\begin{bmatrix}-\frac{\sqrt{3}}{24} & \frac{1}{24}\\ -\frac{1}{24} & -\frac{\sqrt{3}}{24}\end{bmatrix}\begin{bmatrix}x\\y\end{bmatrix}+\begin{bmatrix}\frac{\sqrt{3}}{24}\\ \frac{1}{8}\end{bmatrix},$$

$$W_{16}\begin{pmatrix}x'\\y'\end{pmatrix}=\begin{bmatrix}0 & \frac{1}{12}\\ -\frac{1}{12} & 0\end{bmatrix}\begin{bmatrix}x\\y\end{bmatrix}+\begin{bmatrix}0\\ \frac{1}{12}\end{bmatrix}.$$

Then generator curve is achieved as follows:

$$A = W_1 U W_2 U W_3 U W_4 U W_5 U W_6 U W_7 U W_8 U W_9 U W_{10} U W_{11} U W_{12} U W_{13} U W_{14} U W_{15} U W_{16}$$

B. IFS for the second iteration of the Koch curve

$$W_1\begin{pmatrix}x'\\y'\end{pmatrix}=\begin{bmatrix}\frac{1}{3} & 0\\ 0 & \frac{1}{3}\end{bmatrix}\begin{bmatrix}x\\y\end{bmatrix}+\begin{bmatrix}0\\1\end{bmatrix}, W_2\begin{pmatrix}x'\\y'\end{pmatrix}=\begin{bmatrix}\frac{1}{6} & -\frac{\sqrt{3}}{6}\\ \frac{\sqrt{3}}{6} & \frac{1}{6}\end{bmatrix}\begin{bmatrix}x\\y\end{bmatrix}+\begin{bmatrix}\frac{1}{3}\\0\end{bmatrix},$$

$$W_3\begin{pmatrix}x'\\y'\end{pmatrix}=\begin{bmatrix}\frac{1}{6} & \frac{\sqrt{3}}{6}\\ -\frac{\sqrt{3}}{6} & \frac{1}{6}\end{bmatrix}\begin{bmatrix}x\\y\end{bmatrix}+\begin{bmatrix}\frac{1}{2}\\ \frac{\sqrt{3}}{6}\end{bmatrix},$$

$$W_4\begin{pmatrix}x'\\y'\end{pmatrix}=\begin{bmatrix}\frac{1}{3} & 0\\ 0 & \frac{1}{3}\end{bmatrix}\begin{bmatrix}x\\y\end{bmatrix}+\begin{bmatrix}\frac{2}{3}\\0\end{bmatrix}.$$

Hence, generator curve can be calculated as:

$$A = W_1 U\, W_2 U W_3 U\, W_4.$$

C. Design steps for KLSSSCMFA

Step 1: Design a simple square conventional patch antenna using the above calculated dimensions. This is 0^{th} iteration or S_0 K_0 iteration as depicted in Fig. 1 (a).

Step 2: By applying 1^{st} iteration of Sierpinski carpet to the square patch, the geometry is called Sierpinski first iteration S_1. The 1^{st} iteration of Koch curve on square sides is denoted as K_1. The patch is divided into 9 congruent squares each having side 9.8 mm. Then centermost square is selected and Koch curve is applied on each side of the central square. This final structure is cut from the patch to make complete iteration S_1K_1, as shown in Fig. 1 (b).

Step 3: For iteration 2, the remaining all 8 squares are divided into 9 more congruent squares each having side of 3.267 mm. Among all these squares, the centermost square is selected and is called Sierpinski iteration S_2. As in 1st iteration, apply the Koch curve K_1 on each side of all squares to generate the complete structure for iteration 2. All these eight structures as in iteration 1^{st} are cut from the patch to design the complete 2^{nd} iteration of the proposed geometry as shown in Fig. 1 (c). Koch curve is the type of self-similar fractal structure and can be repeated on each line or side of the square by dividing the side length into three parts and on the center part equilateral triangle is made each having side equal to the length of central part [19].

Step 4: For the third iteration, choose 1st iteration having S_1 and K_1 structure and apply Koch curve K_2 further on each side lengths. The structure is denoted as S_1 with K_2 geometry (third iteration) as obtained denoted in Fig. 1 (d).

Step 5: To design the fourth iteration geometry, chose 2^{nd} iteration as base geometry and apply K_2 on all 8 congruent squares. Last iteration S_2 K_2 is known as final design of the proposed antenna as shown in Fig. 1 (e).

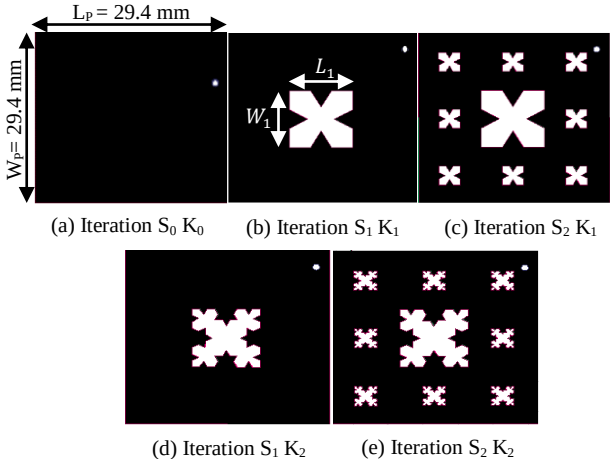

(a) Iteration S_0 K_0 (b) Iteration S_1 K_1 (c) Iteration S_2 K_1

(d) Iteration S_1 K_2 (e) Iteration S_2 K_2

Fig. 1. Design of KLSSSCMA.

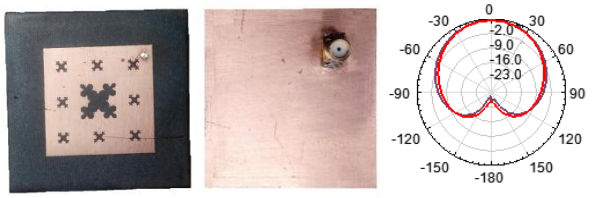

(a) (b) (c)

Fig. 2. (a) Fabricated patch, (b) ground plane, (c) radiation pattern of S_0 K_0 iteration at 3.2 GHz.

III. RESULTS AND DISCUSSIONS

To design the proposed antenna, it is simulated using High-Frequency Simulator Software (HFSS) successfully and all the performance parameters are analyzed thoroughly. S_{11} (dB) parameter is observed concisely for all the proposed iterations. Figures 2 (a) and 2 (b) show the photographic front view and back view of the fabricated S_2 K_2 iteration with probe feed.

A. Simulated results

Figure 3 represents S_{11} (dB) versus frequency plots for all iterations of the proposed antenna. In this figure S_0 K_0, S_1 K_1, S_2 K_1, S_1 K_2 and S_2 K_2 show the impedance matching behavior. S_0 K_0 iteration resonates at one frequency f_1=3.2 GHz with S_{11}= -29.27 dB.

The bandwidth is 1.593 GHz between 2.8350 GHz to 4.4280 GHz covering small portion of both S and C bands range. The S_1K_1 iteration gives multi resonance behavior at f_1=3.2 GHz, f_2=4.6 GHz and f_3=7.6 GHz frequencies and possess S_{11} values of -39.48 dB, -30.38 dB and -25.67 dB respectively at these frequencies. There is

improved BW having value 2.3867 GHz between first two peaks and 1.7572 GHz BW between later peaks. Sierpinski S_2 iteration preserves the multi-resonance behavior of the first iteration with a small shift in all frequency peaks towards lower side due to fractal shaped slots in the geometry. This geometry represents the multifractal geometry with f_1=3.1 GHz, f_2=4.3 GHz and f_3=7.5 GHz. These three peaks have S_{11} values of -20.37 dB, -20 dB and 7.5 dB respectively. Bandwidth becomes 2.6188 GHz at first two peaks and 1.9249 GHz at third peak. It is clear that as the number of iterations is increased, bandwidth also improves. This S_2 K_1 iteration of antenna also covers S and C bands for multiple applications having BW=50.81% for first band and 23.147% for second band. For iteration S_1 K_2, Koch curve is applied on all sides of S_1 K_1 geometry. Further frequency shift in lower side is to consider at f_1=3.0 GHz, f_2=4.2 GHz and f_3=7.3 GHz with S_{11} values of -16.25 dB, -16.34 dB and -11.59 dB respectively. The bandwidth parameter is enhanced to 61.93% between first two peaks and to 34.26% between last peaks. Now K_2 structure is applied to S_2 K_1 base geometry that gives a new shape called S_2 K_2 iteration of KLSSSCMFA. This gives wide bandwidth of 5.5299 GHz from 2.3040 GHz to 7.8339 GHz and covers the bands of WLAN, WiMAX, WPAN, Wi-Fi, satellite communication and military applications. Bandwidth becomes 70.589% as shown in Fig. 3. For all iterations, bandwidth, S_{11}, gain and VSWR are tabulated in Table 3.

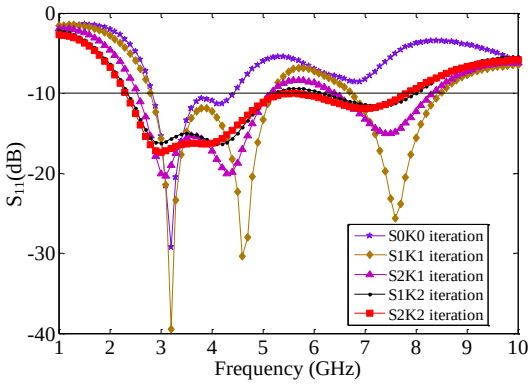

Fig. 3. A comparison of S_{11} values of KLSSSCMFA for S_0 K_0, S_1 K_1, S_2 K_1, S_1 K_2 and S_2 K_2 iterations.

Table 3: Simulation results of all performance parameters of KLSSSCMFA

S. No.	Frequency (GHz)	S_{11} (dB)	VSWR	Gain (dB)	Lower Frequency (GHz)	Upper Frequency (GHz)	Bandwidth (GHz)	Bandwidth %
S_0 K_0 iteration	3.2	-29.27	1.0712	+4	2.8350	4.4280	1.593	5.9756
S_1 K_1 iteration	3.2	-39.48	1.0215	+6	2.7995	5.1866	2.3867	46.024
	4.6	-30.38	1.0624	+4				
	7.6	-25.66	1.1099	+7	6.7287	8.4873	1.7572	20.720
S_2 K_1 iteration	3.1	-20.37	1.2118	+7	2.5350	5.1540	2.6188	50.81490
	4.3	-20.0	1.2221	+4				
	7.5	-15.05	1.4291	+8	6.4026	8.3310	1.9249	23.147
S_1 K_2 iteration	3.0	-16.25	1.3636	+8	2.3488	6.1706	2.9081	61.9356
	4.2	-16.34	1.3595	+4				
	7.3	-11.59	1.7146	+8	5.2569	7.9979	1.827	34.269
S_2 K_2 iteration	3.0	-17.30	1.3136	+9	2.3040	7.8339	5.5299	70.589
	4.0	-16.22	1.3651	+6				
	7.0	-11.88	1.6831	+8				

For the proposed KLSSSCMFA, Voltage Standing Wave Ratio (VSWR) is observed in the desired range (1 to 2) for all iterations as depicted in Fig. 4.

B. Measured results

S_{11} parameter of final iteration of the proposed antenna is measured using Vector Network Analyzer to validate simulated results generated by HFSS. Figure 5 represents a comparison between simulated and measured results for S_2 K_2 iteration. The measured results and the simulated results are almost similar.

Table 4 shows a comparative data of simulated and measured results in terms of S_{11} and bandwidth.

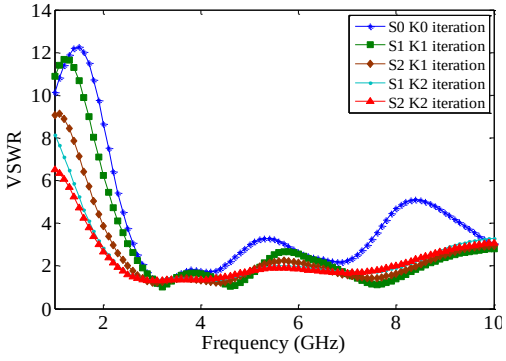

Fig. 4. A coparison of VSWR values of S_0 K_0, S_1 K_1, S_2 K_1, S_1 K_2 and S_2 K_2 iterations.

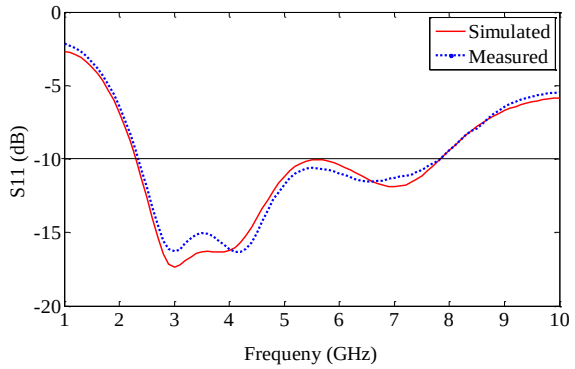

Fig. 5. Simulated and measured S_{11} (dB) versus frequency plot of the proposed antenna.

Table 4: A comparison of measured and simulated results

Frequency (GHz)	Simulated		Measured	
	S_{11} (dB)	BW (GHz)	S_{11} (dB)	BW (GHz)
3.0	-17.35	5.5299	-16.25	5.400
4.0	-16.22		-16.12	
7.0	-11.88		-11.28	

C. Radiation pattern

It represents the field power distribution of an antenna in E and H planes at given frequencies. Fractal nature always tends to give stable radiation pattern. 2D radiation pattern of the proposed antenna first iteration (S_0 K_0) is shown in Fig. 2 (c). Radiation patterns for S_1 K_1, S_2 K_1, S_1 K_2 and S_2 K_2 at corresponding peaks are shown in Fig. 6, Fig. 7, Fig. 8 and Fig. 9 respectively.

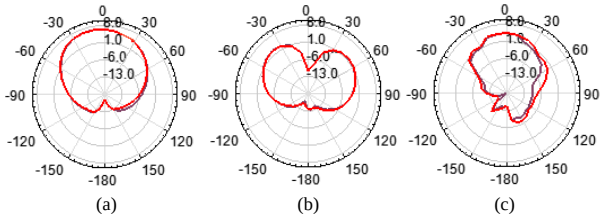

Fig. 6. Radiation patterns of S_1 K_1 iteration at: (a) 3.2 GHz, (b) 4.6 GHz, and (c) 7.6 GHz.

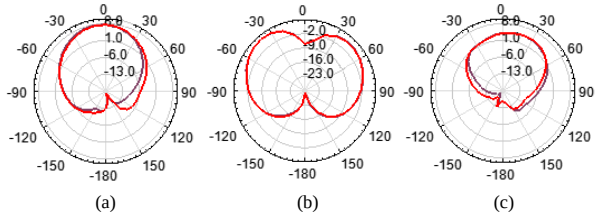

Fig. 7. Radiation patterns of S_2 K_1 iteration at: (a) 3.1 GHz, (b) 4.3 GHz, and (c) 7.5 GHz.

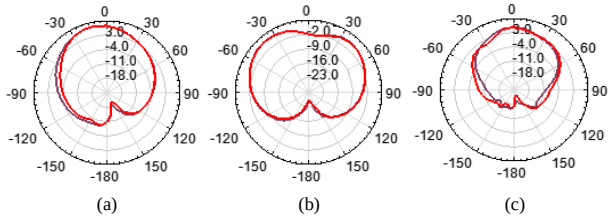

Fig. 8. Radiation patterns of S_1 K_2 iteration at: (a) 3.0 GHz, (b) 4.2 GHz, and (c) 7.3 GHz.

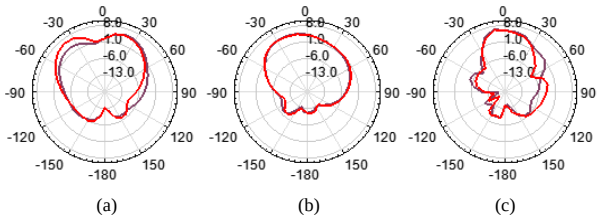

Fig. 9. Radiation patterns of S_2 K_2 iteration at: (a) 3.0 GHz, (b) 4.0 GHz, and (c) 7.0 GHz.

D. Effect of height of substrate on bandwidth

The effect of substrate height (h) on bandwidth (BW) of the proposed antenna is observed. To obtain wideband behavior of the antenna, the height of substrate is varied from 1.6 mm to 3.3 mm as shown in Fig. 10. At lower value of h the proposed antenna shows multiband behavior (three peaks 2.9 GHz, 4.5 GHz and 9.2 GHz). As h is increased, the bandwidth at these peaks increases. At h=2.9 mm, out of these three peaks, two peaks (2.9 GHz and 4.5 GHz) are combined.

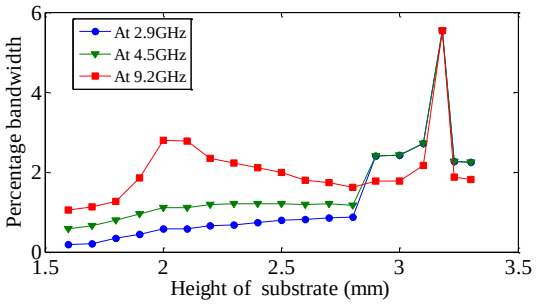

Fig. 10. Variation of bandwidth with height of substrate.

But at h=3.18 mm all three peaks combine and start showing wideband behavior. Beyond this height, bandwidth again starts to decline. Thus, h=3.18 mm substrate height is an optimum height for the design of the proposed antenna.

A comparison of results of the proposed antenna in terms of gain and bandwidth with previous antennas available in literature is shown in Table 5. From this

table it is clear that a maximum bandwidth of 6.9 GHz is obtained by Pharwaha et al. at the cost of low gain 4.41 dB [21]. A maximum gain of 5.8 dB is obtained by Lin et al. at the cost of small bandwidth 66 MHz [20].

Table 5: A comparison of the proposed antenna with other fractal antennas

Author	Gain (dB)	Center Frequency (GHz)	Bandwidth (GHz)
Daotie [3]	5.11	2.50	4.00
Shrestha [11]	2.64	2.45	0.60
Srivastava [13]	3.31	1.84	2.39
Lin [20]	5.80	1.57	0.66
Pharwaha [21]	4.41	3.72	6.90
Wang [22]	5.00	3.00	4.00
Proposed antenna	9.00	3.00	5.53

The proposed antenna has more bandwidth than antennas of Daotie et al. [3], Shrestha et al. [11], Srivastava et al. [13], Lin et al. [20], and Wang et al. [22]. It also has more gain than these antennas.

IV. CONCLUSION

The proposed geometry of KLSSSCMA combines the Sierpinski carpet and Koch curves successfully. S_2K_2 iteration is designed, simulated and fabricated. A wideband range of frequency 5.6 GHz is obtained and has considerable gain (4 dB to 9 dB) over the whole band. KLSSSCMFA covers WLAN, Wi-Max, WPAN, Wi-Fi, satellite communication for uplink and downlink and military applications of S and C bands. The radiation pattern of all iterations at peaks shows the hemisphere pattern with consistency. Variation in substrate height impacts bandwidth parameter and is optimized. For further work, different methods can be applied for modifications in the proposed antenna. Neural network can be implemented for this proposed geometry to optimize different parameters using training data. Curve fitting and Particle Swarm Optimization (PSO) techniques can also be implemented to optimize the geometry of the proposed antenna. This antenna can also be designed for higher iterations using optometric analysis.

REFERENCES

[1] D. H. Werner and S. Ganguly, "An overview of fractal antenna engineering research," *IEEE Antennas Propagation Magazine*, vol. 45, pp. 38-57, Feb. 2003.

[2] S. Tripathi, A. Mohanand, and S. Yadav, "Hexagonal fractal ultra-wideband antenna using Koch geometry with bandwidth enhancement," *IET Microwaves, Antennas & Propagation*, vol. 8, pp. 1445-1450, 12 Sep. 2014.

[3] D. Li and J.-F. Mao, "Coplanar waveguide-fed Koch-like sided Sierpinski hexagonal carpet multifractal monopole antenna," *IET Microwaves, Antennas & Propagation*, vol. 8, pp. 358-366, 2014.

[4] I. S. Bangi, J. S. Sivia, and G. S. Kaureana, "Minkowski and circular curves based wide band microstrip fractal antenna for," *International Journal of Computer Science and Information Security*, vol. 15, no. 6, pp. 162-166, June 2017.

[5] F. S. Zhang, Z. N. Zhao, L. T. Ma, and X. N. Li, "A CPW-fed wideband Koch snowflake fractal monopole for WLAN/WiMAX applications," *Progress in Electromagnetic Research C, PIER C*, vol. 28, pp. 143-153, 2012.

[6] A. Azari, "A new ultra–wideband fractal antenna," *URSI Int. Symp. on Electromagnetic Theory*, vol. 1, pp. 424-427, 2010.

[7] J. S. Sivia and S. S. Bhatia, "Design of fractal-based microstrip rectangular patch antenna for multiband applications," *IEEE International Advance Computing Conference (IACC), 2015. Magazine*, vol. 8, no. 2, pp. 77-82, Apr. 2007.

[8] S. S. Karthikayan, S. S. Gaikwad, M. Singh, and A. Ajey, "Size miniaturized fractal antenna for 2.5GHz application," *IEEE Students' Conference on Electrical, Electronics and Computer Science*, 2012.

[9] S. Rani and A. P. Singh, "On the design and analysis of modified Koch curve fractal antenna," *J. Inst. Eng. India Ser. B*, 94(4), pp. 231-236, 2013.

[10] N. Saluja and R. Khanna, "Design analysis and fabrication of novel coplanar waveguide-fed hybrid fractal-based broadband antenna," *International Journal of Microwave and Wireless Technologies*, pp. 749-52, 2013.

[11] S. Shrestha, S. J. Han, S. K. Noh, S. Kim, H. B. Kim, and D. Y. Choi, "Design of modified Sierpinski fractal based miniaturized patch antenna," *Information Networking (ICOIN), 2013 International Conference on*, pp. 274-279, 28-30 Jan. 2013.

[12] S. Sivasundarapandian and C. D. Suriyakala, "A planar multiband Koch snowflake fractal antenna for cognitive radio," *International Journal of Microwave and Wireless Technologies*, pp. 1-5, 2015.

[13] D. K. Srivastava, A. Khanna, and J. P. Saini, "Design of a wideband gap-coupled modified square fractal antenna," *J. Computer Electron*, Springer, 2015.

[14] B. Biswas, D. R. Poddar, R. Ghatak, and A. Karmakar, "Modified Sierpinski carpet fractal shaped slotted UWB monopole antenna with band notch characteristic," *IEEE Conference*, 2015.

[15] Z. W. Yu, G. M. Wang, X. J. Gao, and K. Lu, "A novel small-size single patch microstrip antenna based on Koch and Sierpinski fractal-shapes,"

Progress In Electromagnetics Research Letters, vol. 17, pp. 95-103, 2010.

[16] M. Abbaspour and H. R. Hassani, "Wideband star-shaped microstrip patch antenna," *Progress In Electromagnetics Research Letters*, vol. 1, pp. 61-68, 2008.

[17] D. Li and Jun-Fa Mao, "Coplanar waveguide-fed Koch-like sided Sierpinski hexagonal carpet multifractal monopole antenna," *IET Microwaves, Antennas & Propagation*, vol. 8, pp. 358-366, 2014.

[18] C. A. Balanis, *Antenna Theory, Analysis and Design*. John Wiley & Sons, New York, 1997.

[19] D. Fazal, Q. U. Khan, and M. B. Ihsan, "Use of partial Koch boundaries for improved return loss, gain and sidelobe levels of the triangular patch antenna," *Electronics Letters*, vol. 48, 2012.

[20] S. Lin, L.-Z. Wang, Y.-D. Wang, X.-Y. Zhang, and H.-J. Zhang, "Design and analysis of a circular polarization microstrip antenna with Koch fractal edges," *Progress In Electromagnetics Research Letters*, vol. 34, 9-19, 2012.

[21] A. P. S. Pharwahaand and S. Rani, "On the design of wearable fractal antenna," *International Journal of Computer, Electrical, Automation, Control and Information Engineering*, vol. 9, no. 7, 2015.

[22] F. Wang and T. Arslan, "Inkjet printed antenna on flexible substrate for wearable microwave imaging applications," *IEEE Loughborough Antenna & Propagation Conference*, 2016.

Amandeep Kaur Sidhu was born in Bathinda, Punjab, India in 1993. She received her B.Tech and M.Tech degrees in Electronics and Communication from Yadavindra College of Engineering, Talwandi Sabo, Punjab, India in 2016. Her research interest is in the field of antenna and wave propagation, fractal and microstrip patch antennas.

Jagtar Singh Sivia was born in 1976 at Bathinda, Punjab, India. He received his B.Tech and M.Tech degrees in ECE from Punjab Technical University Jalandhar, Punjab, India in 1999 and 2005 respectively. He received his Ph.D degree in the area of antenna systems from SLIET, Longowal, Sangrur, Punjab, India. He is a Professor in ECE Department of Punjabi University at Yadawindra College of Engineering Talwandi Sabo, Bathinda, Punjab, India. He has published more than 60 papers in various international journals and conferences. He is a Fellow of the Institution of Engineers (FIE) (India), Indian Society of Technical Education (India) and International Association of Engineers (IAENG).

Review of RF Cloaking Techniques for Antenna Applications

N. Kumutha [1], K. Hariharan [1], N. Amutha [2], and B. Manimegalai [1]

[1] Department of Electronics and Communication Engineering
Thiagarajar College of Engineering, Madurai, 625015, India
kumutha.nas@gmail.com, khh@tce.edu, naveenmega@tce.edu

[2] Department of Electrical and Electronics Engineering
Nalanda College of Engineering, Gokhulpur, 803108, Bihar
nskamutha@gmail.com

Abstract ─ This paper reviews the background phenomenon of various cloaking techniques such as transformation optics, transmission line network, microwave network cloak, scattering cancellation techniques in the applications of antenna field particularly in hiding the obstacle from the electromagnetic source and reducing the mutual coupling between two antennas that was placed closed to each other. Cloaking at multiple frequencies in each cloaking techniques are also compared. The comparative study showed that the scattering cancellation technique based on aperiodic Frequency Selective Surfaces (FSS) structure will dominate the electromagnetic cloaking field in near future.

Index Terms ─ Antennas, cloaking techniques, dual band cloaking, interference reduction, Modulated meta-surface.

I. INTRODUCTION

Electromagnetic cloaking technology is a stealth or camouflage technology that renders an object to be invisible to the Electro Magnetic (EM) spectrum. This can be achieved by cancelling or minimizing the scattering properties of an object. Some of the theories that are adopted in this technology are transformation optics [1, 2], transmission line network [3-7], microwave network [8-11] and scattering cancellation [14-22]. Many theoretical and experimental results are being carried out in the radio frequencies of the electromagnetic spectrum. Recently this technology finds its place in antenna applications. One such application is to hide an object that obstructs the antenna's field performance using a cloak structure which was designed on basis of any one of the above said theories. The hindrance of the antenna may be an object which is either external to the antenna or may be an integral elemental parts of antenna itself as the case of ground plane in monopole antennas and the reflector and director elements in Yagi-Uda antenna. In another perspective, the cloak can also play a role in reducing the mutual coupling between two antennas that are placed close to each other.

Review literatures that describe and compare various EM cloaking technology are not uncommon. However, reviews on the application of EM cloaking in the antenna field are seldom discussed. Thus, in the present review paper, an attempt has been made particularly in comparing various techniques of EM cloaking in antenna applications. Section II briefly describes the principles of various cloaking techniques related to antenna applications in the radio frequency range. The application of those cloaking techniques in hiding an obstacle from the antenna and in reducing mutual interference between two antennas are explained in Section III. Finally, Section IV concludes with the comparison of RF cloaking technique in antenna applications.

II. BACKGROUND PRINCIPLE OF CLOAKING TECHNIQUES

A. Transformation optics

Transformation optics concept was implemented earlier to a three-dimensional meta-material structure for cloaking a large object [1]. The properties of material were varied in order to control the propagation of EM wave as given by below set of equations:

$$\varepsilon'_r = \mu'_r = \frac{R_2}{R_2 - R_1}\frac{(r' - R_1)^2}{r'},$$

$$\varepsilon'_\theta = \mu'_\theta = \frac{R_2}{R_2 - R_1},$$

$$\varepsilon'_\varphi = \mu'_\varphi = \frac{R_2}{R_2 - R_1},$$

where R_1 and R_2 are the radius of object and cloak respectively and $R_1 < r < R_2$.

The EM wave was allowed to bend around the cloaked object so as to make the object invisible to the EM source. The transformation based meta-material

Submitted On: June 2,2018
Accepted On: August 11, 2018

cloak had the limitation of cloaking an object only in narrowband.

B. Transmission line networks

The transformation optics was extended to two-dimensional cloak structure made up of transmission line network of inductors and capacitors [3] and of conical metal plate structures for broadband cloaking [4]. However, the two-dimensional cloaking had a limitation of bulky volumetric cloaking structure.

C. Microwave network cloak

Large sized object can also be cloaked with microwave network cloaking technique [8]. The microwave network cloak comprised of metallic patches interconnected with micro-strip lines. It worked on the principle of superluminal propagation. The cloak structure covering the object was responsible for receiving, transferring and re-transmitting the incoming EM wave from the source to the rear side of the object. So the cloak covering an object is designed in such a way that, the time travelled by the EM waves around the object was made to match with that of EM waves travelling in the same space as if the object was not present. The length of the metallic patches determines the cloaking frequency.

D. Scattering Cancellation (SC) techniques

Scattering cancellation technique, predominantly known as mantle cloaking, utilizes the meta-screen of periodic Frequency Selective Surface (FSS) elements [13]. In this technique, cloaking was based on reducing the scatters of incident wave by the object. The underlying principle was that the reactance of object that scattered wave was made equal and opposite with the surface reactance of periodically patterned FSS structures over the cloak. The reactance of the 2D cylindrical object that exhibit the scattering property was calculated from Mie's expansion [14] as:

$$X_s = \frac{2}{\omega a \gamma \varepsilon_0 (\epsilon_r - 1)},$$

where, $\gamma = a/a_c$, ω, a and a_c are angular frequency, radius of object and cloak respectively, ε_0 and ε_r are the dielectric constant of vacuum and material, and the surface reactance for the periodic arrangement of horizontal strip array of FSS structure was calculated from the Floquet's principle [15] as:

$$X_s = \frac{-j\eta_0 c\pi}{\omega(\epsilon_r + 1)D}\left(\frac{1}{\log\csc\left(\frac{\pi g}{2D}\right)}\right),$$

where η_0 is the free space wave impedance, D and g are the width and gap between the strips respectively.

Thus, the interaction of object and cloak characteristic parameters had its advantageous in cloaking both passive as well as active objects like sensors etc. [16-19].

Modulated meta-surface based scattering cancellation theory is considered as one of an emerging technology in electromagnetic cloaking field. In case of modulated meta-surface cloaking, geometry of the FSS structure was varied in such a way that the equivalent impedance of cloaking structure was optimized with that of the external hindering object appropriately in order to achieve a desired task. This results in the variation of phase velocity and propagation path of a surface wave. The object satisfying only the quasi static condition (object size << operating wavelength) can be cloaked may be considered as its main drawback.

III. APPLICATION OF CLOAKING TECHNIQUES IN ANTENNAS

A. Hiding an object

1) Transformation optics and transmission line network cloak

The application of hiding a scatterer from an antenna environment using transformation optics was first reported in 2008, by enclosing the scatterer with a dispersive cloak [2].

Two-dimensional cloak structure made up of a combination of a periodical set of conical metal plates and a transition layer that couples the incident EM wave to a transmission line network was introduced to the antenna application in 2012 for reducing the blockage of the antenna. Any external metal cylindrical volumetric object that hindered the horn antenna, was covered by the above said two-dimensional cloak structures [5, 6]. The incident EM wave from horn antenna was made to bend around the metal object by the structured cloak, thereby reducing the visibility of the object from its EM wave path. The directive patterns of the horn antenna depicted the success of corresponding cloaking phenomenon. Dual frequency EM cloak was also made possible through the introduction of multiple LC resonating circuits [7]. However, these two-dimensional cloaking had the limitation of bulky volumetric cloaking structure.

2) Microwave network cloak

The structure made up of metallic patches interconnected with microstrip lines was applied to both circular and other arbitrary shaped objects [8, 9]. The distance between the edge of horn antenna and the center of the object is 64 mm. Figure 1 shows such various configurations of microwave network cover. The geometrical shape of the cloak plays an important role in the cloaking performance by reducing the maximum and the averaged scattered width [12]. Also, the limitation in material flexibility of circular cloak can be avoided using polygon structures.

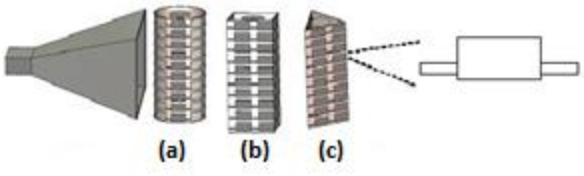

Fig. 1. Various configuration of microwave network cover: (a) circular cloak, (b) square cloak, and (c) triangular cloak.

The variations in the S11 parameter and 3D radiation patterns as shown in Fig. 2 (a) and Fig. 2 (b) brief the significance of cloak geometry.

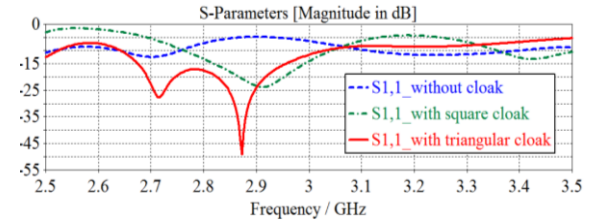

(a)

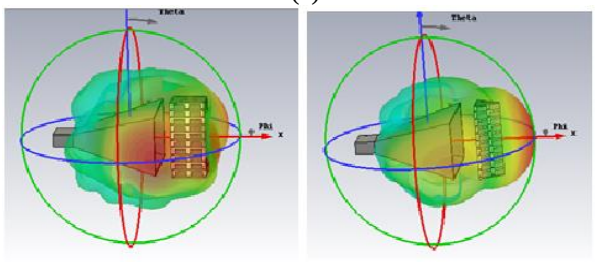

(b)

Fig. 2. (a) Simulated S11 parameter (solid red – triangular cloak, dash dotted green – square cloak, dashed blue – without cloak) for different microwave network cloak geometry; (b) 3D radiation patterns for different microwave network cloak geometry.

Dual band cloaking was also achieved in those interconnected metallic patch cloaks by varying the widths of micro-strip lines as shown in Fig. 3 [10].

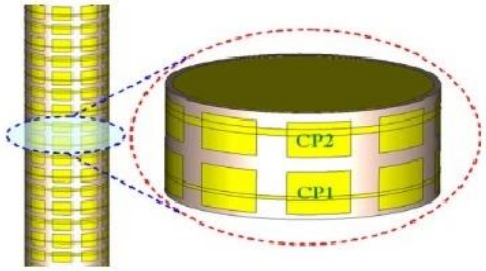

Fig. 3. Microwave network cover for dual band cloak [10].

3) Scattering cancellation techniques

The optimized patterned meta-surface cloak covering the metallic object was placed before the horn or any other antenna. Reduction in scattering cross section ultimately minimized the visibility of a conducting or dielectric object. This was verified through the scattering parameters (S_{11}) and the directive gain pattern of the antenna. Dual band cloaking was also made possible in mantle cloaking by having two layered covers each with the different electrical cross sections of periodic FSS structures but maintaining a constant bi-layer aspect ratio. The structure for dual band mantle cover with two layers is depicted in Fig. 4 [20].

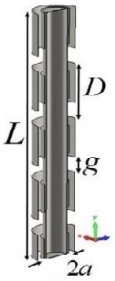

Fig. 4. Structure for dual band mantle cloaking [20].

Aperiodicity in the geometrical structures (modulated meta-surface) was employed for hiding an object from an antenna. Careful design of aperiodicity structure in the cloak results in two different impedances and was able to hide an object from two different frequencies resulting in a dual band cloaking [21].

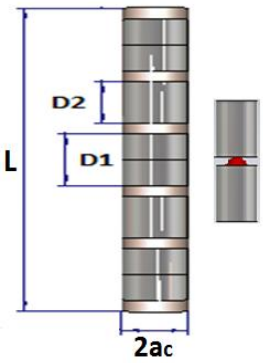

Fig. 5. Structure for modulated meta-surface cloaking.

Figures 5 and 6 shows the structure and simulated results of modulated meta-surface in cloaking at dual band frequencies. Unlike periodic FSS structure where two layered covers were needed to achieve dual band cloaking, aperiodic or modulated meta-surface required only single layer cover to act as dual band cloaking. In simple, a FSS structures incorporated in a single layer

covering an object can reduce the scattering at two different frequencies by introducing the aperiodicity in their geometries.

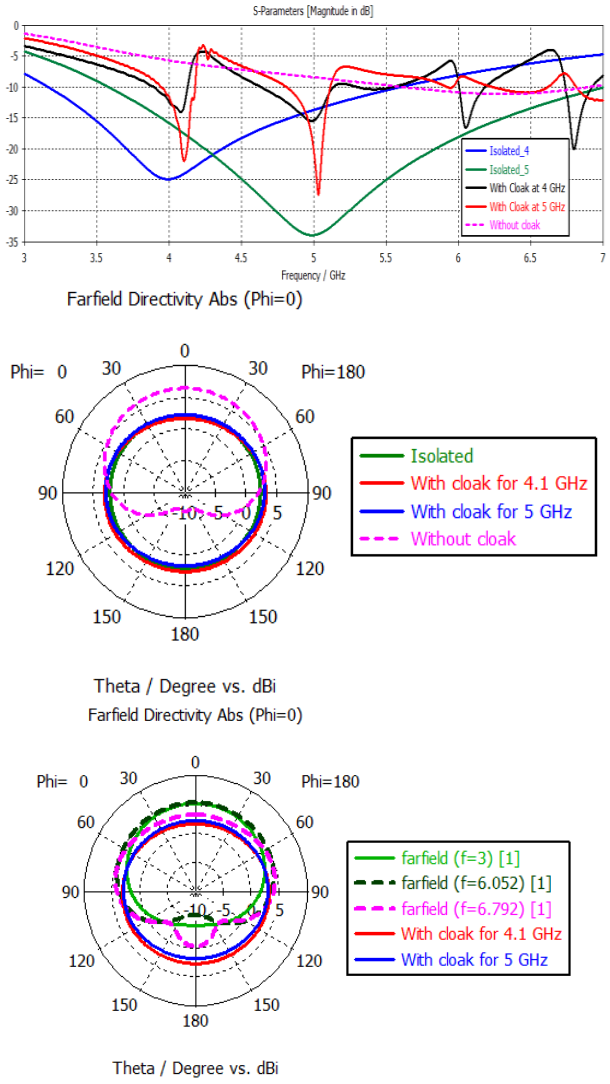

Fig. 6. Simulated results for modulated meta-surface cloaking.

B. Mutual coupling reduction

In the practical scenario of existence of two antennas operating at different frequencies that were located close to each other naturally had mutual coupling between them. The implementation of cloaking techniques to reduce the mutual coupling between two antennas was also tried.

1) Transformation optics and microwave network cloak

Very few works have been reported in hiding an antenna from another antenna using transformation optics and microwave network cloak [2, 11]. But still the transmission line network cloak needs exploration in mutual coupling reduction. Since these techniques can only bend the EM wave around the object without the involvement of object properties, cloaking an antenna at different frequency is only possible rather than cloaking at its own resonance frequency.

2) Scattering cancellation technique

The periodic meta-surface cloak (scattering cancellation technique) covering the antennas as designed in the literatures can reduces the coupling. This was due to the interaction between the electromagnetic fields scattered from the object and cloak cover. The presence of mantle covers on one or both the antennas depends on the operating frequencies of the two antennas [17, 18].

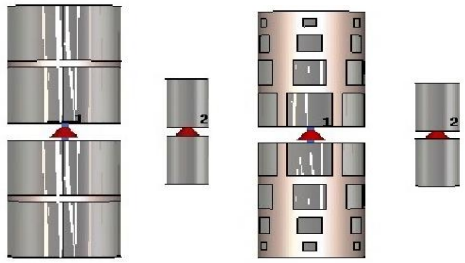

(a) (b)

Fig. 7. Scenario of two dipole antennas placed close to each other with one mantle cover: (a) conventional meta-surface, and (b) modulated patch meta-surface.

The scenario of two dipole antennas placed close to each other with the mantle cover on one dipole antenna is as shown in Fig. 7 (a). Later, modulated meta-surface was also applied for reducing the coupling between antennas. Figure 7 (b) shows the structure for the modulated meta-surface in patch configurations. By this aperiodicity, an improvement of 15% in bandwidth was achieved as shown in Fig. 8 [22].

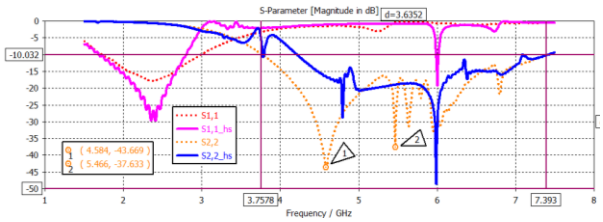

Fig. 8. S Parameter result for modulated patch and horizontal meta-surface cloak in antenna application [22].

IV. DISCUSSION

As an overview, the cloak designed from all the above techniques will be suitable for hiding an obstacle from an antenna. The object and hence its cloak size itself, will be large in transformation optics and

transmission line network cloak technique and needs further exploration in mutual coupling reduction application of antennas operating at same frequency. This can be overcome in scattering cancellation technique but it is applicable only for sub wavelength sized object. Although the microwave network cloak technique experiences the same problem as in transformation optics technique in mutual coupling application, it is possible to hide even the larger sized object with the super thin sized cloak. Finally, dual band cloaking had been performed even in a single cloak layer with the help of microwave network cloak and aperiodic scattering cancellation techniques.

V. CONCLUSION

This paper summarizes the various cloaking techniques and its applications in antennas. It is noted that the cloaking phenomenon does an excellent job in antenna applications by restoring the electromagnetic and radiation properties of an antenna which was interfered by any conducting or dielectric object and by reducing the interference between two neighboring antennas. Table 1 summarizes the various parameters for different cloaking techniques.

Table 1: Comparison of different cloaking techniques

Parameters	Transformation Optics	Transmission Line Network	Microwave Network	Scattering Cancellation	
				Periodic	Aperiodic
Size of the object that can be cloaked	Large	Large	Large	Small (Quasi-static)	Small (Quasi-static)
Cloak structure size	Large	Large	Small	Small	Small
Coupling reduction	Possible for antennas of different frequency	Yet to be verified	Possible for antennas of different frequency	Possible	Possible
Dual band cloaking	Yet to be verified	Multiple layers of cloak structure	Single layer of cloak structure	Multiple layers of cloak structure	Single layer of cloak structure

As discussed in this paper, each cloaking method has its own pros and cons in antenna applications. So the choice of cloaking techniques adopted is based primarily on the requirements. However, from Table 1, it was observed that the scattering cancellation based on aperiodic FSS structure will dominate the electromagnetic cloaking field in near future.

REFERENCES

[1] J. B. Pendry, D. Schurig, and D. R. Smith, "Controlling electromagnetic fields," *Science*, 312, pp. 1780-1782, 2006.

[2] D. H. Kwon and D. H. Werner, "Restoration of antenna parameters in scattering environments using electromagnetic cloaking," *Appl. Phys. Lett.*, vol. 92, p. 113507, 2008.

[3] P. Alitalo, O. Luukkonen, and S. A. Tretyakov, "Transmission line networks cloaking objects from electromagnetic fields," *IEEE Transactions on Antennas and Propagation*, 56, (2), pp. 416-424, 2008.

[4] P. Alitalo and S. A. Tretyakov, "Electromagnetic cloaking of strongly scattering cylindrical objects by a volumetric structure composed of conical metal plates," *Physical Review B*, vol. 82, 245111, December 2010.

[5] P. Alitalo, C. A. Valagiannopoulos, and S. A. Tretyakov, "Simple cloak for antenna blockage reduction," *IEEE International Symposium on Antennas and Propagation (APSURSI)*, USA, 3-8 July 2011.

[6] J. Vehmas, P. Alitalo, and S. A. Tretyakov, "Experimental demonstration of antenna blockage reduction with a transmission-line cloak," *IET Microwave and Antennas Propagation*, vol. 6, no. 7, pp. 830-834, 2012.

[7] J. Shao, H. Zhang, Y. Lin, and X. Hao, "Dual-frequency electromagnetic cloaks enabled by LC-based metamaterial circuits," *Progress in Electromagnetics Research*, vol. 119, pp. 225-237, 2011.

[8] J. Wang, S. Qu, Z. Xu, H. Ma, J. Zhang, Y. Li, and X. Wang, "Super-thin cloaks based on microwave

networks," *IEEE Transactions on Antennas and Propagation*, vol. 61, no. 2, February 2013.

[9] J. Wang, S. Qu, Z. Xu, H. Ma, J. Zhang, Y. Li, and X. Wang, "Design of super thin cloaks with arbitrary shapes using interconnected patches," *IEEE Transactions on Antennas and Propagation*, vol. 63, no. 1, December 2015.

[10] J. Wang, S. Qu, Z. Xu, A. Zhang, H. Ma, J. Zhang, H. Chen, and M. Feng, "Multi-frequency super thin cloaks," *Photonics and Nanostructures – Fundamentals and Applications*, vol. 12 pp. 130-137, 2014.

[11] A. Naqvi, M. S. Khan, and B. D. Braaten, "A 1x2 microstrip array with reduced mutual coupling achieved with a cylindrically shaped cloaking-based surface," *Microwave and Optical Technology Letters*, vol. 58, no. 2, pp. 296-301, February 2016.

[12] C. Li, K. Yao, and F Li, "Medium parameters and electromagnetic characteristics of arbitrary polygon cloaks," *IET Microwaves, Antennas & Propagation*, vol. 4, no. 10, pp. 1672-1679, 2014.

[13] B. A. Munk, *Frequency Selective Surfaces: Theory and Design*. John Wiley & Sons, 2005.

[14] A. Alu, "Mantle cloak: Invisibility induced by a surface," *Physical Review B*, vol. 80, 2009.

[15] Y. R. Padooru, A. B. Yakovlev, P. Y. Chen, and A. Alu, "Analytical modeling of conformal mantle cloaks for cylindrical objects using sub-wavelength printed and slotted arrays," *Journal of Applied Physics*, 112, 034907, August 2012.

[16] A. Monti, A. Toscano, and F. Bilotti, "Metasurface mantle cloak for antenna applications," *IEEE International Symposium on Antennas and Propagation (APSURSI)*, USA, 8-14 July 2012.

[17] A. Monti, J. Soric, A. Alu, F. Bilotti, A. Toscano, and L. Vegni, "Overcoming mutual blockage between neighboring dipole antennas using a low-profile patterned metasurface," *IEEE Antennas and Wireless Propagation Letters*, vol. 11, pp. 1414, 2012.

[18] A. Monti, J. Soric, M. Barbuto, D. Ramaccia, S. Vellucci, F. Trotta, A. Alù, A. Toscano, and F. Bilotti, "Mantle cloaking for co-site radio-frequency antennas," *Appl. Phys. Lett.*, vol. 108, no. 11, p. 113502, 2016.

[19] A. Monti, J. Soric, A. Alù, A. Toscano, and F. Bilotti, "Design of cloaked Yagi-Uda antennas," *EPJ Appl. Metamaterials*, vol. 3, p. 10, 2016.

[20] J. Soric, A. Monti, A. Toscano, F. Bilotti, and A. Alu, "Multiband and wideband bilayer mantle cloaks," *IEEE Transactions on Antennas and Propagation*, vol. 63, no. 7, July 2015.

[21] N. Kumutha, K. Hariharan, N. Amutha, and B. Manimegalai, "Dual band single layered meta-surface cloak," *IEEE International Microwave and RF Conference (IMaRC)*, Ahmedabad, India, 11-13 December 2017 (Presented).

[22] N. Kumutha, K. Hariharan, and B. Manimegalai, "Reduction of interference between two neighbouring antennas by a modulated metasurface," *IEEE International WIE Conference on Electrical and Computer Engineering (WIECON-ECE)*, Bangladesh, pp. 247-250, 2015.

Analysis, Modeling, and Measurement of Shielding Effectiveness for a Cylindrical Waveguide with a Hexagonal Insert Structure

Scott W. Faust [1] and Daniel N. Aloi [2]

[1] Vehicle Electronics and Architecture
U.S. Army TARDEC, Warren, Michigan 48397-5000, United States of America
scott.w.faust.civ@mail.mil

[2] Department of Electrical and Computer Engineering
Oakland University, Rochester, Michigan 48309-4479, United States of America
aloi@oakland.edu

Abstract **–** A theoretical model is presented for the shielding effectiveness of a waveguide containing an insert consisting of several smaller hexagonal or "honeycomb"-shaped waveguides. FEKO, an electromagnetic modeling software package, is used to create computer-aided design (CAD) models of physical waveguides, and to find solutions for the TE_{11} mode of propagation for each model using the Finite Element Method (FEM). S-parameters are used to characterize the shielding effectiveness of the waveguide models through simulation in FEKO and measurement of waveguide samples in the laboratory. The results obtained by each method are compared and discussed.

Index Terms **–** Attenuation, computer-aided design, cutoff frequency, electromagnetic compatibility, finite element method, honeycomb insert, shielding effectiveness, S-parameters, simulation, waveguides.

I. INTRODUCTION

Preparation for electromagnetic compatibility (EMC) testing of liquid-cooled power electronics requires selection of waveguides to pass the coolants in and out of the shielded enclosure. Various waveguide manufacturers provide basic calculations for the cutoff frequency of a circular waveguide pipe penetration based on the diameter and length of the waveguide. Optional "honeycomb" inserts are then quoted as an option to increase the cutoff frequency when the waveguide is loaded with materials other than air, i.e., fluids for cooling, fire suppression, etc. with limited information provided on the efficacy of the honeycomb insert. The attenuation of the overall honeycomb insert structure is typically stated to be that of a single waveguide in the insert. This information is typically limited to the cutoff frequency of the individual insert, leaving the end user unable to determine the crossover point where the shielding effectiveness of the waveguide is less than the rated shielding effectiveness of the enclosure in which it is installed. McInerney et al. (1984) provided limited data on the shielding effectiveness of waveguides filled with various fluids over a limited frequency range (up to 7.5 GHz), including the predicted shielding effectiveness for a waveguide having an insert containing circular apertures. The shielding effectiveness of this insert was attributed to a single aperture within the insert structure [1]. Other authors review waveguides and their use in maintaining shielding effectiveness, with no analytic formula provided to estimate the shielding effectiveness of the waveguide based on the dimensions or number of openings in the honeycomb insert [2, 3, 4].

The goals of this paper are to present a theoretical model for the shielding effectiveness of a waveguide with a honeycomb insert having *N* individual inserts, develop a suitable model for simulation using electromagnetic modeling software, and compare the results obtained through analysis and modeling with measurements of commercially-available waveguides up to 34 GHz.

II. THEORETICAL MODEL

Prior work developed and proposed three theoretical models for a cylindrical waveguide having a honeycomb insert [5]. Each model used a first-order approximation of a single hexagonal "honeycomb" insert as a circular waveguide. This approximation is illustrated by Fig. 1.

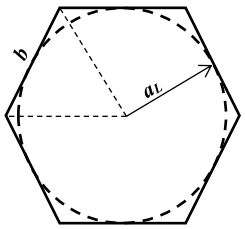

Fig. 1. Circle approximation for the cross-section of a single hexagonal "honeycomb" waveguide insert [5].

Submitted On: February 20, 2018
Accepted On: June 17, 2018

This approximation of the hexagonal insert as a circular waveguide simplifies the calculation of the estimated cutoff frequency for the insert by using the well-known equation for the cutoff frequency of a circular waveguide for the dominant mode of propagation, TE_{11} [6]:

$$f_c = \frac{\chi'_{11}}{2\pi a\sqrt{\mu\varepsilon}}, \quad (1)$$

where $\chi'_{11} = 1.8412$ is the zero of the derivative of the Bessel function for TE_{11}, a is the radius of the circle inscribed within the hexagonal cross-section in meters, μ the permeability, and ε the permittivity of the material within the insert.

The attenuation, or shielding effectiveness of a circular waveguide for a particular mode is:

$$A = 54.58fL\left[\mu\varepsilon\left(\left(\frac{f_c}{f}\right)^2 - 1\right)\right]^{\frac{1}{2}}, \quad (2)$$

where A is the attenuation of the waveguide in decibels, f is the frequency of the electromagnetic wave propagating through the waveguide, L is the length of the waveguide, and f_c the cutoff frequency of the waveguide [2-5]. In writing analytic expressions for the cutoff frequency of a waveguide with a honeycomb insert, the cutoff frequency of the main waveguide, i.e., the waveguide containing the honeycomb insert, is denoted by f_c, whereas the cutoff frequency of an individual insert within the honeycomb structure is represented by $f_{c,insert}$.

Of the three analytic models proposed, preliminary modeling and simulation efforts using FEKO identified one particular model as having the lowest average error between the theoretical and simulation results as compared to other proposed models [5]. This particular model was based on a proposal by Kaiser (2006), that shielding effectiveness of a single opening is improved by dividing its cross-sectional area into N smaller openings [7]. The resulting formula for the shielding effectiveness of the honeycomb insert using this model is [5]:

$$SE \cong 54.58fL_{insert}\left[\mu\varepsilon\left(\left(\frac{f_{c,insert}}{f}\right)^2 - 1\right)\right]^{\frac{1}{2}} + 10\log_{10} N, \quad (3)$$

where L_{insert} is the length of an individual insert.

Equation (3) calculates the shielding effectiveness of a circular waveguide having a honeycomb insert as the shielding effectiveness of a single insert and an attenuation factor based on N smaller inserts or waveguides, with one condition placed on the diameter of a single insert:

$$2a_L < \frac{\lambda}{10}. \quad (4)$$

This condition requires that the diameter of an individual insert be electrically small when compared to the wavelength of the electromagnetic wave incident upon the insert [8].

Two formulas are available to calculate $f_{c,insert}$ for the TE_{11} mode of propagation for the hexagonal insert. The first formula relies on the approximation of the hexagonal as shown in Fig. 1, and the application of equation (1). A second formula, not utilized in the prior work [5], was proposed by Ravelo and Mazari (2010). It applies to a waveguide whose cross-sectional area may be represented as an n^{th}-order polygon. This formula may be written as:

$$f_{c,insert}(\mathrm{n}) = \frac{\chi'_{11}}{4\pi b\sqrt{\mu\epsilon}}\left[1 + \sec\left(\frac{\pi}{\mathrm{n}}\right)\right], \quad (5)$$

with $n=6$ for a hexagonal insert [9]. Both equations (1) and (5) were used as part of MATLAB™ code generated to calculate $f_{c,insert}$ and the overall shielding effectiveness vs. frequency of the waveguide based on equation (3).

III. PHYSICAL WAVEGUIDE SAMPLES

Four samples consisting of commercially-available waveguides were procured. Relevant parameters for these samples are listed in Table 1. The first waveguide (Sample 1) contained no inserts and was utilized as a reference. The remaining three samples (Samples 2-4) each contained a honeycomb insert, with the dimensions of an individual insert varying from waveguide to waveguide.

All waveguide samples consisted of a main body with a nominal length of 101.6 mm, and a nominal inner diameter of 25.4 mm. Of the three waveguides containing a honeycomb insert, the dimension b of an individual insert (as shown in Fig. 1) varied; however, the length L_{insert} was fixed at 25.4 mm and centered within the respective waveguide.

Table 1: Calculated cutoff frequencies for air-filled circular and hexagonal inserts

Sample No.	Insert Opening $2b$ (mm)	b (mm)	a_L (mm)	$f_{c,insert}$ Eqn. (1) (GHz)	$f_{c,insert}$ Eqn. (5) (GHz)
1*	N/A	N/A	12.75*	6.922*	N/A*
2	6.350	3.175	2.75	31.972	29.830
3	4.764	2.382	2.06	42.629	39.773
4	3.176	1.588	1.37	63.944	59.660

*Sample No. 1 is an open, circular WG with an inner diameter of 25.4 mm.

The radius a of an open, circular waveguide insert was used to calculate the corresponding cutoff frequency f_c. The radius a_L (Fig. 1) of the inscribed circle in a honeycomb insert:

$$a_L = \frac{\sqrt{3}}{2} b, \tag{6}$$

was used to calculate $f_{c,insert}$ of a single honeycomb insert. Cutoff frequencies of a single, air-filled, honeycomb insert using equations (1) and (5) for each sample are shown in Table 1. Samples 1 and 2 were selected for both modeling in FEKO and shielding effectiveness measurements. Samples 3 and 4 were not tested, as the upper end of the frequency range of the available test equipment was limited to 40 GHz.

IV. CREATION OF WAVEGUIDE MODELS

A. Construction of the model

A model was constructed for each sample using Altair Hyperworks® CADFEKO in order to analyze the shielding effectiveness of each configuration. Variables were assigned in the model to represent the dimensions of the waveguide and insert [10]. Construction of the overall waveguide was a straightforward task; however, three steps were necessary to create the honeycomb insert.

The first step in creating the model was to construct a single hexagonal waveguide insert with insert length L_{insert} and the length of a single side b. Both values were set to be equivalent to those of the physical sample as provided by the waveguide manufacturer, with a maximum dimension of $2b$ for the cross-section of a single hexagonal waveguide. This is shown in

Fig. 2.

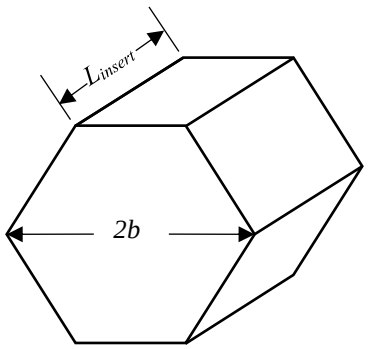

Fig. 2. Dimensions of a single hexagonal insert within the overall honeycomb insert.

The second step in creating the model was to duplicate the single hexagonal waveguide in order to construct the overall honeycomb insert waveguide (HCWG) model. By duplicating and using the *union* function in CADFEKO, the larger insert structure was constructed. This is shown in

Fig. 3 for an insert having thirty-seven (37) individual cells.

By using the variables L_{insert} and b when constructing a single insert as indicated in the previous paragraph, the overall size of the insert structure is automatically adjusted in CADFEKO.

The final step was to combing the HCWG insert model with the larger surrounding waveguide to form the overall model. Adjustment of the relevant dimensions of both the HCWG insert and the surrounding waveguide cylinder required cells of the HC insert falling outside the walls of the surrounding WG cylinder to be trimmed, with partial cells remaining within the interior of the larger WG. Using the dimensions supplied in Table 1, a model was constructed for Sample Number 2 as shown in Fig. 4.

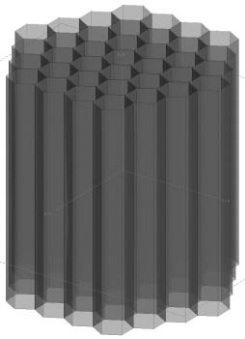

Fig. 3. Hexagonal insert with 37 cells.

The walls of both the main waveguide and the HC inserts were defined in CADFEKO as being constructed of perfect electric conductors (PEC). The medium within the waveguide was initially chosen to be air (ε_r, $\mu_r \approx 1$). By selecting different values for the dielectric constant or relative permittivity of the medium in the waveguide, the model may also be used to simulate a waveguide filled with liquid coolants, e.g., distilled water, ethylene glycol, etc.

B. Preparation for simulation

In the FEKO model, both ends of the waveguide were closed off and designated as waveguide ports. The port located at the -z end of the waveguide was designated as the excitation port (Port 1), and the port at the +z end of the waveguide as the load (Port 2). This is shown in the overall CADFEKO model used to simulate the waveguide with a honeycomb insert in Fig. 4.

Several advantages are realized by utilizing waveguide ports in FEKO. First, FEKO treats these ports by FEKO as being impedance-matched to the waveguide [11]. Second, the need to construct models for transmitting and receiving broadband antennas at either end of the waveguide is eliminated, along with the need to model

an intervening ground plane in which to mount the waveguide. Finally, this reduces the computational resources needed to perform the simulation by reducing the number of elements in the model. A simple solution request for S_{21} is all that is required for FEKO to calculate the shielding effectiveness of the waveguide model.

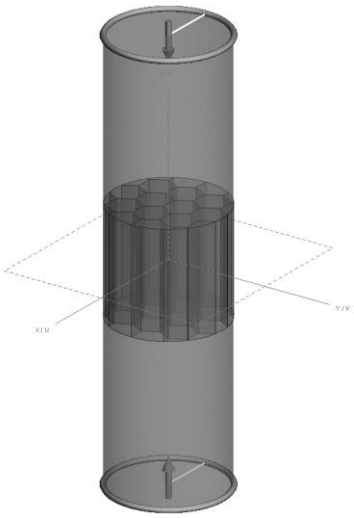

Fig. 4. Combined CADFEKO model for Sample Number 2 with $2b$ = 6.350 mm and L_{insert} = 25.4 mm.

Once the ports were defined, a mesh of the model was created in CADFEKO. This mesh subdivided the model into individual elements in order to use the Finite Element Method (FEM). A coarse mesh size was initially selected to reduce simulation time, resulting in the length of one side of an individual element to be one-sixth the wavelength at the highest simulation frequency, or λ/6 [11]. The selection of this coarse mesh size, however, comes at a cost of reduced accuracy in the calculations for the selected waveguide propagation mode.

Table 2: Mesh size and average edge length

Simulation Frequency Range (GHz)	Mesh Size	Number of Elements	Average Edge Length (mm)
1-18	Coarse	6420	2.276
18-21.5	Standard	32245	0.9811
21.5-28	Standard	43768	0.8424
28-34	Standard	65350	0.6889

A coarse mesh was sufficient for the open WG model (Sample No. 1), but feedback received from the FEKO solver during simulation of the HCWG model (Sample No. 2) resulted in the selection of the standard size mesh. The mesh size (e.g., length of an individual element's edge) also varied based on the maximum frequency for each simulation run. This is shown in Table 2 for both the open waveguide and HCWG models.

C. Simulation methods and calculations

The finite element method (FEM) was chosen to perform the simulation, with the Method of Moments (MoM) solution decoupled from the FEM solution in FEKO. This method is appropriate for complex structures when far-field simulation results (e.g., modeling of antenna patterns) are not required [11].

In the simulation, the ports of the cylindrical waveguide are the circular cross-sections at each end of the cylindrical waveguide. By designating one end of the cylindrical waveguide as the input or active port, FEKO treats the associated cross-section as the plane of excitation. The other end of the waveguide is then treated as an inactive or passive port [12].

The treatment of the ends of the waveguide as matched ports permitted the use of S-parameters to quantify the attenuation, or shielding effectiveness of the waveguide model. S_{21} is defined as the forward transmission coefficient through a network, i.e., the power exiting port 2 with respect to the power incident on port 1 [13]:

$$S_{21} = \frac{b_2}{a_1}\Big|_{a_2=0}. \quad (7)$$

Calculation of the S-parameters in FEKO for the various waveguide models corresponded well with the planned use of a network analyzer for laboratory measurements, as the network analyzer may be configured to present the results in this format.

The configuration-specific request in FEKO to perform this S-parameter analysis used the dominant TE_{11} mode for both the input and output ports. The input port was selected to be the active port, with application of the dominant TE_{11} mode as the source excitation.

To simplify comparison of the results from the simulation with the analytical and measured shielding effectiveness of the waveguide, a common set of frequencies was chosen. These are shown in Table 3.

Table 3: Frequency information analysis, simulation, and measurement

Frequency Range (GHz)	Number of Points	Frequency Step Size (MHz)
1 to 5	17	250
5 to 7	81	25
7 to 18	45	250
18 to 28	41	250
28 to 34	61	100

V. WAVEGUIDE SHIELDING EFFECTIVENESS MEASUREMENTS

Following the methodology of McInerney [1], a test setup was created to measure the shielding effectiveness of the HCWG. The setup utilized a shielded enclosure, a network analyzer, two (2) sets of matched broadband antennas, and coaxial cables appropriate for the frequency range of interest.

Measurements were performed in four (4) configurations:

a) Antenna to antenna coupling at 2 m distance.
b) Coupling through 25.4 mm (1 in.) circular aperture, 1 m distance to aperture.
c) Coupling through 25.4 mm (1 in.) inner diameter open WG, 1 m distance to waveguide opening.
d) Coupling through 25.4 mm I.D. waveguide with N = 14 openings HCWG insert, b = 3.175 mm, 1 m distance to waveguide opening.

A general illustration of each of these configurations is shown in Fig. 5. In each case the boresight of the transmitting antenna was visually aligned with that of the receiving antenna, aperture, and/or waveguide opening.

Each configuration was chosen to serve a specific purpose. Configuration a) was utilized to determine the free-space loss between the transmitting and receiving antennas. Configuration b) was used to characterize the coupling loss associated with the transfer of energy from the incident wave to the waveguide as a first-order approximation.

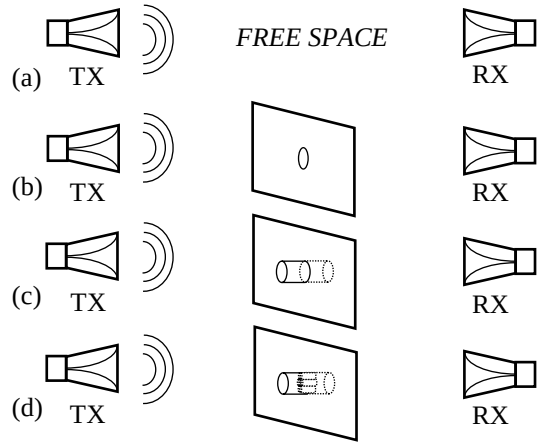

Fig. 5. Test setups for measuring shielding effectiveness of the various configurations.

Configurations c) and d) measured the shielding loss of the entire signal chain, i.e., antenna to waveguide to antenna. The transmit antenna was located external to the shielded enclosure for configurations b)-d); this was intended to prevent reception of unintended signals from the external electromagnetic environment at frequencies below f_c. Cable loss and the preamplifier used for 18 GHz to 34 GHz was characterized over each frequency range of interest. The network analyzer was verified to be within calibration, and configured to perform a sweep using the frequencies indicated in Table 3. A measurement bandwidth of 1 Hz was used when measuring S_{21} to ensure the highest possible dynamic range in accordance with the manufacturer's datasheet for the network analyzer [14].

A. Definition of various factors which contribute to the overall measurement

The measurement of S_{21} with the waveguide installed may be represented by the following equation:

$$S_{21} = G_T + PL + CP_{WG} + SE_{WG} + D_{WG} + PA + G_R + CL. \quad (8)$$

The individual factors are:

G_T Gain of the transmitting antenna,
PA Preamplifier gain,
PL Free space path loss using Friis equation.
CP_{WG} Losses associated with the coupling of the incident electromagnetic field to the waveguide opening,
SE_{WG} Shielding effectiveness of the waveguide,
D_{WG} Directivity of the waveguide opening,
G_R Gain of the receiving antenna,
CL Cable losses associated with the test setup.

Prior to starting the measurement series, values for the cable losses CL and preamplifier gain PA are measured using the same network analyzer, and saved for future use in subsequent calculations.

B. Use of the various configurations to determine the contribution(s) of each individual factor

Configuration a) was used to measure the free space path loss PL between the antennas; this is shown in Fig. 5 (a). This measurement was performed in a semi-anechoic chamber of dimensions 4.88 m x 6.10 m x 3.05 m. Photos of the setup are shown in Fig. 6 for the frequency range of 1 GHz to 18 GHz, and Fig. 7 for the frequency range of 18 GHz to 40 GHz.

The distance between the antennas was 2 m. This corresponds to twice the distance between the antenna and the opening of the waveguide.

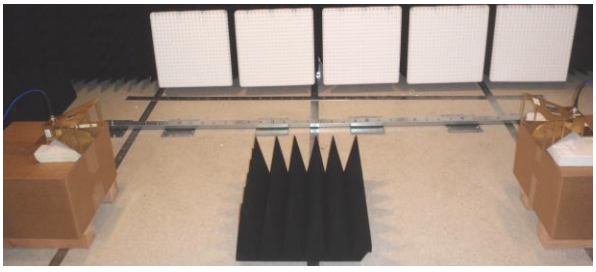

Fig. 6. Test setup for measuring free space loss 1 GHz to 18 GHz (A.H. Systems, Inc. SAS-571 antennas).

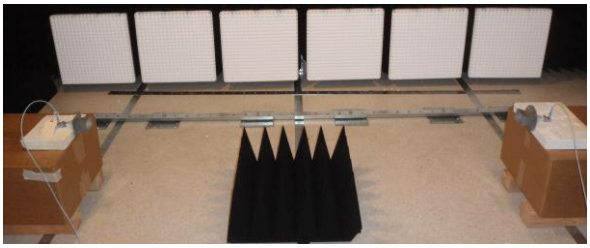

Fig. 7. Test setup for measuring free space loss 18 GHz to 40 GHz (AH-840 Com-Power antennas).

The square patch of absorber located at the center was determined through experimentation to reduce reflections from the ground plane and reduce the variability of the measurement. Measured values for *PL* are calculated using equation (8), with CP_{WG}, SE_{WG}, and G_{WG} set equal to zero, and applying the antenna gains G_T and G_R from calibration.

The measured values for path loss were compared with the theoretical value using the Friis transmission equation with D = 2 m:

$$PL = 20\log_{10}\left(\frac{\lambda}{4\pi D}\right). \quad (9)$$

Configuration b) was used to measure the combined contribution of CP_{WG} and D_{WG} to the measurement. This measurement was performed using the same semi-anechoic chamber; however, the transmit antenna was placed outside the chamber, and the receive antenna was located inside the chamber. The aperture was cut into a bulkhead panel, with the aperture having the same diameter as the inner diameter of the waveguide. The transmit antenna was placed outside the chamber at a distance of 1 m (39.37 in.) from the panel, with the boresight focused on the opening. The receive antenna was placed inside the chamber at the same distance from the panel, with the boresight similarly focused on the opening in the panel. The setup of the transmit antenna external to the semi-anechoic chamber is shown in Fig. 8.

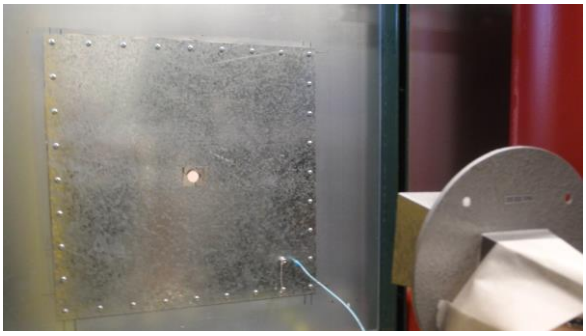

Fig. 8. Transmit antenna position (external to the chamber) for measuring coupling of the electromagnetic wave through the opening, 18 GHz to 40 GHz.

This measurement arrangement provided a combined value for the loss associated with the coupling of the incident electromagnetic wave to the aperture CP_{WG}, and the directivity associated with the wave passing through the aperture D_{WG} while minimizing the attenuation of the wave as it passes through the aperture.

Configuration c) utilized waveguide Sample No. 1 described in Table 1. This waveguide was mounted in the panel opening as shown in Fig. 9.

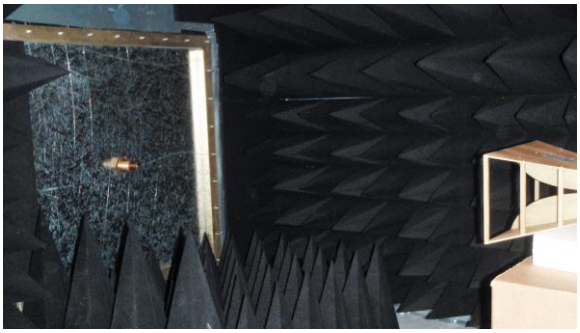

Fig. 9. Receive antenna position (inside the chamber) for measuring coupling of the electromagnetic wave through the opening, 1 GHz to 18 GHz.

Configuration d) used the same setup as shown in Fig. 9, except the open waveguide was replaced with a waveguide sample containing a honeycomb insert.

VI. COMPARISON OF ANALYTIC, SIMULATION, AND MEASURED HCWG SHIELDING EFFECTIVENESS

Shielding effectiveness (SE) measurements were performed on an open waveguide and on a waveguide consisting of N = 14 HCWG inserts with a dimension $2b$ = 6.35 mm as shown in Fig. 2. These are listed as Sample No. 1 and Sample No. 2 in Table 1, respectively.

The frequency range of the measurements was selected based on the cutoff frequency of the respective waveguide sample. The shielding effectiveness of Sample No. 1 was measured over the frequency range of 1 GHz to 18 GHz, and the shielding effectiveness of Sample No. 2 was measured over the frequency range of 18 GHz to 34 GHz. Both samples were air-filled, i.e., ε_r, $\mu_r \approx 1$.

In comparing the results obtained by measurement and simulation, it should be noted the prediction *a priori* of a theoretical level of agreement between simulation and measurement requires determination of the coupling mechanism between the incident TEM wave and the opening of the waveguide, with the required analyses beyond the scope of this paper. The application of the measurement method presented in Section V is intended to facilitate the calculation of the shielding effectiveness of the waveguide from the measurement results, through

the empirical determination of the coupling loss associated with the transfer of energy from the incident electromagnetic wave to the entrance of the waveguide, and the diffraction of the wave exiting the waveguide at the opposite end.

A. Comparison of analytic and simulation results with SE measurements for the open waveguide model

The shielding effectiveness of the open waveguide was measured over the frequency range of 1-18 GHz using the configuration of Fig. 5 (c). Equation (2) was used to predict the shielding effectiveness of the open waveguide, with equation (1) used to calculate the cutoff frequency f_c. A comparison of the measured results to the predicted values of the open waveguide and values obtained by simulation using FEKO indicated a difference in shielding effectiveness below the predicted cutoff frequency. This is shown in Fig. 10.

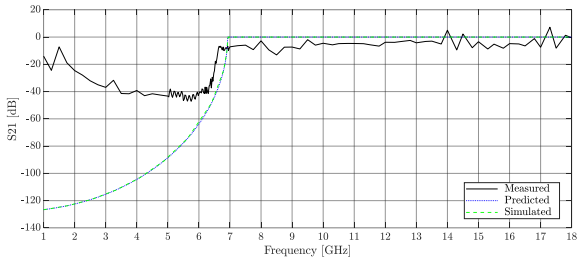

Fig. 10. Comparison of measurement results with predicted and simulated shielding effectiveness values for an open waveguide model with radius a = 12.7 mm, 1 GHz to 18 GHz.

The difference in shielding effectiveness below the cutoff frequency of the waveguide was determined to be the result of two factors when extracting the contribution of the open waveguide's shielding effectiveness from the overall measurement. The primary factor is the values of S_{21} for frequencies lower than 6.28 GHz are below the threshold value of -115 dBm necessary for the network analyzer to accurately measure the magnitude of S_{21}. This threshold value was calculated from the applied source power of +10 dBm and the typical dynamic range of 125 dB as specified by the manufacturer [14]. The secondary factor is the measurement uncertainty of S_{21} increases as the magnitude of S_{21} decreases. The values for S_{21} between 6.28 GHz and 6.6 GHz are lower than -90 dB, the value at which the manufacturer no longer provides typical values for the measurement uncertainty. Above 6.6 GHz the measured values for S_{21} were in the range of -80 dB to -90 dB and considered to be reliable.

The shift in cutoff frequency between the predicted and measured shielding effectiveness values was determined to be related to the radius of the sample open waveguide. Measurements of the diameter of the open waveguide showed the radius to be a = 13.49 mm (1-1/16 in.), resulting in a revised calculated value of f_c = 6.517 GHz for the open waveguide.

B. Comparison of analytic and simulation results with SE measurements for the b = 3.175 mm HCWG model

Calculation of $f_{c,insert}$ for a single b = 3.175 mm HCWG insert using equations (1) and (5) initially relied on the nominal dimensions ($2b$ = 0.25 inch) provided in the waveguide manufacturer's literature. These values are listed in Table 1. Equation (3) was then used to predict the shielding effectiveness over the frequency range of 18-34 GHz of a waveguide having a HCWG insert structure compromised of N = 14 individual honeycomb inserts.

Measurement of Sample No. 2 using the configuration of Fig. 5 (d), however, revealed the cutoff frequency of the sample was significantly lower than the predicted value using equation (3) for both the circular and hexagonal calculations. A comparison of the measured results and predicted shielding effectiveness values is shown in Fig. 11.

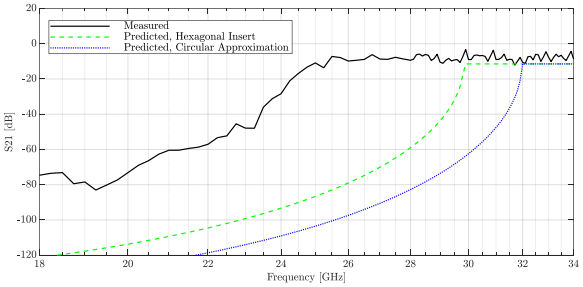

Fig. 11. Comparison of measurement results with predicted shielding effectiveness values for b = 3.175 mm, 18 GHz to 34 GHz.

After thoroughly checking the test setup for errors, closer inspection of the HCWG revealed the hexagonal inserts did not exactly match the manufacturer's specified dimension. The cross-sectional area was also observed to be asymmetric, i.e., measurement of a sample of three (3) individual hexagonal cross-sections produced different results for each cross-section. The circular approximation was discarded, and equation (5) applied for calculation of the predicted values of $f_{c,insert}$.

The cutoff frequency of a single insert in the sample was estimated from the data to be approximately 25 GHz. Using equation (5) with a value of $f_{c,insert}$ = 25 GHz, a predicted value of b=3.788 mm was obtained. The average value for measurements of three (3) individual HC inserts in Sample No. 2 was b=3.737 mm. The corresponding cutoff frequency for an individual insert in Sample No. 2 was then calculated using equation (5) to be $f_{c,insert}$ = 25.347 GHz. Figure 12 shows the

comparison of the measured results for Sample No. 2 with the revised values for the predicted shielding effectiveness of the waveguide using equation (3) with N = 14, and equation (5) for the cutoff frequency of a single HCWG insert.

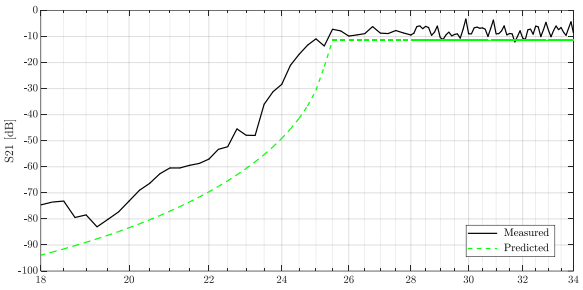

Fig. 12. Comparison of measurement results with the revised predicted shielding values for b = 3.737 mm, 18 GHz to 34 GHz.

Based on this new information, the HCWG model with N = 14 inserts used in the FEKO simulation was modified to be consistent with the actual, and not the published dimensions of Sample No. 2. The FEKO simulation was repeated, and the results were compared with the predicted and measured shielding effectiveness values over the frequency range 18 GHz to 28 GHz. This comparison is shown in Fig. 13.

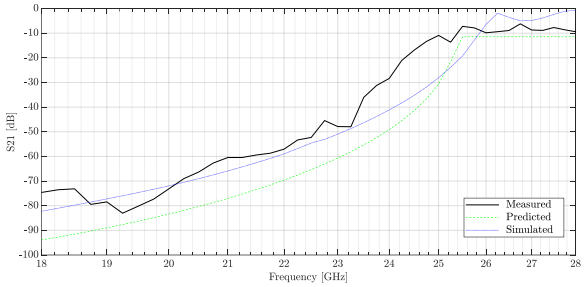

Fig. 13. Comparison of measurement results with predicted and simulated shielding effectiveness values for b = 3.737 mm, 18 GHz to 28 GHz.

C. Discussion of results

The predicted shielding effectiveness of an open waveguide based on equation (2) was consistent with the values obtained through both simulation and measurement when the cumulative effect of losses associated with the measurement setup were considered. Analysis of the measurement data below 6 GHz indicated the values of the cable loss, free-space loss, and coupling losses between the incident wave and waveguide opening, when combined with the predicted shielding effectiveness of the waveguide, were below the nominal dynamic range of the network analyzer, in this case 125 dB [14].

The predicted shielding effectiveness of the waveguide containing a HCWG insert based on equation (3) was within the uncertainty of the measurement above the cutoff frequency of a single HCWG insert. The average value of the measured shielding effectiveness above $f_{c,insert}$ = 25.347 GHz was $\bar{x}$ = -8.16 dB with the sample standard deviation of $\sigma_{\bar{x}}$ = ±1.91 dB. Treating $\sigma_{\bar{x}}$ as a standard uncertainty, application of a coverage factor of k = 2 for a 95% confidence level indicated the variability in the results was consistent with the published uncertainty of ±4 dB from 20 GHz to 40 GHz for the selected network analyzer when performing a S_{21} magnitude measurement [14, 15]. Below this cutoff frequency, equation (3) predicted values for shielding effectiveness higher than those obtained by both measurement and simulation.

VII. CONCLUSIONS

Software modeling and laboratory measurements of waveguide samples with HCWG inserts has assisted in improvement of the original model. The first-order approximation of a single HCWG insert as a circle leads to results for the cutoff frequency of a single insert that exceed the values calculated using the analytical formula presented by Ravelo and Mazari (2010). The contribution to the shielding effectiveness of the waveguide, resulting from the division of the larger waveguide into numerous smaller apertures by installation of the HCWG insert, was lower than that predicted by Kaiser (2006); however, the difference between the predicted value and the average measured value was within the stated measurement uncertainty of the selected network analyzer at frequencies above the cutoff frequency of the insert. Planned future work includes investigation of the difference between measurement and simulation results, and application of the model to liquid-filled waveguides.

REFERENCES

[1] M. K. McInerney, S. Ray, R. McCormack, S. Castillo, and R. Mittra, "The effect of fluids on waveguides below cutoff penetrations as related to electromagnetic shielding effectiveness," Champaign, 1984.

[2] F. Choubani, J. David, and N. E. Mastorakis, "Experiment on the shielding by hollow conducting tubes," *IEEE Transactions on Electromagnetic Compatibility*, vol. 48, no. 2, pp. 342-347, May 2006.

[3] G. G. Medveczky and T. Dickten, "High quality shielding with predictable and verifiable effectiveness," *IEEE*, pp. 565-570, 1999.

[4] L. H. Hemming, "Applying the waveguide below cut-off principle to shielded enclosure design," in *IEEE International Symposium on Electromagnetic Compatibility*, Anaheim, 1992.

[5] S. W. Faust, "An improved waveguide model to support analysis of electromagnetic shielding for liquid cooled power electronics," in *Proceedings of the 2016 Ground Vehicle Systems Engineering and Technology Symposium (GVSETS)*, Novi, 2016.

[6] C. A. Balanis, Advanced Engineering Electromagnetics. Hoboken, NJ: John Wiley & Sons, 2012.

[7] K. L. Kaiser, Electromagnetic Shielding. Boca Raton: CRC Press, 2006.

[8] C. R. Paul, Introduction to Electromagnetic Compatibility. K. Chang, Ed., New York: John Wiley & Sons, 1992.

[9] B. M. B. Ravelo, "Characterization of the regular polygonal waveguide for the RF EM shielding application," *Progress in Electromagnetics Research*, vol. 12, no. M, pp. 95-105, 2010.

[10] Altair Engineering, Inc., *Hyperworks 14.0 Release FEKO*, Troy, Michigan: Altair Engineering, Inc., 2016.

[11] Altair, FEKO Training Class (Suite 7.0) Course Notes, Troy, Michigan: Altair, 2015.

[12] Altair, User Manual for FEKO 14.0, Troy, Michigan: Altair, 2015.

[13] Agilent Technologies, *Agilent AN 154 S-Parameter Design Application Note*, United States: Agilent Technologies, 2000.

[14] Rohde & Schwarz, "www.rohde-schwarz.com," 22 March 2017. [Online]. Available: https://cdn.rohde-schwarz.com/pws/dl_downloads/dl_common_library/dl_brochures_and_datasheets/pdf_1/service_support_30/ZNB_dat-sw_en_5214-5384-22_v0900_96dp.pdf. [Accessed 8 December 2017].

[15] United Kingdom Accreditation Service, *The Expression of Uncertainty in EMC Testing*. 1 ed., Feltham, Middlesex: UKAS, 2002.

Scott W. Faust is an Electrical Engineer with the Vehicle Electronics and Architecture (VEA) group at the U.S. Army Tank Automotive Research, Development and Engineering Center (TARDEC) in Warren, Michigan, USA. He received the B.S. degree in Electrical Engineering from the Rose- Institute of Technology, USA, in 1990, and the M.S. degree Hulman in Electrical and Computer Engineering from Oakland University, USA, in 1994. Mr. Faust is presently a Ph.D. Candidate in the School of Engineering and Computer Science (SECS) at Oakland University. In addition, Mr. Faust is a Part-Time Faculty/ Lecturer at Oakland University, where he teaches a graduate course in electromagnetic engineering. Mr. Faust is certified by the International Association for Radio, Telecommunications, and Electromagnetics (iNARTE) as an Electromagnetic Compatibility Engineer.

Daniel N. Aloi is a Professor and Department Chair in the Electrical and Computer Engineering Department, and the Founding Director of the Applied Electromagnetics and Wireless Lab at Oakland University in Rochester, Michigan, USA. He received his B.S., M.S. and Ph.D. degrees in Electrical Engineering from Ohio University in 1992, 1996 and 1999, respectively. He has been employed at Oakland University since January 2002. Aloi was a Sr. Project Engineer at OnStar, Inc. (2000-2001) and a Visiting Assistant Professor at Ohio University (1999-2000). His research areas include applied electromagnetics and various areas of the global positioning system (GPS) in the automotive and aviation industries. He has authored over 90 papers and six patents.

Voltage Parameter Identification of AC Overhead Transmission Lines by Using Measured Electric Field Data

Dongping Xiao, Qi Zheng, Yutong Xie, Qichao Ma, and Zhanlong Zhang

State Key Laboratory of Power Transmission Equipment & System Security and New Technology
Chongqing University, Chongqing, 400044, China
xiaodongping@cqu.edu.cn, 20161113031t@cqu.edu.cn, 20151102059t@cqu.edu.cn, 20151113002t@cqu.edu.cn, zhangzl@cqu.edu.cn

Abstract ─ With the development of smart power grids, the demand for real-time voltage monitoring along overhead transmission lines (OTLs) has been growing. However, the existing voltage measurement of OTLs by using potential transformers involves formidable difficulties. This study proposes a non-contact measurement method in which the voltages on AC OTLs are inversely calculated on the basis of the measured data of the power frequency electric field under OTLs. To improve the accuracy and stability of the inverse calculation, an accurate mathematical model and modified inverse algorithms are investigated and then a set of feasible approaches are proposed. First, considering an overhead conductor's actual physical form and the meteorological conditions of its operating environment, a 3-D catenary model is built, and the mathematical relations between 3-D electric fields and the voltages on OTLs are identified. Second, the improved particle swarm algorithm is used to search the optimal measurement positions of the electric field to improve the ill-posedness of inverse problems. Third, the iterative Tikhonov regularization method, in which the number of iterations is considered as the variable, is adopted to further improve the ill-posedness of inverse problems and reduce the susceptibility of regular solutions to regularization parameter α. Fourth, root mean square values and phase parameters of AC voltages are identified from the sinusoidal fitting curves obtained by the real-time inverse calculation. Results of the simulation and experiment examples show that inverse solutions of high precision can be obtained under the condition with relatively high errors of electric field measurement. Moreover, the advantages of the proposed inversion method, such as fast computing speed and good stability, are demonstrated.

Index Terms ─ 3-D model, AC overhead transmission lines, electric field, inversion, iterative Tikhonov regularization, parameter identification, position optimization, voltage.

I. INTRODUCTION

Root mean square (RMS) values and voltage phase of AC overhead transmission lines (OTLs) reflect the operating status and health level of power grids. The conventional method of measuring voltages on OTLs is to use the potential transformers that are installed in substations. With the development of smart power grids, the demand for real-time voltage monitoring along OTLs has become increasingly apparent. However, installing a large number of potential transformers along operating OTLs is not feasible because of certain formidable difficulties, such as the requirement for power-off installation and the increasing probability of ferro-resonance and insulation fault [1-2]. Given such bottleneck, studying new voltage measurement methods is necessary.

Numerous studies on the electromagnetic environment of high-voltage OTLs reveal that the power-frequency electric field around OTLs is significantly correlated with the power-frequency voltages on OTLs [3-5]. On the basis of this correlation, we propose the idea of inversely calculating voltages by using the measured data of the electric field. This non-contact voltage measurement has prominent advantages in safety and operation flexibility. The main challenge in applying this method to engineering is the improvement of the accuracy and stabilization of the inverse calculation. Calculation accuracy is influenced by the precision of electric field measurement on site and the precision of the mathematical model and inversion algorithm. This study focuses on the latter.

In most studies, 2-D models that ignore the sag and span of OTLs and other factors have been used to assess the electric field around OTLs [4-6]. However, these 2-D models are too rough to solve the proposed inverse problem. Certain studies have built a 3-D simulation model but only with consideration of equally high suspension case and a limited length of OTLs [7-8]. In the present study, considering the actual meteorological and orographic environment and the physical form of

Submitted On: January 28, 2018
Accepted On: June 17, 2018

OTLs, the 3-D model of OTLs is built, and then the mathematical relations between the 3-D electric fields and voltages are proposed.

The calculation of voltages on AC OTLs based on measured electric field data is an electromagnetic inverse problem, which has serious ill-posedness. Many studies have been devoted to dealing with the ill-posed problem [9-13], in which Tikhonov regularization has been widely used. The error between the solution of Tikhonov regularization and the true value strongly depends on the value of regularization parameter α, and minor differences in α may lead to distinctly different inverse solutions. For the selection strategy of α, priori estimate and posterior estimate are available [14-17]. Priori estimate requires some priori information of the true value, but obtaining it in practical engineering applications is difficult. By contrast, posterior estimate is based on measured data and error level. From posterior estimate, several specific methods have been developed, and they include the Morozov's discrepancy principle, generalized cross inspection criteria, and L-curve criterion. However, the process of α-selection based on the methods mentioned above is tedious, and the reselection of α is required when the measurement error level changes. After analyzing the causes of ill-posedness in the special inverse problem, this study proposes a series of approaches that search the optimal positions of electric field measuring points to reduce the condition number of the observation matrix. Then, iterative Tikhonov regularization is processed to obtain inverse solutions point by point in the time domain.

II. MATHEMATICAL MODEL AND OPTIMIZATION METHOD

A. 3-D model of OTLs' voltage and electric field

Given the self-heavy, wind and ice load on OTLs and other factors, an OTL suspended between two towers is in the shape of catenary. For universal situations, a suspended OTL of unequal height (Fig. 1) is considered. In Fig. 1, the coordinate origin is set at the ground projection of the left suspension point.

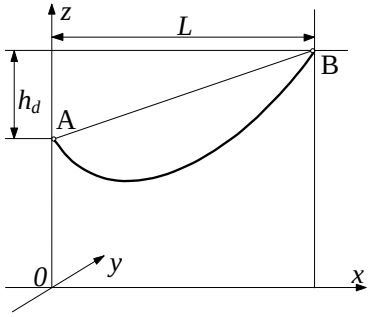

Fig. 1. Structural diagram of suspended OTL of unequal height.

The catenary can be described by Equation (1) [18]:

$$z(x)=\frac{h_d}{a\sinh(L/a)}\left[a\sinh\left(\frac{x}{a}\right)\sinh\left(\frac{L-x}{a}\right)\right]-\sqrt{1+\left(\frac{h_d}{a\sinh(L/a)}\right)^2}, \quad (1)$$

where $a=2\sigma_0/\gamma$ is defined as the sag coefficient in which σ_0 is the horizontal stress of the conductor and γ is the conductor load, h_d is the height difference between the two suspension points, and L is the line span.

When $h_d = 0$, OTLs are suspended at equal heights, and the corresponding catenary equation can be simplified to the following:

$$z(x)=-a\sinh(x/a)\sinh\left[(L-x)/a\right] \quad (0\le x\le L). \quad (2)$$

Parameters σ_0 and γ depend on the mechanical and physical characteristic of OTL, length of span, and weather conditions [19-20]. They can be calculated on the basis of given operating conditions. The introduction of these parameters helps improve the accuracy of the electric field calculation. Considering that phase conductors of the same type in the same span have a uniform catenary form is reasonable.

One phase of high-voltage OTLs usually contains a bundle of sub-conductors. When the radius of a circle, along which the bundled sub-conductors are arranged, is smaller than the distance between the conductors and observation point, such bundle can be equivalent to one conductor.

Power frequency electric field can be regarded as quasi-static electric field. The electric field generated by AC OTLs is usually calculated with the Charge Simulation Method [21-23], in which the effect of the conducting ground is equivalent to that of mirror image conductors. Suppose that the n^{th} phase conductor is l_n and that its mirror image is l'_n. Their equivalent charge densities are $+\tau_n$ and $-\tau_n$. The potential at the spatial observation point C (x_m, y_m, z_m) is given by the following:

$$U_{nm}=\frac{1}{4\pi\varepsilon_0}\left[\int_{l_n}\left(\frac{1}{R_{nm}}-\frac{1}{R'_{nm}}\right)\tau_n dl_n\right], \quad (3)$$

where ε_0 is the dielectric constant of air and R_{nm} and R'_{nm} are the distances from the n^{th} phase conductor and its mirror image to the observation point C, respectively:

$$\boldsymbol{R}_{nm}=(x_m-x_n)\boldsymbol{e}_x+(y_m-y_n)\boldsymbol{e}_y+(z_m-z_n)\boldsymbol{e}_z,$$

$$\boldsymbol{R}'_{nm}=(x_m-x_n)\boldsymbol{e}_x+(y_m-y_n)\boldsymbol{e}_y+(z_m+z_n)\boldsymbol{e}_z,$$

$$R_{nm}=|\boldsymbol{R}_{nm}|,\quad R'_{nm}=|\boldsymbol{R}'_{nm}|.$$

The spatial structure for the calculation is shown in Fig. 2.

Equations (1) or (2) are substituted into (3) and the integral variable is converted into x_n. The discretization and numerical integration are carried out by using the Method of Moment. With the synthetical consideration of computational complexity and accuracy, the (2K+1)

continuous spans of OTLs near point *C* are intercepted to calculate the potential.

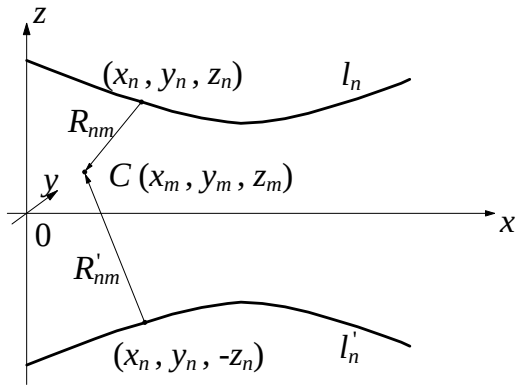

Fig. 2. Diagram of the spatial structure for calculation.

Point *C* is named as the match point if it is set on the surface of the phase conductor. The potential at point *C* is generated by the total *N* phases of OTLs. Then, the mathematical relationship between the known surface potential and the simulated charge density is expressed in matrix form as:

$$\boldsymbol{U} = \boldsymbol{P}\boldsymbol{\tau}, \tag{4}$$

where $\boldsymbol{P}$ is an *N*-dimensional square matrix and the elements in $\boldsymbol{P}$ can be calculated by numerical integration according to Equation (3).

Then, the 3-D electric field components at point *C* are calculated by the following:

$$\begin{aligned}\boldsymbol{E}_m(x,y,z) &= \frac{1}{4\pi\varepsilon_0}\sum_{n=1}^{N}\left[\int_{l_n}\left(\frac{\boldsymbol{R}_{nm}}{R_{nm}^3}-\frac{\boldsymbol{R}'_{nm}}{R'^3_{nm}}\right)\tau_n dl_n\right] \\ &= E_{mx}\boldsymbol{e}_x + E_{my}\boldsymbol{e}_y + E_{mz}\boldsymbol{e}_z.\end{aligned} \tag{5}$$

By setting *M* measuring points, the matrix equation can be written as follows:

$$\boldsymbol{E} = \boldsymbol{G}\boldsymbol{\tau}. \tag{6}$$

According to Equations (4) and (6), the mathematical relationship between the surface potential of OTLs and the electric fields at the measuring points is given by the following:

$$\boldsymbol{E} = \boldsymbol{G}\boldsymbol{P}^{-1}\boldsymbol{U} = \boldsymbol{K}\boldsymbol{U}, \tag{7}$$

where $\boldsymbol{K}$ is defined as the observation matrix.

Errors and noises inevitably exist in actual measurements. Only E^{δ} ($\|E - E^{\delta}\| < \delta$) can be obtained. If the positions of the measuring points are selected randomly, the condition number of matrix $\boldsymbol{K}$ (i.e., cond($\boldsymbol{K}$)) may be large. Consequently, a small noise in $\boldsymbol{E}$ may cause the inverse solution U^{δ} to severely deviate from the true value $\boldsymbol{U}$.

B. Position optimization algorithm in 3-D space

Section II.A shows that the observation matrix $\boldsymbol{K}$ is determined by the structure of OTLs and the positions of electric field measuring points. When the structure of OTLs is fixed, reducing cond($\boldsymbol{K}$) by optimizing the positions of measuring points is convenient and feasible. It can reduce the susceptibility of inverse calculation to measurement noise [24].

In this study, the particle swarm optimization algorithm is adopted to search the optimal measuring positions. The fitness function of the algorithm is set as follows:

$$\text{FitFun} = \text{cond}(\boldsymbol{K}). \tag{8}$$

In the iteration process of searching the optimal solution, values of the fitness function of each particle are calculated and compared. Moreover, the historical optimal position of each individual particle $\boldsymbol{X}_{Hbest}$, $\boldsymbol{Y}_{Hbest}$, $\boldsymbol{Z}_{Hbest}$ and the global historical optimal positions of the particle swarm $\boldsymbol{X}_{Gbest}$, $\boldsymbol{Y}_{Gbest}$, $\boldsymbol{Z}_{Gbest}$ are dynamically updated, thereby guiding a convergence to the global optimal position. The velocities and positions of particles in the $(i+1)^{\text{th}}$ generation of particle swarm on the *x*-axis are determined by the following [25]:

$$\begin{aligned}\boldsymbol{V}_x^{i+1} &= \omega\boldsymbol{V}_x^{i} + c_1 r_{x1}^{i+1}(\boldsymbol{X}_{Hbest} - \boldsymbol{X}^{i}) \\ &\quad + c_2 r_{x2}^{i+1}(\boldsymbol{X}_{Gbest} - \boldsymbol{X}^{i}),\end{aligned} \tag{9a}$$

$$\boldsymbol{X}^{i+1} = \boldsymbol{X}^{i} + \boldsymbol{V}_x^{i+1}, \tag{9b}$$

where ω is the inertia weight, c_1 and c_2 are two learning factors, and r_{x1}^{i+1} and r_{x2}^{i+1} are two random numbers with values ranging from 0 to 1, respectively.

The iteration processes of particle swarm on the *y*- and *z*-axis are similar to Equations (9a) and (9b).

The iterative process stops when it reaches the predetermined maximum iteration number or the predetermined fitness function threshold. Consequently, the global optimal fitness function value G_{best} and the corresponding optimal position $\boldsymbol{X}_{Gbest}$, $\boldsymbol{Y}_{Gbest}$, $\boldsymbol{Z}_{Gbest}$ are the outputs.

C. Iterative Tikhonov regularization method

The conventional Tikhonov regularization method turns the inverse calculation problem into a minimization problem [26]:

$$\begin{cases}\min \boldsymbol{J}_{\alpha}(\boldsymbol{U}) \\ \boldsymbol{J}_{\alpha}(\boldsymbol{U}) = \| \boldsymbol{K}\boldsymbol{U} - \boldsymbol{E}^{\delta} \|^2 + \alpha \| \boldsymbol{U} \|^2\end{cases}, \tag{10}$$

where α is the regularization parameter.

The approximate regularization solution can be obtained using the following expression:

$$\boldsymbol{U}_{\alpha}^{\delta} = (\alpha\boldsymbol{I} + \boldsymbol{K}^{*}\boldsymbol{K})^{-1}\boldsymbol{K}^{*}\boldsymbol{E}^{\delta}. \tag{11}$$

An iterative Tikhonov regularization method is proposed to achieve a high convergence order [27],

$$\begin{cases}\boldsymbol{U}_{\alpha}^{0,\delta} = 0 \\ \boldsymbol{U}_{\alpha}^{i,\delta} = \alpha(\alpha\boldsymbol{I} + \boldsymbol{K}^{*}\boldsymbol{K})^{-1}\boldsymbol{U}_{\alpha}^{i-1,\delta} \\ \qquad + (\alpha\boldsymbol{I} + \boldsymbol{K}^{*}\boldsymbol{K})^{-1}\boldsymbol{K}^{*}\boldsymbol{E}^{\delta} \qquad i = 1, 2, \cdots\end{cases}, \tag{12}$$

where *i* is the iterative order number. When *i*=1, the conventional Tikhonov regularization is similar to

Equation (11).

The iterative Tikhonov regularization method can be implemented in two ways. One way is to select a fixed i ($i \geq 1$), and perform the iterative calculation to achieve the optimization of $\alpha(\delta)$. Several studies have adopted this approach and developed certain selection criteria of $\alpha(\delta)$. However, the selection procedure of $\alpha(\delta)$ is cumbersome, and $\alpha(\delta)$ greatly influences inverse solutions. Once a slight change occurs in the analytical conditions, $\alpha(\delta)$ must be reselected. Another way is to select a fixed α ($\alpha \geq 0$) that is determined by priori estimation and then perform the iterative calculation with the uncertain parameter i. The regularization solution can be obtained conveniently and quickly by reasonably setting the iterative termination conditions. Thus, the second approach is adopted.

The theorem in [27] is used to select α and set the iterative termination conditions. Suppose that $i(\delta)$ is the smallest integer that meets the iterative termination condition,

$$\| \boldsymbol{K}\boldsymbol{U}_{\alpha}^{i,\delta} - \boldsymbol{E}^{\delta} \| \leq \tau\delta \ (\tau > 1). \tag{13}$$

A constant α_0 exists to make $i \geq r + 1/2$ when $\alpha \geq \alpha_0$:

$$\alpha_0 = \frac{(2r+1)\| \boldsymbol{K} \|^2}{1 - \dfrac{(r+1)^2\delta^2}{\| \boldsymbol{E} \|^2}} - \| \boldsymbol{K} \|^2 . \tag{14}$$

D. Characteristic parameter determination of sinusoidal voltage

The characteristic parameters of the power frequency voltage are the RMS and phase. One approach is to use the phasors of electric field components to inversely calculate the phasors of voltages. This calculation process is simple, but the accuracy is not up to expectation. Another procedure is proposed in this study. The multi-point synchronous real-time electric field measurement is carried out by our self-made device. Then, the voltage value can be calculated point by point in the time domain according to the mathematical models and the optimization method described above. The characteristic parameters of sinusoidal voltages can be determined by the sinusoidal function fitting. This method has good anti-interference ability and self-tuning function, and thus, it can improve the calculation accuracy.

III. NUMERICAL EXAMPLE AND ANALYSIS

A. Structure of OTLs and analysis condition

The selected simulation example involves 220 kV single-circuit OTLs. The phase conductor is 2×LGJ-400/35, and the length of the span is 300 m. Two suspension cases are shown in Figs. 3 (a) and 3 (b). Figure 3 (c) shows the layout of the phase conductors on each tower in Case I and on the left-side tower in Case II. Figure 3 (d) shows the layout of the phase conductors on the right-side tower in Case II.

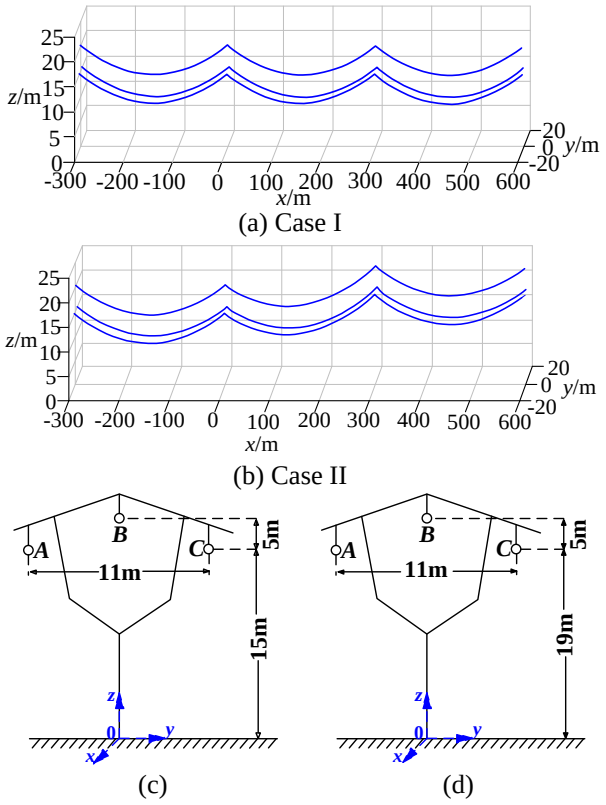

Fig. 3. Structure diagram of transmission line conductors.

Other analysis conditions are set as follows.

1) Three-phase symmetrical voltages of OTLs are:

$$\dot{\boldsymbol{U}} = \begin{bmatrix} \dot{U}_A \\ \dot{U}_B \\ \dot{U}_C \end{bmatrix} = \begin{bmatrix} 127.02\angle 0° \\ 127.02\angle -120° \\ 127.02\angle 120° \end{bmatrix} \text{kV} \cdot$$

2) Given the mathematical principle for solving matrix equations as well as the accessibility of the real-time and synchronous measurement of electric fields, three measuring points, which meet the minimum number of measuring points for calculating three-phase voltages, are set near the ground. In view of the structural symmetry of the three-phase OTLs, the three measuring points are symmetrically arranged relative to the y-axis on a cross section.

3) For the meteorological conditions, breezeless, ice-free, and average outdoor temperature conditions are assumed. Accurate values of the electric field can be calculated according to Equations (1)-(5), and the measured electric field data are simulated by adding the random white noise with the noise level of σ.

B. Position optimization of measuring points

For Case I, the space range of the position

optimization is set as $0 \le x \le 150$m, $-15\text{m} \le y \le 15$m, and $1\text{m} \le z \le 3$m. The results of several optimizations are cond($\boldsymbol{K}$) = G_{best} = 14.87, thus, the corresponding optimal measuring positions are (150 -7.5 3), (150 0 3), and (150 7.5 3).

Moreover, two sets of measuring points (10 -5 1), (10 0 1), (10 5 1) and (100 -10 2), (100 0 2), (100 10 2) are randomly selected, and the corresponding cond($\boldsymbol{K}$) is calculated.

Under the condition of 10% measurement error, the directly inverse calculation is performed to obtain the corresponding inverse solution $\boldsymbol{U}^{\delta}$ at three sets of measuring points. The results of the inverse calculation are different because of the addition of random noise. The means and variances of 10 calculations are determined statistically, as shown in Table 1.

Table 1 shows that different positions of the measuring points lead to different cond($\boldsymbol{K}$) and $\boldsymbol{U}^{\delta}$. The greater the cond($\boldsymbol{K}$) is, the more $\boldsymbol{U}^{\delta}$ deviates from the accurate $\boldsymbol{U}$. The greater the variance is, the worse the calculation stability appears. Thus, the position optimization of measuring points presents a significant improvement in the ill-posedness of inverse problems.

For Case II, the optimal measuring positions to be found are (120 -6.5 2.9), (120 0 3), (120 6.5 2.9), and the corresponding cond($\boldsymbol{K}$) is 29.74. The inverse solution $\boldsymbol{U}^{\delta}$ obtained by the directly inverse calculation is as follows:

$$\dot{\boldsymbol{U}}^{\delta} = \begin{bmatrix} 136.91\angle 1.57^\circ \\ 153.54\angle -123.78^\circ \\ 135.13\angle 117.68^\circ \end{bmatrix} \text{kV} .$$

Compared with other randomly selected measuring points, the optimal measuring positions determines the minimum cond($\boldsymbol{K}$). Moreover, the accuracy and stability of the inverse calculation are significantly improved. This outcome is similar to the conclusion in Case I.

Although the position optimization of measuring points improves the performance of the directly inverse calculation, the accuracy of inverse solutions requires further improvement. Thus, the iterative regularization method is required.

C. Iterative Tikhonov regularization in time-domain

Suppose that the electric field data measured in real time with a noise level of 10% are obtained at the three optimal measuring points in Case I. The directly inverse calculation and the traditional Tikhonov regularization calculation with α=10^{-6} and α=10^{-5}, respectively, are performed. Figure 4 shows the comparison among the accurate three-phase voltages and the three inverse solutions in a sinusoidal period. Figure 4 reveals that a certain error exists between the directly inverse solutions and accurate values. The accuracy of inverse solutions is improved when the single Tikhonov regulation calculation with α=10^{-6} is carried out. However, the accuracy is significantly decreased when α=10^{-5}. This result suggests that the regularization parameter α must be carefully selected in the traditional Tikhonov regularization.

Suppose that τ=1.4. The iterative Tikhonov regularization is carried out when α=10^{-6} and α=10^{-5} respectively. When α=10^{-6}, the iteration numbers of the inverse calculation at 20 points of time in a period are [1 1 1 1 1 2 1 1 1 1 2 2 2 1 1 1 1 1 1 2]. When α=10^{-5}, the iteration numbers are [4 4 4 4 4 3 5 5 2 4 4 2 2 4 4 3 5 2 2 4]. Thus, the iteration number increases when the selected value of α is unsatisfactory. Figure 5 presents the comparison among the accurate voltages and the inverse solutions of the iterative regularization in a sinusoidal period. Figure 5 shows that the difference between the two inverse solutions is insignificant when α approaches two different values. Therefore, the iterative Tikhonov regularization method with the variable of the iteration number can decrease the susceptibility of α to the inverse solution by adjusting the number of iterations.

The iterative Tikhonov regularization is carried out successively based on 20 sets of measured data in a sinusoidal period. The iteration number varies each time, but is certainly no more than 5. The simulation is conducted with a regular computer configuration with Intel Core I5 CPU, 3.2 GHz clock and 4 GB frequency of memory. It takes 0.012s for calculation using MATLAB software. The speed of calculation is acceptable.

The RMS and phase of the three-phase voltages are extracted from the sinusoidal fitting curves on the basis of the 20 sets of real-time inverse solutions in a period. The results of the three-phase voltage phasors are statistically shown in Table 2. Moreover, the root-mean-square errors (RMSEs) between the inverse solutions and the accurate values are computed to reflect the deviation of the inverse solutions from the accurate values.

Table 2 also shows that the point-by-point iterative Tikhonov regularization is superior to other methods in terms of accuracy.

The point-by-point iterative Tikhonov regularization with $\alpha = 10^{-6}$ is adopted under different measurement error levels. Tables 3 and 4 show the results.

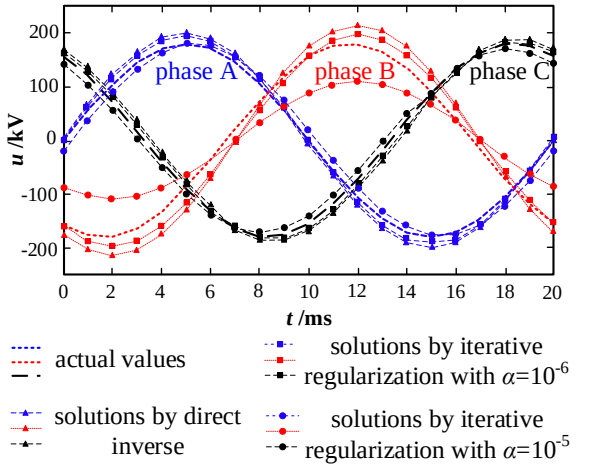

Fig. 4. Comparison among actual values, directly inverse solutions, and single regularization solutions.

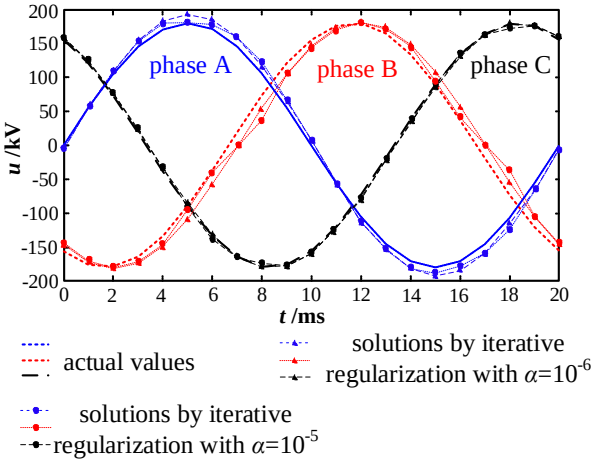

Fig. 5. Comparison among actual values and iterative regularization solutions.

Various factors affect measurements in a real complicated engineering environment; thus, a measurement error of up to 25% is set in the example. Tables 3 and 4 show that the error of solution increases as the measurement error increases. However, when the measurement error is less than 20% in Case I and less than 15% in Case II, the accuracy of the inverse solutions calculated on the basis of the proposed position optimization and point-by-point iterative Tikhonov regularization is satisfactory. For many other methods, the inverse solutions almost deviate from the actual values when the measurement error exceeds 10%. The analysis results of the examples verify the accuracy and robustness of the presented method.

IV. EXPERIMENTAL VERIFICATION

Figure 6 presents the simulation experimental platform of the three-phase AC OTLs. The real-time electric field data are synchronously measured by the three self-made devices.

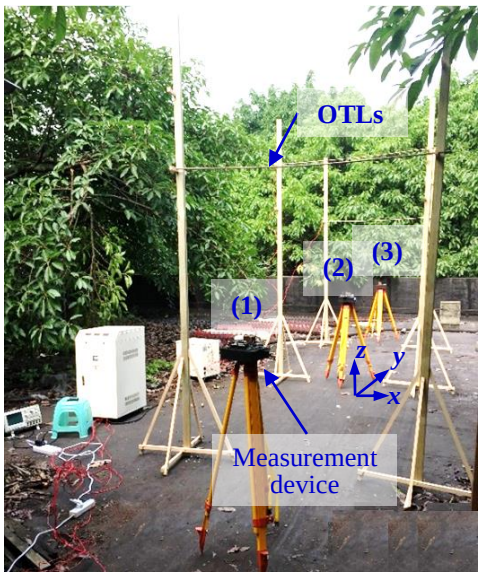

Fig. 6. Experimental site.

The three-phase AC voltages on OTLs are measured by a system that contains high-voltage probes and oscilloscope. They do not show complete three-phase symmetry:

$$\dot{\boldsymbol{U}} = \begin{bmatrix} \dot{U}_A \\ \dot{U}_B \\ \dot{U}_C \end{bmatrix} = \begin{bmatrix} 9.26\angle -158^\circ \\ 8.91\angle -33^\circ \\ 8.47\angle 83^\circ \end{bmatrix} \text{kV} \cdot$$

Figure 7 shows the measured *Ez* components at three points.

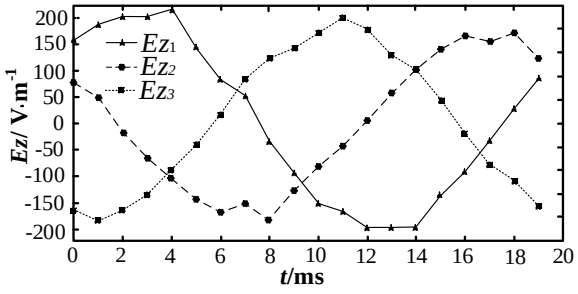

Fig. 7. Measured *Ez* at three points in the time-domain.

The iterative Tikhonov regularization with $\alpha = 10^{-4}$ is adopted to inversely calculate the three-phase voltages point by point in the time domain. The comparison between actual values and the solutions is shown in Fig. 8. The phasors of the three-phase voltage can be obtained by sine curve fitting:

$$\dot{\boldsymbol{U}}^{\delta} = \begin{bmatrix} \dot{U}_A^{\delta} \\ \dot{U}_B^{\delta} \\ \dot{U}_C^{\delta} \end{bmatrix} = \begin{bmatrix} 9.25\angle -154^\circ \\ 8.89\angle -30^\circ \\ 8.51\angle 88^\circ \end{bmatrix} \text{kV} \cdot$$

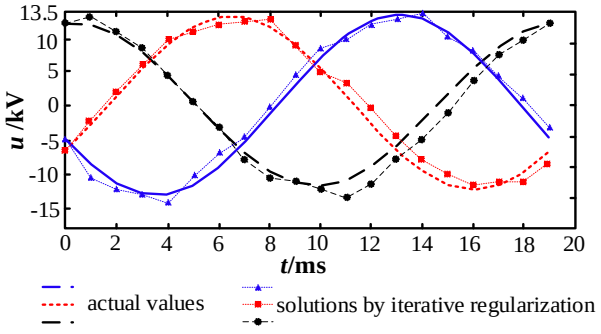

Fig. 8. Comparison between actual values and solutions of three-phase voltages.

The maximum RMS error and phase error of the calculated three-phase voltages are 10 V and 5°, respectively. This result shows that the proposed non-contact measurement of voltage on OTLs has engineering feasibility and accuracy

V. CONCLUSION

The aim of the study is to realize the non-contact measurement of voltages on AC OTLs through inverse calculation based on measured electric field data under OTLs. An accurate mathematical model and modified inverse solution algorithms are proposed to improve the accuracy, stability, and robustness of the inverse calculation. They are summed up as follows.

An accurate 3-D mathematical model between the voltages and the electric fields of OTLs is built with consideration of the real engineering environment and physical form of OTLs.

The position optimization of measuring points is presented to minimize the condition number of the observation matrix and reduce the sensitivity of inverse solutions to measurement noise. The particle swarm algorithm for position optimization is proved to perform well in global optimization.

The iterative Tikhonov regularization method with varying iteration numbers is developed to further improve the ill-posedness of inverse problems. Compared with the traditional Tikhonov regularization method, the method presented avoids the complex computation of selecting regularization parameters α and decreases the susceptibility of α to inverse solutions by adjusting the number of iterative calculations.

The process of point-by-point regularization performs real-time correction for the inverse calculation, thereby improving the calculation accuracy.

The analysis results of the given examples and experiments verify that through the combination of the above four improvements, inverse solutions with satisfactory accuracy can be obtained under the condition with high measurement errors. Moreover, the rapidity, stability, and robustness of the inverse calculation are demonstrated.

ACKNOWLEDGMENT

This work was supported by the National Natural Science Foundation of China (NSFC 51407016, 51577017) and National "111" Project of China (Grant No. B08036).

Table 1: Comparison of the inverse solutions when setting different measuring points

Measuring Positions $(x_k\ y_k\ z_k)$/m	Cond($\boldsymbol{K}$)	Inverse Solution $\boldsymbol{U}^{\delta}$	
		Mean Value/kV	Variance (RMS Phase)
$\begin{cases}(10\ -5\ 1)\\(10\ 0\ 1)\\(10\ 5\ 1)\end{cases}$	266.44	$A:\ 139.92\angle -1.72°$ $B:\ 216.10\angle -58.57°$ $C:\ 135.13\angle 121.37°$	(47.02 23.54) (162.10 105.55) (49.13 26.59)
$\begin{cases}(100\ -10\ 2)\\(100\ 0\ 2)\\(100\ 10\ 2)\end{cases}$	36.66	$A:\ 141.36\angle 1.59°$ $B:\ 166.62\angle -125.94°$ $C:\ 129.41\angle 118.32°$	(18.73 2.84) (32.19 18.79) (10.03 7.33)
$\begin{cases}(150\ -7.5\ 3)\\(150\ 0\ 3)\\(150\ 7.5\ 3)\end{cases}$	14.87	$A:\ 128.74\angle -0.967°$ $B:\ 121.33\angle -121.51°$ $C:\ 124.35\angle 121.22°$	(13.37 1.67) (22.31 11.21) (8.19 3.81)

Table 2: Statistics of various inverse solutions of three-phase voltages

Accurate Values	Directly Inversion	Single Regularization when α=10^{-6}	Single Regularization when α=10^{-5}	Iterative Regularization when α=10^{-6}	Iterative Regularization when α=10^{-5}
$127.02\angle 0^\circ$	$140.48\angle 1.01^\circ$	$138.17\angle -0.17^\circ$	$127.07\angle -6.55^\circ$	$132.22\angle -1.22^\circ$	$131.37\angle -1.28^\circ$
$127.02\angle -120^\circ$	$151.84\angle -126.40^\circ$	$139.30\angle -126.45^\circ$	$77.22\angle -126.80^\circ$	$128.55\angle -124.45^\circ$	$127.91\angle -126.90^\circ$
$127.02\angle 120^\circ$	$131.64\angle 115.78^\circ$	$129.82\angle 117.17^\circ$	$121.41\angle 124.56^\circ$	$128.27\angle 118.37^\circ$	$129.41\angle 118.83^\circ$
RMSE of RMS	16.54	9.73	28.92	3.21	2.92
RMSE of Phase	4.46	4.07	6.05	2.83	4.11

Table 3: Statistics of inverse solutions obtained under different measurement errors in Case I

Measurement Error/ %	$\dot{U}_A^\delta$/kV	$\dot{U}_B^\delta$/kV	$\dot{U}_C^\delta$/kV	RMSE of RMS	RMSE of Phase
0	127.02∠0°	127.02∠-120°	127.02∠120°	0	0
± 5	128.85∠0.29°	129.26∠-120.23°	128.35∠119.83°	1.86	0.24
± 10	132.22∠-1.22°	128.55∠-124.45°	128.27∠118.37°	3.21	2.83
± 15	123.40∠-1.24°	134.77∠ -122.44°	130.67∠113.45°	5.38	4.09
± 20	115.22∠-2.61°	121.12∠-114.02°	133.07∠112.85°	8.37	5.58
± 25	133.94∠3.07°	140.24∠-112.87°	137.68∠137.91°	10.61	11.27

Table 4: Statistics of inverse solutions obtained under different measurement errors in Case II

Measurement Error/ %	$\dot{U}_A^\delta$/kV	$\dot{U}_B^\delta$/kV	$\dot{U}_C^\delta$/kV	RMSE of RMS	RMSE of Phase
0	127.02∠0°	127.02∠-120°	127.02∠120°	0	0
± 5	124.21∠0.79°	130.25∠-115.25°	131.24∠119.06°	3.48	2.88
± 10	121.77∠0.75°	131.15∠-113.16°	134.06∠117.74°	5.61	4.18
± 15	131.25∠-1.15°	139.78∠ -124.06°	121.83∠113.87°	8.33	4.29
± 20	125.28∠-2.27°	108.45∠ -112.70°	130.36∠128.11°	10.93	6.43
± 25	137.11∠4.37°	151.43∠-115.96°	138.09∠108.25°	16.55	7.60

REFERENCES

[1] C. Venkatesh and K. S. Swarup, "Performance assessment of distance protection fed by capacitor voltage transformer with electronic ferro-resonance suppression circuit," *Electric Power Systems Research*, vol. 112, pp. 12-19, 2014.

[2] D. Topolanek, M. Lehtonen, and M. R. Adzman, "Earth fault location based on evaluation of voltage sag at secondary side of medium voltage/low voltage transformers," *IET Generation Transmission & Distribution*, vol. 9, no. 14, pp. 2069-2077, 2015.

[3] Z. Tong, Z. Dong, and T. Ashton, "Analysis of electric field influence on buildings under high-voltage transmission lines," *IET Science Measurement & Technology*, vol. 10, no. 4, pp. 253-258, 2016.

[4] A. M. Farah, M. Afonso, and A. Vasconcelos, "A finite-element approach for electric field computation at the surface of overhead transmission line conductors," *IEEE Magnetics Society*, vol. PP, no. 99, pp. 1-4, 2017.

[5] R. M. Sarmento, "Electric and magnetic fields in overhead power transmission lines," *IEEE Latin America Transactions*, vol. 10, no. 4, pp. 1909-1915, 2012.

[6] R. M. Radwan, A. M. Mahdy, and M. Abdel, "Electric field mitigation under extra high voltage power lines," *IEEE Trans. Dielectrics and Electrical Insulation*, vol. 20, no. 1, pp. 54-62, 2013.

[7] F. Yang, H. Wu, and W. He, "Investigation on the electric field inverse problem of HV transmission lines and discussion on its application," *ACES Journal*, vol. 25, no. 2, pp. 129-136, 2010.

[8] A. Z. E. Dein, "Parameters affecting the charge distribution along overhead transmission lines'

conductors and their resulting electric field," *Electric Power Systems Research*, vol. 108, pp. 198-210, 2014.

[9] A. Ilyin, S. I. Kabanikhin, and D. B. Nurseitov, "Analysis of ill-posedness and numerical methods of solving a nonlinear inverse problem in pharmacokinetics for the two-compartmental model with extravascular drug administration," *Journal of Inverse and Ill-Posed Problems*, vol. 20, pp. 39-64, 2012.

[10] S. Lu and J. Flemming, "Convergence rate analysis of Tikhonov regularization for nonlinear ill-posed problems with noisy operators," *Inverse Problems*, vol. 28, pp. 104003, 2012.

[11] T. Ogawa, "Complex-valued network inversion with regularization for ill-posed inverse problems," *Computer Technology & Application*, vol. 3, pp. 408-417, 2012.

[12] Z. Zhang, Z. Zhu, and Q. Xin, "Analysis and application of inverse detecting method based on local electric field," *ACES Journal*, vol. 27, no. 7, pp. 566-573, 2012.

[13] S. I. Kabanikhin, *Inverse and Ill-posed Problems*. DE GRUYTER, Berlin, 2011.

[14] J Xu, F Schreier, and A Doicu, "Assessment of Tikhonov-type regularization methods for solving atmospheric inverse problems," *Journal of Quantitative Spectroscopy and Radiative Transfer*, vol. 184, pp. 274-286, 2016.

[15] H. Mao, "Adaptive choice of the regularization parameter in numerical differentiation," *Journal of Computational Mathematics*, vol. 33, pp. 415-427, 2015.

[16] C. Shi, C. Wang, and G. Zheng, "A new posteriori parameter choice strategy for the convolution regularization of the space-fractional backward diffusion problem," *Journal of Computational and Applied Mathematics*, vol. 279, pp. 233-248, 2015.

[17] J. L. García Pallero, J. L. Fernández-Martínez, and Z. Fernández-Muñiz, *The Effect of the Noise and the Regularization in Inverse Problems: Geophysical Implication*, Mathematics of Planet Earth, Springer, Berlin Heidelberg, 2014.

[18] P. Kumar and A. K. Singh, *Single Measurement Based Mechanical State Estimation for Overhead Transmission Lines with Level Spans. IEEE Press*, New Jersey, 2014.

[19] F. Bassi, G. Giannuzzi, and M. Giuntoli, "Mechanical behaviour of multi-span overhead transmission lines under dynamic thermal stress of conductors due to power flow and weather conditions," *International Review on Modelling & Simulations*, vol. 6, pp. 1112-1122, 2013.

[20] F. Liu and R. D. Findlay, "Investigation of mechanical properties of single layer ACSR based on an integrated model," *Electric Power Systems Research*, vol. 78, pp. 209-216, 2008.

[21] P. G. Huray, *Static Electric Fields Maxwell's Equations*. Wiley-IEEE Press, USA, 2010.

[22] S. S. Chowdhury, A. Lahiri, and S. Chakravorti, "Surface resistance modified electric field computation in asymmetric configuration using surface charge simulation method: a new approach," *IEEE Trans. Dielectrics & Electrical Insulation*, vol. 19, no. 3, pp. 1068-1075, 2012.

[23] R. Djekidel, C. Abdelghani, and H. Abdechafik, "Efficiency of some optimization approaches with the charge simulation method (CSM) for calculating the electric field under EHV power lines," *IET Generation Transmission & Distribution*, vol. 11, no. 17, pp. 4167-4174, 2017.

[24] D. Xiao, Y. Xie, and H. Liu, "Position optimization of measuring points in voltage non-contact measurement of AC overhead transmission lines," *ACES Journal*, vol. 32, no. 10, pp. 908-914, 2017.

[25] F. Chen and Y. B. Tian, "Modeling resonant frequency of rectangular microstrip antenna using CUDA-based artificial neural network trained by particle swarm optimization algorithm," *ACES Journal*, vol. 29, no. 12, pp. 1025-1034, 2014.

[26] M. Grasmair, "Variational inequalities and improved convergence rates for Tikhonov regularisation on banach spaces," *Journal of Inverse and Ill-Posed Problems*, vol. 21, pp. 379-394, 2013.

[27] S. George and M. Kunhanandan, "An iterative regularization method for ill-posed Hammerstein type operator equation," *Journal of Inverse and Ill-posed Problems*, vol. 17, pp. 831-844, 2009.

Dongping Xiao received the B.Sc. degree in Industrial Automation from Chongqing University, Chongqing, China, in 1999, and the M.Sc. and Ph.D. degrees in Electrical Engineering from Chongqing University, in 2004 and 2009, respectively. From 2012 to 2013, she was a Visiting Scholar with Washington State University, USA. Currently, she is an Associate Professor at the College of Electrical Engineering, Chongqing University, China. Her main fields of interests include calculation and simulation of electromagnetic field, electromagnetic measurement and running state monitoring of power transmission equipment.

Design and Analysis of a Novel Variable Frequency Transformer

Xianming Deng [1], Na Liu [1], Yuanda Sun [1], Qifen Guo [2], and Miaofei Zhang [3]

[1] School of Electrical and Power Engineering
China University of Mining and Technology, Xuzhou, Jiangsu, 221116, China
xmdengcumt@126.com, liuna@cumt.edu.cn, 1026980211@qq.com

[2] State Grid Chuzhou Power Supply Company, Chuzhou, 239000, China
594507070@qq.com

[3] School of Computer Information Engineering, Chuzhou University, Chuzhou, Anhui, 239000, China
zhang_miaofei289@126.com

Abstract ─ Cross-regional power supply and regional power grid interconnection is the future development of the power grid. At present, AC and DC asynchronous interconnection methods have disadvantages of complicated control and poor system stability. A grid interconnection solution based on variable frequency transformer (VFT) is a possible solution. Based on the introduction of the basic structure and operation principles of VFT, this paper presents a new structure in which a VFT and a drive motor share a core of electrical steel. The new structure VFT is modeled and analyzed by finite element analysis. Through the analysis of the air gap magnetic field of the VFT, the coupling analysis and operating characteristics analysis of the power winding and the control winding verify the design.

Index Terms ─ Finite element analysis, grid interconnection, variable frequency transformer.

I. INTRODUCTION

The interconnection of large power grids has been a development trend of power systems. The interconnection of power grids in various regions is also a necessary means of power grid development to a large scale. There are two main ways of interconnection of regional grids: AC synchronous and DC asynchronous. It is difficult for an AC synchronous interconnection to achieve large-scale long-distance transmission of electric energy; DC asynchronous interconnection relies on a large number of power electronic devices as the main converter equipment. Moreover, problems are complex, high installation and maintenance cost, and insufficient system stability. With long term study and innovation, the United States General Electric Company (GE) has proposed an interconnection device different from DC asynchronous and AC synchronous, this device uses a high-frequency wound induction motor as the core device of the VFT [1-2].

Since the first VFT was applied in 2004, wide attention has been paid, with related experiments and simulation carried out. When VFT is used in interconnection of local railway power grid and state power grid, it can meet the requirement of security and stability interconnection; When VFT is used for asynchronous interconnection of wind power grid and large power grid, the voltage stability and low voltage crossing ability of the wind farm can be improved. In the field of normal power transmission and new energy power generation, the way of using VFT interconnected power grids is a new direction for power systems and energy sources. VFT has a broad space for development.

In this paper, based on the structure of frequency conversion transformer, a novel structure of frequency conversion transformer is put forward, which integrates the driving motor by sharing the core of electrical steel. The finite element analysis [3] is carried out to demonstrate structural design by analyzing its advantages and characteristics compared with the original.

II. THE VFT WORKING PRINCIPLE

As is shown in Fig. 1, the VFT is composed of a collector ring, a DC drive motor, and a rotating transformer [4]. The collector ring is used to conduct current between the resolver rotor winding and the three-phase stationary bus. When the stator side of the resolver is connected to the power grid, it will generate a rotating magnetic field at the same frequency in the transformer. If the rotor does not rotate, the rotating magnetic field will induce electromagnetic force (EMF) at the same frequency on the rotor side. Therefore the rotary transformer is equivalent to a conventional transformer. If the rotor rotates at a certain speed, the frequency of induced voltage on the rotor side is different from that on the stator side, so that the interconnection between

Submitted On: March 15, 2018
Accepted On: June 17, 2018

different frequency grids can be realized. If there is frequency differences between the two sides of the power grid, taking the frequency of the two power grid respectively as f_1, f_2, the rotor of the resolver transformer rotates continuously with the speed of the frequency deviation of the two power grids in proportion, the rotor speed at this time is:

$$n_r = \frac{60(f_1 - f_2)}{p}. \quad (1)$$

In Equation (1), n_r and p are respectively the mechanical speed and the number of pole pairs in the resolver rotor.

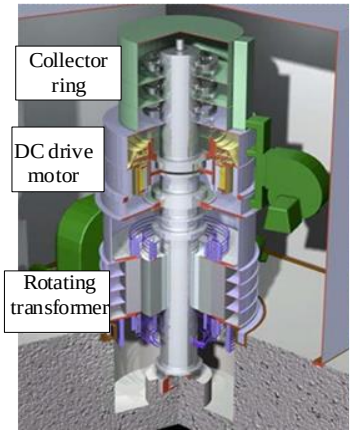

Fig. 1. VFT profile view.

The DC motor is coaxial with the rotor of the rotating transformer to control the rotating speed and power transfer of the rotor in the rotating transformer. In the case of interconnection between two power grids, the position of the resolver rotor related to its stator can be changed by adjusting the torque to drive the DC motor, so that the direction and the size of the power transmission can be changed [5]. The VFT is essentially a phase-shifting transformer with an adjustable phase angle. The expression of transmission power is as follows [6]:

$$P_{VFT} = \frac{V_1 V_2}{X_{12}} \sin(\theta_1 - \theta_2 - \theta_{rm}) = \frac{V_1 V_2}{X_{12}} \sin(\theta_{net}). \quad (2)$$

In Equation (2), V_1 is the VFT stator terminal three-phase voltage; V_2 is the three-phase synthesis voltage of VFT rotor side; X_{12} is the reactance between the stator and rotor winding; θ_1 is the angle of V_1; θ_2 is the angle of V_2; θ_{rm} is the angle between the rotor and the stator. The relationship between the phase angle of the fixed rotor voltage phase and the principle of power transmission can be expressed in the phase diagram of Fig. 2.

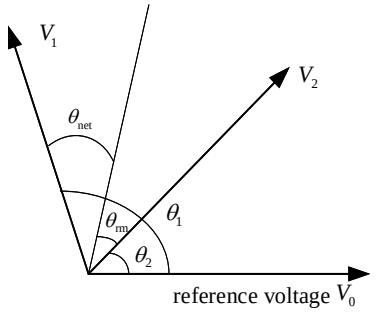

Fig. 2. Voltage phase of the VFT stator and rotor terminal.

III. VFT DESIGN

A. The basic structure of the proposed VFT

The original structure of the VFT system requires motor drive combination and the rotary transformer be connected in a coaxial way. The system structure is complicated, with a long axial shaft. Also, the number of bearing seats is large, and the amplitude of the shaft vibration and the waveform is high as well. In this paper, on the basis of the original structure in Fig. 1, a new structure of VFT is proposed. The rotating transformer and the driving motor share a set of stator and rotor core, which combine the rotating transformer and the driving motor. The method can reduce the axial length of the frequency transformer, simplify its structure, reducing the size of the frequency transformer and saving the manufacturing cost. It can also facilitate the assembly and maintenance on site, thus improving the operation reliability to a certain extent.

As the proposed transformers and drive motors share a set of stator and rotor core, the coupling effect should be taken. To facilitate design, the driving motor is equipped with a permanent magnet synchronous motor (PMSM). The number of stator slot in the PMSM is 48, the rotor structure is built-in and the pole logarithm is 6. On this basis, by increasing the stator slot of the PMSM, a set of stator control winding is added. 24 rotor slots with armature windings are used, which combine the drive motor and the rotating transformer. The longitudinal section, B-B section and circuit diagram of the structure are shown in Fig. 3, Fig. 4, and Fig. 5, respectively.

The numbers in Fig. 3 to Fig. 5 represent: 1-Stator core; 2-Stator slot; 3-Three-phase power winding of the stator; 4-Three-phase control winding of the stator; 5-Rotor core; 6-Rotor slot; 7-Permanent magnet slot; 8-Three-phase power winding of the rotor; 9-Permanent magnets; 10-Three-phase slip ring; 11-Three-phase brush; 12-Shaft. GRID1 represents three-phase grid 1, and GRID2 represents three-phase grid 2; RPC is a reversible inverter. The yellow part in Fig. 4 is the power winding of the stator rotor, the blue part is the control winding of the stator, and the green part is the permanent magnet of

the rotor. The three-phase power winding of the stator in Fig. 5 is connected to the GRID1, and the control winding of the stator is connected to a reversible inverter. On the rotor side, the power windings of the rotor in the rotor slots are connected to the GRID2 via three-phase slip rings and three-phase brushes on the shaft.

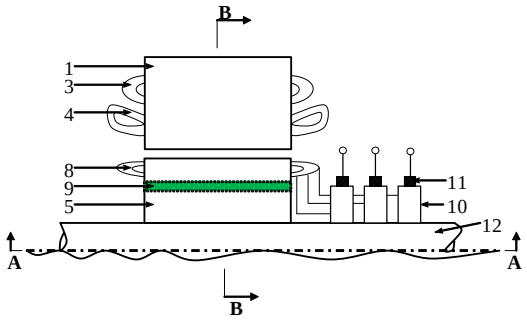

Fig. 3. Longitudinal profile diagram of the VFT.

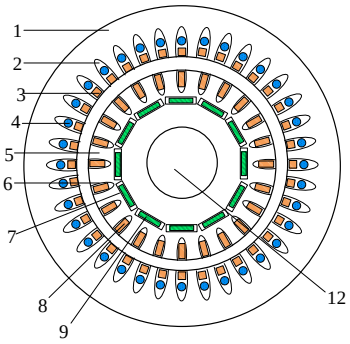

Fig. 4. B-B sectional view of the VFT.

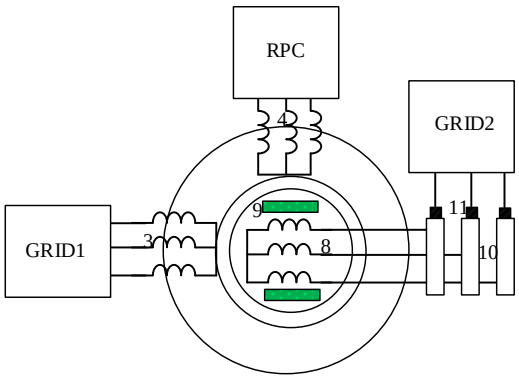

Fig. 5. Circuit structure diagram of the VFT.

B. The working principle of the new structure of the VFT

The VFT consists of two subsystems: the variable voltage variable frequency (VVVF) subsystem and the permanent magnet synchronous drive subsystem. The VVVF subsystem consists of a stator core, a rotor core, a set of three-phase power winding of the stator, a set of three-phase power winding of the rotor, three-phase slip rings and brushes. The number of pole pairs in the three-phase power windings in the stator equals to that in the rotor windings, which is set to P_p; The power windings of the stator are directly connected to the GRID1, and the power windings of the rotor are connected to GRID2 via slip rings and brushes. The permanent magnet synchronous drive subsystem is composed of the stator core, the rotor core, the three-phase control winding of the stator and the permanent magnet. The number of pole pairs in the stator control windings is the same as that in the permanent magnet, which is set to be P_c. The stator control winding is connected and controlled by a reversible inverter. Based on the knowledge of motor, it is possible to transfer the AC power between the power windings of the stator and the rotor, satisfying the following formula:

$$U_1 = \frac{N_1 f_1 k_{w1}}{N_2 f_2 k_{w2}} \cdot U_2 . \tag{3}$$

In the formula, U_1 and U_2 are the voltage of the power winding in the stator and rotor respectively; N_1 and N_2 are the turns of power windings in stator and rotor respectively, and their winding coefficients are respectively k_{w1}, k_{w2}. The frequency of the power winding in the stator and rotor is recorded as f_1, f_2. It is known from the formula (3) that the voltage is changed by designing or adjusting the number of turns of the power winding in the stator and rotor.

When the frequency of the power grid connected to the stator and the rotor is unequal, it is known from the previous analysis that the rotational speed *n* of the rotor in the stable operation should satisfy the following formula:

$$n_r = \frac{60(f_1 - f_2)}{p_p} . \tag{4}$$

The VVVF subsystem and the permanent magnet synchronous drive subsystem share the same rotor, so the speed of the PMSM in the drive subsystem must also meet formula (4). The PMSM can be controlled by the reversible inverters and meet the speed requirement. By controlling the inverters, we can control the torque exerted on the rotor of PMSM, thus controlling the power transmission angle θ_{net} to achieve the purpose of controlling the size and direction of transmission power on both sides.

IV. FINITE ELEMENT ANALYSIS OF THE PROPOSED VFT

Specific parameters of the proposed VFT are shown in Table 1. In this paper, the finite element method is used for structural modeling.

Table: 1 Design parameters of the proposed VFT

Parameter	Numerical Value
Rated power/MW	100
Phase	3
PMSM control winding phase	3
Rated voltage of two sides power grid/kV	15
Frequency range of interconnected power grid/Hz	45-55
Control circuit rated voltage/kV	1
Drive circuit rated power/kW	30
Power winding pole pairs	1
Pole-arc factor	0.72
Stator outer diameter/mm	11200
Stator inner diameter/mm	6740
Rotor outer diameter/mm	6710
Rotor inner diameter/mm	1250
Rated speed/(r/min)	300
Rated frequency difference/Hz	±5
Rated efficiency of VFT/%	92

A. Analysis of air gap magnetic field

When the power windings of the stator are excited, circuit of the rotor winding is set to the open state, with three-phase windings a supply of 15kV, 50Hz three-phase symmetrical rated voltage. The distribution of the flux lines of the VFT, the air-gap flux density and the air-gap flux density harmonics are shown in Fig. 6 (a), Fig. 6 (b) and Fig. 6 (c). As can be seen from Fig. 6 (a), when the circuit of the stator windings is excited, the internal magnetic field turns into one pole pair and the magnetic line distribution is proper. From Fig. 6 (b) and Fig. 6 (c), it can be seen that the air gap flux density is basically sinusoidal in one cycle with less odd harmonic content when the circuit of stator power winding gets excitation. Because the winding is three phase symmetry, there is no even subharmonic in the air gap magnetic density.

When permanent magnets are excited, the circuit of the power windings in the stator and the rotor, as well as the circuit of the control windings in the stator are opened. The rotor speed is 300r/min, and the permanent magnet excitation direction is radial, the distribution of the flux lines of the VFT, the air-gap flux density and the air-gap flux density harmonics are shown in Fig. 7 (a), Fig. 7 (b) and Fig. 7(c). As can be seen from Fig. 7 (a), when the permanent magnets are excited, their internal magnetic fields are distributed into six pole pairs. Some magnetic saturation occurs at the magnetic bridge, which limits the magnetic flux leakage, but there is also some weak magnetic flux leakage. The magnetic circuit design is reasonable. As can be seen from Fig. 7 (b) and Fig. 7 (c), when the permanent magnets are excited alone, the air gap flux density has a six-period sinusoidal distribution in the air-gap circumference. Because the width of the six permanent magnets the rotor is limited, the sine degree in each cycle is deficient, and the harmonic content is relatively large.

When the power windings of the stator and permanent magnet get the excitation at the same time, we set the rotor power winding and the stator control winding to the open state. In this case, the distribution of the flux lines in the VFT, the air-gap flux density and the number of air-gap flux density harmonics are shown in Fig. 8 (a), Fig. 8 (b) and Fig. 8 (c). As can be seen from Fig. 8 (a), generally, the internal magnetic field has one pole pair, and the pole pair consists of six smaller poles. In the edge of the polar magnetic fields, the interference of the six smaller pairs is obvious. In general, the distribution of the internal magnetic field is reasonable when getting excited together. As can be seen from Fig. 8 (b), when the stator power windings and the permanent magnets are excited together, the air gap magnetic density is superposed by one pair pole as a basic excitation plus six smaller pair poles, and a sinusoidal distribution is generated on the whole air gap circumference. In part, it becomes a sine distribution of six cycles. From the harmonic orders of Fig. 8 (c), it can be seen that period one and six have the most of the harmonic content meanwhile the clutter is relatively less.

The analysis of the three cases is taken when t=50ms.

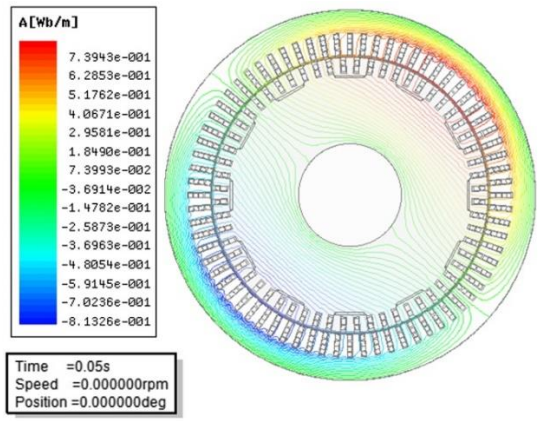

(a) Distribution magnetic force lines

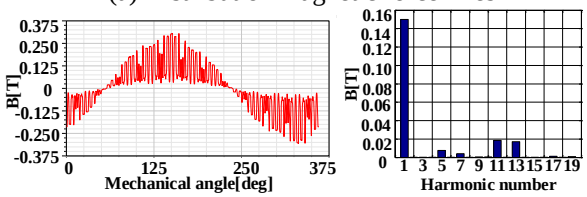

(b) Air gap magnetic flux density (c) Harmonic orders

Fig. 6. Independent excitation on stator power winding.

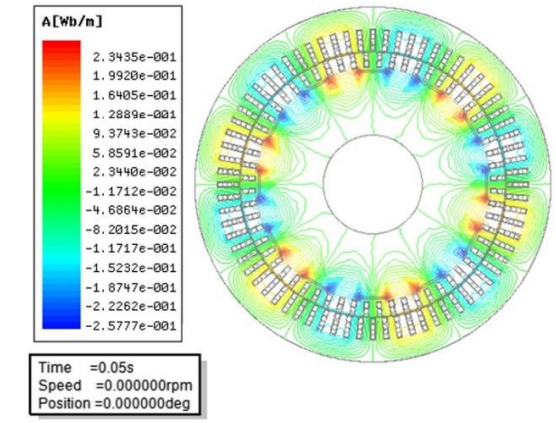

(a) Distribution curve of magnetic force line

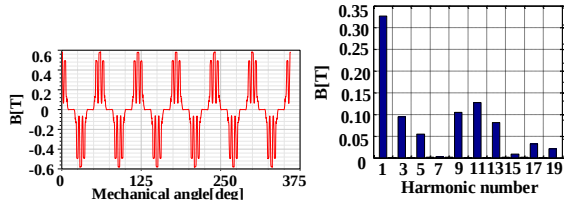

(b) Air gap magnetic flux density (c) Harmonic orders

Fig. 7. Independent excitation on permanent magnets.

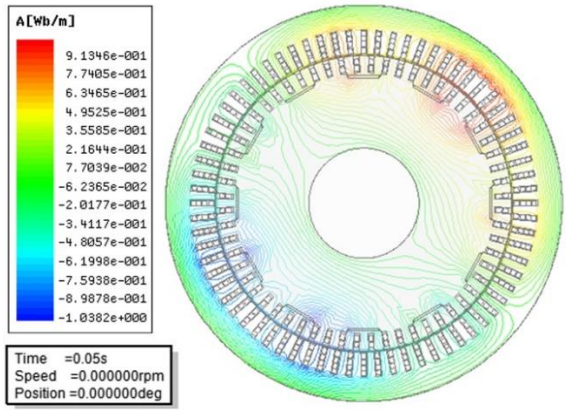

(a) Distribution curve of magnetic force line

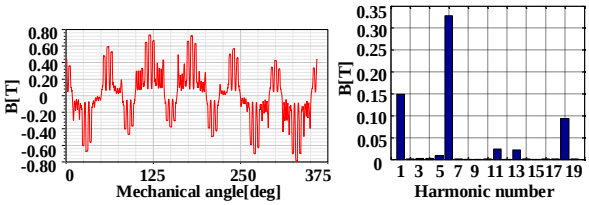

(b) Air gap magnetic flux density (c) Harmonic orders

Fig. 8. Excitation on stator power windings and permanent magnets.

B. Coupling analysis of the power windings and the control windings

Because the rotating transformer and the driving motor share the same iron core, their coupling relationship must be considered. When the pole pairs number of three phase power windings and the number of pole pairs in control windings meet the following conditions $P_c >> P_p$, $P_c = 2 \times k \times P_p$, ($k$=1, 2, 3……), the direct coupling relationship between three-phase power windings and three-phase control windings will be eliminated, and the loss power of the power and control windings will be greatly reduced. Therefore, structural design of the VVVF subsystem and permanent magnet synchronous drive subsystem pole pairs is particularly important. In this paper, the VVVF subsystem power winding pole pairs $P_p = 1$, the permanent magnet synchronous control subsystem pole pairs $P_c = 6$. By analysing the induced electromotive force, we can get to know the mutual influence due to coupling between the power control windings.

(1) The influence on rotor winding excited by stator control winding

When the circuit of the state power winding is not connected to the power grid, the control winding of the stator is applied with a rated voltage of 50 Hz and 1 kV which is shown in Fig. 9 (a) from t=100ms, and the induced EMF generated in the power winding of the rotor is shown in Fig. 9 (b). The amplitude of the induced voltage is 2.2V, which is about 0.15% of the rated voltage on the rotor side power winding. It can be seen that when the stator is excited, there is almost no potential induction in the power winding.

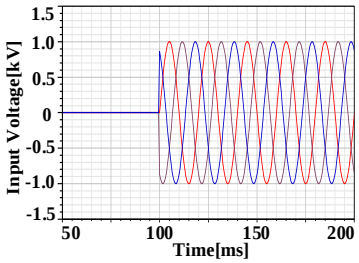

(a) Voltage on stator control winding

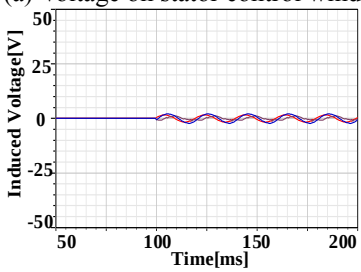

(b) Induction voltage on rotor power winding

Fig. 9. Influence of stator windings on rotor power windings.

(2) The influence on stator control winding excited by stator and rotor power windings

The circuit of control winding on stator is open

from the moment t=100ms, which is shown in Fig. 10 (a). Apply the same excitation 15kV, 50Hz voltage to the stator and rotor power windings, and the rotor does not turn at this time. The induction EMF of the control windings in the stator, as is shown in Fig. 10 (b), is about 0.6V, about 0.6% of the rated stator voltage value. It can be seen that when the power winding is excited, there is little induction EMF in the control winding.

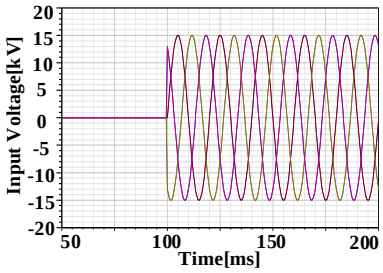

(a) Voltage on stator power winding

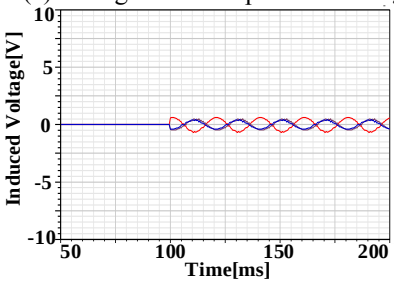

(b) Induction voltage on stator control winding

Fig. 10. The control winding EMF inducted by the stator and rotor power windings.

The simulation results show the weak coupling relationship between the power winding and the control winding of the VFT which realizes the decoupling of the two windings and meets the design requirements.

C. Analysis of operation characteristics

(1) No-load operation state

The power winding of the stator is connected to the 15kV and 50Hz power grid, the rotor speed is zero, the control winding of the stator has no control voltage, and the circuit of the power winding in the rotor is open. At t=800ms, the power frequency of the stator power winding changes to 45 Hz, the voltage amplitude is constant, and the rotor speed rotates reversely at 300 r/min at this time. According to the working principle of the VFT, it is known that the frequency of the induction voltage in the rotor power windings should remain unchanged at 50Hz. Figure 11 (a) is the stator winding voltage curve, Fig. 11 (b) is the speed curve of the rotor. Figure 11 (c) is the induced EMF waveform of the rotor power winding. It can be seen that when the frequency of the stator side power supply changes, the induced EMF of the rotor keeps constant at 50 Hz, and the waveform is ideal. Figure 11 (d) shows the stator power winding current waveform. Under no-load condition, the peak value of the current is about 50A. After a period of speed change, the dynamic steady state is reached. When smoothing, the peak value is about 57A. Figures 11 (e) and (f) show the curves of iron loss and copper loss, respectively. It can be seen that the iron loss is 81.54kW before the frequency of the stator power winding changes, and the iron loss is about doubled after the changes. This is due to the constant of the stator voltage, the decrease of frequency and the increase of magnetic induction intensity. The factors above result in the increase of iron consumption. The copper consumption is also increased from 36.9kW to 49.8kW, due to the increase of current.

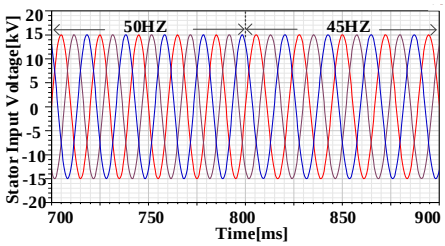

(a) Voltage on stator winding

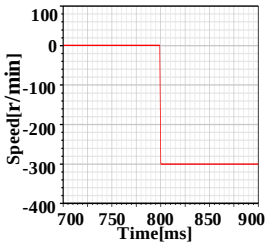

(b) Rotor speed

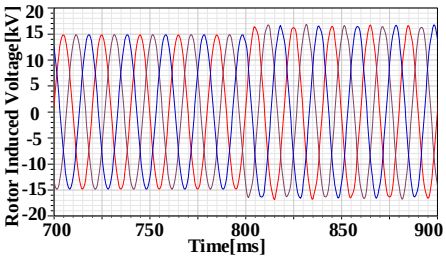

(c) Induction voltage on rotor winding

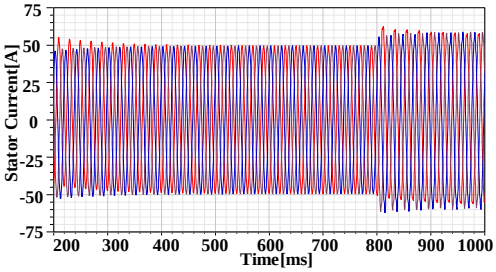

(d) Current on stator winding

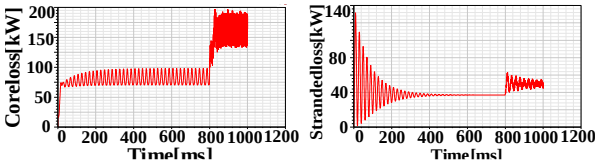

(e) Iron loss (f) stator copper loss

Fig. 11. Analysis of rotor side on no-load open state.

(2) Load running state

When the circuit of the rotor winding is connected to the resistance, it can simulate the load situation of the rotor side. The stator power windings are connected to the 15kV and 50Hz power grid. The rotor speed is zero and the stator control windings have no control voltage. At this point, the rotor side correspondingly induces an EMF at the same frequency 50 Hz.

At *t*=800ms, the grid frequency of the stator-side is changed to 45Hz, the voltage is constant. At this time the rotor speed rotates reversely at 300 r/min. Figure 12 (a) is the voltage variation curve of the stator side, and Fig. 12 (b) is the speed change curve of the rotor. Figure 12 (c) is induction voltage waves of the rotor side. The frequency of the rotor side voltage remains the same whenever the stator voltage frequency changes, which realizes the grid connection of two different frequencies. Figures 12 (d) and (e) are current waveforms of the stator and rotor side, with amplitudes about 510A and 508A respectively. After a change of speed, they will enter a steady state and eventually become stable. Figures 12 (f) and (g) are the curves of iron consumption and power transfer respectively. It is known that the iron consumption is about 37.06kW before the stator side frequency and the speed changes. The iron consumption changes to 92.8kW after the change. For the power transferred on the stator side, it can be seen from Fig. 12 (g) that before the stator side frequency changes at *t*=800ms, the transmission power is 3.68MW, and after the change the transmission power is 4.21MW.

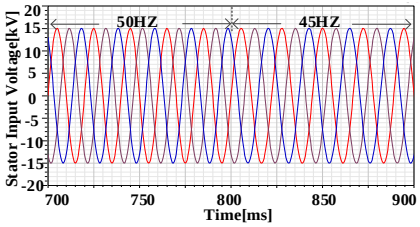

(a) Voltage on stator winding

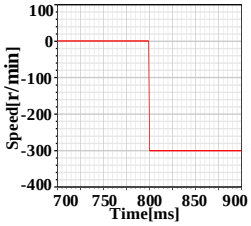

(b) Rotor speed

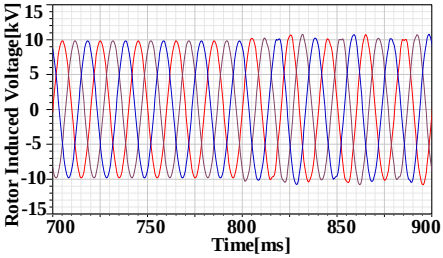

(c) Induction voltage on rotor winding

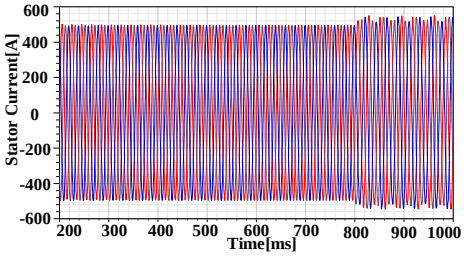

(d) Current on stator winding

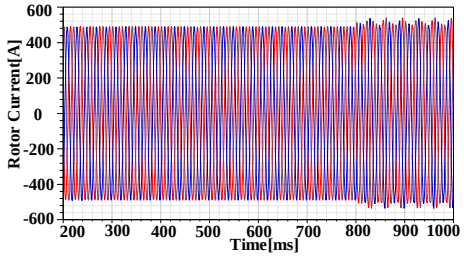

(e) Current on rotor winding

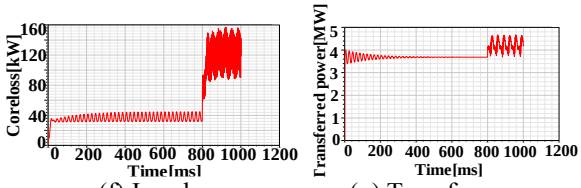

(f) Iron loss (g) Transfer power

Fig. 12. Analysis of the rotor side on the load state.

The proposed VFT can change the driving torque of the permanent magnet synchronous drive subsystem by adjusting the stator control windings. In this way, we can control the size and direction of the active power delivered by the VFT. Change the amplitude and power angle of the stator winding voltage when the rotor side is on load state, that is, at first, the stator side is connected to the 15kV, 45Hz power grid, and the rotor rotates in the reverse direction of 300r/min, then change the amplitude and power angle of the stator winding voltage at *t*=800ms, and the result of power transfer is shown in Fig. 13.

In Fig. 13 (a), when *t*=800ms, the control voltage is positive phase sequence 750V, 30Hz, power angle is 10°, the input power of permanent magnet synchronous system is about 0.628MW, the transmission power is 7.57MW. In Fig. 13 (b), the control voltage is positive phase sequence 1000V, 30Hz, power angle is 15°, the input power of permanent magnet synchronous system

is about 0.9425MW, and the transmission power is 10.82MW. Both cases basically meet the power transfer relationship, to a certain extent, proving that the proposed VFT design is reasonable.

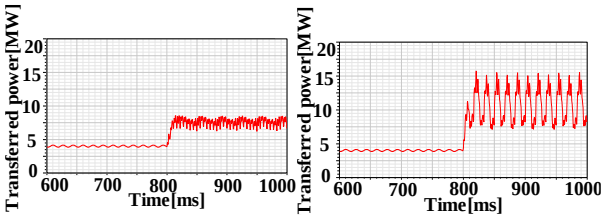

Fig. 13. Transfer power at different control voltage.

V. CONCLUSION

In this paper, a structure of inverter with integrated drive motor is proposed. This VFT is modeled and analyzed by finite element analysis. By comparing and analyzing the magnetic field relationship between the VFT subsystem and the permanent magnet synchronous control system under their respective operation and interaction, the analysis of the air gap magnetic field, the coupling analysis of the power winding and the control winding shows that their mutual influence is small, and thus a reasonable decoupling is realized. The simulation of grid connection between stator and rotor power winding is carried out. After frequency mutation at one side, adjusting the rotor speed by controlling winding can keep the frequency of the other side relatively stable, and transmit power smoothly. By changing the input torque and power provided by the permanent magnet control system, the power of the winding will change along the rotor side, which proves effectiveness of the proposed VFT structure.

ACKNOWLEDGMENT

This work has been supported by the Top-notch Academic Programs Project of Jiangsu Higher Education Institutions PPZY2015B132 and the National Natural Science Foundation of China (U1610113).

REFERENCES

[1] B. B. Ambati and V. Khadkikar, "Variable frequency transformer configuration for decoupled active-reactive powers transfer control," *IEEE Transactions on Energy Conversion*, vol. 31, no. 3, pp. 906-914, 2016.

[2] A. Merkhouf, S. Upadhyay, and P. Doyon, "Variable frequency transformer - An overview," *Power Engineering Society General Meeting, IEEE*, 2006.

[3] R. Lerch, M. Kaltenbacher, H. Landes, J. Hoffelner, M. Rausch, and M. Schinnerl, "Advanced transducer modeling using the finite element method," *International Journal of Applied Electromagnetics & Mechanics*, vol. 17, no. 1, pp. 59-73, 2003.

[4] A. Merkhouf, P. Doyon, and S. Upadhuay, "Variable frequency transformer-concept and electromagnetic design evaluation," *IEEE Journals & Magazines*, vol. 23, no. 4, pp. 989-996, 2008.

[5] F. I. Bakhsh, M. Irshad, and M. S. J. Asghar, "Modeling and simulation of variable frequency transformer for power transfer in-between power system networks," *India International Conference on Power Electronics*, pp. 1-7, 2011.

[6] E. T. Raslan, A. S. Abdel-Khalik, M. A. Abdulla, and M. Z. Mustafa, "Performance of VFT when connecting two power grids operating under different frequencies," *IET International Conference*, pp. 1-6, 2010.

[7] K. Jemaï, "Intelligent integration strategies of wind farms in a super grid," *Journal of Intelligent & Fuzzy Systems*, vol. 31, no. 1, pp. 275-290, 2016.

Xianming Deng was born in Sichuan, China. He received his B.S., M.S., and Ph.D. in Electrical Engineering from China University of Mining and Technology, Jiangsu, China. He is currently a Professor in the School of Electrical and Power Engineering of China University of Mining and Technology. His current research interests include power electronics and motor drive.

Na Liu was born in Anhui, China. She received her B.S. in Electrical Engineering from China University of Mining and Technology, Jiangsu, China. She is currently receiving a Master education at China University of Mining and Technology. Her current research interests include power electronics and motor drive.

Yuanda Sun was born in Henan, China. He received his B.S. in Electrical Engineering from University of Electronic Science and Technology of China, Sichuan, China. He is currently receiving a Master education at China University of Mining and Technology. His current research interests include power electronics and motor drive.

Qifeng Guo was born in Jiangsu, China. He received his B.S. and M.S. in Electrical Engineering from China University of Mining and Technology, Jiangsu, China. He is currently an Electrical Engineer in State Grid Chuzhou Electric Power Supply Company. His current research interests include design and applications of permanent-magnet machines and drives, and distributed resources connected to power grid.

Miaofei Zhang was born in Inner Mongolia, China. She received her B.S. in Electronic Science and Technology and her M.S. in Communication and Information System from China University of Mining and Technology, Jiangsu, China. She is currently an Assistant in School of Computer Information Engineering of Chuzhou University. Her current research interests include wireless technology and micro-electromechanical systems.

Performance Analysis of Outer Rotor Wound Field Flux Switching Machine for Direct Drive Application

N. Ahmad [1], F. Khan [1], N. Ullah [1,2], and M. Z. Ahmad [3]

[1] Department of Electrical Engineering
COMSATS Institute of Information and Technology, Abbottabad, Pakistan
n.ahmadmwt@gmail.com, faisalkhan@ciit.net.pk

[2] U.S.-Pakistan Center for Advanced Studies in Energy
University of Engineering & Technology, Peshawar, Pakistan

[3] Research Center for Applied Electromagnetics
Universiti Tun Hussein Onn Malaysia, Locked Bag 101, BattuPahat, Johor, 86400 Malaysia
zarafi@uthm.edu.my

Abstract ─ One of the premium in-wheel applications is direct drive, evolving enormously for HEV's. An alternative and lot of research especially on the outer rotor field excitation flux switching machine is required to overcome the problems like demagnetization and high cost of rare earth magnetic material used in interior permanent magnet synchronous machine (IPMSM). Salient rotor pole and non-overlapping winding embedded in electrical machine design possess some pertinent features such as; reduce copper losses, low-cost, and usage in high speed applications. Therefore, this paper emphasizes on the design of three-phase outer rotor wound field FSM employing optimization, performance analysis and MEC models of proposed 12-slot/13-pole FSM corresponding to different rotor positions are combined as GRN and are solved utilizing incidence matrix methodology using MATLAB. Moreover, FSM flux behavior, no-load, and load analysis were examined using JMAG software and based on FEA. Results obtained from GRN methodology and corresponding FEA results close resemblance with and errors less than ~1.2%, hence validating accuracy of GRN methodology. The proposed design for hybrid electric vehicle torque characteristic is compared with existing IPMSM and 6-slot/7-pole non-overlapping stator wound flux switching machine (NSWFS).

Index Terms ─ Deterministic optimization, flux switching machine, HEV's, outer rotor, MEC.

I. INTRODUCTION

Electric and hybrid electric vehicles are used to minimize environmental pollution and reduce usage of fossil fuels. HEV is an ideal solution to control global warming, reduce energy crisis, and minimize CO_2 emission [1]. Due to increased consumption of fossil fuels, their reservoirs are going down and price is going up. HEV is attracting interests of research community and automobile industry due to its unique property of utilizing electrical power (Batteries, Fuel Cells, etc.). Design of electric motor drives for EVs must show characteristics of high power density, high torque at low speed, quick torque response, high robustness, low torque ripples and noise, reliability, constant power at high speed and cost effective [2]-[3].

Design and structure of Flux Switching Machine (FSM) resembles with doubly salient permanent magnet machine [4]-[5], combining features of Permanent Magnet Machine and Switched Reluctance Machine. Flux sources (Permanent Magnet or Field Excitation Coil and Armature Winding) are confined to stator, leaving rotor completely passive. Due to this unique topology FSM is suited for high speed applications. FSM are categorized as Field Excited FSM (FEFSM), Permanent magnet FSM (PMFSM), and Hybrid Excited FSM (HEFSM). PMFSM and FEFSM comprise of FEC and PM respectively as their major flux sources whilst PM and FEC both are reasons for flux sources for HEFSM [6]-[7]. PMFSM comprise of rare earth magnet material and exhibits high efficiency and high torque density depending upon the type of material [8]-[9]. PM have drawbacks such as less robust, costly, reduction of flux density due temperature rises and time span. After discovery of rare earth PM material, it attracted interest of research community and industries.

To overcome the above-mentioned obstacles, the three phase non-overlapping field wound winding FSM with twenty-four teeth stators (12 slots for armature and 12 slots for field winding) is discussed in [10]. Model discussed [11] inner rotor non-overlapping stator wound

Submitted On: February 22, 2018
Accepted On: August 11, 2018

field synchronous machine that incorporated minimum torque ripple and high torque density. The inner rotor machine can belt with combustion engine. Outer rotor FEFSM used in HEV in wheel have advantages to eliminate mechanical transmission, drive belts, and differential gears and has high efficiency, increased vehicle space, and weight reduction [12].

ORFEFSM received attention of designers in the recent past and a lot of research is carried out in this field. Magnetic Equivalent Circuits (MEC) modeling, Finite Element Analysis (FEA) and Fourier Analysis (FA) are popular designing methodologies. MEC models with Reluctance Network Method (RNM) topology are preferred over other two methods due to disadvantages of FEA (computational complexity) and FA (less accuracy).

This paper emphasizes on the design of three-phase outer rotor wound field FSM employing salient rotor pole and non-overlapping winding. The profile of flux linkage and verified by MEC model and GRN network. Moreover, flux linkage, copper losses, iron losses, and efficiency versus current density are analyzed on 2D FEA. This study employing deterministic optimization in the enhancement of average torque, compared to existing IPM and 6-slot\7-pole NSWFS machines.

II. DESIGN METHODOLOGY

The basic principle of FEFSM depends upon the position of rotor because magnetic flux linkage may be either negative or positive in the armature winding with respect to the rotor position while stator, armature and excitation coil are stationary. Figure 1 illustrates the cross-sectional view of machine and design parameters are demonstrated in Table 1. The performance parameters of the proposed design are comparatively lower than wound field flux switching machine discussed in [13], [14]. The proposed motor 12-slot/ 13-pole ORFEFSM, in order to enhance the average electromagnetic torque characteristic, deterministic optimization technique is carried out. The magnetic flux distribution of un-optimized and optimized design depicts in Fig. 3.

In deterministic optimization back iron length, rotor pole width, stator pole width, and stator slot (FEC and armature) are consider as optimal free variables, and the optimal objective is electromagnetic torque. Firstly, change the rotor parameters (rotor pole width and length) while keeping constant all stator parameters to achieve optimal torque.

A. Optimization procedure

The proposed 12-slot/13-pole outer rotor FEFSM is optimized to enhance the torque characteristic. The initial torque achieved is 88.04 Nm, while the target torque 138 Nm. To achieve better performance, the rotor and stator parts have design parameters S1 to S7, as shown in Fig. 2 (a).

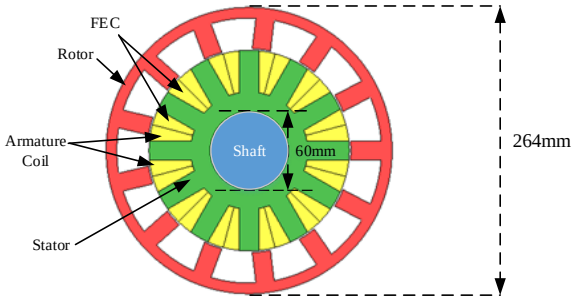

Fig. 1. Cross section of 12S/13P.

Table 1: Design parameters and comparison

Design Parameter	Un-Optimized	Optimized	IPM	NWFS
Number of stator slot	12	12	48	6
Number of rotor pole	13	13	8	7
Axial length (mm)	50.8	50.8	50.8	132
Stator outer diameter (mm)	132	132	132	50.8
Air gap(mm)	0.73	0.73	0.73	0.73
Split ratio	0.7	0.82	0.61	0.66
Stator tooth width (mm)	20	24	7.3	33.5
Back iron (mm)	9	10	20.2	17.5
Rotor pole arc (degree)	--	---	--	21.0
Rotor pole width	18	20	--	--

S1 and S2 are the rotor parameters, S3 is the radius of the stator, S4 is back iron of stator, S5 and S6 are the stator poles width, and S7 is armature coil parameter. Whereas, S1 and S2 are the depth and width of rotor pole, respectively. Deterministic optimization technique is applied to achieve targets requirements. In deterministic optimization technique, the air gap and slot area of armature coil and FEC are kept constant while a free parameter is changed. Firstly, change the rotor parameters S1 and S2 while keeping all free parameters of the stator constant. In order to accomplish maximum torque, rotor pole depth, S1 and rotor pole width, S2 are changed while other parameters are kept constant. Moreover, S3 is the most dominant parameter for attaining maximum torque and is updated as follows. Increasing the stator radius S3 will result in increasing the stator back iron length S4, while keeping armature slot area S7 and FEC slot area S6 constant. Once the maximum torque is achieved, the stator radius S3 and S4 are kept constant and S5, S6 and S7 are changed. Similarly, the optimal S5 value is also kept constant and S6 is updated. The torque improvements are shown in Fig. 2 (b).

Secondly, keeping constant rotor parameters and altering stator parameters (stator back iron length, stator

pole width, and stator slots). This process repeated up to three times to achieve maximum torque. The design optimization process and modification is reiterated until the maximum torque performance is achieved. After optimization process, the structure difference between initial and final design, as illustrated in Fig. 3. Moreover, the armature slot of final design has 29.93% higher depth than FEC slot to produce optimal magnetic flux.

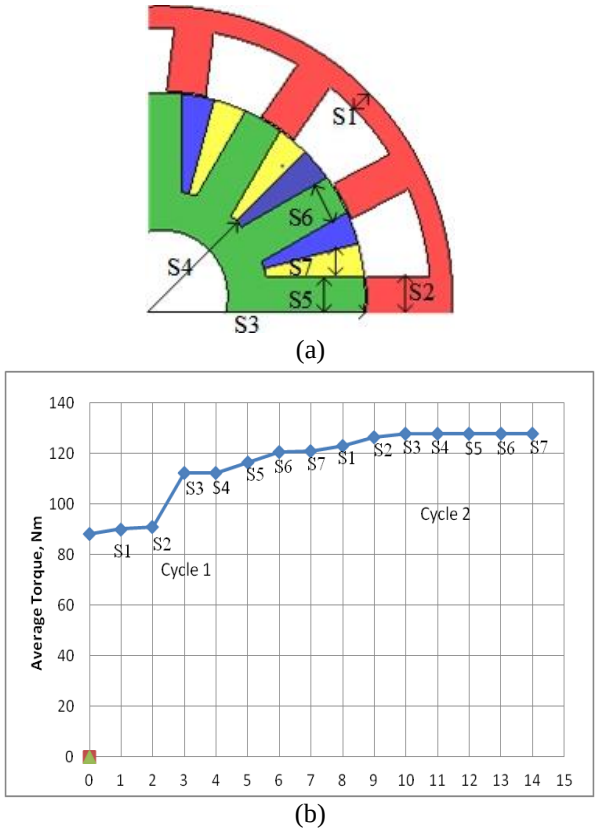

Fig. 2. (a) Design parameter for optimization; (b) average torque effect on different parameters.

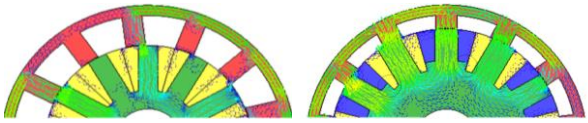

Fig. 3. The structure difference between initial and final design: (a) un-optimized and (b) optimized.

III. PERFORMANCE ANALYSIS

A. Coil test analysis

The operation principle of outer rotor FEFSM for HEV application is verified by coil arrangement test and investigating the magnetic flux linkage in each armature coil slot. Then a DC is supplied to FEC while AC is supplied to armature coils at maximum current density. Figure 4 illustrated the position of armature coil and Table 2 depicts combination of armature coil. The conventional three phase system simulated by 2D FEA using JMAG designer is represented by U, V, and W respectively as shown in Fig. 5. The direction of FEC coil is clockwise. The coil test is performed on no load condition and observed the magnetic flux linkage. The three phase flux linkage is verified by Magnetic Equivalent Circuit (MEC) as below discussed.

Table 2: Armature coil phase representation

Phases	Armature Coil
U	A1, A2, A7, A8
V	A5, A6, A11, A12
W	A3, A4, A9, A10

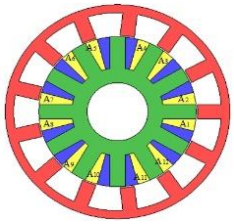

Fig. 4. Position of armature coil.

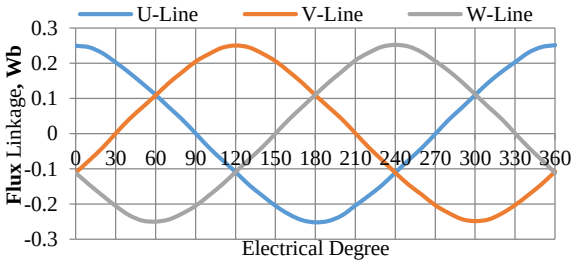

Fig. 5. Three phase flux linkage.

1) Magnetic equivalent circuit modules

Reluctance networks of 12slot/13pole ORFEFSM air gap magnetic equivalent circuit modules corresponding to different rotor positions, rotor magnetic equivalent circuit modules and stator magnetic equivalent circuit modules are combined as Global Reluctance Network (GRN). To avoid computational complexity, half machine is modeled under different segments corresponding to rotor position. Air gap flux distribution mainly contribute to performance of ORFEFSM, as conversion of electrical machine energy takes place in this medium. Air gap MEC modules are sensitive to rotor tooth position, each MEC module repeats itself after specified rational position which suggest possibilities of reducing verities of GRN.

As the rotor position changes, air gap flux paths or flux tubes changes resulting in changed flux tube permeance and also flux concentration. Area that encloses

flux lines is defined as flux tubes [15]. To reduce errors and uplift accuracy of GRN, flux tubes permeance must be calculated accurately. Flux tubes for different rotor positions were analyzed based on position state shifting and concluded about periodic nature as these flux tubes are repeated, therefore half machine model is investigated. Various combinations of air gap magnetic equivalent circuit modules corresponding to different rotor positions are implemented, variation of air gap flux distribution is expressed as series of MEC modules and is termed as GRN.

Figure 6 (a) and Fig. 6 (c) shows flux tubes having identical lengths of flux lines. Equation (1) is used to calculate total reluctance (R) of flux tube as a line integral through the curve:

$$R = \int_l \frac{1}{\mu A} dl. \quad (1)$$

Where, μ is material's permeability, l is curve of enclosed flux lines, dl length element through l, and A is area of the face perpendicular to l. Both A and μ may vary through the curve l.

Figure 6 (b) and Figs. 6 (d-f) shows the flux tubes having different lengths of flux lines and identical cross-section faces. Equation (2) is used to calculate total permeance (P) of flux tube as a surface integral over the head face of this tube:

$$P = \iint_A \frac{\mu}{l} dA. \quad (2)$$

2) Air Gap MEC modules

FEA on 13/12 ORFEFSM is performed to model air gap magnetic flux distribution when rotor tooth travels in different segments. Where, A, dA, l, and μ are head face of flux tube, surface element on the head face, total length of a flux line originated from one face element, and material's permeability, respectively. Both l and μ can change over surface A. Six types of flux tubes are used in this paper (as shown in Fig. 6) and their respective permeance (P) calculation formulas are shown in Table 3. X-axis of flux tubes show flux paths (equally distributed lines) and Y-axis represents magnetic properties of each flux path (assumed to be homogenous). Figure 6 (a) and Fig. 6 (b) shows two types of flux tubes and their permeance calculations are done using cylindrical coordinate system to reduce computational complexity, while Figs. 6 (c-f) flux tubes permeance calculations are done using Cartesian coordinate system.

FEA are grouped into certain number of flux tubes as shown in Fig. 7 (a) (interval 1), Fig. 8 (a) (interval 2), Fig. 9 (a) (interval 3), Fig. 10 (a) (interval 4) and Fig. 11 (a) (interval 5). Figure 6 represents different types of flux tubes selected from Table 3 for permeance calculations. Permeance calculation for each flux tube is done by using equations introduced in Table 3. Five different airgap MEC modules with variable permeances are shown in Fig. 7 (b) (interval 1), Fig. 8 (b) (interval 2), Fig. 9 (b) (interval 3), Fig. 10 (b) (interval 4) and Fig. 11 (b) (interval 5) as shown in Table 4. Multiple parallel permeances are reduced to single branch permeance and four different topologies are presented in Fig. 7 (c) (interval 1), Fig. 8 (c) (interval 2), Fig. 9 (c) (interval 3), Fig. 10 (c) (interval 4) and Fig. 11 (c) (interval 5).

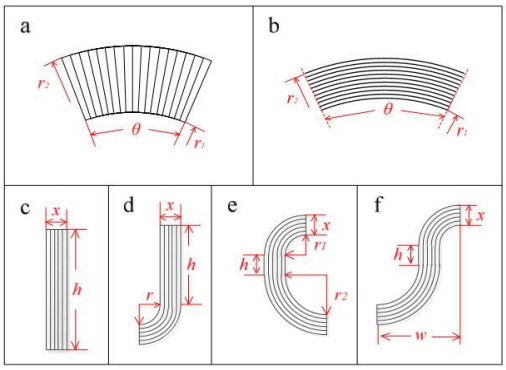

Fig. 6. Flux tubes.

Table 3: Formulas

Flux Tubes	Permeance (P)	Flux Tubes	Permeance (P)
a	$\frac{\mu L\theta}{\ln(\frac{r_2}{r_1})}$	d	$\frac{2\mu L.\ln\left(1+\frac{\pi x}{\pi r+2h}\right)}{\pi}$
b	$\frac{\mu L\ln(\frac{r_2}{r_1})}{\theta}$	e	$\frac{\mu L.\ln(1+\frac{2\pi x}{\pi r_1+\pi r_2+2h})}{\pi}$
c	$\frac{\mu Lx}{h}$	f	$\frac{2\mu Lx}{(\pi w+2h)}$

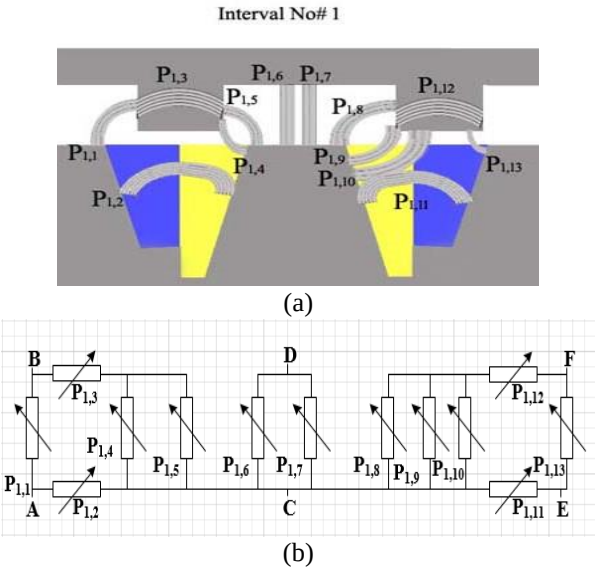

(a)

(b)

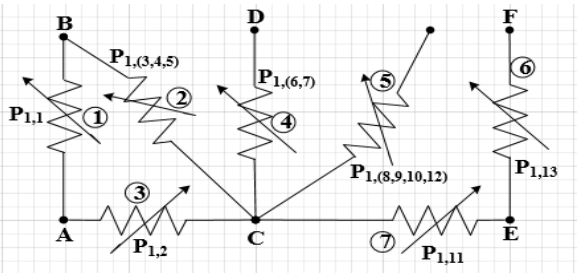

(c)

Fig. 7. Air gap MEC Module 1: (a) flux tubes corresponding to rotor tooth for interval No. 1, (b) detailed MEC, and (c) MEC topology.

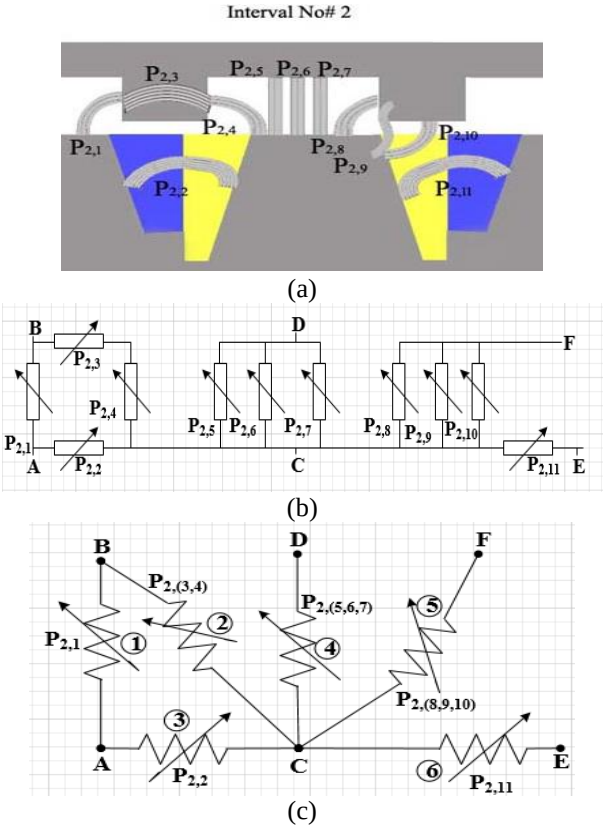

(a)

(b)

(c)

Fig. 8. Air gap MEC Module 2: (a) flux tubes corresponding to rotor tooth for interval No. 2, (b) detailed MEC, and (c) MEC topology.

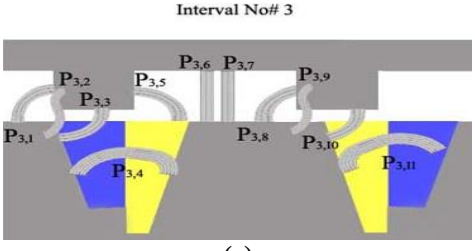

(a)

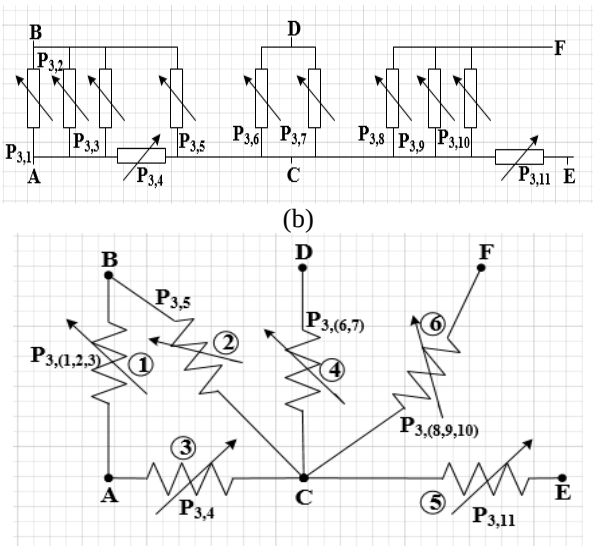

(b)

(c)

Fig. 9. Air gap MEC Module 3: (a) flux tubes corresponding to rotor tooth for interval No. 3, (b) detailed MEC, and (c) MEC topology.

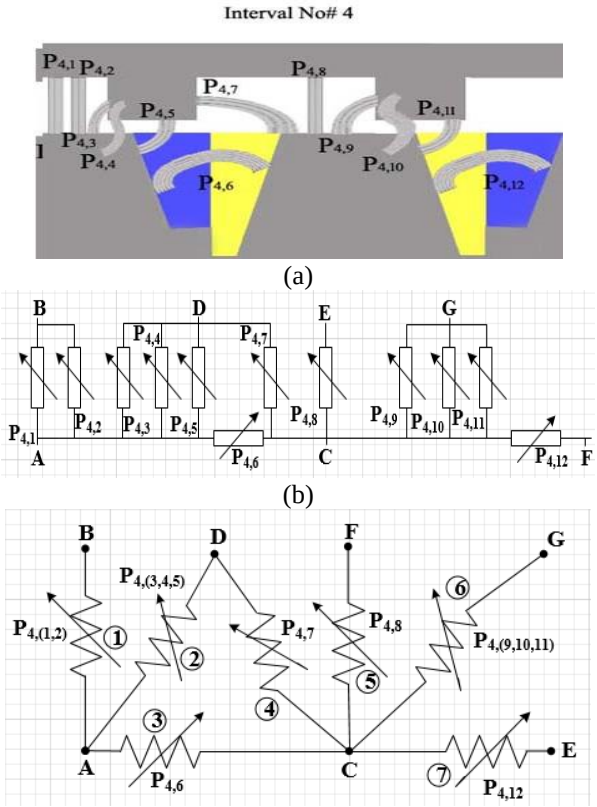

(a)

(b)

(c)

Fig. 10. Air gap MEC Module 4: (a) flux tubes corresponding to rotor tooth for interval No. 4, (b) detailed MEC, and (c) MEC topology.

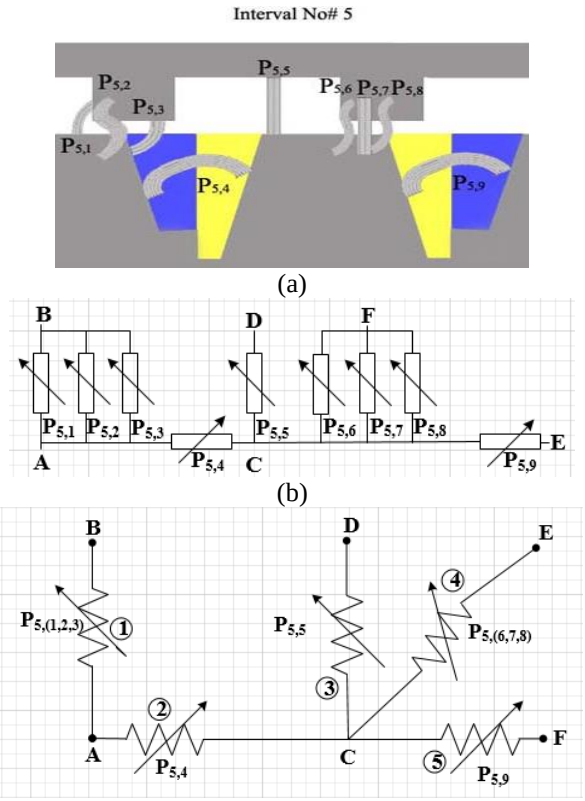

Fig. 11. Air gap MEC Module 5: (a) flux tubes corresponding to rotor tooth for interval No. 5, (b) detailed MEC, and (c) MEC topology.

Table 4: Flux tubes in different air gap MEC Modules

Flux Tube Number	1	2	3	4	5	6	7	8	9	10	11	12	13
P1,j	D	E	B	D	D	C	C	D	D	D	E	B	D
P2,j	D	E	B	D	C	C	C	D	F	D	E	-	-
P3,j	D	F	D	E	D	C	C	D	F	D	E	-	-
P4,j	C	C	D	F	D	E	D	C	D	F	D	E	-
P5,j	D	F	D	E	C	F	C	F	E	-	-	-	-

3) Solution methodology

Five air gap MEC modules numbered as T1-T5, S1-S6, and A1-A5, respectively are used to model ORFEFSM due to its periodic nature. Repeatability of this specific 13/12 ORFEFSM allows to model only half of the machine as shown in Fig. 12. Air gap MEC modules are sensitive to rotor tooth position and results in different reluctance network topologies corresponding to change in rotor position.

Magnetic potentials of each node are computed by describing MEC modules mathematically as matrices; these matrices are merged to form GRN and solved using incidence matrix method [16] in MATLAB. Main features of incidence matrix method are explained as follows.

Incidence matrix A of a circuit having m nodes and n branches is m x n matrix, in which:

$$\boldsymbol{A}_{i,j} = \begin{cases} 1, & if\ branch\ j\ begins\ from\ node\ i, \\ -1, & if\ branch\ j\ ends\ to\ node\ i, \\ 0, & if\ branch\ j\ ends\ to\ node\ i. \end{cases} \quad (3)$$

Other important variables of aforementioned m x n matrix are defined as matrix or vector as follows:

A: incidence matrix (m x n matrix),
U: mmf drop across each branch (n x 1 vector),
V: magnetic potential on each node (m x 1 vector),
E: mmf source in each branch (n x 1 vector),
Φ: flux through each branch (n x 1 vector),
R: reluctance of each branch (n x n diagonal matrix),
Λ: permeance of each branch (n x n diagonal matrix).

Following equations are derived according to Kirchhoff Circuit Laws:

$$U = \boldsymbol{A}^t . V, \quad (4)$$

$$\boldsymbol{A} . \Phi = 0, \quad (5)$$

$$U = \boldsymbol{R} . \Phi + \mathrm{E} = \boldsymbol{\Lambda}^{-1} . \Phi + \mathrm{E}. \quad (6)$$

Equation for magnetic potential (utilizing **A**, **Λ**, and E) can be written as:

$$V = (A . \Lambda . A^t)^{-1} . (A . \Lambda . \mathrm{E}). \quad (7)$$

Magnetic potentials of each node are calculated by using Eq. (7) that ultimately helps to compute magnetic flux through each flux tube.

4) Validation with finite element analysis

Accuracy of nonlinear magnetic equivalent circuit models and GRN methodology for 12slot/13pole ORFEFSM is validated by comparing open-circuit phase flux linkage with corresponding FEA results. Magnetic parameters and geometric dimensions of 12slot/13pole ORFEFSM are summarized in Table 1. Comparison of open-circuit phase flux linkage obtained for GRN methodology and FEA is presented in Fig. 13. Error of open-circuit phase flux linkage between GRN methodology and FEA results is also computed and shown in Fig. 14. Results obtained from GRN methodology fairly match FEA results, as errors are less than ~1.2%, hence validating accuracy of GRN methodology.

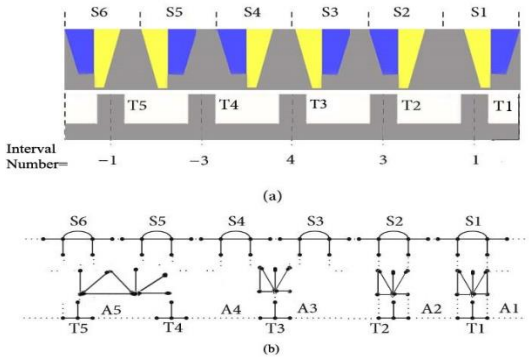

Fig. 12. Global MEC of 12S-13P ORFEFSM.

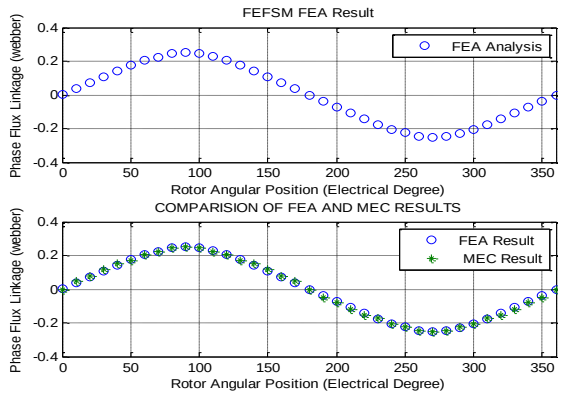

Fig. 13. Combine FEA and MEC.

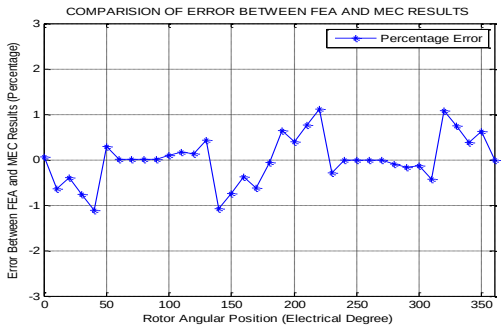

Fig. 14. Error between FEA and MEC.

B. Flux linkage

Figure 15 presents the magnetic flux linkage of ORFEFSM un-optimized and optimized design under the armature current density J_a is set to be 0A\mm^2 and it can be observed that the flux linkage boosted with armature current density while keeping the maximum current density of field excitation coil constant. Figure 15 depicts that highest flux linkage of optimized design is 0.252Wb and un-optimized design 0.143Wb and the optimized flux linkage 76.22 percent greater than un-optimized design.

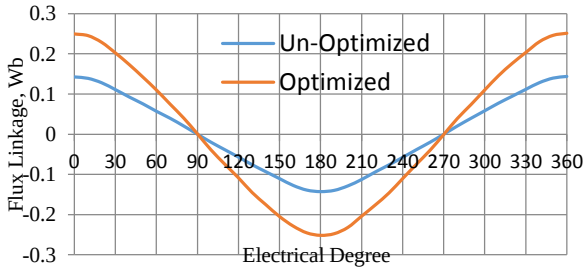

Fig. 15. U-flux lines.

C. Average electromagnetic torque

Figure 16 presents the torque verses armature current density (Ja) curves at various armature current density keeping current density (Je) of FEC coil constant. Figure 16 depicts the torque comparison between un-optimized and optimized design and also shows that's by increasing armature current density the torque will increased too and 0A\mm^2 to 30A\mm^2 varies armature current density and kept constant maximum field excitation coil current density and simulated the design and observed average electromagnetic torque. In comparison the optimal torque of optimized design 129.513Nm is achieved by ORFEFSM at maximum field excitation and armature current density (J_a = J_e = 30A\mm^2), which is approximately 45.52 percent greater than un-optimized design. One of the best advantages of FEFSM is the control the average electromagnetic torque by both armature and field current.

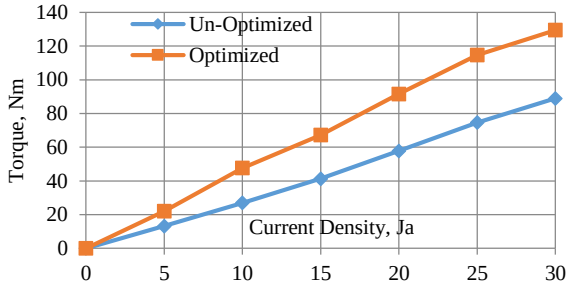

Fig. 16. Comparison of average electromagnetic torque.

D. Efficiency and losses

Figure 17, as illustrated, the efficiency, copper losses, and iron losses of the proposed design 12-slot\13-pole ORFEFSM. The copper losses are calculated from the Eq. 8 [17]:

$$Pc = \rho(2L + 2L_{end}) \times J \times I \times N \times N_{slot}. \quad (8)$$

Where L, L_{end}, and Pc is the stack length, estimated end coil length, and copper losses respectively, while N, J, N_{slot}, and I are number of turns, current density, number of stator slot, and current respectively and ρ is resistivity of copper, having 2.224×10^{-8} Ωm constant value. In Figs. 17 (a), (b) depicts the copper losses and iron losses analysis of 12-slot\13-pole ORFEFSM. The copper and iron losses decreases with employing optimization and after optimization the copper losses reduce up to 10 percent while iron losses up to 32.85 percent decreases. It's observed that the increasing armature current density also increase in copper losses and while decrease in iron losses.

The copper losses of FEC coil and armature windings are analytically determined from their geometries, by taking into consideration the end coil effect. Furthermore, the iron losses including eddy current and hysteresis losses are calculated by 2D- FEA solver providing loss data sheet of 35H210 material.

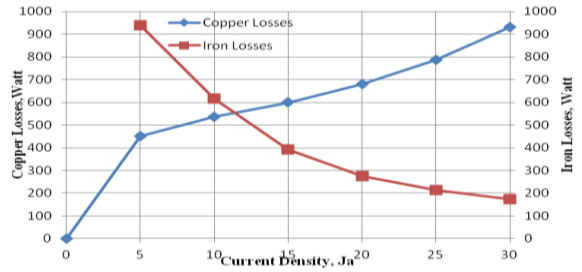

(a)

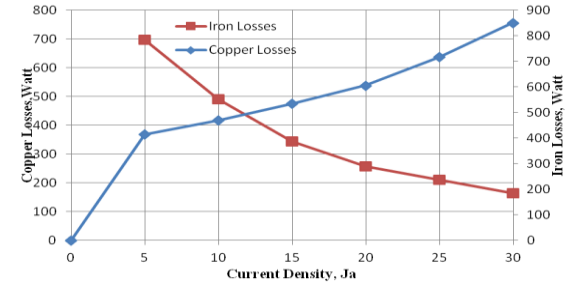

(b)

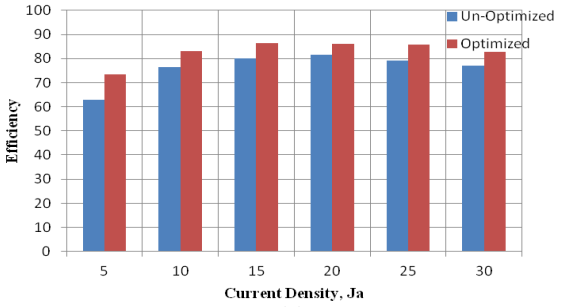

(c)

Fig. 17. (a) Copper and iron losses of un-optimized design, and (b) copper and iron losses of optimized design; (c) efficiency analysis.

Figure 17 (c) illustrates that un-optimized and optimized design efficiency bar graph between the efficiency versus the armature current J_a while keeping constant field excitation coil current density J_e. The efficiency of both designs of machine is lowest at J_a 5 A/mm^2 as presented in Fig. 17 (c). Due to less current density there are less copper losses and high iron losses due to high speed. The average efficiency of both un-optimized and optimized machine is 76.175 percent and 82.90 percent respectively and 8.2 percent efficiency of optimized design greater than un-optimized design. The copper losses are calculated form Eq. 8 and using bundle of wires. The current density at 15 A/mm^2 the machine has low speed which causes less iron losses leads to maximum efficiency. Increase in current density beyond 15 A/mm^2, copper losses increases and ultimately decrease in efficiency is observed.

IV. TORQUE COMPARISON

Figure 18 illustrates the torque verses armature current density (Ja) curves at various armature current density keeping current density (Je) of FEC coil constant. At the highest Ja and Je of 30A\mm^2 of ORFEFSM is achieved 129.53Nm torque. As armature current density increasing torque also increase approximately linear. In the figure it compares ORFEFSM with IPM and 6-slot\7-pole NSWFS.

Internal Permanent Machine (IPM) is successfully installed and commercialized for HEV's by the Toyota Prius company. The performance parameter of IPM and 6-slot\7-pole NSWFS are published in [14]. These two machines use as bench mark. A 6-slot\7-pole NSWFS is relatively the best machine compared with other machines because of high torque density. This machine achieving approximately 60% torque density of IPM torque density at same current density. Figure 18 depicts the average torque verses current density of IPM and 6-slot\7-pole NSWFS machine [15].

The proposed motor 12-slot\13-pole ORFEFSM has been optimized to achieving maximum average torque. For performance comparison make 12-slot\13-pole motor similar size as IPM machine. The figure shows that 12-slot\13-pole ORFEFSM can achieve average torque approximately 57% of IPM and 95% of 6-slot\7-pole NSWFS.

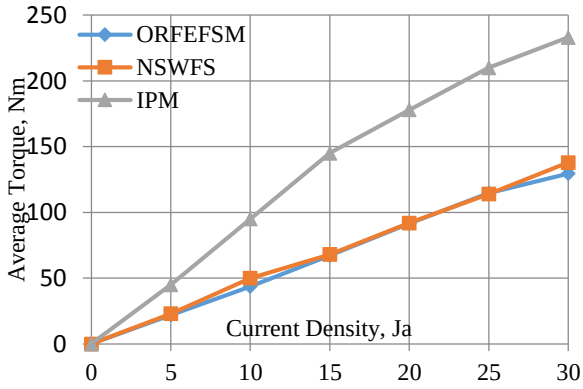

Fig. 18. Average electromagnetic torque comparison.

V. CONCLUSION

The proposed machine comprises of outer rotor, non-overlapping winding, and robust rotor structure resulting in reduced copper losses, low cost, high efficiency, and high-speed applications. The no-load and load analysis were examined to validate the efficacy of proposed machine design. Moreover, the profile of flux linkage, average electromagnetic torque, copper losses, iron losses and torque versus current density were analyzed on 2D FEA. Magnetic equivalent circuit (MEC) in air gap corresponding to different rotor positions and combined MEC models as Global Reluctance Network (GRN) and are solved utilizing incidence matrix methodology. Accuracy of nonlinear magnetic equivalent circuit models and GRN methodology for 12slot/13pole ORFEFSM is validated by comparing open-circuit

phase flux linkage with corresponding FEA results, and shows less than ~1.2% error. The initial design achieved inadequate power and torque production. Therefore, a deterministic optimization technique was adopted in this study that assisted in enhancement of power, torque, and efficiency compared to existing IPM and 6-slot\7-pole NSWFS machines.

REFERENCES

[1] W. Fei, P. C. K. Luk, J. X. Shen, Y. Wang, and M. Jin, "A novel permanent-magnet flux switching machine with an outer-rotor configuration for in-wheel light traction applications," *IEEE Transactions on Industry Applications*, vol. 48, pp. 1496-1506, 2012.

[2] J. T. Chen and Z. Q. Zhu, "Comparison of all-and alternate-poles-wound flux-switching PM machines having different stator and rotor pole numbers," *IEEE Transactions on Industry Applications*, vol. 46, pp. 1406-1415, 2010.

[3] Z. Q. Zhu and D. Howe, "Electrical machines and drives for electric, hybrid, and fuel cell vehicles," *Proceedings of the IEEE*, vol. 95, pp. 746-765, 2007.

[4] I. Boldea, C. Wang, and S. A. Nasar, "Design of a three-phase flux reversal machine," *Electric Machines & Power Systems*, vol. 27, pp. 849-863, 1999.

[5] R. P. Deodhar, S. Andersson, I. Boldea, and T. J. Miller, "The flux-reversal machine: A new brushless doubly-salient permanent-magnet machine," *IEEE Transactions on Industry Applications*, vol. 33, pp. 925-934, 1997.

[6] C. Pollock, H. Pollock, R. Barron, J. R. Coles, D. Moule, A. Court, *et al.*, "Flux-switching motors for automotive applications," *IEEE Transactions on Industry Applications*, vol. 42, pp. 1177-1184, 2006.

[7] X. Liu and Z. Q. Zhu, "Comparative study of novel variable flux reluctance machines with doubly fed doubly salient machines," *IEEE Transactions on Magnetics*, vol. 49, pp. 3838-3841, 2013.

[8] J. T. Chen and Z. Q. Zhu, "Comparison of all-and alternate-poles-wound flux-switching PM machines having different stator and rotor pole numbers," *IEEE Transactions on Industry Applications*, vol. 46, pp. 1406-1415, 2010.

[9] E. Sulaiman, T. Kosaka, and N. Matsui, "A new structure of 12slot-10pole field-excitation flux switching synchronous machine for hybrid electric vehicles," in *Power Electronics and Applications (EPE 2011), Proceedings of the 2011-14th European Conference on*, , pp. 1-10, 2011.

[10] F. Khan, E. Sulaiman, and M. Ahmad, "Coil test analysis of wound-field three-phase flux switching machine with non-overlapping winding and salient rotor," in *Power Engineering and Optimization Conference (PEOCO), 2014 IEEE 8th International*, pp. 243-247, 2014.

[11] F. Khan, E. Sulaiman, and M. Z. Ahmad. "A novel wound field flux switching machine with salient pole rotor and nonoverlapping windings," *Turkish Journal of Electrical Engineering & Computer Sciences*, vol. 25, pp. 950-964, 2017.

[12] W. Fei, P. Luk, J. Shen, and Y. Wang, "A novel outer-rotor permanent-magnet flux-switching machine for urban electric vehicle propulsion," in *Power Electronics Systems and Applications, 2009. PESA 2009. 3rd International Conference on*, pp. 1-6, 2009.

[13] Z. Q. Zhu, Y. Zhou, and J. T. Chen, "Electromagnetic performance of nonoverlapping stator wound field synchronous machine with salient pole rotor," *IEEE Transactions on Magnetics*, vol. 51, pp. 1-4, 2015.

[14] Z. Q. Zhu, Y. Zhou, J. T. Chen, and J. E. Green, "Investigation of nonoverlapping stator wound-field synchronous machines," *IEEE Transactions on Energy Conversion*, vol. 30, pp. 1420-1427, 2015.

[15] V. Ostovic, *Dynamics of Saturated Electric Machines*. Springer Science & Business Media, 2012.

[16] L. O. Chua and P. Y. Lin, *Computer-Aided Analysis of Electronic Circuits: Algorithms and Computational Techniques*. Prentice Hall Professional Technical Reference, 1975.

[17] F. Khan, E. Sulaiman, and M. Z. Ahmad, "Review of switched flux wound-field machines technology," *IETE Technical Review*, vol. 34, pp. 343-352, 2017.

Naseer Ahmad was born in 1992 in Lakki Marwat, KPK, Pakistan. He received his Bachelor degree in Electrical Power Engineering in 2015 Form UET, Peshawar, Pakistan and is currently enrolled in M.S. Electrical Power Engineering from COMSATS Institute of Information Technology, Abbottabad, Pakistan. His research interests are Optimization and Outer rotor flux switching machine.

Faisal Khan was born in Charsadda, KPK, Pakistan, on 20 June 1986. He received his B.S. and M.S. degree in Electrical Engineering from COMSATS Institute of Information Technology, Pakistan, in 2009 and 2012, respectively. He has been a Lecturer at COMSATS Institute of

Information Technology, Pakistan since 2012. He did his Ph.D. degree in Electrical Engineering at Department of Electrical Power Engineering, University Tun Hussein Onn Malaysia. His research interests include design and optimizations of wound field flux switching machines with salient rotor, Permanent magnet flux switching machines, Hybrid Excited flux switching machines and Linear Machines.

Noman Ullah is serving as Lecturer at Electrical Engineering Department, COMSATS Institute of Information Technology, Abbottabad, Pakistan. He earned B.S. in Electrical (Power) Engineering from COMSATS Institute of Information Technology, Abbottabad, and Masters in Electrical (Power) Engineering from University of Engineering & Technology, Peshawar in 2012 and 2015, respectively. His research interest includes analytical modelling and design of Permanent Magnet, Field Excited and Hybrid Excited Flux Switching Machines.

Md Zarafi Ahmad was born in Johor, Malaysia, on 11 July 1979. He received his B.E. degree in Electrical Engineering from University Technology Mara in 2003 and M.E. degree in Electrical Engineering from University Technology Malaysia in 2006. He did his Ph.D. degree in Electrical Engineering at Department of Electrical Power Engineering, University Tun Hussein Onn Malaysia. He has been Senior Lecturer at University Tun Hussein Onn Malaysia since 2006. His research interests including electrical machine and drive control.

Comparison of Analytical Methodologies for Analysis of Single Sided Linear Permanent Magnet Flux Switching Machine: No-Load Operation

Noman Ullah [1,2], Muhammad Kashif Khan [2], Faisal Khan [1], Abdul Basit [2], Wasiq Ullah [1], Tanvir Ahmad [2], and Naseer Ahmad [1]

[1] Department of Electrical Engineering
COMSATS University Islamabad (Abbottabad Campus), Abbottabad, 22060, Pakistan
(nomanullah, faisalkhan)@ciit.net.pk

[2] U.S.-Pakistan Center for Advanced Studies in Energy
University of Engineering & Technology, Peshawar, 25000, Pakistan
(abdul.basit, tanvir.ahmad)@uetpeshawar.edu.pk, kashifkhanmarwat@yahoo.com

Abstract ─ A novel single sided Linear Permanent Magnet Flux Switching Machine (LPMFSM) with twelve mover slots and fourteen stator teeth (12/14), having two additional end teeth on both sides of mover is presented. Presence of both Armature Winding (AW) and Permanent Magnet (PM) on mover structure results in completely passive, robust, and low cost stator. While, demerits such as less slot area, complex flux density distribution, and magnetic saturation caused by passive stator demands to be analyzed by time consuming and computationally complex numerical modelling techniques, i.e., Finite Element (FE) Analysis, requiring expensive hardware/software. In this paper, two cost effective and fast response analytical techniques are developed to analyze no-load performance of LPMFSM. Two no-load characteristics, i.e., open-circuit flux linkage and detent force are analyzed by Equivalent Magnetic Circuit (termed as analytical technique No. 1) and Lumped Parameter Equivalent Magnetic Circuit (termed as analytical technique No. 2). Both analytical methodologies are compared and validated with corresponding globally accepted FE Analysis. Analysis revealed that LPEMC is better approach for initial design of LPMFSM.

Index Terms ─ Equivalent Magnetic Circuit, Finite Element Analysis, Linear Permanent Magnet Flux Switching Machine, Lumped Parameter Equivalent Magnetic Circuit.

I. INTRODUCTION

Rotary machines used for translational motion exhibit low efficiency and high cost due to requirement of sophisticated gear system for conversion of rotational torque to linear thrust force. Linear motors can provide direct linear thrust force, increased reliability due to reduction of mechanical conversion system, faster dynamic response, and good overload capability [1].

LPMFSM combines features of Linear Permeant Magnet Synchronous Machine (LPMSM) and Linear Switched Reluctance Machine with additional advantages of high power density [2], bipolar flux linkage, ability to re-magnetize PMs by changing the winding connections appropriately when PM performance is degraded, robust stator structure [3], lowered manufacturing cost [4], and compatibility with extreme environmental conditions due to better temperature control. LPMFSM can be used for long stroke applications such as rail transportation systems [5], short stroke oscillatory applications [6] such as rope-less elevators and long telescopes, and also as linear generator for wave energy extraction [7].

Numerous modelling techniques can be implemented for design and analysis of linear machines. These techniques can be enveloped as: (a) analytical, and (b) numerical techniques. Analytical techniques are preferred at initial design stage, and numerical methods are implemented for verification and refinement at the end of design process [8].

Limitations and demerits of LPMFSM such as complex mover structure and less slot area (due to presence of both PMs and armature windings), complex flux density distribution, and magnetic saturation caused by passive stator demands to be analyzed by time consuming and computationally complex numerical modelling techniques, i.e., FEA, requiring expensive hardware/software.

To increase computational ease, fast but accurate analytical modelling techniques are essential in the early development phase for the analysis and assessment of different concepts. Authors of [9] researched an analytical model based on formal solution of Maxwell's equations and examined open-circuit performance (cogging force, electromotive force, and iron losses) for Permanent Magnet Linear Machine (PMLM). Author

Submitted On: May 15, 2018
Accepted On: June 17, 2018

claimed about: (a) very good agreement of analytical model results with corresponding FEA results, and (b) reduction of computational time by almost six times required for FE Analysis. Three dimensional analytical magnetic charge model is implemented on transverse flux machine to minimize machine volume with fixed constraints on magnetic flux density and slot leakage, calculated propulsion force shows errors of only 8.9% to corresponding FE Analysis results [10]. On-load detent force calculations by considering magnetic saturation utilizing Frozen Permeability (FP) method is done in [11], and is validated by Maxwell Stress Tensor (MST) method and FE Analysis. Recently, authors of [12] researched an analytical method to calculate right/left detent end force of LPMSM, investigated novel technique to minimize fundamental and high-order harmonics of detent force, and finally analytical calculations are verified with experimental results.

However, literature about analytical techniques developed for LPMFSM is very limited ([13], [14]), and require immediate attention to enhance pre-design predictions. Authors of [13] combined response surface methodology with FE Analysis to calculate influence of design parameters on the LPMFSM net thrust force. Hybrid analytical approach based on strong coupling of EMC and formal solution of Maxwell's equations for LPMFSM to predict magnetic flux density, cogging force, and electromotive force is developed in [14].

In this paper, a novel single sided LPMFSM with twelve mover slots and fourteen stator teeth (12/14), having two additional end teeth on both sides of mover is developed and simulated for open-circuit flux linkage utilizing JMAG Commercial FEA Package v. 14. Objective of this paper is to develop and compare two different analytical techniques for LPMFSM to analyze no-load characteristics of LPMFSM. Design variables and dimensions of LPMFSM are presented in Section II. Operating principle of LPMFSM is discussed in Section III. Section IV explains division of LPMFSM into different equivalent circuit modules, i.e., stator, mover, PM, and air-gap. Solution methodologies used for two different analytical modelling techniques (EMC and LPEMC) is presented in Section V. Analytical techniques are compared with each other in terms of accuracy and validated with globally accepted FE Analysis in Section VI. Finally conclusions are drawn in Section VII.

II. DESIGN METHODOLOGY

Figure 1 shows a rotary twelve-stator-slot and ten-rotor-teeth (12/10) Permanent Magnet Flux Switching Machine (PMFSM) with trapezoidal armature coil slot structure. Its open-circuit flux linkage was investigated in [15], cogging torque and electromagnetic torque were also investigated. Results show that its open-circuit flux linkage is higher than that of 12/10 PMFSM with rectangular armature coil slot structure, when other machine design parameters (such as coil slot area, number of turns per phase, PM thickness, stack length etc.) are kept constant. Rotary 12/10 PMFSM is unrolled at position shown in Fig. 1 to obtain LPMFSM. Performance of initial design suffers from an unbalanced magnetic circuit, to compensate the problem two additional end teeth are added at both sides of mover as shown in Fig. 2. Unbalanced magnetic circuit can introduce significant detent force and contribute to thrust force ripples. Additional end teeth mitigates problem of unbalanced magnetic circuit and reduces detent force [16]. Design variables are depicted in Fig. 3, and dimensions are illustrated in Table 1.

III. OPERATING PRINCIPLE

Operating principle of LPMFSM is illustrated in Fig. 4. When relative position of stator poles and a particular mover tooth is (assuming $\theta_e = 0°$) as shown in Fig. 4 (a), the coil flux-linkage is assumed as positive maximum value. When the mover moves to position $\theta_e = 90°$ as shown in Fig. 4 (b), the flux linkage of coil approaches to zero value. Flux linkage in coil is assumed as negative maximum value (as shown in Fig. 4 (c)) after further 90° movement, i.e., $\theta_e = 180°$. When the mover moves by one stator pole pitch ($\theta_e = 270°$, Fig. 4 (d)), the flux linkage of coil again approaches zero value. Figure 4 (e) explains that idealized flux linkage of LPMFSM is bipolar.

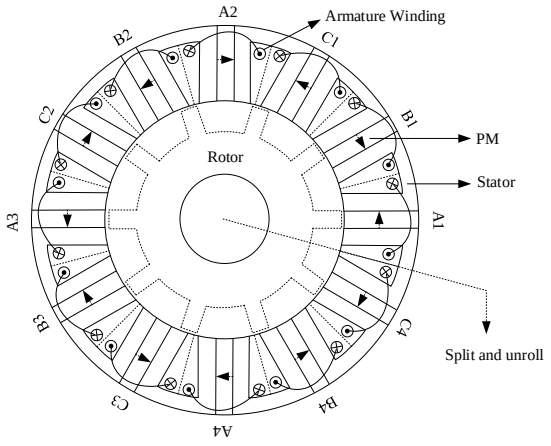

Fig. 1. Rotary 12/10 PMFSM.

IV. EQUIVALENT CIRCUIT MODULES

A. Air-gap equivalent circuit modules

In this paper, magnetic flux distribution within the region of air-gap between stator and mover is termed as air-gap Equivalent Circuit (EC). FE Analysis revealed that stator tooth position effects magnetic flux distribution within the air-gap region. To account air-gap magnetic flux distribution variation, multiple air-gap EC modules are modeled corresponding to different stator positions.

One mover pole pitch of 12/14 LPMFSM is modelled at different stator positions. Six different air-gap EC modules are constructed when one mover pole pitch covers linear displacement of one stator pole pitch.

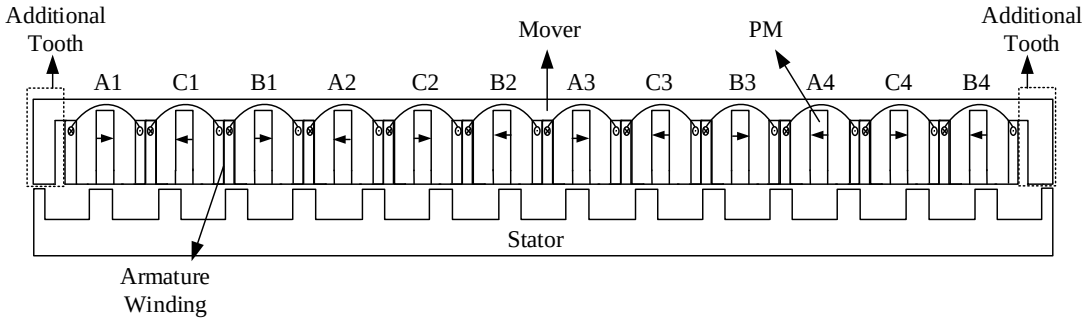

Fig. 2. Cross section of 12/14 LPMFSM.

As stator tooth enters different mover's position, different air-gap EC module is used with PM as its central axis. Due to periodic nature of LPMFSM (as illustrated in Section III), only six air-gap equivalent circuit modules are required.

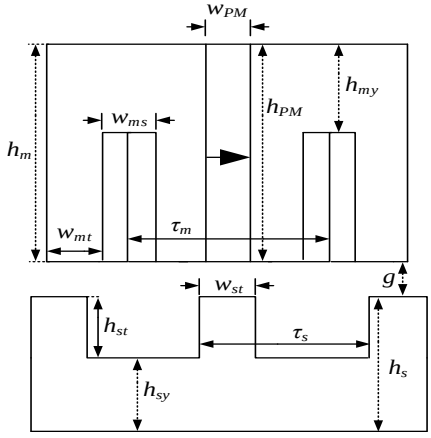

Fig. 3. Design parameters of mover and stator.

Flux lines follow specific paths to link between mover and stator, these paths are termed as Flux tubes [15, 17]. Six different flux tubes are observed during FE Analysis as shown in Fig. 5. Permeance of these flux tubes is calculated using formulas tabulated in Table 2 [17].

B. PM EC module

PM is modeled as Magnetomotive force ($\mathcal{F}_{PM}$) source with permeance in series. Equation (1) is used to calculate $\mathcal{F}_{PM}$:

$$\mathcal{F}_{PM} = \frac{B_r . w_{PM}}{\mu_0 \mu_r} . \quad (1)$$

C. Stator EC module

Unit section and its corresponding EC module of 12/14 LPMFSM stator is shown in Fig. 6 (a) and Fig. 6 (b). Branches of stator EC are illustrated by numbers, while nodes are introduced by alphabets. Permeance of stator back iron and stator tooth (P_{si} and P_{st}) are calculated using (2) and (3), respectively:

$$P(si) = \frac{\mu_0 \mu_r h_{sy} L}{t_s + h_{sy}} , \quad (2)$$

$$P(st) = \frac{\mu_0 \mu_r w_{st} L}{w_{st}} . \quad (3)$$

Table 1: Design dimensions of LPMFSM

Items	**Parameter**	**Unit**
Stator pole pitch $\boldsymbol{t_s}$	36	mm
Mover pole pitch $\boldsymbol{t_m}$	42	mm
Stack Length **L**	120	mm
Velocity $\boldsymbol{v}$	1.41	m/s
Mover tooth width $\boldsymbol{w_{mt}}$	10.5	mm
Stator tooth width $\boldsymbol{w_{st}}$	15.75	mm
Mover slot width $\boldsymbol{w_{ms}}$	10.5	mm
Mover back iron height $\boldsymbol{h_{my}}$	15.75	mm
Stator back iron height $\boldsymbol{h_{sy}}$	20	mm
Magnet width $\boldsymbol{w_{PM}}$	10.5	mm
Mover height $\boldsymbol{h_m}$	50	mm
Stator height $\boldsymbol{h_s}$	35	mm
Stator tooth height $\boldsymbol{h_{st}}$	15	mm
Magnet height $\boldsymbol{h_{PM}}$	10.5	mm
Air gap length $\boldsymbol{g}$	1	mm
PM remanence $\boldsymbol{B_r}$	1.2	T
PM relative permeability $\boldsymbol{\mu_r}$	1.05	-
Number of turn per coil $\boldsymbol{N_{coil}}$	116	-

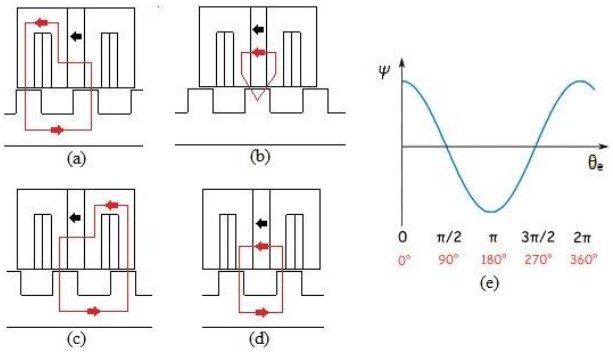

Fig. 4. Operating principle: (a) $\theta_e = 0°$, (b) $\theta_e = 90°$, (c) $\theta_e = 180°$, (d) $\theta_e = 270°$, and (e) Ideal flux linkage.

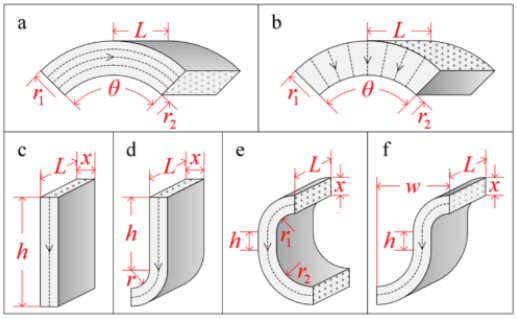

Fig. 5. Flux tubes obtained from FE Analysis.

Table 2: Permeance calculation formulas for flux tubes

Flux tube	Permeance	Flux tube	Permeance
a	$\frac{\mu L\theta}{\ln(\frac{r_2}{r_1})}$	d	$\frac{2\mu L.\ln\left(1+\frac{\pi x}{\pi r+2h}\right)}{\pi}$
b	$\frac{\mu L\ln(\frac{r_2}{r_1})}{\theta}$	e	$\frac{\mu L.\ln(1+\frac{2\pi x}{\pi r_1+\pi r_2+2h})}{\pi}$
c	$\frac{\mu Lx}{h}$	f	$\frac{2\mu Lx}{(\pi w+2h)}$

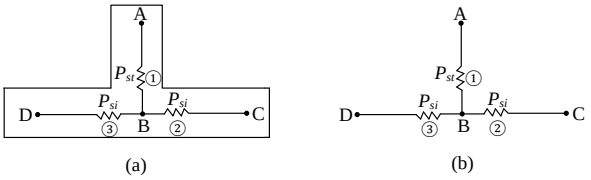

Fig. 6. Stator EC module: (a) stator section, and (b) EC of stator section.

D. Mover EC module

Unit section and its corresponding EC module of 12/14 LPMFSM mover is shown in Fig. 7 (a) and Fig. 7 (b). Branches of mover EC are illustrated by numbers, while nodes are introduced by alphabets. Permeance of mover back iron and mover tooth (P_{mi} and P_{mt}) are calculated using (4) and (5), respectively. Permeance of mover leakage (P_{ml}) is calculated using (6):

$$P(mi) = \frac{\mu_0 \mu_r h_{my} L}{t_m + h_{my}}, \tag{4}$$

$$P(mt) = \frac{\mu_0 \mu_r w_{mt} L}{w_{mt}}, \tag{5}$$

$$P(ml) = \frac{\mu_0 w_{PM} L}{t_m + w_{PM}}. \tag{6}$$

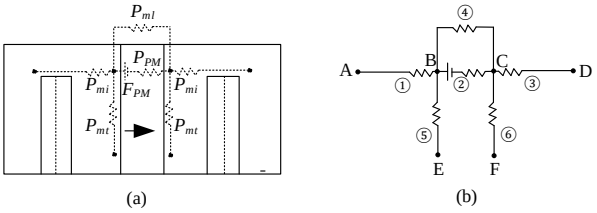

Fig. 7. Mover EC module: (a) mover section, and (b) EC of mover section.

V. SOLUTION METHODOLOGY

This section introduces features of incidence matrix and general equation utilized (for both analytical techniques) to compute magnetic potentials of each node and detent force. Mover, stator and air-gap EC modules are described as matrices, these matrices are merged and solved using incidence matrix method [18] utilizing MATLAB Software.

Incidence matrix A of a circuit having *x* nodes and *y* branches is *x* x *y* matrix, in which:

$$\boldsymbol{A}_{x,y} = \begin{cases} 0, & when\ branch\ y\ is\ not\ connected\ to\ node\ x, \\ -1, & when\ branch\ y\ ends\ to\ node\ x, \\ 1, & when\ branch\ y\ begins\ from\ node\ x. \end{cases} \tag{7}$$

Magnetic potentials of each node are calculated by using (8) that ultimately helps to compute magnetic flux through each flux tube [15]:

$$V = (\boldsymbol{A}.\boldsymbol{\Lambda}.\boldsymbol{A}^t)^{-1}.(\boldsymbol{A}.\boldsymbol{\Lambda}.\mathrm{E}), \tag{8}$$

where, E is mmf source in each branch (n x 1 vector), and Λ is n x n diagonal matrix representing permeance of each branch.

Equation (9) is generalized form of MST method and is used to compute detent force of LPMFSM by extracting radial and axial component of magnetic flux density from FE Analysis:

$$F_x = \frac{GCD(N_{ms}, N_{sp}).L}{\mu_0} \int_0^{L_{Perp}} B_x(x,y).B_y(x,y).dx, \tag{9}$$

where, N_{ms} is number of mover slots, N_{sp} is number of stator teeth, and L_{Perp} is axial length in x-direction.

A. Equivalent magnetic circuit

In this paper, EMC methodology accounts six different air-gap equivalent circuit modules (termed as Segment No. 1 - 6) and does not account permeances of mover and stator equivalent modules for node potential calculations. Reluctance/Permeance network for Phase "C" of 12/14 LPMFSM is shown in Fig. 8 (a). Permeances of different types of flux tubes identified for Segment No. 1 – Segment No. 6 are tabulated in Table 3. Reluctance network of 12/14 LPMFSM air-gap EC modules corresponding to six different stator segments is generated and solved for magnetic potentials using (8). Equation (9) is used to compute detent force by extracting air-gap magnetic flux density (as shown in Figs. 9 (a-b)) from FE Analysis.

B. Lumped parameter equivalent magnetic circuit

Lumped parameter reluctance network of LPMFSM's consists of six air-gap EC modules (illustrated in Table 3), fourteen stator EC modules (Fig. 6 (b)), and twelve mover EC modules (Fig. 7 (b)). Permeance of stator back iron and stator tooth is calculated using (2) and (3), respectively. Permeance of mover back iron, mover tooth, and mover leakage is calculated using (4), (5), and (6), respectively.

Table 3: Types of flux tubes in six different air-gap EC modules

Segment Number	Flux Tube Number								
	1	**2**	**3**	**4**	**5**	**6**	**7**	**8**	**9**
1	d	d	b	d	c	d	d	c	d
2	d	c	d	f	d	c	d	d	-
3	d	d	c	d	f	d	c	d	-
4	d	c	d	b	d	d	d	d	b
5	d	d	d	b	d	c	d	d	-
6	b	d	c	d	d	d	d	c	-

Reluctance/Permeance network for Phase "C" of 12/14 LPMFSM is shown in Fig. 8 (b) which clearly indicates that LPEMC methodology accounts stator back iron and teeth, mover back iron, teeth, and leakage, and air-gap EC modules. Magnetic potential calculations are done using (8). Equation (9) is used to compute detent force by extracting mover teeth magnetic flux density (as shown in Figs. 9(c-d)) from FE Analysis.

VI. COMPARISON OF ANALYTICAL TECHNIQUES

Open-circuit flux linkage obtained for mover pole pitch from analytical modelling techniques (EMC and LPEMC) are compared with globally accepted FE Analysis results in Fig. 10 (a) and Fig. 10 (b), respectively. Point-to-point percentage error is shown in Fig. 11 (a). Analysis of open-circuit flux linkage of reveals that EMC methodology suffers with errors less than ~8.5%, while LPEMC methodology shows errors less than ~7.5%. Peak-to-peak open-circuit flux linkage obtained by analytical methodologies (EMC and LPEMC) and FE Analysis is shown in Fig. 11 (b).

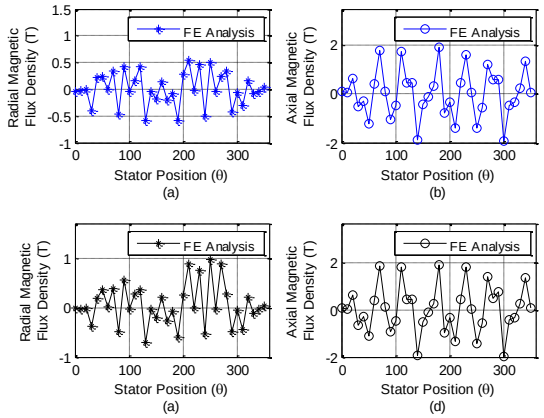

Fig. 9. FE Analysis magnetic flux densities: (a) air-gap radial component, (b) air-gap axial component, (c) mover radial component, and (d) mover component.

Detent force for periodic boundary of one mover pole pitch is also computed by EMC and LPEMC methodology, and compared with corresponding FE Analysis results in Fig. 12 (a) and Fig. 12 (b), respectively. Point-to-point percentage error of detent force is shown in Fig. 13 (a), and reveals that EMC methodology suffers with errors less than ~18%, while LPEMC methodology shows errors less than ~14.5%. Average detent force obtained by analytical methodologies (EMC and LPEMC) and FE Analysis is shown in Fig. 13 (b). Limitations of analytical methodologies are: (a) does not account magnetic saturation, (b) permeability of iron core is assumed to be infinite, and (c) analytical methodologies provide shuffled values of calculated quantities and sorting must be done to compare wave-forms.

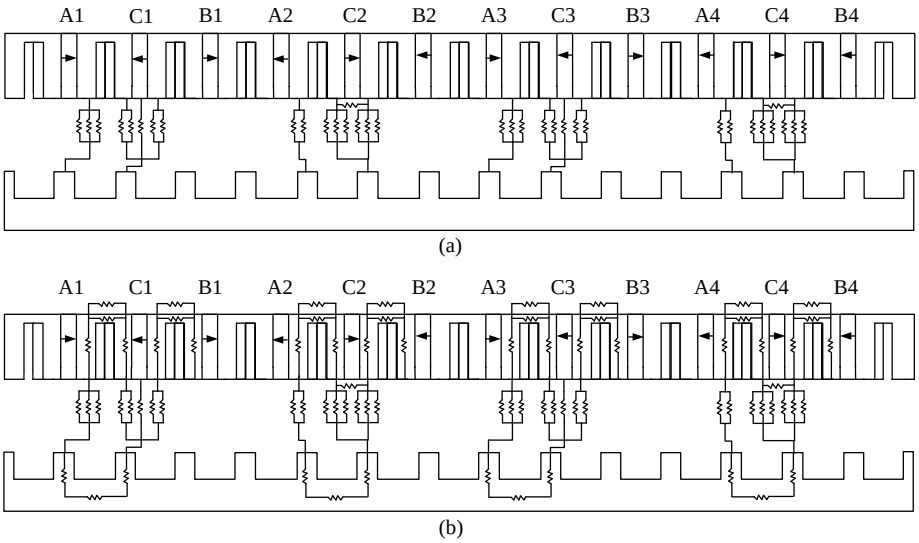

Fig. 8. Phase C reluctance/permeance network: (a) EMC and (b) LPEMC.

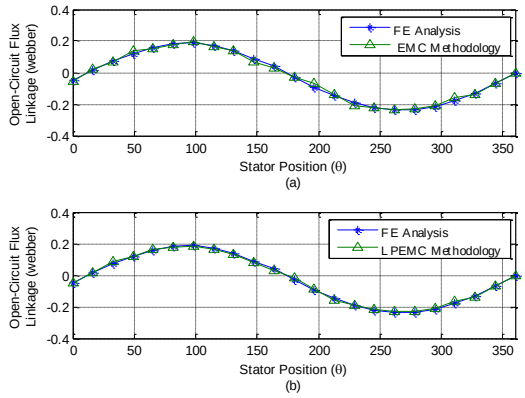

Fig. 10. Open-circuit flux linkage: (a) comparison of FE Analysis and EMC, and (b) comparison of FE Analysis and LPEMC.

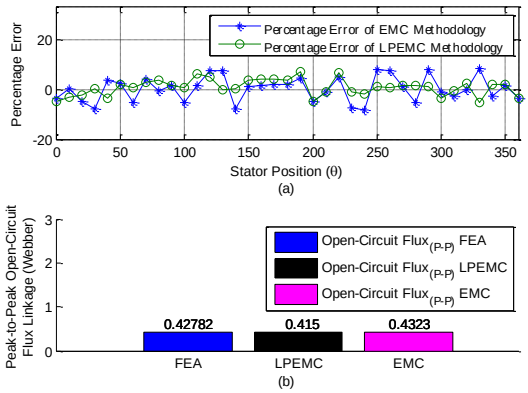

Fig. 11. Open-circuit flux linkage: (a) point-to-point percentage error, and (b) peak-to-peak open-circuit flux linkage.

VII. CONCLUSION

Aim of this paper is to simulate novel single sided LPMFSM using JMAG Commercial FEA Package v. 14, develop two analytical modelling techniques for prediction of no-load characteristics, i.e., open-circuit flux linkage and detent force, and compare both analytical methodologies with corresponding globally accepted FE Analysis results. Analytical technique No. 1 (EMC) represents peak error of less than ~8.5% for open-circuit flux linkage and ~18% for detent force, while analytical technique No. 2 (LPEMC) represents peak error of less than ~7.5% for open-circuit flux linkage and ~14.5% for detent force. This paper validates both analytical techniques and made authors to recommend LPEMC approach for initial design of LPMFSM.

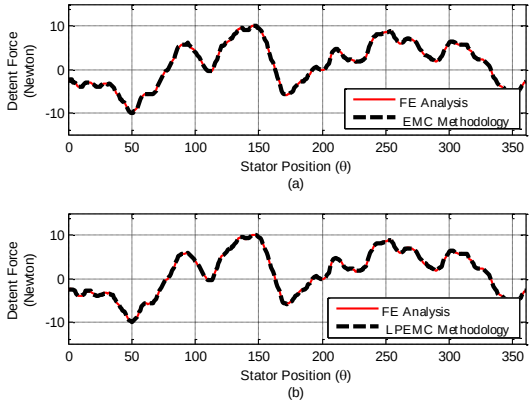

Fig. 12. Detent force: (a) comparison of FE Analysis and EMC, and (b) comparison of FE Analysis and LPEMC.

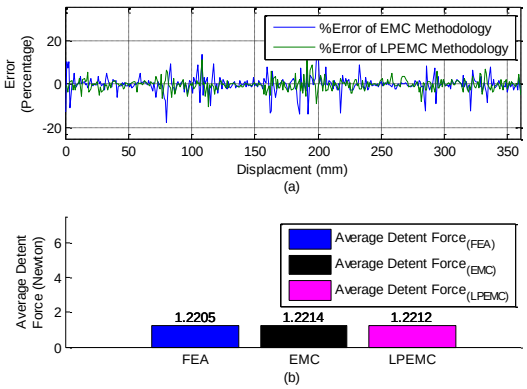

Fig. 13. Detent force, (a) point-to-point percentage error, and (b) average detent force.

REFERENCES

[1] J. F. Gieras and Z. J. Piech, *Linear Synchronous Motors: Transportation and Automation Systems*. Boca Raton, FL, USA: CRC, 2000.

[2] C. F. Wang, J. X. Shen, Y. Wang, L. L. Wang, and M. J. Jin, "A new method for reduction of detent force in PM flux-switching linear motors," *IEEE Trans. Magn.*, vol. 45, no. 6, pp. 2843-2846, 2009.

[3] J. Ou, Y. Liu, M. Schiefer, and M. Doppelbauer, "A novel PM-free high-speed linear machine with amorphous primary core," *IEEE Trans. Magn.*, vol. 53, no. 11, 2017.

[4] C. Hwang, P. Li, and C. Liu, "Design and analysis of a novel hybrid excited linear flux switching permanent magnet motor," *IEEE Trans. Magn*., vol. 48, no. 11, pp. 2969-2972, Nov. 2012.

[5] R. Cao, M. Cheng, C. Mi, W. Hua, X. Wang, and W. Zhao, "Modeling of a complementary and modular linear flux-switching permanent magnet motor for urban rail transit applications," *IEEE Trans. Energy Convers*., vol. 27, no. 2, pp. 489-497, June 2012.

[6] A. Gandhi and L. Parsa, "Thrust optimization of a flux-switching linear synchronous machine with yokeless translator," *IEEE Trans. Magn.*, vol. 49, no. 4, pp. 1436-1443, Apr. 2013.

[7] L. Huang, H. Yu, M. Hu, J. Zhao, and Z. Cheng, "A novel flux-switching permanent-magnet linear generator for wave energy extraction application," *IEEE Trans. Magnetics*, vol. 47, pp. 1034-1037, 2011.

[8] S. Ouagued, Y. Amara, and G. Barakat, "Comparison of hybrid analytical modelling and reluctance network modelling for predesign purposes," *Mathematics and Computers in Simulation*, vol. 130, pp. 3-21, 2016.

[9] Y. Laoubi, M. Dhifli, G. Verez, Y. Amara, and G. Barakat, "Open circuit performance analysis of a permanent magnet linear machine using a new hybrid analytical model," *IEEE Trans. Magn.*, vol. 51, no. 3, Mar. 2015.

[10] M. F. J. Kremers, J. J. H. Paulides, and E. A. Lomonova, "Toward accurate design of a transverse flux machine using an analytical 3-D magnetic charge model," *IEEE Trans. Magn.*, vol. 51, no. 11, Nov. 2015.

[11] Y. Yao, Q. Lu, X. Huang, and Y. Ye, "Fast calculation of detent force in PM linear synchronous machines with considering magnetic saturation," *IEEE Trans. Magn.*, vol. 53, no. 6, June 2017.

[12] H. Hu, X. Liu, J. Zhao, and Y. Guo, "Analysis and minimization of detent end force in linear permanent magnet synchronous machines," *IEEE Trans. Industrial Electronics*, vol. 65, no. 3, Mar. 2018.

[13] B. Zhang, M. Cheng, R. Cao, Y. Du, and G. Zhang, "Analysis of linear of flux-switching permanent-magnet motor using response surface methodlogy," *IEEE Trans. Magn.*, vol. 50, no. 11, Nov. 2014.

[14] Y. Laoubi, M. Dhifli, G. Barakat, and Y. Amara, "Hybrid analytical modeling of a flux switching permanent magnets machines," *International Conference on Electrical Machines (ICEM)*, pp. 1018-1023, 2014.

[15] N. Ullah, F. Khan, W. Ullah, M. Umair, and Z. Khattak, "Magnetic equivalent circuit models using global reluctance networks methodology for design of permanent magnet flux switching machine," *15th International Bhurban Conference on Applied Sciences and Technology (IBCAST)*, pp. 397-404, 2018.

[16] C. Wang, J. Shen, Y. Wang, L. Wang, and M. Jin, "A new method for reduction of detent force in permanent magnet flux-switching linear motors," *IEEE Trans. Magn.*, vol. 45, no. 6, pp. 2843-2846, June 2009.

[17] V. Ostovic, *Dynamics of Saturated Electric Machines*. Berlin Heidelberg, Germany: Springer-Verlag New York Inc., 1989.

[18] L. O. Chuaand and P. M. Lin, *Computer-Aided Analysis of Electronic Circuits-Algorithms and Computational Techniques*. Prentice Hall, Englewood Cliffs, NJ, USA, 1975.

Noman Ullah received his B.Sc. and M.Sc. degree in Electrical (Power) Engineering from University of Engineering & Technology, Peshawar, Pakistan in 2012 and 2015, respectively. He is working as Lecturer at COMSATS University Abbottabad, Pakistan. He is Reviewer of IEEE

Transactions on Transportation Electrification. His research interests includes analytical modelling of electrical machines.

Faisal Khan received his Ph.D. Electrical Engineering degree from Universiti Tun Hussein Onn Malaysia in 2016. He is working as Assistant Professor at COMSATS University Abbottabad, Pakistan.

Abdul Basit received his Ph.D. from the Department of Wind Energy of the Technical University of Denmark in 2015. Basit is currently employed as an Assistant Professor at UET Peshawar, Pakistan.

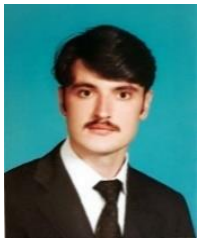

Wasiq Ullah received his B.Sc. degree in Electrical (Power) Engineering from COMSATS University Abbottabad, Pakistan in 2018 and currently enrolled as M.Sc. Electrical (Power) Engineering student from COMSATS University Abbottabad, Pakistan. He is working as Research Member with Electrical Machine Design Group.

Naseer Ahmad received his Bachelor degree in Electrical (Power) Engineering in 2015 from University of Engineering and Technology, Peshawar, Pakistan and currently enrolled as M.Sc. Electrical (Power) Engineering student form COMSATS University Abbottabad, Pakistan.

The 2D Type-3 Non-Uniform FFT in CUDA

Amedeo Capozzoli, Claudio Curcio, Angelo Liseno, and Jonas Piccinotti

Università di Napoli Federico II
Dipartimento di Ingegneria Elettrica e delle Tecnologie dell'Informazione
Via Claudio 21, I 80125 Napoli (Italy)
a.capozzoli@unina.it

Abstract ─ We present the parallel implementation on Graphics Processing Units (GPUs) of a type-3 Non-Uniform FFT (NUFFT) approach, namely, of a NUFFT for which data and results are located at irregular points. The performance of the algorithm is assessed against that of a parallel implementation of the same algorithm on multi-core CPUs using OpenMP directives.

Index Terms ─ CUDA, Non-Uniform FFT, OpenMP.

I. INTRODUCTION

In many areas of electromagnetics, the need arises of evaluating Non-Uniform Discrete Fourier Transforms (NUDFTs), namely DFTs with data and/or results on irregular grids. Imaging [1], solutions to differential and integral equations [2], fast array antenna analysis [3] and synthesis [4] and antenna diagnosis [5] are just few examples.

Unfortunately, the calculation of a NUDFT does not promptly benefit of the use of standard Fast Fourier Transforms (FFTs) ($O(NlogN)$ complexity) which on the contrary require Cartesian input and output grids. This solicited the development of Non-Uniform FFT (NUFFT) algorithms capable to perform accurate computations essentially with the same $O(NlogN)$ complexity. NUFFTs achieve such a complexity by exploiting fast and accurate pre- and/or post-interpolation stages, properly tailored to the problem at hand, from/to regular to/from irregular grids.

Apart from fast approaches, efficiency and effectiveness in the calculation of a NUDFT can be pursued also by adopting high performance, massively parallel computing (HPC) platforms as Graphics Processing Units (GPUs). The use of HPC is of course not disjoined from the numerical aspect since the appropriate exploitation of parallel hardware requires the choice of conveniently parallelizable algorithms.

The purpose of this paper is to present and discuss the parallel implementation on GPUs of a type-3 NUFFT approach (henceforth, NUFFT-3), namely, of a NUFFT for which data and results are located at irregular points.

NUFFT-3 finds important applications from the electromagnetic point of view. Indeed, it has been applied in [6] to effectively compute the aggregation and disaggregation stages of the Fast Multipole Method. Furthermore, it is of interest in aperiodic antenna analysis and synthesis when the far-field pattern is required into a non-uniform grid of the spectral plane [7].

NUFFT-3 has been originally dealt with using Gaussian interpolation windows [1, 8] or as a combination of type-1 and type-2 transforms [9, 10]. Most recently, we have improved [6] the choice of the Gaussian window parameters over that detailed [1, 8]. Despite type-1 and type-2 NUFFTs have been extensively researched also from the point of view of GPU approaches, it should be also noticed that only standard sequential CPU implementations for the NUFFT-3 have appeared throughout the literature, with neither parallel CPU nor GPU cases ever dealt with. Accordingly, in this paper, a NUFFT-3 GPU implementation is described for the first time.

Our approach is based on the recent scheme in [6]. Its timing performance is assessed against that of a parallel implementation of the same algorithm on multi-core CPUs, while its accuracy performance is pointed out thanks to a case of electromagnetic interest.

II. TYPE-3 NUFFT

Let $\{(x_i, y_i)\}_{i=0}^{N-1}$ be a set of N 2D non equispaced points, $\{f\}_{i=0}^{N-1}$ a set of corresponding coefficients and $\{(s_k, t_k)\}_{k=0}^{K-1}$ a set of K 2D non-equispaced spectral points. The transformation:

$$F_k = \sum_{i=0}^{N-1} f_i \, e^{-jx_i s_k} e^{-jy_i t_k}, \tag{1}$$

is referred to as a 2D NUDFT-3 [1].

The problem of computing the F_k's amounts to the fact that Eq. (2) is not in the form of a standard Discrete Fourier Transform (DFT) since spatial and spectral points are irregularly located. Fortunately, reformulating the problem by interpolating non-uniformly sampled exponentials by uniformly sampled ones is in order. This can be achieved by the Poisson formula [11]:

$$e^{-j\xi x} = \sqrt{2\pi} \frac{\sum_{m\epsilon\mathbb{Z}} \mathcal{F}[\Phi(\xi) e^{-j\xi x}; m] e^{jm\xi}}{\sum_{m\epsilon\mathbb{Z}} \Phi(\xi + 2m\pi) e^{-j2m\pi x}}, \tag{2}$$

where Φ is an appropriate interpolation window and

Submitted On: June 4, 2017
Accepted On: March 26, 2018

$\mathcal{F}$ denotes Fourier transformation. Accordingly, a computational scheme analogous to a Non-Uniform FFT (NUFFT) procedure of Type-3 [1, 6] can be set up. We briefly illustrate such a procedure by assuming the window functions Φ to be Gaussian [1, 6].

A. Step #1

The contributions from non-uniformly spaced input sampling points corresponding to $\mathbf{exp}[-\boldsymbol{j}(\boldsymbol{s_k x_i} + \boldsymbol{t_k t_i})]$ are "spread" by Gaussian windows $\mathbf{exp}[-\frac{x^2}{4\tau_x} - \frac{y^2}{(4\tau_y)}]$ with parameters $\boldsymbol{\tau_x}$ and $\boldsymbol{\tau_y}$, to a regular grid $(\boldsymbol{n\Delta x}, \boldsymbol{m\Delta y})$. Step #1 thus produces [6]:

$$f_\tau^{-\sigma}(n\Delta x, m\Delta y) = \frac{e^{[\sigma_x(n\Delta x)^2+\sigma_y(n\Delta y)^2]}}{\sqrt{4\sigma_x\sigma_y}} \sum_{i=0}^{N-1} f_i e^{-\left[\frac{(n\Delta x - x_i)^2}{4\tau_x}+\frac{(m\Delta y - y_i)^2}{4\tau_y}\right]}, \quad (3)$$

where the presence of the exponential function $\mathbf{exp}[\boldsymbol{\sigma_x x^2} + \boldsymbol{\sigma_y y^2}]$ is related to the pre-compensation of the Gaussian window used in Step #3. Due to the rapid decay of the exponential functions, $\boldsymbol{f_i}$ significantly contributes to only few samples of $\boldsymbol{f_\tau^{-\sigma}(n\Delta x, m\Delta y)}$. On defining $\boldsymbol{Int}[\boldsymbol{\alpha}]$ as the nearest integer to $\boldsymbol{\alpha}$, by letting $\boldsymbol{\xi_i} = \boldsymbol{Int}[\frac{x_i}{\Delta x}]$ and $\boldsymbol{\eta_i} = \boldsymbol{Int}[\frac{y_i}{\Delta y}]$, $\boldsymbol{i = 0, \dots, (N-1)}$, denote the nearest regular grid points to $\frac{x_i}{\Delta x}$ and $\frac{y_i}{\Delta y}$, respectively, and assigning $\boldsymbol{n' = n - \xi_i}$ and $\boldsymbol{m' = m - \eta_i}$, the contributions of each $\boldsymbol{f_i}$ to $\boldsymbol{f_\tau^{-\sigma}(n\Delta x, m\Delta y)}$ can be ignored when $|\boldsymbol{n'}| > \boldsymbol{m_{sp}}$ or $|\boldsymbol{m'}| > \boldsymbol{m_{sp}}$, where $\boldsymbol{m_{sp}}$ is a parameter properly selected according to the required accuracy. In other words, the summation in (3) provides a non-negligible contribution to only $(\boldsymbol{2m_{sp} + 1}) \times (\boldsymbol{2m_{sp} + 1})$ terms.

B. Step #2

The "spread" contributions are transformed to the spatial frequency domain via a standard FFT. In other words, the second step produces

$$F_\tau^{-\sigma}(p\Delta s, q\Delta t) \cong \frac{\Delta x \Delta y}{4\pi} \sum_{n=-\frac{M_{rx}}{2}}^{\frac{M_{rx}}{2}} \sum_{m=-\frac{M_{ry}}{2}}^{\frac{M_{ry}}{2}} f_\tau^{-\sigma}(n\Delta x, m\Delta y)\, e^{-jpn\Delta x\Delta s} e^{-jqm\Delta y\Delta t}. \quad (4)$$

C. Step #3

The "transformed" data are interpolated from the FFT output uniform grid to the non-uniform grid $\{(\boldsymbol{s_k}, \boldsymbol{t_k})\}_{\boldsymbol{k=0}}^{\boldsymbol{K-1}}$, again by Gaussian windows, $\mathbf{exp}[-\frac{s^2}{4\sigma_x} - \frac{t^2}{(4\sigma_y)}]$. The final output is thus:

$$F_k = \frac{\Delta s \Delta t}{4\pi\sqrt{\tau_x\tau_y}} e^{\tau_x s_k^2} e^{\tau_y t_k^2} \sum_{n=-\frac{M_{rx}}{2}}^{\frac{M_{rx}}{2}} \sum_{m=-\frac{M_{ry}}{2}}^{\frac{M_{ry}}{2}} F_\tau^{-\sigma}(n\Delta s, m\Delta t)\, e^{-\frac{(n\Delta s - s_k)^2}{4\sigma_x}} e^{-\frac{(m\Delta t - t_k)^2}{4y}}. \quad (5)$$

Similarly to Step #1, the presence of the Gaussian functions $\mathbf{exp}[\boldsymbol{\tau_x s^2} + \boldsymbol{\tau_y t^2}]$ is related to the post-compensation of the Gaussian windows used in Step #1. Again due to the rapid decay of the involved exponential functions, $\boldsymbol{F_\tau^{-\sigma}(n\Delta s, m\Delta t)}$ significantly contributes to only few samples of $\boldsymbol{F_k}$. In particular, on letting $\boldsymbol{\tilde{\xi}_k} = \boldsymbol{Int}[\frac{s_k}{\Delta s}]$ and $\boldsymbol{\tilde{\eta}_k} = \boldsymbol{Int}[\frac{t_k}{\Delta t}]$, $\boldsymbol{k = 0, \dots, K-1}$, and $\boldsymbol{p' = p - \tilde{\xi}_k}$ and $\boldsymbol{q' = q - \tilde{\eta}_k}$, the contributions of $\boldsymbol{F_\tau^{-\sigma}(n\Delta s, m\Delta t)}$ can be ignored when $|\boldsymbol{p'}| > \boldsymbol{m_{sp}}$ and $|\boldsymbol{q'}| > \boldsymbol{m_{sp}}$. In other words, the summation in (5) can be truncated to $(\boldsymbol{2m_{sp} + 1}) \times (\boldsymbol{2m_{sp} + 1})$ terms.

D. "Centering" and choice of the relevant parameters

Before applying the above procedure, a "centering" of the input and output sampling points is required, see [6]. Similarly, for the choices of $\boldsymbol{\Delta x}$, $\boldsymbol{\Delta y}$, $\boldsymbol{\tau_x}$, $\boldsymbol{\tau_y}$, $\boldsymbol{\sigma_x}$, $\boldsymbol{\sigma_y}$ and $\boldsymbol{m_{sp}}$, see [6] and Table 1. In such a table, $\boldsymbol{R}$ is chosen strictly larger than 2, $\boldsymbol{X} = \boldsymbol{max}\{|\boldsymbol{x_i'}|\}_{\boldsymbol{n=0}}^{\boldsymbol{N-1}}$, $\boldsymbol{Y} = \boldsymbol{max}\{|\boldsymbol{y_i'}|\}_{\boldsymbol{n=0}}^{\boldsymbol{N-1}}$, $\boldsymbol{S} = \boldsymbol{max}\{|\boldsymbol{s_k'}|\}_{\boldsymbol{k=0}}^{\boldsymbol{K-1}}$, $\boldsymbol{T} = \boldsymbol{max}\{|\boldsymbol{t_k'}|\}_{\boldsymbol{k=0}}^{\boldsymbol{K-1}}$ following the "centering" step, $\boldsymbol{m_{sp}} = \boldsymbol{2\pi b}$, b is chosen according to successive approximations of the following equation:

$$\boldsymbol{b} = \frac{\boldsymbol{1}}{\boldsymbol{\gamma}} \boldsymbol{log}\left(\frac{\boldsymbol{4\alpha}}{\boldsymbol{e}}\boldsymbol{b} + \frac{\boldsymbol{9\alpha}}{\boldsymbol{e}}\right), \quad (6)$$

with

$$\boldsymbol{\alpha} = \boldsymbol{2} + \frac{\boldsymbol{1}}{\sqrt{\boldsymbol{2\pi}}}, \quad \boldsymbol{\gamma} = \boldsymbol{\pi^2}\left(\boldsymbol{1} - \frac{\boldsymbol{2}}{\boldsymbol{R^2}}\right), \quad (7)$$

and e is the requested accuracy [6].

Table 1: Summary of the parameters choice

$\Delta x = \frac{\pi}{RS}$	$\Delta y = \frac{\pi}{RT}$
$\Delta s = \frac{2\pi}{\Delta x M_{rx}}$	$\Delta t = \frac{2\pi}{\Delta y M_{ry}}$
$M_{rx} \geq 2\left(\frac{XSR^2}{\pi} + 2\pi Rb\right)$	$M_{ry} \geq 2\left(\frac{YTR^2}{\pi} + 2\pi Rb\right)$
$\tau_x = b\Delta x^2$	$\tau_y = b\Delta y^2$
$\sigma_x = b\Delta s^2$	$\sigma_y = b\Delta t^2$

III. IMPLEMENTATIONS

The illustrated NUFFT-3 algorithm has been implemented in both GPU and CPU multithreaded codes. The latter has been developed in C++ parallelized by OpenMP directives. Such a choice matches with the use of the CUDA environment to develop the GPU counterpart. Both the codes are structured according to the above Steps and have been highly optimized. To perform a fair comparison, the CPU implementation has benefitted of most of the optimizations applied to the CUDA code. In the following, some implementation details are presented.

A. GPU multithreaded implementation

Step #1. The computation of $f_\tau^{-\sigma}(n\Delta x, m\Delta y)$ is the

most critical step of the three and requires some care since different approaches could be envisaged. The difficulty is due to the need of "pseudo-randomly" accessing the elements of $f_\tau^{-\sigma}(n\Delta x, m\Delta y)$ when selecting the $(2m_{sp}+1)\times(2m_{sp}+1)$ indices (n,m) to which each coefficient f_i contributes.

A first parallelization strategy would be to commit a thread to compute a single matrix element $f_\tau^{-\sigma}(n\Delta x, m\Delta y)$ using a 2D thread grid with each thread associated to a different (n,m) couple. However, in this way, the generic thread should perform, due to the "pseudo-random" filling, a time-consuming browsing of the input elements to establish whether they contribute to the committed element of $f_\tau^{-\sigma}(n\Delta x, m\Delta y)$ or not.

As an alternative, our code employs a 1D thread grid with each thread associated to a different input index i. In this, way, the browsing is avoided since each thread is assigned to a different f_i and updates the $(2m_{sp}+1)\times(2m_{sp}+1)$ corresponding elements of $f_\tau^{-\sigma}(n\Delta x, m\Delta y)$. However, notice that, by this solution, more than one thread may need to simultaneously update (namely, read, compute and store a new value) the same $f_\tau^{-\sigma}(n\Delta x, m\Delta y)$. When this happens, a "race condition" occurs. To preserve data integrity, atomic operations have been exploited ensuring the semantic correctness of the algorithm. Although serializing the updating operations, they have become very fast in the recent CUDA architectures.

Step #2. This step is implemented using cuFFT and a customized CUDA kernel executing the FFT shift operation.

Step #3. Parallelizing the calculation of Eq. (5) is easier than that of eq. (3), as it does not suffer from race condition hazards. The implemented code employs a 1D thread grid where each thread is associated to a different output index k.

B. CPU multithreaded implementation

Step #1 has been implemented in an analogous to what done for the CUDA case. More in detail, the parallelization has been applied according to the input index i. Accordingly, the `#pragma omp atomic` has been used to prevent race conditions.

Concerning Step #2, the FFT step required by Eq. (4) has been achieved by the multithreaded version of the FFTW routine contained in the Intel Math Kernel Library (MKL).

Finally, Step #3 has been implemented analogously to that done for the CUDA case, by applying the parallelization strategy to the output index k.

IV. NUMERICAL RESULTS

The performance of GPU and CPU implementations has been assessed with random spatial and spectral location vectors (x_i, y_i) and (s_k, t_k) and random complex coefficients f_i. Two cases have been considered: the case when $N = K,\ K = 2^p,\ p = 8, \ldots, 20$ and the case when $N = K^2,\ K = 2^p,\ p = 8,9,10$. The former case is of interest for scattering by impenetrable objects, i.e., when only the scatterer's surface must be discretized, where discretization is essentially 1D and $N = K$. The latter case, instead, is of interest for the scattering by penetrable objects [12], i.e., when the scatterer's interior must be discretized, where discretization is essentially 2D and $N = K^2$. The computational speeds have been measured by averaging a number of 10 realizations for each individual test. The codes have been run on an Intel Core i7-6700K, 4GHz, 4 cores (8 logical processors), equipped with an NVIDIA GTX 960 card, compute capability 5.2.

Figure 1 (upper panel) displays, for the case $N = K$, the partial timings of the three mentioned calculation steps for the CUDA implementation. As it can be seen, the most computationally demanding operations are the spatial and spectral interpolations, namely, Step #1 and Step #3. Despite employing atomic operations, the spatial interpolation step is only slightly more demanding than the spectral implementation. This is due to two reasons. First, the implementation of Step #1 has been highly optimized. Second, atomic operations are extremely fast for the Maxwell architecture.

Table 2: Partial timings (in [ms]) for the CUDA implementation and for the case $N = K^2$

K	Step #1	Step #2	Step #3
256	38	0.8	0.9
512	150	0.8	0.9
1024	600	1.0	0.9

The partial timings of the three steps for the case $N = K^2$ and for the CUDA implementation are reported in Table 2. Due to the larger number of input points as compared to the output ones, now Step #1 is the most time consuming part of the computation.

Figure 1 (lower panel) displays the speedup obtained by the parallel GPU implementation, against the OpenMP one, for the two cases of $N = K$ and $N = K^2$. The GPU timings do not comprise CPU-GPU memory movements, as the use of the NUFFT-3 CUDA code is understood to be exploited within a fully GPU-based computation. As it can be seen, speedups of up to 8 are obtained for the case $N = K$. Larger speedups are achieved for the case $N = K^2$ since, in this case, Step #1 is the most time consuming one and more significantly benefits of the GPU acceleration. Notably, according to Amdahl's law [13], the amount of achievable speedup depends on the portion of the code that can be parallelized. A speedup of 5/6 can be already considered a satisfactory result.

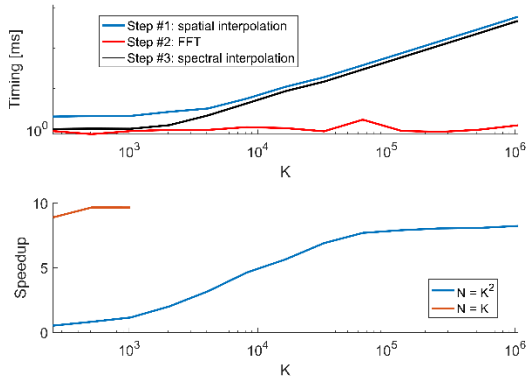

Fig. 1. Upper panel: Partial timings of the CUDA implementation: case $N = K$. Lower panel: Speedup of the CUDA implementation against the OpenMP one. Red line: case $N = K$. Blue line: case $N = K^2$.

We now show a test case of electromagnetic interest. As already mentioned, aggregation and disaggregation in the FMM [14, 15] can be effectively performed by a NUFFT-3 [6]. We consider a 2D Electric Field Integral Equation (EFIE) applied to the scattering of a perfectly conducting circular cylinder of radius a=2.5λ under TM (Transverse Magnetic) plane wave illumination. The cylinder's surface has been discretized in 1536 segments, grouped in 32 clusters [6]. More in detail, we compare the cases when aggregation and disaggregation are evaluated in an exact way and by a NUFFT-3. The good accuracy of the NUFFT-based version is witnessed by the very low relative root mean square error between the two compared cases and equal to $8.78 \cdot 10^{-11}$.

V. CONCLUSIONS AND FUTURE DEVELOPMENTS

We have discussed the parallel implementation on GPUs of a NUFFT-3. State-of-art implementation of NUFFT-3 are only sequential CPU ones. Here, the performance of the GPU approach has been compared to that of a purposely developed parallel CPU one using OpenMP directives. The provided parallelizations amount at a proper organization of the computations, but they do not alter the accuracy of the parallelized NUFFT-3 algorithm.

We now plan to extend the approach to the use of more efficient interpolating window functions.

REFERENCES

[1] J.-Y. Lee and L. Greengard, "The type 3 non-uniform FFT and its applications," *J. Comput. Phys.*, vol. 206, no. 1, pp. 1-5, June 2005.

[2] C. Liu, *et al.*, "Focusing translational variant bistatic forward-looking SAR data based on two-dimensional non-uniform FFT," *Progr. Electromagn. Res. M*, vol. 37, pp. 1-10, 2014.

[3] A. Capozzoli, *et al.*, "Fast CPU/GPU pattern evaluation of irregular arrays," *ACES J.*, vol. 25, no. 4, pp. 355-372, Apr. 2010.

[4] A. Capozzoli, C. Curcio, A. Liseno, and G. Toso, "Fast, phase-only synthesis of aperiodic reflect-arrays using NUFFTs and CUDA," *Progr. Electromagn. Res.*, vol. 156, pp. 83-103, 2016.

[5] A. Capozzoli, C. Curcio, and A. Liseno, "NUFFT-accelerated plane-polar (also phaseless) near-field/far-field transformation," *Progr. Electromagn. Res. M*, vol. 27, pp. 59-73, 2012.

[6] A. Capozzoli, C. Curcio, A. Liseno, and A. Riccardi, "Parameter selection and accuracy in type-3 non-uniform FFTs based on Gaussian gridding," *Progr. Electromagn. Res.*, vol. 142, pp. 743-770, 2013.

[7] A. Capozzoli, C. Curcio, A. Liseno, and G. Toso, "Fast, phase-only synthesis of aperiodic reflect-arrays using NUFFTs and CUDA," *Progr. Electromagn. Res.*, vol. 156, pp. 83-103, 2016.

[8] A. Dutt and V. Rokhlin, "Fast fourier transforms for nonequispaced data," *SIAM J. Sci. Comp.*, vol. 14, no. 6, pp. 1368-1393, 1993.

[9] F. Knoll, *et al.*, "Reconstruction of undersampled radial PatLoc imaging using total generalized variation," *Magn. Reson. Med.*, vol. 70, no. 1, pp. 40-52, July 2013.

[10] S. Tao, *et al.*, "NonCartesian MR image reconstruction with integrated gradient nonlinearity correction," *Med. Phys.*, vol. 42, no. 12, pp. 7190-7201, 2015.

[11] R. M. Trigub and E. S. Belinsky, *Fourier Analysis and Approximation of Functions*. Springer Science+ Business Media, Dordrecht, NL, 2004.

[12] A. Capozzoli, *et al.*, "Efficient computing of far-field radiation in two dimension," *IEEE Antennas Wireless Prop. Lett.*, vol. 16, pp. 2034-2037, 2017.

[13] G. M. Amdahl, "Validity of the single processor approach to achieving large scale computing capabilities," *Proc. of the AFIPS '67 Conf.*, Atlantic City, NJ, pp. 483-485, Apr. 18-20, 1967.

[14] M. Vikram and B. Shanker, "An incomplete review of fast multipole methods–from static to wideband–as applied to problems in computational electromagnetics," *ACES J.*, vol. 24, no. 2, pp. 79-108, Apr. 2009.

[15] C. Craeye, *et al.*, "Efficient numerical analysis of arrays of identical elements with complex shapes," *ACES J.*, vol. 24, no. 2, pp. 224-232, Apr. 2009.